

Doctoral dissertation

**The control of the coordination structure using nitrile
group and alkyl group for ether-based polymer
electrolytes realizing high lithium-ion conductivity**

(エーテル系ポリマー電解質での高リチウムイオン伝導性を
実現するニトリル基とアルキル基を用いた配位構造の制御)

March, 2022

Ryansu Sai

Graduate School of Sciences and Technology for Innovation

Yamaguchi University

**The control of the coordination structure using nitrile
group and alkyl group for ether-based polymer
electrolytes realizing high lithium-ion conductivity**

(エーテル系ポリマー電解質での高リチウムイオン伝導性を
実現するニトリル基とアルキル基を用いた配位構造の制御)

Ryansu Sai

Department of Applied Chemistry

Graduate School of Sciences and Technology for Innovation

Yamaguchi University

Ube, Japan

2022

1

Contents

General Introduction

Background of the work	5
Outline of the work	38

Chapter 1 **Role of polar side chains in Li⁺ coordination and transport properties of polyoxetane-based polymer electrolytes**

1.1 Introduction	48
1.2 Experimental section	49
1.3 Results and discussion	53
1.4 Conclusions	68

Chapter 2 **Steric effect on Li⁺ coordination and transport properties in polyoxetane-based polymer electrolytes bearing nitrile groups**

2.1 Introduction	72
2.2 Experimental section	73
2.3 Results and discussion	77
2.4 Conclusions	92

Chapter 3 **Importance of lithium coordination structure to lithium-ion transport in polyether electrolytes with cyanoethoxy side chains: an experimental and theoretical approach**

3.1 Introduction	95
3.2 Experimental section	97
3.3 Results and discussion	103
3.4 Conclusions	125

Chapter 4	Effect of alkyl side chain length on the lithium-ion conductivity for polyether electrolytes: importance of lithium-ion coordination structure	
4.1	Introduction	129
4.2	Experimental section	131
4.3	Results and discussion	142
4.4	Conclusions	164
	General conclusions	168
	Publication list	170
	Acknowledgements	171



**YAMAGUCHI
UNIVERSITY**

General introduction

Background of the work

1. Lithium-ion battery

Battery is an energy storage device you can carry with, which enables using electronic devices without external power supply. Furthermore, rechargeable battery, called secondary battery, have made it possible to carry more sophisticated electronic devices like laptop, smartphone, and tablet. However, these electronic devices would not fit in your pocket or handbag without the development of lithium-ion battery (LIB).

Lithium-ion battery is the ideal energy storage device mainly due to high volumetric and gravimetric energy density (called energy density and specific energy, respectively) (Figure 1), which is derived by lithium with high negative electrode potential (-3.05 V vs. standard hydrogen electrode, SHE).¹ High energy density and high operating voltage (nominal value is 4.0 V)² of LIB are matched for the demand of miniaturization of electronic devices. Lithium-ion battery quickly became popular from 1991, when Sony first commercialized, as you can see from the increase of sales (Figure 2).² In 2004, number of LIB sales in Japan reached 50% of secondary battery sales, and then it has further grown to nearly 70% in 2017.³

In addition to the application for small electronic devices, LIB has been founded to be used for large electronic devices such as electric vehicles (EVs) which requires high energy density and high operating voltage. The replacement of gasoline-powered vehicles to EVs was matched the social demand of the reduction of greenhouse gas and particulate emissions generated from gasoline-powered vehicles driving. The contribution to low environmental impact by EVs will be maximized when the renewable energy, such as solar-power, wind-power, geothermal-power, and hydropower, becomes the main energy sources.

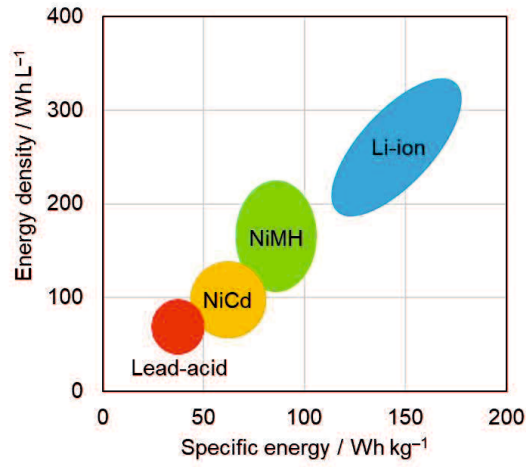


Figure 1 Energy density of conventional secondary batteries, where NiCd means nickel-cadmium battery, NiMH is nickel-hydrogen battery, and Li-ion is lithium-ion battery.^{2,4} Energy density means the volumetric energy density, and specific density means the gravimetric energy density.

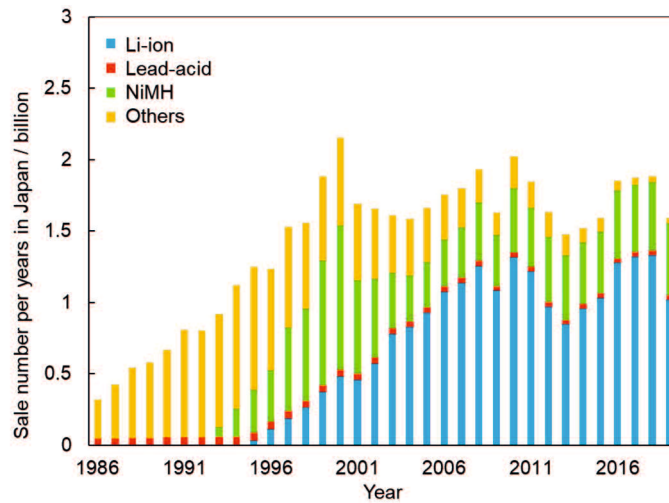


Figure 2 Transition of sale number per years of secondary batteries in Japan from 1986 to 2019.^{3,5}

Lithium-ion battery changed our lifestyle and natural environment, and three lithium-ion battery researchers, Michael Stanley Whittingham, John Bannister Goodenough, and Akira Yoshino, awarded the Nobel Prize in Chemistry 2019 for the contribution of the realization of smart devices which are essential to our life and the reduction of our dependence on fossil fuels.⁶

However, as you can see from Figure 2, number of LIB sales in the domestic market has become saturated since 2008, probably because of the sales of the small electronic devices have slow down. On the other hand, since 2013, sales number has begun to increase again, which directly reflects the sales of in-vehicle batteries as mentioned above (Figure 3). It is expected that the usage of LIBs continuous to be developed for more extensive purpose in the future, such as EVs and so on. In comparison, the safety issues of LIB have got more attention.

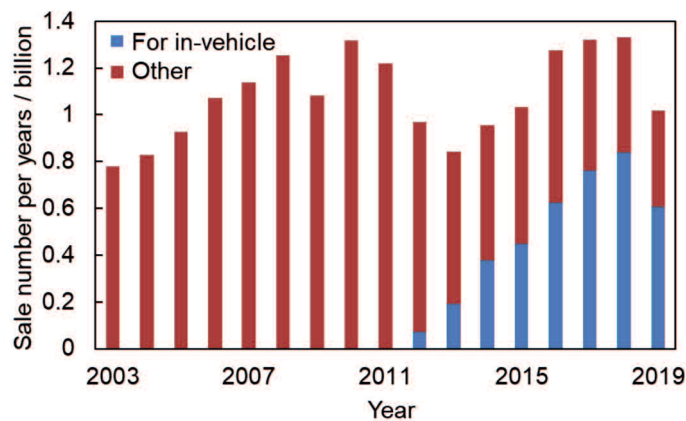


Figure 3 Transition of sale number per years of LIBs for each application in Japan from 2003 to 2019.⁵

2. Safety issues

Terrible fire accident caused from LIBs are often reported. For example, series of fire accidents of Boeing 787 instilled us distrust in LIBs.^{7,8} Even after these serious accidents, perfect countermeasures against accidents could not be taken, and the number of accidents caused by LIBs continue to increase (Figure 4). It is difficult to completely solve this problem since high performances of LIBs depend on instability of lithium.

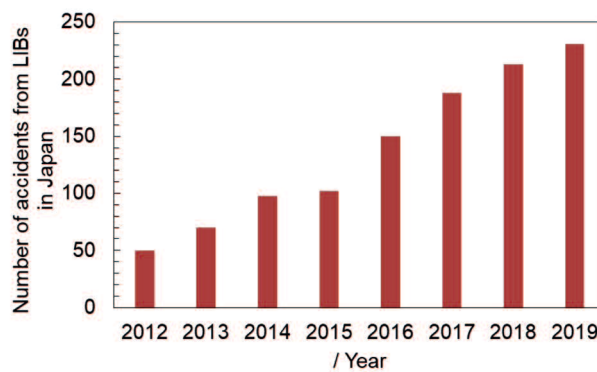


Figure 4 Transition of accident number due to LIBs in Japan from 2012 to 2019.^{9,10}

The accidents of LIB are due to the constituent materials break out thermal runaway, which is the chained (electro)chemical reaction continuous the heat generation and promoted by heats generated itself. Thermal runaway can be initiated under high temperature state in LIB over the thermal decomposition temperature of constituent materials ($\geq 80^{\circ}\text{C}$).^{11,12} And then, internal temperature of battery reaches around 130°C , polymer separator meltdown causes the fatal short circuit between negative/ positive electrodes contacting over a wide surface, conducting thermal runaway.¹¹ High temperature state, the trigger of thermal runaway, is caused by several case; an internal heat from , Joule heat from high ohm resistor or from abrupt large current during short circuits, and reaction heat of (electro)chemical or unwanted side reactions, in addition to the case that battery stored in a high temperature. Figure 5 shows the major accident causes of LIBs.^{7,8,13,14}

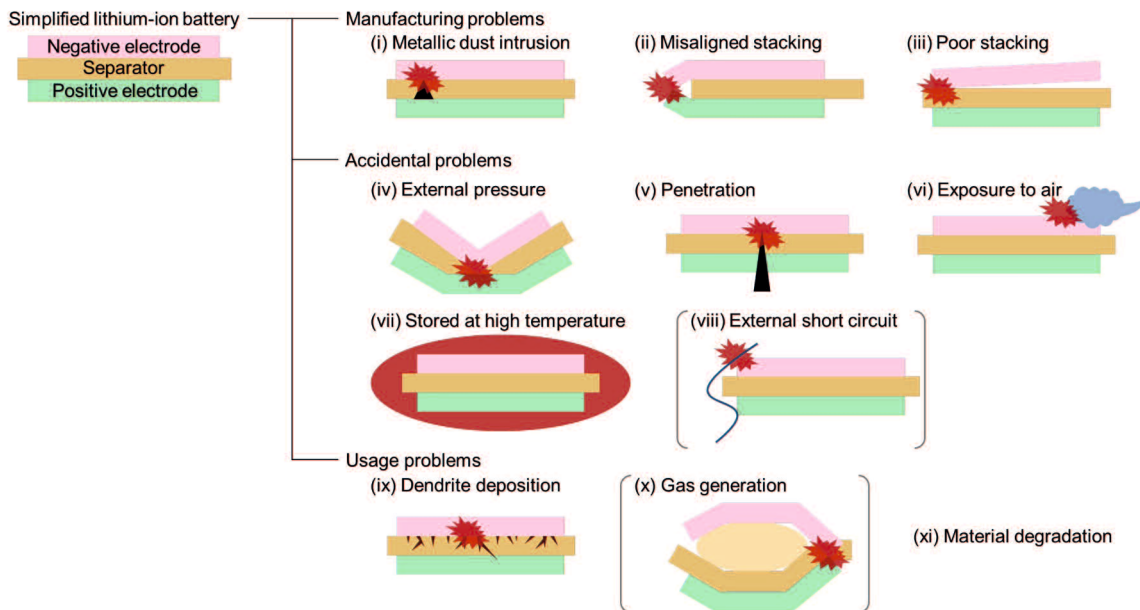


Figure 5 Fire accident causes of LIB.^{7,8,13,14} Some problems have been caused by defective manufactured batteries; (i) metallic dusts intrude from metal case or insufficient cleaning parts, which penetrate separators and lead short circuits, (ii) misaligned stacking permits the electrodes can contact to short circuit beyond the separators with, (iii) poor stacking of electrodes and separators limits lithium-ion pathways for separators and leads high ohm resistor. Some problems have been caused by sudden accidents such as electronic devices fall or car collision; (iv) external pressure distorts the battery and leads short circuit, (v) penetration of the electronic conductor makes short circuit directly, (vi) exposing air leaked from broken battery case reacts with negative electrode under charged state which generates excessive heat, (vii) battery stored at high temperature such as in uncooled warehouses or hot regions, and (viii) external short circuits due to improper battery usage, but which can be avoid with protection circuits. Some problems have been caused during using the battery; (ix) lithium dendrite deposition due to the lithium unaccommodated into electrode structures under severe conditions, (x) internal pressure from generated gas from electrolytes degradation distorts the battery and leads short circuit, but which can be avoid with venting system, and (xi) material degradation under severe conditions accelerates heat generation.

A short circuit will occur with the applying strong impact or something penetration into LIB.¹⁴ Furthermore, the cell case of LIB is damaged, the charged materials can react with air and cause thermal runaway. The damage of cell case is caused by not only physical impact but also moisture corrosion. For other cases, when LIB charged with excessive high rate, lithium dendrites often grow between the electrode,^{15,16} leading a short circuit. Internal short circuit also can be caused by internal high pressure due to the generated gas from materials

degradation by thermal/ electrochemical reasons.¹⁷ Although the venting system have reduced the risk of internal pressure, these thermal/electrochemical damages still can generate heat and it lead to thermal runaway. These material degradations further cause capacity loss during charge/discharge cycles.¹⁸ Overcharging accelerates those damages,¹⁹ though the protection circuits have suppressed some overcharging.

The fire accident will become even more dire with the application expansion and the upsize of LIBs in the future. One of the causes the serious fire accident is flammable organic solvents used in the electrolyte. It is one of the fundamental solutions to replace the electrolyte to a flame-retardant material. Battery safety improvement is one of the mainly focus for materials research such like that.

3. Materials research

Lithium-ions (Li^+) and electrons are taken out from the negative electrode and taken into the positive electrode as shown below during battery discharging (Figure 6);



Electrons flow from battery and into an external electronic device as an electric current, and at the same time, the electrolyte transport Li^+ between the two electrodes. Commercially available LIB consists of stacked multiple layers of electrodes, current collector, and separator impregnated with electrolyte (Figure 7).

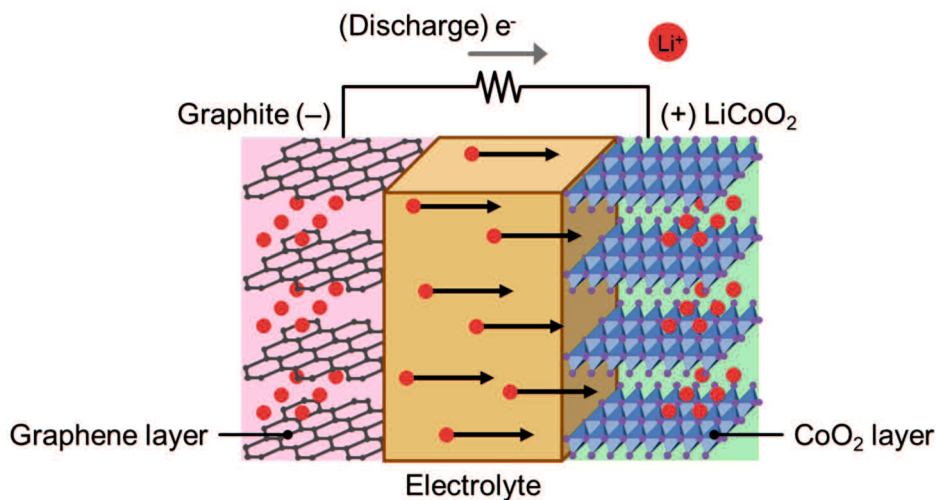


Figure 6 Lithium-ion (Li^+) behavior in LIB during discharge,² where (-) electrode shows negative electrode constructed with graphite and (+) electrode shows positive electrode constructed with lithium cobalt (III) oxide (LiCoO_2). Lithium(-ion) behaves during battery discharging as follows; (i) stored lithium between graphene layers for negative electrode is oxidated, (ii) negative electrode takes out electron and Li^+ into external electronic devices and into electrolyte, respectively, (iii) Li^+ is conducted in electrolytes to counter electrode, and then (iv) Li^+ intercalates between cobalt oxide layers and reduction with the connection of electron flowed out from external electric devices.

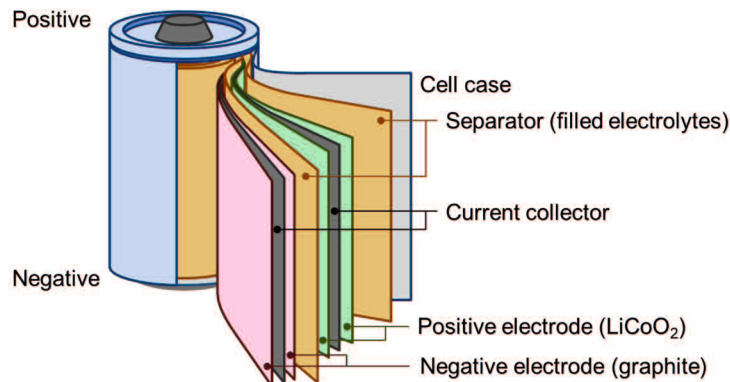


Figure 7 The constitution of LIB with cylindrical shape, which is one of the famous battery shapes.^{4,20} Electrode materials (graphite for negative and lithium cobalt (III) oxide for positive) is mixed with some additives; poly(vinylidene fluoride) or other insoluble polymers as the binder and carbon material as electron conductive agents, and these mixture applied on the current collector; aluminum foil for positive electrode and copper foil for negative electrode. The separator between electrodes separates the electrodes do not contact each other to short circuit and holds electrolytes.

Materials research for LIB has been required coexistence of high battery safety and high battery performance. The performance of LIBs heavily depends on the negative/ positive electrodes, solid electrolyte interface (SEI), and electrolytes as following;

- Battery operating voltage is determined with the gap between the redox potentials of stored lithium into each positive and negative electrodes.
- Battery capacity is mainly dominated with specific capacity correlating the density of reactable lithium containment in each electrode materials.
- Charge/ discharge cycle stability of LIB needs thermal, mechanical, and electrochemical stabilities of constitution material, which can protect with solid electrolyte interface (SEI).
- Rate properties of battery are governed with Li^+ transport properties in the electrolyte.

I will focus each material composing LIB below to understand the research has been done up to today's and next LIBs and how to have developed them.

3.1. Negative electrode

Active materials for negative electrode are one of the dominant factors for the performance of LIB. Graphite is mainly used for the negative electrode in commercial LIBs due to some advantages; (i) the comparable redox potential with lithium metal (0.05 V vs. Li/Li⁺) and relatively high specific capacity (372 mAh g⁻¹),²¹ (ii) the ease of battery production due to high chemical stability, and (iii) the suppression of lithium dendrite formation since graphene-layered structure stores lithium between its layers stably (Figure 6).²² Akira Yoshino won the Nobel Prize in 2019 for the development of the LIB system using graphite negative electrode.^{6,23} Although graphite contributes both battery power and safety, some concerns remained for structural stability during long cycle life.²⁴ Therefore, lithium titanate (Li₄Ti₅O₁₂, LTO) is also used commercially for the negative electrode in addition to graphite.²⁵ Lithium titanate has high thermal and structural stability, in addition to practical redox potential (1.6 V vs. Li/Li⁺) and specific capacity (175 mAh g⁻¹).²⁶

On the other hand, there is the demand to further increase battery energy density. The optimal solution is the application of the lithium metal to negative electrode, but it is difficult to avoid the short-circuit risk due to the lithium dendrites precipitation. Instead, group IV elements, silicon, germanium, and tin, have been attention for next negative electrode materials due to their advantages; (i) high lithium capacity of 4.4 equivalent mole and which results high specific capacity (4200 mAh g⁻¹, 1620 mAh g⁻¹, and 993 mAh g⁻¹, respectively) and (ii) lithium stored stably with the forming alloy compared than lithium metal.²⁷ The challenges with these materials mainly focus on how solve the concerns about the volume change under the (de-)lithiated state using encapsulation material, geometric strategy, or compounds with other elements.^{27,28,29}

3.2. Positive electrode

The active material for positive electrode is also important for the performance of LIB. Lithium metal oxide is normally used for the active material of positive electrode,²⁵ which can store lithium between the layers of the metal oxides (Figure 6). These layered structure for positive electrode was started by Whittingham, one of the Nobel laureates for LIB.^{6,30} Following that, Goodenough *et al.* reported Lithium cobalt (III) oxide (LiCoO_2 , LCO) having relatively high specific capacity (155 mAh g^{-1}), high stability under the lithiated state, and high voltage for the positive electrode counter to lithium metal electrode ($3.9 \text{ V vs. Li/Li}^+$).^{25,31,32} Therefore, lithium cobalt (III) oxide (LCO) and LCO-derivate ceramics, lithium nickel cobalt aluminum oxide ($\text{LiNi}_{0.80}\text{Co}_{0.15}\text{Al}_{0.05}$, NCA) and lithium nickel manganese cobalt oxide ($\text{LiNi}_x\text{Mn}_y\text{Co}_{1-x-y}\text{O}_2$, NMC), are applied for the commercial LIB.^{31,33} However, these materials can be decomposed under high temperature state ($\geq 100 \text{ }^\circ\text{C}$) and generates O_2 gas,³⁴ sometimes promotes thermal runaway.^{11,17} Thermal stable materials, lithium iron (II) phosphate (LiFePO_4 , LFP) and lithium manganese (III, IV) oxide (LiMn_2O_4 , LMO), are also used for positive electrode commercially.³¹

Although lithium metal oxides have performed the sufficient operation for current electronic devices, positive electrode materials are required higher energy density for future demand. Recent material research for positive electrode seems to be directed for the realization of next-generation lithium batteries using lithium-metal, such as lithium-sulfur battery or lithium-air battery (Figure 8).^{35,36} Both batteries still have the concern about cycle stability, and researchers mostly focus on the solvation of this concern.^{37,38}

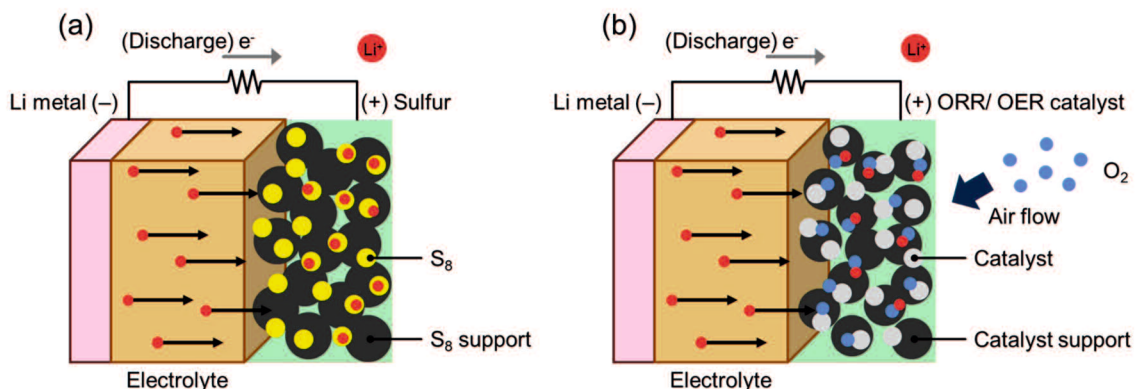


Figure 8 The construction of next-generation lithium batteries. (a) Lithium-sulfur battery,^{39,40} where (-) electrode shows negative electrode constructed with lithium metal and (+) electrode shows positive electrode constructed with sulfur (S₈) on/ in supporting material such as porous carbon. (b) Lithium-air battery,^{38,40} where (-) electrode shows negative electrode constructed with lithium metal and (+) electrode shows positive electrode constructed with the catalyst on supporting materials such as porous carbon. During battery discharging, air flows into positive electrode composites and the catalyst accelerates oxygen reduction reaction (ORR). And oxygen evolution reaction (OER) is occurred during battery charging at positive electrode.

3.3. Solid electrolyte interface (SEI)

Electrolyte materials are often decomposed (electro)chemically and form passivation layer on electrodes during the battery operation, called solid interface electrolyte (SEI).⁴¹ Solid electrolyte interface (SEI) is important factor for the safety and cycle stability of LIB which can suppress the decomposition of electrolytes and electrodes.²⁴

Electrolyte materials, solvent molecules and anions, cause the reductive decomposition mainly during battery first charging, and decomposition multi products deposit on the electrode with microphase cohesion as a mosaic (Figure 9a).⁴² These decomposition products cover the electrode surface and suppress the unwanted reactions such as further reduction of electrolytes and the co-intercalation of solvent molecules with Li⁺ into electrode structure (Figure 9b).⁴² Solid electrolyte interface is needed to include the component with low electron conductivity, high Li⁺ conductivity, and structural stability for high battery performance.⁴³ Components consisting SEI is determined by the electrolyte materials and influenced by electrode surface.⁴⁴ For more functionalization of SEI, it is widely researched

that artificial SEI using Li^+ conducting polymers⁴⁵ or using metal oxides,⁴⁶ and electrolyte additives controlling SEI component.^{47,48}

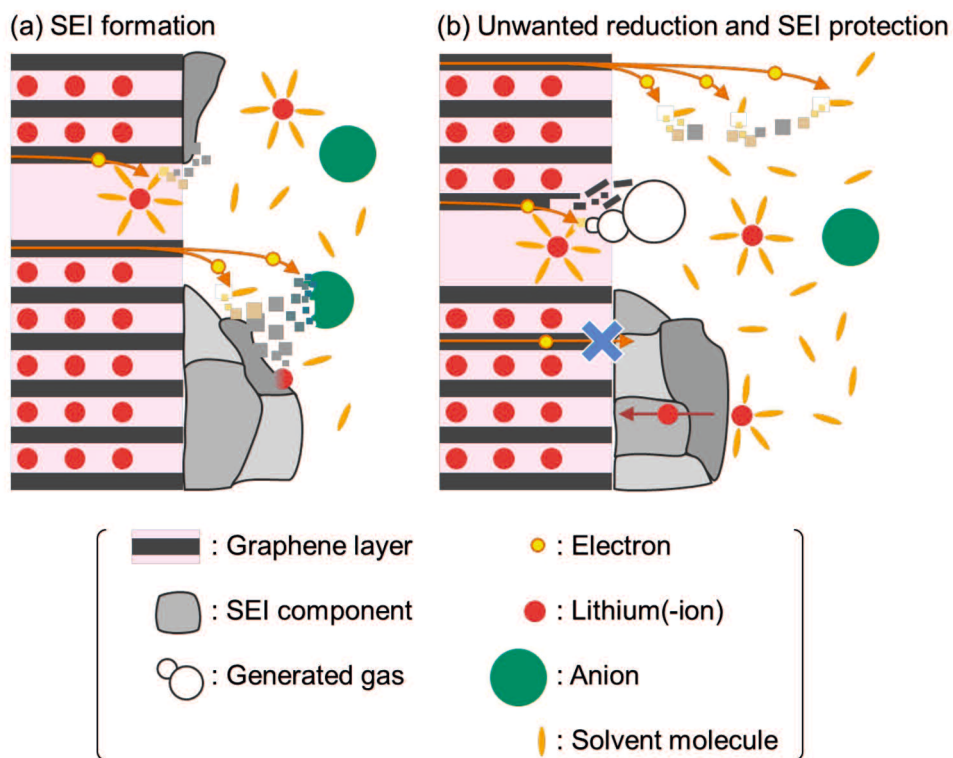


Figure 9 The mechanism of (a) solid electrolyte interface (SEI) formation on graphite of negative electrode during battery first charging and (b) SEI protection of graphite against unwanted reduction such as the excessive reduction of solvent molecule and the graphite destruction by gas generated from solvent molecule degradation, caused by exuded electron and co-intercalated solvent molecule, respectively.

I listed the electrolyte as the important materials for LIB in the introduction of this section, in addition to negative/ positive electrodes and solid electrolyte interface (SEI). This dissertation mainly focuses on the electrolytes, thus which will be picked up and be discussed in detail in next section.

4. Electrolyte research

Electrolytes play very important role for Li^+ transport between the electrodes during battery charging/ discharging (Figure 6), and dividing negative and positive electrodes electronically in the battery. Electrolytes govern some important performances of LIBs for (i) battery safety and (ii) rate properties.

Electrolytes heavily affect the safety of LIB as mentioned section 2. and section 3.3. Low thermal/ electrochemical stability of electrolyte materials can lead thermal runaway, though the design strategy of solid electrolyte interface (SEI) can suppress some risks of battery accidents. Battery rate performances is limited by Li^+ conductive rate, electron conductive rate, or lithium reaction rate in LIB. Especially, Li^+ conduction in the electrolyte is the rate-limiting step for LIB performance, among multi steps moving electrons or Li^+ in each material or at them interface (Figure 10).⁴⁹ For improving LIB performance, electrolytes must be designed to satisfy high thermal/ electrochemical stability (or to form stable SEI) and to high lithium-ion transport properties.

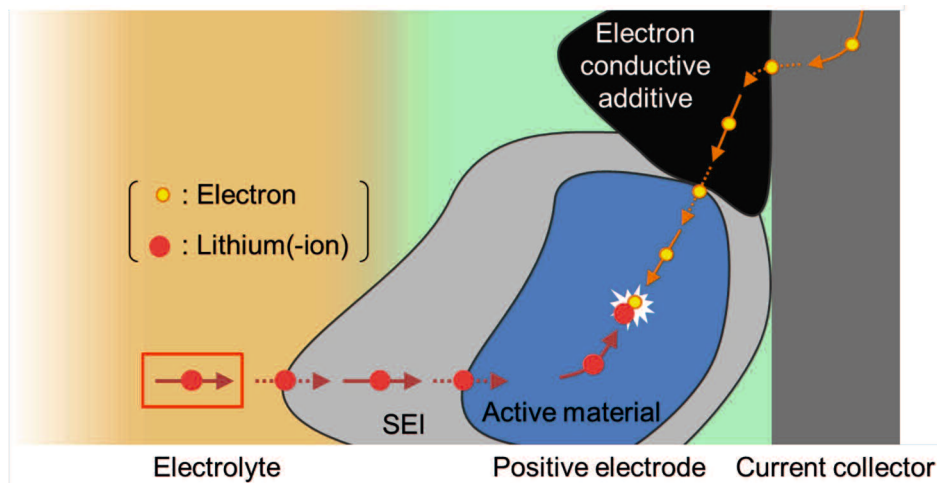


Figure 10 The motion model of Li^+ and electrons around the positive electrode during battery charging. Electrons move through current collector, electron conductive additive (carbon), active material (lithium metal oxide), and the interfaces between each material phases. Lithium-ions move through electrolyte, solid electrolyte interface (SEI), active material (lithium metal oxide), and the interfaces between each material phases. Finally, Li^+ connects with electron and be reduced in active material. Lithium-ion transport in the electrolyte is the rate-limiting step of LIB performance.

4.1. Liquid electrolyte

Liquid electrolytes are the most popular electrolytes applied to almost battery including LIB, which basically composed with liquid solvents and metal salts consisted with reactive metal-ions, here in Li^+ , and counter anion. Liquid solvents and lithium salts should be selected for high Li^+ conductivity, as not to compromise electrochemical stability.

4.1.1. Lithium-ion conductivity for liquid electrolyte

Lithium-ion conductivity is defined with the multiplying the amount and the mobility of Li^+ .

4.1.1.1. The amount of lithium-ion

The amount of Li^+ is equal to the amount of dissolved lithium salt into electrolytes. There are three hypothetical stages of lithium salt dissolution for subdivided processes (Figure 11);^{50,51} (i) dispersion of lithium salt crystal to ion pair, (ii) dissociation of ion pair to Li^+ and counter anion, and (iii) solvation, meaning the multiple interaction of solvent molecules to ion. Salt dissolution is mostly governed by (ii) dissociation and (iii) solvation process. These two processes relate to the interaction of anion and solvent molecule to Li^+ .

For highly dissociation of ion pair, it needs to counteract electrostatic interaction between Li^+ and counter anion. Electrostatic interaction works between Li^+ and polar group having localized electron density on the anion structure. Thus, electron density is required to be delocalized widely over anion structure for weakened electrostatic interaction. Design of anion structure can delocalize electron density using large anion size and electron-withdrawing group (Figure 12).⁵² Electrostatic interaction is also relaxed by the dielectric field effect, which brought by high polarity of solvents described as dielectric constant (ϵ).⁵⁰ Dielectric constant of solvents is affected by intramolecular polarization induced by solvent polar groups (Figure 13).

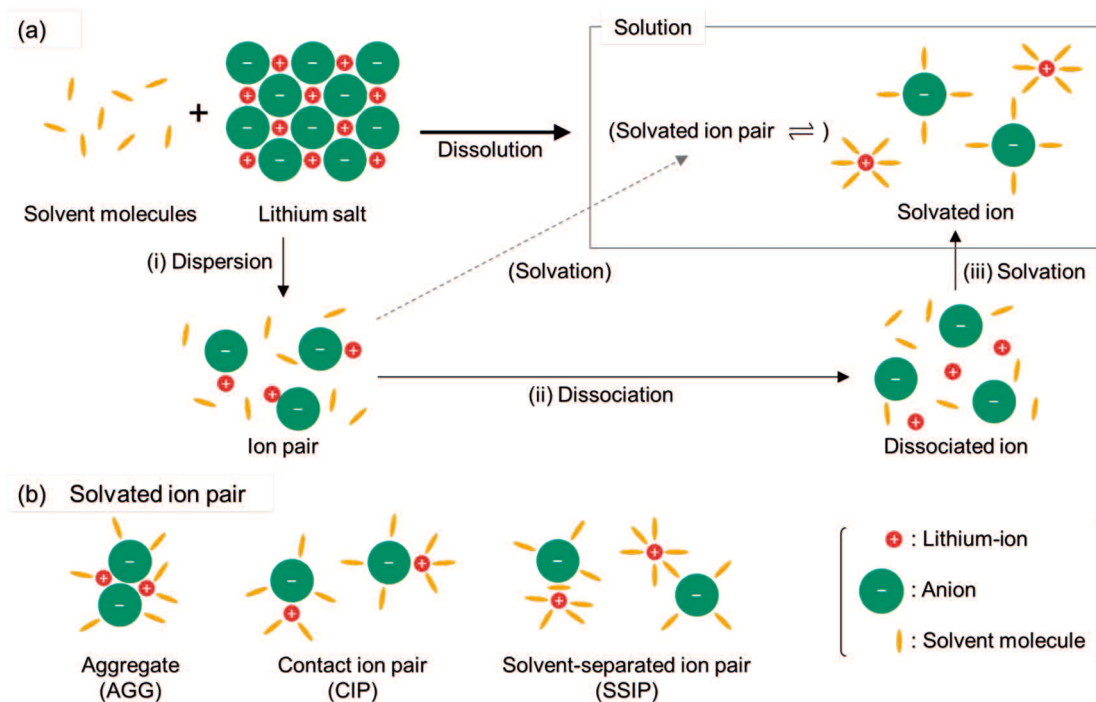


Figure 11 (a) Subdivided processes of lithium salt dissolution into the solvent including three hypothetical stages; (i) lithium salt dispersion to ion pair into solvent, (ii) ion pair dissociation to each Li^+ and counter anion, and (iii) solvation of ions by solvent molecules. Un-dissociated ion pairs are often solvated and equilibrates with solvated ions. (b) Several states of solvated ion pair; aggregation of multiple ions (AGG), maintaining contact ion pair (CIP), and solvent separated ion pair (SSIP).

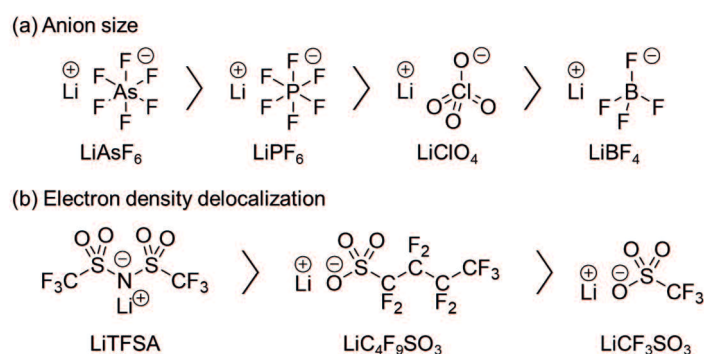


Figure 12 Typical lithium salt structures and the order of lithium salt dissociability which agrees with the order of (a) anion size and (b) electron density delocalization.⁵² The names of lithium salt are described as following; LiAsF_6 is lithium hexafluoroarsenate, LiPF_6 is lithium hexafluorophosphate, LiClO_4 is lithium perchlorate, LiBF_4 is lithium tetrafluoroborate, LiTfSA is lithium bis(trifluoromethanesulfonyl)amide (also called lithium bis-(trifluoromethane sulfonyl)imide, LiTFSI), $\text{LiC}_4\text{F}_9\text{SO}_3$ is lithium perfluorobutanesulfonate, and LiCF_3SO_3 is lithium triflate.

Dissociated ions are stabilized by the multiple electrostatic interaction with solvent molecules, called solvation. Solvent molecules interact to Li^+ with polar groups having electron donating ability, described as donor number (DN) (Figure 13).⁵³ Electron donating ability increases with some polar groups having highly localized electron density such as ether group, carbonate group, amide groups, sulfoxide group, and so on. Lithium-ion stabilization is also affected by the steric structure of solvent molecules occupying Li^+ solvation site (4–6). For example, Li^+ is stabilized by chelating effect, but these stabilization is inhibited by steric crowding around Li^+ .⁵⁴ The solvation to anion also can be the influential factor to contribute salt dissolution.^{55,56} Solvents have the accepting ability of donated electron from anion, which described as acceptor number (AN) (Figure 13)⁵³ Accepting ability is brought by electron-withdrawing group on solvent structure, which leads the localization of low electron density. But the anion solvation less/no contributes on the salt dissolution compared than the Li^+ solvation due to isolated stability with delocalized electronic density.

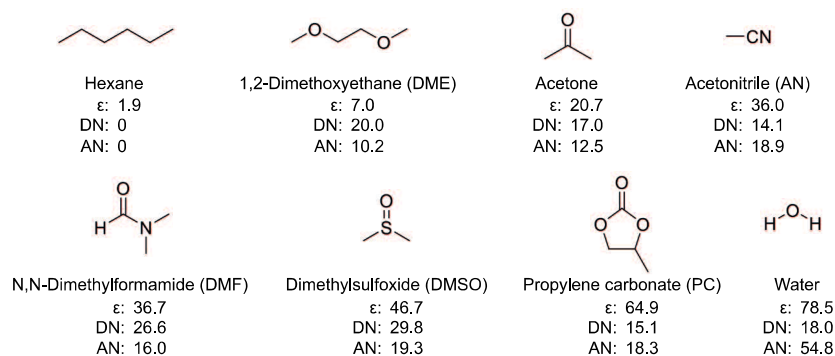


Figure 13 Typical solvent structure and the descriptors of its polar properties, where ϵ is dielectric constant, DN is donor number, and AN is acceptor number.^{53,57,58,59}

Ion pair is sometimes solvated maintaining un-dissociation, when the stabilization of ion pair dissociation is not enough with excessive high salt concentration or with strong electrostatic interaction between anion and Li^+ . Solvated ion pair can form several structures around ions; aggregation of multiple ions (AGG), contact ion pair (CIP), and solvent-separated ion pair (SSIP) (Figure 11).^{60,61} For these conditions, the amount of Li^+ is determined with the equilibrium between ion pair and dissociated ions, including stable solvated ions or transition de-solvated ions.

4.1.1.2. The mobility of lithium-ion

The mobility of Li^+ is evaluated as self-diffusivity of dissociated lithium-ion. Lithium-ions are transported with a combination of two transport mechanism in the electrolytes; (i) Li^+ migrates with solvent molecules maintaining the solvation structure, and (ii) Li^+ is exchanged from interacting solvent molecules to free solvent molecules (Figure 14).⁶²

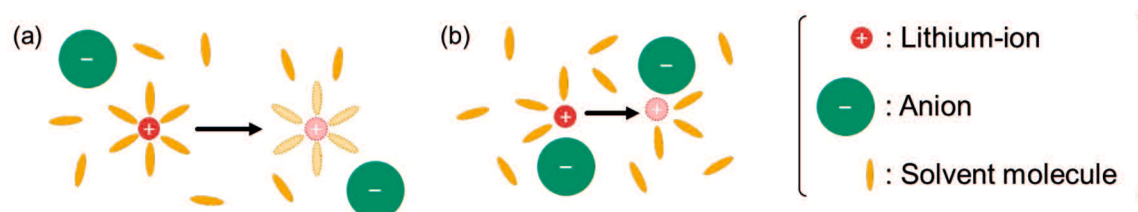


Figure 14 Lithium-ion transport mechanisms in liquid electrolytes; (a) Li^+ migrates maintaining the solvation structure, and (b) Li^+ is exchanged from solvating molecules to free molecules.

Solvent molecules transport Li^+ by the self-diffusion of solvation structure (Figure 14a), which is often called Vehicle mechanism. This mechanism governs Li^+ transport when a stable solvation structure is formed, such as ether-based electrolyte including 1,2-dimethoxyethane (DME) (Figure 13).⁶³ Solvated Li^+ diffuses like a spherical particle, and it is important that low viscosity and small solvation structure around Li^+ for high self-diffusivity, according to Stokes-Einstein relation.⁵⁶ Electrolyte viscosity heavily depends on the original solvent viscosity, which is related to intermolecular interaction and molecular weight. The interaction between Li^+ and anion and/or solvent molecules also can be the influential factor for the electrolyte viscosity increasing.

Lithium-ion also can be transported by the exchange from interacting solvent to free solvent, like Grotthuss mechanism (proton exchange mechanism in aqueous solution). Ion exchange mechanism often called ion hopping mechanism, when the ion migration is independent and rapid from solvent molecule migrations. The mechanism works when Li^+ form relatively unstable solvation structure with solvent molecules.^{62,63} The electrolytes using nitrile-based or sulfone-based had reported to transport Li^+ majorly with the ion exchange mechanism at high salt concentration.^{60,64} Viscosity is still one of the influential factors for this mechanism, but it was suggested that the transport of Li^+ is not completely

depends on the viscosity.⁶⁵ Instead of the viscosity, steric structure around Li^+ was suggested to be important for frequently and continuous ion exchange.⁶⁴

The electrolytes determine the battery performance, and which required (i) a high polar property for the dissolution of lithium salt, and (ii) a low viscosity not to inhibit Li^+ self-diffusion. In addition, the interaction and steric structure around Li^+ is also important factor affecting not only the differences of the Li^+ transport mechanism, but also the electrolyte properties relating the transport mechanism.

4.1.2. Conventional liquid electrolyte

Commercial LIBs are applied with liquid electrolytes filling into the separator consisting of polyethylene (PE) or polypropylene (PP) to prevent the direct contact of electrodes. Liquid electrolytes are generally composed mixed solution of ring carbonates, such as ethylene carbonate (EC) or propylene carbonate (PC), and linear carbonate, such as dimethyl carbonate (DMC) or diethyl carbonate (DEC), with the dissolved lithium salts, mainly lithium hexafluorophosphate (LiPF_6). These liquid electrolytes perform high electrochemical stability, high Li^+ transport properties, and good SEI formability.²⁴

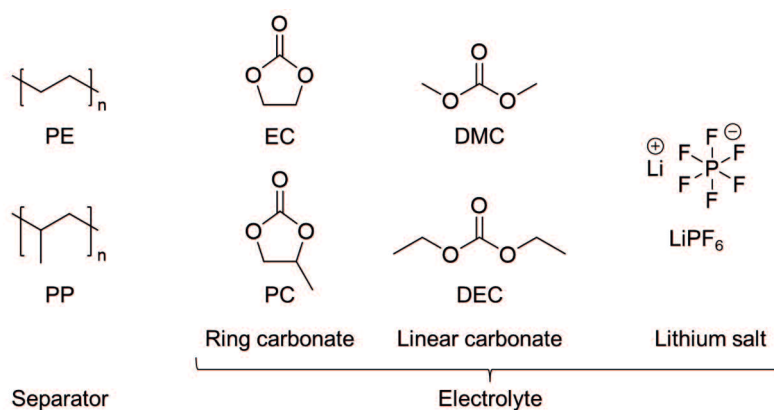


Figure 15 The basic component of conventional electrolytes. Polyethylene (PE) or polypropylene (PP) is used as separator. Ethylene carbonate (EC) or propylene carbonate (PC) are used as electrolyte for highly lithium-salt dissociation. Dimethyl carbonate (DMC) or diethyl carbonate (DEC) are used as electrolyte for low viscosity. Lithium hexafluorophosphate (LiPF_6) is used as lithium salt.

Harris found the high stability of propylene carbonate (PC) to lithium metal, which lead today's using liquid carbonates for the electrolytes in lithium batteries.^{24,66} Ring carbonates, propylene carbonate or ethylene carbonate, have high polarity which conduct high salt solubility, but Li^+ mobility decreased in ring carbonates due to its high viscosity. To decrease viscosity, linear carbonate performing low viscosity used as the co-solvents for commercial electrolytes.²⁴ As a result, commercial electrolytes show about 10 mS cm^{-1} of ionic conductivity.⁶⁷ Furthermore, it has been reported that good SEI is formed on the graphite negative electrodes within commercial carbonate-based electrolytes. The components of SEI, Li_2O , Li_2CO_3 , semi-carbonate, LiF , and polyolefin, protect the graphite electrode with wrapping over surface,^{24,41,42} and the Li^+ transport in SEI layer is supported through Li_2O and Li_2CO_3 phase.⁶⁸

Although carbonate-based electrolyte has been widely used to LIBs because of advantages mentioned above, it still has the concern about the low thermal stability. For carbonate-based electrolytes, the semi-carbonate contained in SEI is thermally decomposed around $90 \text{ }^\circ\text{C}$, which generates oxygen gas in LIB. The solvent molecules then decompose around $100 \text{ }^\circ\text{C}$ to produce flammable gases, ethene or propene, which react with oxygen gas and burned.¹¹ Low thermal stability of carbonate-based electrolytes sometimes concludes the injurious fire accidents. Therefore, it is expected the alternatives having high thermal stability to conventional electrolyte for next-generation electrolytes.

4.1.3 Next-generation liquid electrolytes

Previous research has suggested two strategies for thermal stable electrolytes; (i) using more stable materials for additives/ matrix or (ii) increasing thermal stability of conventional solvents. Some approaches using liquid materials are shown in Figure 16. These liquid-type electrolytes are easy to replace conventional electrolytes industrially with the similar liquid state, and they are expected to be realization in the near future.

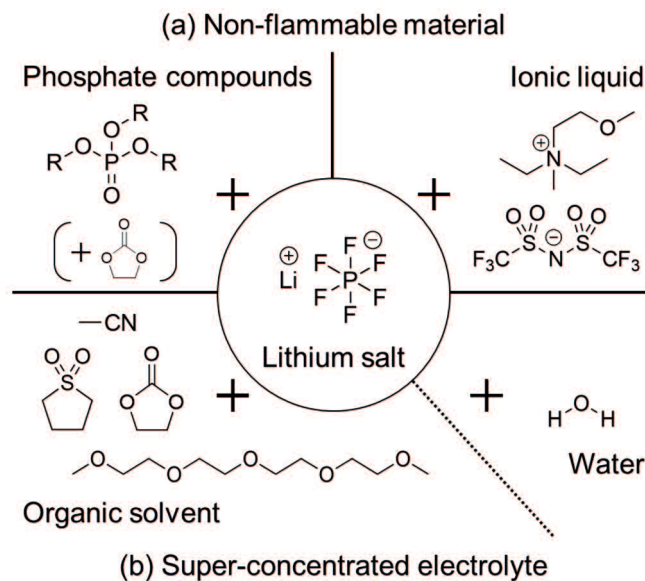


Figure 16 The strategies of next-generation liquid electrolytes with high thermal stability; (a) non-flammable material such as phosphate compounds or ionic liquid for electrolyte additive/ matrix, respectively, or (b) super-concentrated electrolyte using conventional solvents including various organic solvents or water.

Phosphate compounds is the one of the famous fire extinguisher materials. Phosphorus oxide radical (PO^*) is generated from phosphate compounds at high temperature and which can trap hydrogen and hydroxyl radicals having strong combustion ability generated during the thermal decomposition of electrolytes.⁶⁹ The electrolytes using phosphate compounds as additives are reported to perform high thermal stability.⁷⁰ Ionic liquids are well known with low vapor pressure due to the electrostatic interaction between constituent ions, conducting the high thermal stability. Therefore, ionic liquids had been attended as the alternatives to organic solvents for matrix of liquid electrolytes.⁷¹

Super-concentrated electrolytes, often called solvent-in-salt, is prepared from common solvent and excessive amount of lithium salt. All solvent molecules interact to Li^+ and be stable thermally and (electro-)chemically under the super-concentrated state. Super-concentrated electrolytes not only increase thermal stability of carbonate-based electrolytes,⁷² but also allows the thermally/ (electro-)chemically instable solvents, including various organic solvents and surprisingly water, application to the electrolytes for LIB.^{73,74}

In addition, these electrolytes sometimes perform a unique Li^+ transport mechanism, so they are attracting much attention from researchers.^{64,75}

However, these strategies shown in Figure 16 are needed few more investigation because they perform only low Li^+ conductivity compared to conventional electrolytes, due to high viscosity, low priority of Li^+ transport among ion species, or other reasons.

On the other hand, solid materials have been also studied for the realization of the next or after generation electrolytes.

4.2. Solid electrolyte

Solid electrolytes, the electrolytes using solid materials, generally have higher thermal stability than liquid materials. The safety concern due to liquid electrolytes leaking from LIBs also can be eliminated to use solid electrolytes. In addition, high mechanical stability of solid electrolytes will suppress short-circuit of electrodes contact without separator. The batteries using solid electrolytes replacing liquid electrolytes, called all-solid-state battery, can reduced separator and the industrial process of filling liquid electrolyte to separator. Furthermore, solid electrolytes will contribute to the realization of next-generation lithium secondary battery using lithium metal for negative electrode, because of its high mechanical stability suppressing the growth of lithium dendrite.

Solid electrolytes are roughly classified into (i) inorganic electrolyte, (ii) gel electrolyte or (iii) polymer electrolyte (Figure 17).

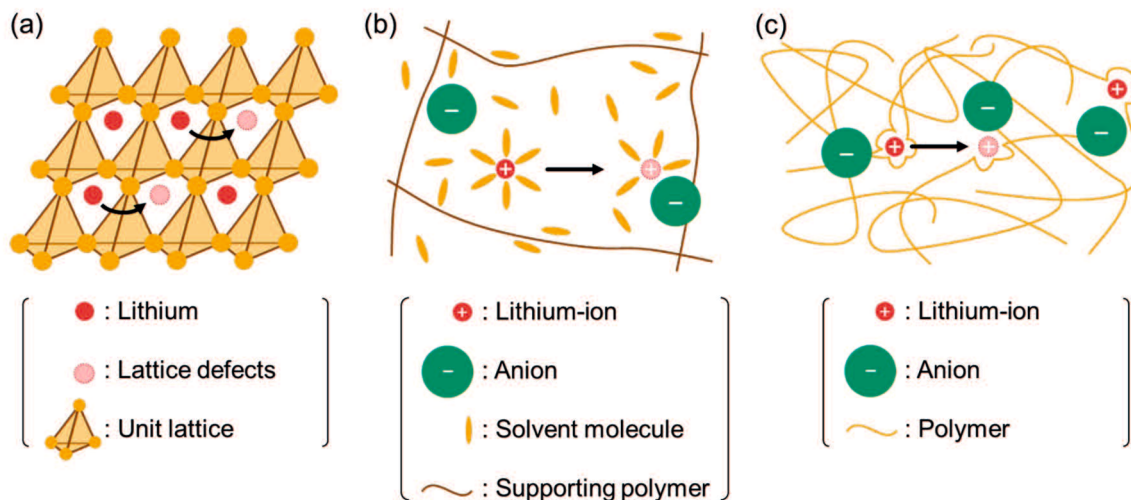


Figure 17 Lithium-ion transport mechanism in each solid electrolyte; (a) inorganic electrolyte transport Li^+ through lattice defects, (b) gel electrolyte transport Li^+ by solvation molecules movement similar to liquid electrolyte, and (c) polymer electrolyte transport Li^+ by polymer segmental motion.

4.2.1. Inorganic electrolyte

Inorganic electrolyte is composed of lithium-containing ceramics. Lithium-ion moves mainly hopping through lattice defects (Figure 17a).⁷⁶ Although Li^+ mobility of this mechanism is slow compared to liquid electrolyte, inorganic electrolytes exhibit high total Li^+ conductivity due to extremely high Li^+ concentration in the structure. By the recent structural research, $\text{Li}_{9.54}\text{Si}_{1.74}\text{P}_{1.44}\text{S}_{11.7}\text{Cl}_{0.3}$ has been reported 25 mS cm^{-1} of Li^+ conductivity which exceeds that of liquid electrolytes at room temperature.⁷⁷ Furthermore, higher thermal stability is performed for inorganic electrolytes than for liquid electrolytes and other solid electrolytes.

However, inorganic electrolytes suffer from poor mechanical stability, conducting to be broken easily by physical impact. In addition, electrode-electrolyte interface is formed poorly due to difficult contact of non-flexible inorganic electrolytes to electrode material, which makes the inhibition of the Li^+ transport at the interface.⁷⁸

4.2.2. Gel electrolyte

Gel electrolyte is composed with liquid electrolytes and the supporting polymer. The supporting polymer needs to perform high affinity to liquid electrolyte and self-standing ability under the filled state with liquid electrolyte. It is applied for the supporting polymer that the polymers with the both of high mechanical stability and low solubility into the filling liquid electrolyte, or with network structure.⁷⁹ Most properties of gel electrolytes depend on the filling liquid electrolyte, including Li^+ transport properties, thermal stability, and electrochemical stability, except mechanical stability (Figure 17b). Therefore, gel electrolytes can perform relatively high mechanical stability maintaining Li^+ transport property. In addition, solvent molecules in gel electrolyte are stabilized thermally/electrochemically compared than normal liquid electrolytes maybe due to enthalpy change of dissolution of supporting polymer.⁸⁰ Gel electrolyte will be further functionalized combining with next-generation liquid electrolytes mentioned above.⁸¹

Although conventional/next-generation liquid electrolyte can be replaced by gel electrolytes easily compared than other solid electrolytes, the battery safety will not be solved dramatically since the properties depending on the liquid electrolyte. The concern about liquid leaking is also remained when supporting polymer is aged.

4.2.3. Polymer electrolyte

Polymer electrolyte (PE) is composed lithium salt and polar polymer, which have been widely studied from the first report by Peter V. Wright.^{82,83} Polar polymer interacts to Li^+ using polar groups on polymer chain, similar to solvent molecules for liquid electrolytes, and then, Li^+ is transported by polymer segmental motion (Figure 17c). Polymer materials generally shows higher thermal stability than short molecules. For example, the flashpoint of poly(ethylene oxide) (PEO) is 254°C, which is higher than that of short molecules with similar structures like 1,2-dimethoxyethane (-6°C) or triethylene glycol dimethyl ether (111°C).⁸⁴ Polymer materials also have high mechanical stability and high flexibility, which affords good adhesiveness to electrodes forming more effective electrode-electrolyte

interface compared than inorganic electrolytes. Flexible PEs would be more tolerant to electrode volume changes during charge/discharge, especially for conversion reactions.

I believe PEs are the best electrolytes among solid electrolytes since the mechanical advantages will contribute for industrial processability. However, there are some barriers to commercialize PEs, such as insufficient electrochemical stability, difficulty of synthesis, and so on. Among these problems, PEs have been mainly suffered from (i) the dilemma between the mechanical strength or Li^+ conductivity and (ii) further low Li^+ conductivity compared than other liquid/ solid electrolytes. Lithium-ion mobility of PEs mainly depends on the segmental mobility of polymer chains (Figure 17c), but which is relatively slow. Furthermore, it is necessary high segmental mobility and low crystallinity of polymers for high Li^+ conductivity, but which decrease mechanical strength and sometimes the self-standing ability is lost. The next section describes the studies that have been done to solve these problems.

5. Polymer electrolyte research

To increase each performance of PEs including mechanical stability and Li^+ conductivity, many strategies has been proposed and which can be roughly classified into three categories; (i) composite material, (ii) polymer architecture modification, and (iii) repeating unit design.

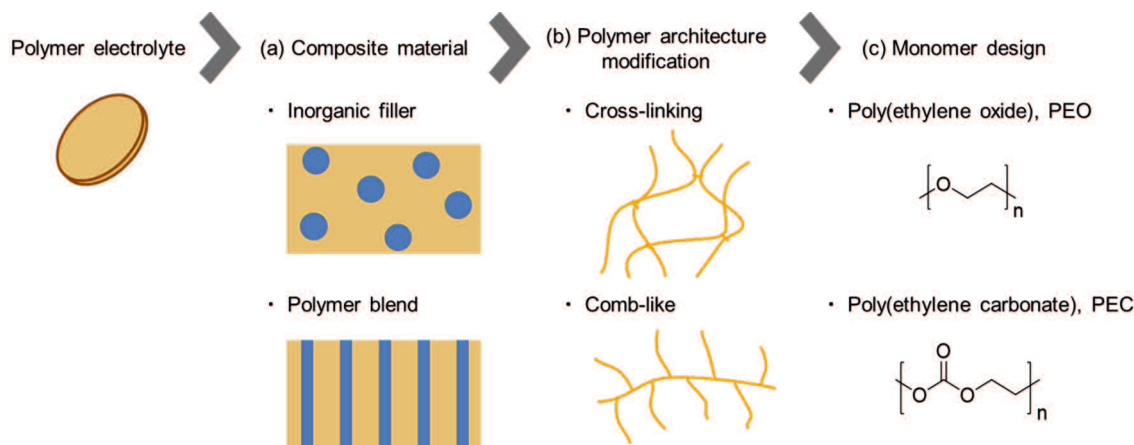


Figure 18 Polymer electrolyte strategies and examples; (a) composite material, such as inorganic filler additive or blend of two or more polymers, (b) polymer architecture modification, such as cross-linking between polymer chains or comb-like branch structure, and (c) monomer (polymer repeating unit) design, such as poly(ethylene oxide) or poly(ethylene carbonate).

5.1. Composite material

Polymer materials can keep various additives distributed, which make ease of composite with other materials. Composite PEs can be functionalized easily by added functional materials (Figure 18a).

Polymer electrolyte has succeeded to gain high mechanical strength with nanostructured inorganic fillers into PE. The mechanical strength derived from inorganic nano-particle have suppressed lithium dendrite growing on lithium metal electrode even using PEO with high segmental mobility.⁸⁵ Furthermore, the inorganic nano-particle is also contribute to increase the ionic conductivity, because voids is provided around the inorganic nano-particle which gives a volume for the ease of polymer segmental motion.⁸⁶ For further high mechanical stability, strength, and flexibility, various modification of nano fillers have been researched;

chemical modification of filler surface using acid treatment or polymer chain bonding,^{85,87} and structural modification using metal-organic-frame (MOF) or nano-fiber frame prepared by electrospinning.^{88,89} The composite of PE and inorganic electrolyte have been tried to solve concerns of each other about Li⁺ conductivity and mechanical stability.^{90,91,92}

Besides the composite with inorganic fillers, the polymer blend strategies have been reported using two or more functional polymers for previous research. For example, the bifunctional system with high mechanical stability and ionic conductivity have been archived with the blend of mechanical stable polymer and polar polymer, which system is similar to the gel electrolyte composed the supporting polymer and Li⁺ conductive solvent.⁹³ However, the combination of polymer blend is limited due to the difference of solubility in the solution for each composing polymer. And also, the distribution of the composing polymers is hardly controlled for the nano- or micro-order. Copolymers have been studied to expand the variety of the polymer combination and to control blended polymer state. Block copolymer composed with high mechanical strength polystyrene (PSt) and high ionic conductive poly(ethylene oxide) (PEO) performed high strength without significantly decreasing the ionic conductivity. This is because the micro-phase separation between hard PSt phase and conductive PEO phase, which maintain the polymer properties independent on each other polymers.^{94,95,96} Random copolymer and alternating copolymer afford the delocalized distribution of composing polymers, and which can perform both (averaging-) properties of composing polymers.^{96,96,97}

5.2. Polymer architecture modification

Polymer material can be synthesized to different architectures (Figure 18b) with the several polymerization conditions, thereby controlled the physical properties.

Cross-linking between the polymer chains partially immobilizes the polymer chains, which forms a highly self-standing membrane for PEs.⁹⁹ It is expected that PE can be easily changed the mechanical strength by controlling cross-link density. The restriction of segmental mobility by cross-linking is partial and can maintain relatively high Li⁺ conductivity.¹⁰⁰

A comb-like polymer, having many branches on a polymer main chain, has many free chain ends, which exhibits higher segmental mobility than the center of polymer chain. These branch structures also decrease crystallinity of polymers, which is one of the causes of low ionic conductivity decreasing Li^+ conductive amorphous region.^{101,102} Therefore, comb-like PEs performed high ionic conductivity. It also has been reported that comb-like polymers form an even better electrode-electrolyte interface than common PEs.¹⁰³

The mechanical strength has been greatly improved and separated from Li^+ transport properties for these strategies. Although low Li^+ conductivity has also improved somewhat, that is not enough. For the fundamental solution of low Li^+ conductivity, it is necessary to redesign the monomer, meaning the polymer repeating unit, based on the Li^+ transport mechanism.

5.3. Lithium-ion transport mechanism for polymer electrolytes

Lithium-ion conductivity of PEs is more than two order magnitude lower than that of liquid electrolyte; poly(ethylene oxide) and lithium bis(trifluoromethane-sulfonyl)amide system (PEO-LiTFSa) has about 0.05 mS cm^{-1} of ionic conductivity and 0.1–0.2 of Li^+ transference number, which is the most basic and known to have a relatively high conductivity among PEs.^{104,105} As mentioned for section 4.1.1, Li^+ conductivity is determined with the amount and the mobility of Li^+ . Low Li^+ conductivity for PEs is due to the low Li^+ mobility, despite the Li^+ amount is comparable that of the liquid electrolyte.

The amount of Li^+ for PEs is determined by the amount of lithium salt and the ratio of dissociated ion, and influential factors are the same as the liquid electrolytes such as the salt concentration, anion structure, dielectric properties of the polymer, and donating/accepting ability of polar groups on the polymer (Figure 11).

Lithium-ion mobility is performed in PEs with a combination of following mechanisms in amorphous region; (i) Li^+ is coordinated with polar groups on polymer chains and transported by polymer segmental motion, (ii) Li^+ moves with the exchanging of interacted site to adjacent polar groups along the polymer chain, and (c) Li^+ moves with the exchanging

of interacted site to another polymer chain (Figure 19).^{106,107,108} Unlike liquid electrolytes, a large size of polymer chain inhibits the self-diffusion of the center of chain mass, and which not contribute to the Li^+ transport for PEs.¹⁰⁹ Therefore, dependency of Li^+ transport on viscosity is decreased with the increase of polymer weight.¹¹⁰

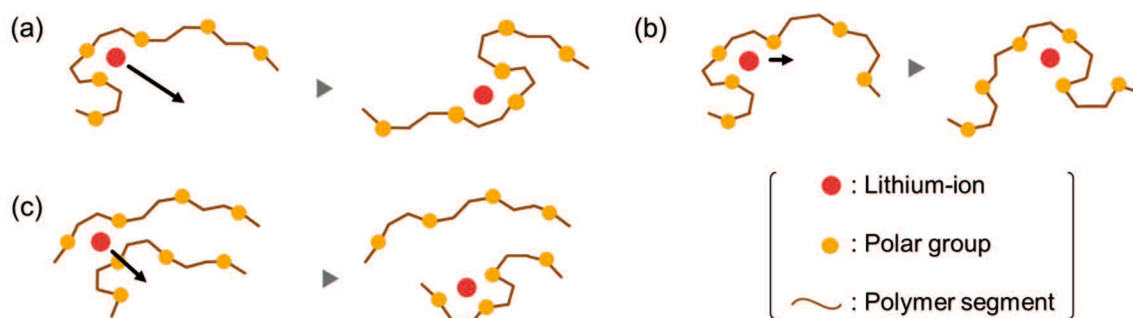


Figure 19 Lithium-ion transport mechanisms in PEs; (a) Li^+ is transported by polymer segmental motion maintaining the coordination structure, (b) Li^+ migrate during the exchange the coordination site intrachain along polymer chain, (c) Li^+ is exchanged the coordination site to the free site on another polymer chain.

Polymer chain can transport Li^+ by the segmental motion maintaining the structure with multiple interaction of polar groups to Li^+ , called coordination structure (Figure 19a). These Li^+ transport by segmental motion carries relative long-range displacement.¹⁰⁶ However, not all Li^+ transport between electrodes can be covered this mechanism, due to the steric limitation of the entangled polymer chains. Co-contribution is important with other mechanisms for efficient Li^+ transport.

Lithium-ion is also transported by exchanging the coordination site between polar groups similar to liquid electrolytes. This lithium-ion exchange mechanism is often called Li^+ hopping mechanism. Lithium-ion can be exchanged between adjacent polar groups along polymer chain (Figure 19b) and between two polymer chains via co-ordination with the polymer chains (Figure 19c). Short-range, but frequent Li^+ displacement is performed by the exchange between adjacent polar groups.¹⁰⁶ Since this exchange mechanism is triggered by the rotation of the molecular bond around the local coordination structure, the rotation ability of the molecular chain is important factor, and which correlates with the segmental mobility of polymer chains.

The mechanism of Li^+ exchanged between two polymer chains is less frequently, but which is considered to contribute on the continues Li^+ transport between electrodes. The exchange mechanism between polymer chains depends on the segmental mobility because the reorganization of the coordination structure via the segmental motion is necessary to complete the Li^+ exchange.¹⁰⁶ In addition to segmental mobility, these Li^+ exchange mechanisms are needed an optimized distribution of polar groups to design for the continuous Li^+ transport pathway; too low density of polar groups decrease the ion exchange frequency, but too high density is involved excessive frequent reorganization of coordination structure and delayed Li^+ transport.¹⁰⁸

Each transport mechanism for the PE is governed/ correlated with the segmental mobility of the polymer chains. The high segmental mobility is performed at temperatures significantly exceeding from the glass transition temperature (T_g). Therefore, PEs with low glass transition temperature tend to show relatively high ionic conductivity. Glass transition temperature for PEs is determined by polymer chain structure and increased with various interactions, including the hydrophobic interaction between neat alkyl chains, dipole-dipole interaction between polar groups, and electrostatic interaction between ion and polar groups.

For the liquid electrolytes mentioned in section 4.1.1, I explained the significant effect of the interaction between the Li^+ and the solvent molecules on the Li^+ transport; the contribution on the stability of the dissociated Li^+ , the inhibition of Li^+ migration with the increase of viscosity, and the effect on Li^+ transport mechanism. Similarly, the interaction between Li^+ and polymers is one of the influential factors on the Li^+ transport for the PEs. The coordination structure is further important which reflected the steric stability around Li^+ in addition to the effect of the interaction between Li^+ and polar group, because the polar groups cannot ignore the steric restriction bring by the connection on molecular backbone (Figure 20).

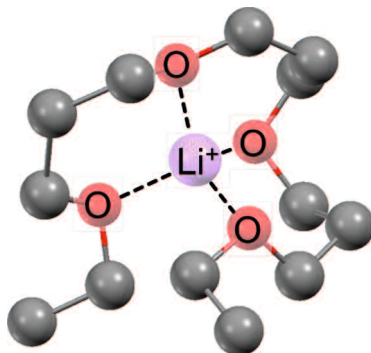


Figure 20 An image of the coordination structure formed by the multiple interaction between Li^+ and ether groups connected by molecular backbone.

The strong interaction between Li^+ and polar groups contributes to the lithium salt dissociation and to the efficient Li^+ migration coupling with polymer segmental motion. But this strong interaction can form the stable coordination structure suppressing the bond rotation of the polymer chain and decrease the polymer segmental mobility.¹¹¹ Furthermore, these stable coordination structure anchors Li^+ on polymer chains and suppresses Li^+ exchange between polar groups.¹¹²

The dominant factors for Li^+ conductivity in PEs are (i) lithium salt dissolubility, (ii) the polymer segmental mobility, (iii) the efficient Li^+ migration coupling with polymer segmental motion, and/or (iv) fast and continuous Li^+ exchange between polar groups. And the coordination structure is the control key for these dominant factors and Li^+ transport mechanism. In order to control such minute and local coordination structure, it is necessary to design a monomer, which is the smallest unit constituting the polymer.

5.4. Monomer design

Researchers have studied various monomer structures for PEs to perform high electrolyte properties including thermal stability, electrochemical stability, mechanical stability, and especially Li^+ conductivity (Figure 18c, Figure 21).

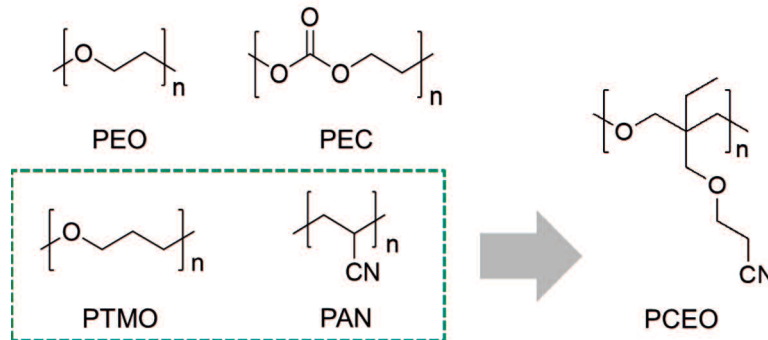


Figure 21 Several monomer structures used for PE research, where PEO is poly(ethylene oxide), PTMO is poly(trimethylene oxide), PEC is poly(ethylene carbonate), PAN is poly(acrylonitrile), PCEO is poly(3-(2-cyanoethoxymethyl)-3-ethyloxetane).

Poly(ethylene oxide) (PEO), often called poly(ethylene glycol) (PEG), is most popular structure among polar polymers used for PEs. Poly(ethylene oxide) is composed with continuous structures of ethylene oxide, which perform high segmental mobility ($T_g = 65^\circ\text{C}$).¹¹³ Consisting ether groups have high donating ability bring high lithium salt dissolubility and coupled Li^+ transport with polymer segmental motion.^{106,114} However, polymer segmental mobility becomes even lower as the increase of salt concentration, because too stable coordination structure around Li^+ is formed with the strong interaction between Li^+ and polar groups and which reduces the rotatability of the covalent bond consisted polymer.¹¹¹ Too stable coordination structure also reduces relative mobility of Li^+ compared to anion due to the trap of Li^+ on polymer chain.¹⁰⁵

Poly(trimethyleneoxide) (PTMO), also called polyoxetane, is another linear polyether capable of solvating Li^+ to yield ion-conducting PE. Quantum chemical studies of Li^+ binding to poly(alkyloxide) predicted that the energy barrier for Li^+ transport between the coordination sites in PTMO is smaller than that in PEO due to its steric crowding in the coordination structure, although the binding energy of ether group with Li^+ for PTMO is

comparable to or slightly larger than that for PEO.¹¹² Polymer electrolytes with trimethyleneoxide (TMO) groups in the side chains had better ionic conductivity than PEs with EO groups at low temperatures.¹¹³ A recent study using the dynamic bond percolation model in combination with a long-timescale atomic molecular dynamics (MD) simulation suggested that alternating copolymer P(EO-TMO) exhibits faster Li⁺ diffusion than PEO, whereas Li⁺ diffusion is much slower in the PTMO homopolymer because of the low coordination site density and slow hopping rate among the coordination sites.¹⁰⁸

Poly(ethylene carbonate) (PEC) has carbonate groups like conventional electrolytes, and which is one of the candidates of matrix polymer for PEs. Segmental mobility of PEC increases with increasing lithium salt concentration in combination with specific anions, unlike PEO electrolytes.¹¹⁵ This is because the new interaction between carbonate group and Li⁺ relaxes the original intrachain interaction between the polymer backbone and carbonate group.¹¹⁶

Similar trends of increasing segmental mobility have been observed with nitrile-based polymers, such as poly (acrylonitrile) (PAN). This is due to the relaxation of the dipole-dipole interaction between the nitrile groups due to the new interaction between nitrile group and Li⁺.¹¹⁷ Interestingly, nitrile-based PEs can transport Li⁺ even at low temperatures near the T_g , where the segmental mobility of polymer chains is reduced. This is because the Li⁺ transport is decoupled from the polymer segmental mobility.¹¹⁸

Although polymer electrolyte studies have been proposed using various polar polymers, none of them have sufficient ionic conductivity exceeding the benchmark (1 mS cm^{-1}).⁸² One reason for the insufficient ionic conductivity is that the design guidelines of polymer structure have not been established clearly. In order to establish the design guideline of the polymer structure, the search of optimized coordination structure is further important to achieve the high salt dissociation, high segmental mobility, and efficient Li⁺ transport.

Our group have focused on polymers containing ether and nitrile groups that exhibit different behaviors for Li⁺ transport mechanism and glass transition temperature. Ye *et al.* prepared polyoxetane-based functionalized homo- and copolymers with oligoethylene oxide and nitrile groups in the side chains. The PEs containing lithium salts showed a relatively

high ionic conductivities of 0.28 mS cm^{-1} for the linear copolymer at 80°C .¹¹⁹ Our group also reported polyoxetane-based PEs with nitrile¹²⁰ and tris(cyanoethoxymethyl)¹²¹ groups; the high ionic conductivities of these PEs were likely caused by enhanced dissolution of the lithium salt *via* Li^+ coordination with nitrile functionalities. Polyoxetane-based PEs with nitrile groups, poly(3-(2-cyanoethoxymethyl)-3-ethyloxetane) (PCEO, Figure 21), in the previous study¹²⁰ were revisited and compared with similar polymer structures to investigate the role of the polymer structural factors, including polar groups or alkyl groups, in the coordination structure of Li^+ and the ionic transport properties.

Outline of the work

In this study, I focused on the coordination structure around Li^+ to establish the polymer design strategy for high Li^+ transport properties. The simple system consisting of polar polymer and lithium salt was used to elucidate the effect of coordination structure on Li^+ transport properties. The coordination structure and electrolyte properties were compared between PEs with/without polymer structural factors and between for each lithium salt concentration. For the comparison between polymer structural factors, I used a polymer series having polyoxetane structure for polymer backbone and local modification on side chain. In addition to some advantage of polyoxetane mentioned for section 5.4., four-membered ethers (*i.e.*, oxetanes) are more chemically stable than three-membered cyclic ethers (*i.e.*, epoxides); thus, various polymer structural factors can be readily introduced into the oxetane monomeric structure, and simple ring-opening cationic polymerization (ROCP) yields modified polyoxetane-based PEs. Polymer electrolytes prepared with lithium bis(trifluoro-methanesulfonyl)amide (LiTFSA) as lithium salt, which is well known to perform high salt dissociation and structural stability.

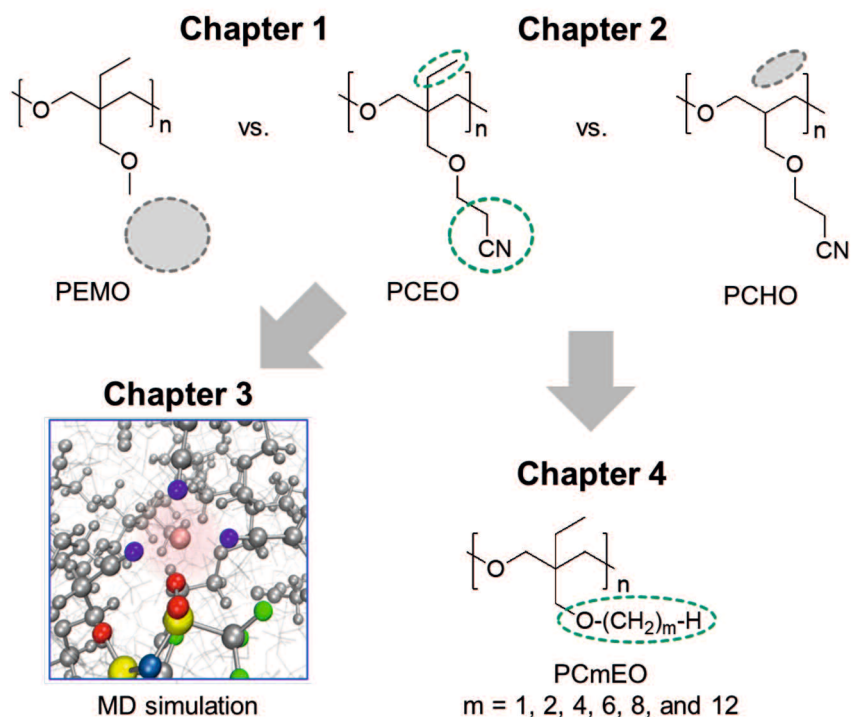


Figure 22 The figure flow of this dissertation outline; (Chapter 1) the comparison of poly(3-ethyl-3-methoxymethyloxetane) (PEMO) and poly(3-(2-cyanoethoxymethyl)-3-ethyloxetane) (PCEO) to clarify the effect of nitrile group, (Chapter 2) the comparison of PCEO and poly(3-(2-cyanoethoxymethyl)-oxetane) (PCHO) to clarify the effect of ethyl group on polymer main chain, (Chapter 3) molecular dynamics (MD) simulation for PCEO electrolytes to clarify the detail of the Li^+ transport mechanism, and (Chapter 4) the comparison of poly(3-ethyl-3-(*alkyl*)oxymethyloxetane) (PCmEO, m = 1, 2, 4, 6, 8, and 12) to clarify the effect of alkyl group.

In Chapter 1, I investigate the effects of polar side chains on Li^+ coordination and ionic transport properties. Polyoxetane-based polymers with ether or nitrile groups were synthesized by ROCP, which was poly(3-(2-cyanoethoxymethyl)-3-ethyloxetane) (PCEO) and poly(3-ethyl-3-methoxymethyloxetane), (PEMO) respectively. The thermal, ionic transport, and electrochemical properties and the local structure around Li^+ coordination were studied in the presence of LiTFSA. The glass transition temperature (T_g) of the PEs with ether side chains increased with increasing LiTFSA content because stable coordination structure was formed by ether groups interacting Li^+ and which suppressed of polymer segmental mobility. By contrast, the PEs with the nitrile functionality shown the opposite trend at higher

salt concentrations. In addition to the unique trend for the T_g values of the PEs in the presence of LiTFSA, the nitrile groups played pivotal roles as coordination sites for Li^+ in the first coordination shell and as a polar medium to increase the permittivity of the PEs. These characteristics of the nitrile groups can endow PEs with improved ion transport properties.

In Chapter 2, I report the effects of the absence of ethyl groups on the main chain of PCEO on Li^+ ion coordination, thermal properties, and ionic transport, by employing a structural analog, poly(3-(2-cyanoethoxymethyl)-oxetane) (PCHO). I found that the steric hindrance derived from the ethyl groups in PCEO resulted in more-pronounced Li^+ coordination with the nitrile side chains, and thereby more effective Li^+ ion transport was achieved. We also demonstrated successful charge/discharge cycling of a Li/LiFePO₄ cell using nitrile-functionalized PE.

In Chapter 3, we combine spectro(electro)chemical analyses with molecular dynamics (MD) simulations to understand the complex interaction within the electrolyte, consisting of PCEO mixed with various concentrations of LiTFSA, to clarify the Li^+ coordination structure as well as its relevance to Li^+ conductivity. Applicability of MD simulations was validated by high-energy X-ray total scattering measurements. The local coordination structures around Li^+ were successfully estimated by the distribution function obtained from MD simulations, which suggested the preferable coordination of the nitrile group with Li^+ over the other elements, including ether oxygen. Further support came from infrared (IR) spectroscopy, where the estimated coordination number (N) obtained from the IR peak area of the deconvoluted CN stretching vibration (*ca.* 2250–2280 cm^{-1}) agreed well with the MD result. Arrhenius plots of the ionic conductivity shown a curved shape, indicating that the segmental motion of the polymer main chain was responsible for Li^+ transportation in PCEO electrolytes. The Li^+ conductivity varied with the salt concentration and was sensitive to the Li^+ coordination structure. The highest Li^+ conductivity was achieved at an intermediate salt concentration, where Li^+ coordinated mostly by the nitrile group ($N = 2.2$), followed by the TFSA anion ($N = 1.3$), and only a small contribution was from ether oxygen ($N = 0.5$). The characteristic cocontribution of a nitrile group and ether oxygen to the Li^+ coordination structure can be responsible for the improved Li^+ conduction, by accelerating the interchain Li^+ transfer, involving a decoordination process, (short-range Li^+ conduction) while

maintaining good segmental mobility of the polymer (long-range Li⁺ conduction). The results emphasize the importance of the coordination structure to the electrolyte property, which can provide additional knobs to improve the ionic conductivity as well as the Li⁺ transference number, leading to further improvements in the performance of PEs.

In Chapter 4, the electrolyte properties of a simple polyether having alkyl side chains with varied length $-(\text{CH}_2)_m-\text{H}$, $m = 1, 2, 4, 6, 8,$ and 12) were compared and established a valid design strategy based on the properties of the alkyl side chain. Various spectro-electrochemical measurements successfully connected the electrolyte properties and the alkyl side chain length. Steric hindrance of the alkyl side chain effectively suppressed the interaction between ether oxygen and lithium-ion ($m \geq 2$), increasing the glass transition temperature and the activation energy of lithium-ion transfer at the electrode-electrolyte interface. The strong hydrophobic interactions aligned and/or aggregated the long alkyl group ($m \geq 8$), creating a rapid lithium-ion transport pathway and enhancing lithium-ion conductivity. A clear trend was observed for the following three crucial factors determining bulk lithium-ion transport properties along with the extension of the alkyl side chain; (i) salt dissociability decreased due to non-polarity of the alkyl side chain, (ii) segmental mobility of polymer chains increased due to the internal plasticizing effect, and (iii) lithium-ion transference number increased due to the inhibition of the bulky anion transport by its steric hindrance. The highest lithium-ion conductivity was confirmed for the PEs with an alkyl side chain with moderate length ($m = 4$) at $70\text{ }^\circ\text{C}$, indicating the optimized balance between salt dissociability, polymer segmental mobility, and selective lithium-ion transfer. The length of an alkyl side chain thus can be a critical factor in improving the performance of PEs, including thermal stability and lithium-ion conductivity. Precise tuning of the alkyl side chain-related parameters such as steric hindrance, polarity, internal plasticizing effect, and self-alignment optimizes the polymer segmental mobility and salt dissociability, which is crucial for realizing high lithium-ion conductivity for PEs.

References

1. Trasatti, S. *Pure & Appl. Chem.* **1986**, *58*, 955–966.
2. Julien, C.; Mauger, A.; Vijn, A.; Zaghbi, K. *Lithium batteries; science and technology*; Springer: Switzerland, 2016.
3. Statistical data. Battery association of Japan. <http://www.baj.or.jp/statistics/index.html> (accessed Oct 1, 2020).
4. Winter, M.; Brodd, R. *J. Chem. Rev.* **2004**, *104*, 4245–4269.
5. *Yearbook of current production statistics 2007–2019*, Research and statistics department minister's secretariat; Ministry Economy, Trade and Industry (METI) Japan: Tokyo, 2007–2019.
6. The Nobel Prize in Chemistry 2019. The Noble Prize organization. <https://www.nobelprize.org/prizes/chemistry/2019/popular-information/> (accessed Oct 1, 2020).
7. Goto, N.; Endo, S.; Ishikawa, T.; Tamura, S.; Shuto, Y.; Tanaka, K. *Aircraft serious incident investigation report*; Japan Transport Safety Board (JSTB): Tokyo, 2014.
8. Kolly, J. M.; Panagiotou, J.; Czech, B. A. *The Investigation of a lithium-ion battery fire onboard a boeing 787 by the US national transportation safety board*; National Transportation Safety Board (NTSB): Washington DC, 2014.
9. *News release: 急増! ノートパソコン、モバイルバッテリー、スマホの事故*, National Institute of Technology and Evaluation: Tokyo, 2017.
10. *News release: 急増! 非純正リチウムイオンバッテリーの事故*, National Institute of Technology and Evaluation: Tokyo, 2020.
11. Wang, Q.; Ping, P.; Zhao, X.; Chu, G.; Sun, J.; Chen, C. *J. Power Sources* **2012**, *208*, 210–224.
12. Zhao, R.; Liu, J.; Gu, J. *Appl. Energy* **2016**, *173*, 29–39.
13. Feng, X.; Ouyang, M.; Liu, X.; Lu, L.; Xia, Y.; He, X. *Energy Storage Mater.* **2018**, *10*, 246–267.
14. Huang, S.; Du, X.; Richter, M.; Ford, J.; Cavalheiro, G. M.; Du, Z.; White, R. T.; Zhang, G. *J. Electrochem. Soc.* **2020**, *167*, 090526.
15. Guo, Z.; Zhu, J.; Feng, J.; Du, S. *RSC Adv.* **2015**, *5*, 69514–69521.
16. Xiao, J. *Science* **2018**, *366*, 426–427.
17. Liu, X.; Ren, D.; Hsu, H.; Feng, X.; Xu, G. L.; Zhuang, M.; Gao, H.; Lu, L.; Han, X.; Chu, Z.; Li, J.; He, X.; Amine, K.; Ouyang, M. *Joule* **2018**, *2*, 2047–2064.
18. Dubarry, M.; Truchot, C.; Liaw, B. Y. *J. Power Sources* **2012**, *219*, 204–216.
19. Kang, Y.; Wang, J.; Du, L.; Liu, Z.; Zou, X.; Tang, X.; Cao, Z.; Wang, C.; Xiong, D.; Shi, Q.; Qian, Y.; Deng, Y. *ACS Appl. Energy Mater.* **2019**, *2*, 8615–8624.
20. Tarascon, J.-M.; Armand, M. *Nature* **2001**, *414*, 359–367.
21. Ashuri, M.; He, Q.; Shaw, L. L. *Nanoscale* **2016**, *8*, 74–103.
22. Yoshino, A.; Otsuka, K.; Nakajima, T.; Koyama, A.; Nakajyo, S. *Nippon Kagaku Kaishi* **2000**, *2000*, 523–534.
23. Yoshino, A.; Sanechika, K.; Nakajima, T. 二次電池 Japan Patent S62-90863, 1987.

24. Xu, K., *Chem. Rev.* **2004**, *104*, 4303–4417.
25. Blomgren, G. E. *J. Electrochem. Soc.* **2017**, *164*, A5019–A5025.
26. Yao, X.L.; Xie, S.; Chen, C.H.; Wang, Q.S.; Sun, J.H.; Li, Y.L.; Lu, S.X. *Electrochim Acta* **2005**, *50*, 4076–4081.
27. Ashuri, M.; He, Q.; Shaw, L. L. *Nanoscale* **2016**, *8*, 74–103.
28. Liu, X.; Wu, X.-Y.; Chang, B.; Wang, K.-X. *Energy Storage Mater.* **2020**, *30*, 146–169.
29. Mou, H.; Xiao, W.; Miao, C.; Li, R.; Yu, L. *Front. Chem.* **2020**, *8*, 1–14.
30. Whittingham, M. S. *Science* **1976**, *192*, 1126–1127.
31. Mizushima, K.; Jones, P. C.; Wiseman, P. J.; Goodenough, J. B. *Mater. Res. Bull.* **1980**, *15*, 783–789.
32. Yoshino, A. *Analytical sciences: the international journal of the Japan Society for Analytical Chemistry* **2013**, *10*, 580–584.
33. Zubi, G.; Dufo-López, R.; Carvalho, M.; Pasaoglu, G. *Renew. Sustain. Energy Rev.* **2018**, *89*, 292–308.
34. Barkholtz, H. M.; Preger, Y.; Ivanov, S.; Langendorf, J.; Torres-Castro, L.; Lamb, J.; Chalamala, B.; Ferreira, S. R. *J. Power Sources* **2019**, *435*, 226777.
35. Rana, M.; Ahad, S. A.; Li, M.; Luo, B.; Wang, L.; Gentle, I.; Knibbe, R. *Energy Storage Mater.* **2019**, *18*, 289–310.
36. Choi, N.-S.; Chen, Z.; Freunberger, S. A.; Ji, X.; Sun, Y.-K.; Amine, K.; Yushin, G.; Nazar, L. F.; Cho, J. Bruce, P. G. *Angew. Chem. Int. Ed.* **2012**, *51*, 9994–10024.
37. Ueno, K.; Park, J.-W.; Yamazaki, A.; Mandai, T.; Tachikawa, N.; Dokko, K.; Watanabe, M. *J. Phys. Chem. C* **2013**, *117*, 20509–20516.
38. Balaish, M.; Kraysberg, A.; Ein-Eli, Y. *Phys. Chem. Chem. Phys.* **2014**, *16*, 2801–2822.
39. Rana, M.; Ahad, S. A.; Li, M.; Luo, B.; Wang, L.; Gentle, I.; Knibbe, R. *Energy Storage Mater.* **2019**, *18*, 289–310.
40. Bruce, P. G.; Freunberger, S. A.; Hardwick, L. J.; Tarascon, J.-M. *Nat. Mater.* **2012**, *11*, 19–29.
41. Peled, E.; Menkin, S. *J. Electrochem. Soc.* **2017**, *164*, A1703–A1719.
42. An, S. J.; Li, J.; Daniel, C.; Mohanty, D.; Nagpure, S.; Wood, D. L. *Carbon* **2016**, *105*, 52–76.
43. Kawaura, H.; Harada, M.; Kondo, Y.; Kondo, H.; Sugauma, Y.; Takahashi, N.; Sugiyama, J.; Seno, Y.; Yamada, N. L. *ACS Appl. Mater. Interfaces* **2016**, *8*, 9540–9544.
44. Peled, E.; Golodnitsky, D.; Ulus, A.; Yufit, V. *Electrochim. Acta* **2004**, *50*, 391–395.
45. Bae, J.; Qian, Y.; Li, Y.; Zhou, X.; Goodenough, J. B.; Yu, G. *Energy Environ. Sci.* **2019**, *12*, 3319–3327.
46. Li, C.; Zhang, H. P.; Fu, L. J.; Liu, H.; Wu, Y. P.; Rahm, E.; Holze, R.; Wu, H. Q. *Electrochim. Acta* **2006**, *51*, 3872–3883.
47. Nie, M.; Demeaux, J.; Young, B. T.; Heskett, D. R.; Chen, Y.; Bose, A.; Woicik, J. C.; Lucht, B. L. *J. Electrochem. Soc.* **2015**, *162*, A7008–7014.

48. Park, Y.; Shin, S. H.; Hwang, H.; Lee, S. M.; Kim, S. P.; Choi, H. C.; Jung, Y. M. *J. Mol. Struct.* **2014**, *1069*, 157–163.
49. Tian, R.; Park, S.-H.; King, Paul J. K.; Cunningham, G.; Coelho, J.; Nicolosi, V.; Coleman, J. N. *Nat. Commun.* **2019**, *10*, 1933.
50. Pal, B.; Yang, S.; Ramesh, S.; Thangadurai, V.; Jose, R. *Nanoscale Adv.* **2019**, *1*, 3807–3835.
51. Otaki, H. *溶液化学-溶質と溶媒の微視的相互作用 (化学選書)*; Shokabo Co., Ltd.: Tokyo, 1985.
52. Ue, M. *J. Electrochem. Soc.* **1994**, *141*, 3336–3342.
53. Gutmann, V. *Electrochim. Acta* **1976**, *21*, 661–670.
54. Inada, Y.; Niwa, Y.; Iwata, K.; Funahashi, S.; Ohtaki, H.; Nomura, M. *J. Mol. Liq.* **2006**, *129*, 18–24.
55. Eckert, F.; Leito, I.; Kaljurand, I.; Kütt, A.; Klamt, A.; Diedenhofen, M. *J. Comput. Chem.* **2009**, *30*, 799–810.
56. Hayamizu, K.; Aihara, Y.; Arai, S.; Martinez, C. G. *J. Phys. Chem. B* **1999**, *103*, 519–524.
57. Marcus, Y. *J. Solut. Chem.* **1984**, *13*, 599–624.
58. Mayer, U.; Gutmann, V.; Gerger, W. *Monatsh. Chem.* **1975**, *106*, 1235–1257.
59. Marcus, Y. *Ions in Solution and their Solvation*; John Wiley & Sons, Inc.: United States, 2015.
60. Seo, D. M.; Borodin, O.; Balogh, D.; O'Connell, M.; Ly, Q.; Han, S.-D.; Passerini, S.; Henderson, W. A. *J. Electrochem. Soc.* **2013**, *160*, A1061–A1070.
61. Hwang, S.; Kim, D.-H.; Shin, Jeong H.; Jang, J. E.; Ahn, K. H.; Lee, C.; Lee, H. *J. Phys. Chem. C* **2018**, *122*, 19438–19446.
62. Borodin, O.; Smith, G. D. *J. Phys. Chem. B* **2006**, *110*, 4971–4977.
63. Borodin, O.; Smith, G. D. *J. Solut. Chem.* **2007**, *36*, 803–813.
64. Dokko, K.; Watanabe, D.; Ugata, Y.; Thomas, M. L.; Tsuzuki, S.; Shinoda, W.; Hashimoto, K.; Ueno, K.; Umebayashi, Y.; Watanabe, M. *J. Phys. Chem. B* **2018**, *122*, 10736–10745.
65. Okamoto, Y.; Tsuzuki, S.; Tatara, R.; Ueno, K.; Dokko, K.; Watanabe, M. *J. Phys. Chem. C* **2020**, *124*, 4459–4469.
66. Harris, W. S. *Electrochemical Studies in Cyclic Esters. Ph.D. Thesis*, University of California: Berkeley, CA, 1958.
67. Lundgren, H.; Behm, M.; Lindbergh, G. *J. Electrochem. Soc.* **2014**, *162*, A413–A420.
68. Chen, Y. C.; Ouyang, C. Y.; Song, L. J.; Sun, Z. L. *J. Phys. Chem. C* **2011**, *115*, 7044–7049.
69. Scharte, B. *Materials* **2010**, *3*, 4710–4745.
70. Kozono, S.; Nakagawa, H.; Inamasu, T.; Katayama, Y.; Nukuda, T. *GS Yuasa Technical Report* **2005**, *2*, 26–31.
71. Watanabe, M.; Thomas, M. L.; Zhang, S.; Ueno, K.; Yasuda, T.; Dokko, K. *Chem. Rev.* **2017**, *117*, 7190–7239.

72. Wang, J.; Yamada, Y.; Sodeyama, K.; Chiang, C. H.; Tateyama, Y.; Yamada, A. *Nat. Commun.* **2016**, *7*, 12032.
73. Yamada, Y.; Furukawa, K.; Sodeyama, K.; Kikuchi, K.; Yaegashi, M.; Tateyama, Y.; Yamada, A. *J. Am. Chem. Soc.* **2014**, *136*, 5039–504.
74. Suo, L.; Borodin, O.; Gao, T.; Olguin, M.; Ho, J.; Fan, X.; Luo, C.; Wang, C.; Xu, K. *Science* **2015**, *350*, 938–943.
75. Zhang, C.; Ueno, K.; Yamazaki, A.; Yoshida, K.; Moon, H.; Mandai, T.; Umebayashi, Y.; Dokko, K.; Watanabe, M. *J. Phys. Chem. B* **2014**, *118*, 5144–5153.
76. Zhang, B.; Tan, R.; Yang, L.; Zheng, J.; Zhang, K.; Mo, S.; Lin, Z.; Pan, F. *Energy Stor. Mater.* **2018**, *10*, 139–159.
77. Kato, Y.; Hori, S.; Saito, T.; Suzuki, K.; Hirayama, M.; Mitsui, A.; Yonemura, M.; Iba, H.; Kanno, R. *Nat. Energy* **2016**, *1*, 16030.
78. Liu, Y.; Guo, X.; Nan, C.-W.; Chi, S.-S.; Zhao, N.; Fan, L.-Z. *Energy Stor. Mater.* **2019**, *17*, 309–316.
79. Song, J. Y.; Wang, Y. Y.; Wan, C. C. *J. Power Sources* **1999**, *77*, 183–197.
80. Murata, K.; Izuchi, S.; Yoshihisa, Y. *Electrochim. Acta* **2000**, *45*, 1501–1508.
81. Ishikawa, A.; Sakai, T.; Fujii, K. *Polymer* **2019**, *166*, 38–43.
82. Fergus, J. W. *J. Power Source* **2010**, *195*, 4554–4569.
83. Wright, P. V. *Br. Polym. J.* **1975**, *7*, 319–327.
84. Tang, S.; Zhao, H. *RSC Adv.* **2014**, *4*, 11251–11287.
85. Liu, S.; Imanishi, N.; Zhang, T.; Hirano, A.; Takeda, Y.; Yamamoto, O.; Yang, J. *J. Power Sources* **2010**, *195*, 6847–6853.
86. Srivastava, S.; Schaefer, J. L.; Yang, Z.; Tu, Z.; Archer, L. A. *Adv. Mater.* **2014**, *26*, 201–234.
87. Vélez, J. F.; Aparicio, M.; Mosa, J. *Electrochim. Acta* **2016**, *213*, 831–841.
88. Yuan, C.; Li, J.; Han, P.; Lai, Y.; Zhang, Z.; Liu, J. *J. Power Sources* **2013**, *240*, 653–658.
89. Jung, J.-W.; Lee, C.-L.; Yu, S.; Kim, I.-D. *J. Mater. Chem. A* **2016**, *4*, 703–750.
90. Li, Z.; Sha, W.-X.; Guo, X. *ACS Appl. Mater. Interfaces* **2019**, *11*, 26920–26927.
91. Meesala, Y.; Jena, A.; Chang, H.; Liu, R.-S. *ACS Energy Lett.* **2017**, *2*, 2734–2751.
92. Chen, L.; Li, Y.; Li, S.-P.; Fan, L.-Z.; Nan, C.-W.; Goodenough, J. B. *Nano Energy* **2018**, *46*, 176–184.
93. Ulaganathan, M.; Rajendran, S. *Ionics* **2010**, *16*, 515–521.
94. Schulze, M. W.; McIntosh, L. D.; Hillmyer, M. A.; Lodge, T. P. *Nano Lett.* **2014**, *14*, 122–126.
95. Bouchet, R.; Maria, S.; Meziane, R.; Aboulaich, A.; Lienafa, L.; Bonnet, J.-P.; Phan, T.N.T.; Bertin, D.; Gigmes, D.; Devaux, D.; Denoyel, R.; Armand, M. *Nat. Mater.* **2013**, *12*, 452–457.
96. Mindemark, J.; Torma, E.; Sun, B.; Brandell, D. *Polymer* **2015**, *63*, 91–98.
97. Cao, C.; Li, Y.; Feng, Y.; Long, P.; An, H.; Qin, C.; Han, J.; Li, S.; Feng, W. *J. Mater. Chem. A* **2017**, *5*, 22519–22526.

98. Łasińska, A. K.; Marzantowicz, M.; Dygas, J. R.; Krok, F.; Florjańczyk, Z.; Tomaszewska, A.; Zygadło-Monikowska, E.; Zukowska, Z.; Lafont, U. *Electrochim. Acta* **2015**, *169*, 61–72.
99. Miwa, Y.; Tsutsumi, H.; Oishi, T. *Polym. J.* **2001**, *33*, 927–933.
100. Nishimoto, A.; Agehara, K.; Furuya, N.; Watanabe, T.; Watanabe, M. *Macromolecules* **1999**, *32*, 1541–1548.
101. Nishimoto, A.; Watanabe, M.; Kohjiya, S. *Electrochim. Acta* **1998**, *43*, 1177–1184.
102. Marzantowicz, M.; Dygas, J.R.; Krok, F.; Tomaszewska, A.; Florjańczyk, Z.; Zygadło-Monikowska, E.; Lapienis, G. *J. Power Sources* **2009**, *194*, 51–57.
103. Watanabe, M.; Endo, T.; Nishimoto, A.; Miura, K.; Yanagida, M. *J. Power Sources* **1999**, *81–82*, 786–789.
104. Vallée, A.; Besner, S.; Prud'Homme, J. *Electrochim. Acta* **1992**, *37*, 1579–1583.
105. Pożyczka, K.; Marzantowicz, M.; Dygas, J. R.; Krok, F. *Electrochim. Acta* **2017**, *227*, 127–135.
106. Diddens, D.; Heuer, A.; Borodin, O. *Macromolecules* **2010**, *43*, 2028–2036.
107. Brooks, D. J.; Merinov, B. V.; Goddard, W. A.; Kozinsky, B.; Mailoa, J. *Macromolecules* **2018**, *51*, 8987–8995.
108. Webb, M. A.; Savoie, B. M.; Wang, Z.-G. Miller III, T. F. *Macromolecules* **2015**, *48*, 7346–7358.
109. Teran, A. A.; Tang, M. H.; Mullin, S. A.; Balsara, N. P. *Solid State Ion.* **2011**, *203*, 18–21.
110. Angell, C. A. *Electrochim. Acta* **2017**, *250*, 368–375.
111. Siqueira, L. J. A.; Ribeiro, M. C. C. *J. Phys. Chem.* **2005**, *122*, 194911.
112. Redfern, P. C.; Curtiss, L. A. *J. Power Sources* **2002**, *110*, 401–405.
113. Kerr, J. B.; Han, Y. B.; Liu, G.; Reeder, C.; Xie, J.; Sun, X. *Electrochim. Acta* **2004**, *50*, 235–242.
114. Edman, L. *J. Phys. Chem. B* **2000**, *104*, 7254–7258.
115. Tominaga, Y.; Nanthana, V.; Tohyama, D. *Polym. J.* **2012**, *44*, 1155–1158.
116. Motomatsu, J.; Kodama, H.; Furukawa, T.; Tominaga, Y. *Macromol. Chem. Phys.* **2015**, *216*, 1660–1665.
117. Florjańczyk, Z.; Zygadło-monikowska, E.; Wieczorek, W.; Ryszawy, A.; Tomaszewska, A.; Fredman, K.; Golodnitsky, D.; Peled, E.; Scrosati, B. *J. Phys. Chem. B* **2004**, *108*, 14907–14914.
118. Forsyth, M.; MacFarlane, D. R.; Hill, A. J. *Electrochim. Acta* **2000**, *45*, 1243–1247.
119. Ye, L.; Feng, Z.-g.; Su, Y.-f.; Wu, F.; Chen S.; Wang, G.-q. *Polym. Int.* **2005**, *54*, 1440–1448.
120. Shintani, Y.; Tsutsumi, H. *J. Power Sources* **2010**, *195*, 2863–2869.
121. Nakano, Y.; Tsutsumi, H. *Solid State Ionics* **2014**, *262*, 774–777.



**YAMAGUCHI
UNIVERSITY**

Chapter 1

Role of polar side chains in Li⁺ coordination and transport properties of polyoxetane-based polymer electrolytes

1.1. Introduction

I prepared two different polyoxetane-based PEs bearing ether or nitrile groups in their side chains. Polyoxetane-based PEs with nitrile groups in the previous study¹ were revisited to investigate the role of the polar side groups in the coordination structure of Li⁺ and the ionic transport properties in more detail. The local structure of Li⁺ ions in the PEs with different salt concentrations was studied by Raman spectroscopy. Spectroscopic analysis enabled us to estimate the coordination number of each functional group and the counter anion of the lithium salt. The effects of the polar side chains on the ionic transport properties were also elucidated in terms of the diffusion coefficients of the ions (measured by pulsed-field-gradient (PFG-) NMR) and the ionic conductivity. To demonstrate the potential application in lithium metal batteries, I also investigated the electrochemical anodic and cathodic stabilities of polyoxetane-based PEs.

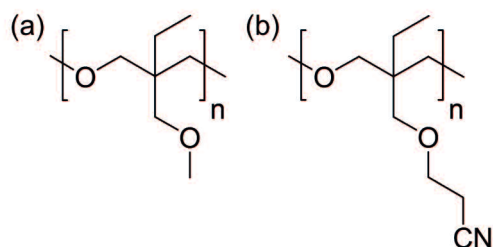


Figure 1.1 Matrix polymers: (a) PEMO and (b) PCEO.

1.2. Experimental section

1.2.1. Preparation of monomer

The monomers, 3-(2-cyanoethoxymethyl)-3-ethyloxetane with a nitrile group (CEO) and 3-ethyl-3-methoxymethyloxetane with an ether group (EMO) were prepared from 3-ethyl-3-hydroxymethyloxetane (EHO) according to a reported procedure.^{2,3} CEO was synthesized by Michael addition. EHO (23.0 mL, 0.202 mol) was mixed with acrylonitrile (24.0 mL, 0.366 mol) in pure water (50 mL) containing a 20% tetraethylammonium hydroxide solution (2.6 mL) as a catalyst, and the mixture was stirred at room temperature for 22 h. The reaction mixture was extracted with chloroform and the solution was washed with water. After the solution was dehydrated with magnesium sulfate, volatile chloroform was removed using a rotary evaporator. The residue was distilled under reduced pressure (124°C, 1 mmHg). Yield: 23.3 g, 68%.

CEO ¹H NMR (δ , ppm from trimethylsilane (TMS) in CDCl₃): 0.90 (t, 3H, $J_{\text{CH}_3-\text{CH}_2} = 7.50$ Hz, $-\text{CH}_3$), 1.76 (q, 2H, $J_{\text{CH}_2-\text{CH}_3} = 7.50$ Hz, $-\text{CH}_2-\text{CH}_3$), 2.44 (t, 2H, $J_{\text{CH}_2-\text{CH}_2} = 6.25$ Hz, $-\text{CH}_2-\text{CH}_2-\text{CN}$), 3.63 (s, 2H, $-\text{C}-\text{CH}_2-\text{O}-$), 3.72 (t, 2H, $J_{\text{CH}_2-\text{CH}_2} = 6.43$ Hz, $-\text{CH}_2-\text{CH}_2-\text{CN}$), 4.45 (dd, 4H, $J_{-\text{CH}_2-\text{O}-\text{CH}_2-} = 6.00$ Hz, ring, $-\text{CH}_2-\text{O}-\text{CH}_2-$).

EMO was synthesized from EHO (20 mL, 0.176 mol), methyl methane sulfonate (18 mL, 0.212 mol), and 8.41 g of 40–60 wt% sodium hydride (~0.21 mol). Sodium hydride dispersed in mineral oil was washed with hexane prior to use. The above reactants were stirred in 300 mL of tetrahydrofuran (THF) in an ice bath for 3 h, and then at room temperature for 16 h. THF was removed from the reaction mixture using a rotary evaporator. The remaining solution was diluted with dichloromethane, and the solution was washed with water. The organic extract was dehydrated with magnesium sulfate, and dichloromethane was removed by distillation. The residue was distilled under reduced pressure (55°C, 64 mmHg). Yield: 7.59 g, 33.1%.

EMO ¹H NMR (δ , ppm from TMS in CDCl₃): 0.89 (t, 3H, $J_{\text{CH}_3-\text{CH}_2} = 7.25$ Hz, $-\text{CH}_3$), 1.74 (q, 2H, $J_{\text{CH}_3-\text{CH}_2} = 7.33$ Hz, $-\text{CH}_2-\text{CH}_3$), 3.40 (s, 3H, $-\text{O}-\text{CH}_3$), 3.51 (s, 2H, $-\text{C}-\text{CH}_2-\text{O}-$), 4.42 (dd, 4H, $J_{\text{CH}_2-\text{O}-\text{CH}_2} = 5.75$ Hz, ring, $-\text{CH}_2-\text{O}-\text{CH}_2-$).

1.2.2. Preparation of the polymer

CEO and EMO were polymerized using a ring-opening cationic polymerization (ROCP) using boron trifluoride diethyl etherate (BF₃-Et₂O) as an initiator. The molar ratio of the monomer (20 mmol) to the initiator (0.4 mmol) was adjusted to 50:1. The monomer was dissolved in 1,2-dichloroethane; then, BF₃-Et₂O was added to the solution (total volume: 5 mL). The polymerization was performed under an Ar atmosphere at 0°C in a salt ice bath for 5 h and 1 h for CEO and EMO, respectively. The ROCP was quenched using 5 mL of a 4 M NaCl/1 M NaOH aqueous solution. Chloroform was then added to the resulting solution, and the mixture was washed with water. The organic phase containing the polyoxetanes was concentrated by rotary evaporation. The residual viscous solution was poured into a large amount of 2-propanol and methanol for polymerized CEO (PCEO) and EMO (PEMO), respectively, to reprecipitate the polyoxetanes. The polymers were finally collected by filtration using a glass filter and dried at 60°C under vacuum overnight. PCEO and PEMO were obtained in 47.3% and 71.5% yields, respectively. The successful ROCP was further confirmed by ¹H NMR as the disappearance of double-doublet signals ($\delta = \sim 4.4\text{--}4.5$ ppm for the monomers) of methylene protons in the four-membered ring structure for the oxetane monomers. The chemical structures of PEMO and PCEO are shown in Figure 1.1.

PCEO ¹H NMR (δ , ppm from TMS in CDCl₃): 0.86 (t, 3H, $J_{\text{CH}_3\text{-CH}_2} = 7.50$ Hz, $-\text{CH}_3$), 1.40 (q, 2H, $J_{\text{CH}_2\text{-CH}_3} = 7.33$ Hz, $-\text{CH}_2\text{-CH}_3$), 2.59 (t, 2H, $J_{\text{CH}_2\text{-CH}_2} = 6.00$ Hz, $-\text{CH}_2\text{-CH}_2\text{-CN}$), 3.23 (s, 4H, $-\text{C}-\text{CH}_2\text{-O-}$), 3.36 (s, 2H, $-\text{C}-\text{CH}_2\text{-O-}$), 3.62 (t, 2H, $J_{\text{CH}_2\text{-CH}_2} = 6.25$ Hz, $-\text{CH}_2\text{-CH}_2\text{-CN}$).

PEMO ¹H NMR (δ , ppm from TMS in CDCl₃): 0.84 (t, 3H, $J_{\text{CH}_3\text{-CH}_2} = 7.50$ Hz, $-\text{CH}_3$), 1.37 (q, 2H, $J_{\text{CH}_2\text{-CH}_3} = 7.50$ Hz, $-\text{CH}_2\text{-CH}_3$), 3.19 (s, 3H, $-\text{O}-\text{CH}_3$), 3.23 (s, 2H, $-\text{C}-\text{CH}_2\text{-O-}$), 3.29 (s, 2H, $-\text{C}-\text{CH}_2\text{-O-}$).

1.2.3. Preparation of the polymer electrolytes

PEs were prepared by mixing the polymer and 1 M LiTfSA in THF; then, the mixtures were heated under vacuum to completely remove the solvent. In this report, the molar ratio of the repeating monomer unit to LiTfSA is represented as “*a*” ($a = 40, 30, 20, 10, 5,$ and 3) for PEMO_{*a*}LiTfSA and PCEO_{*a*}LiTfSA. The complete dissolution of LiTfSA was confirmed by transparent appearance of PCEO_{*a*}LiTfSA even at higher salt concentrations. Due to their white-turbidity based on higher crystallinity of the host polymer, the dissolution

of LiTFSA in PEO_aLiTFSA was confirmed by a linear relationship between integral intensity of Raman band for TFSA anions and the concentration of LiTFSA. The concentrations of LiTFSA (c_{Li}) were estimated using the corresponding monomer densities (0.917 g cm⁻³ for EMO and 1.005 g cm⁻³ for CEO) and the reported density of molten LiTFSA (1.970 g cm⁻³). The high temperature data of the density of molten LiTFSA⁴ was extrapolated to room temperature. For calculating the density of the PEs, the additivity of the volumes of the monomers and LiTFSA was assumed.

1.2.4. Measurements

¹H NMR spectra of the synthesized substances were recorded using a FT-NMR spectrophotometer (JNM-LA-500, JEOL). The molecular weight of the polymers was measured using a gel permeation chromatography (GPC) system (SCL-10AVP, LC-10ADVP, DGU-12A, CTO-10AVP, and RID-10A, Shimadzu) with a column (GPC Linear LF-804, Shodex). GPC was performed using THF as the eluant and polystyrene standards for column calibration.

A differential scanning calorimeter (DSC7020, HITACHI) was used to determine the melting point (T_m) and glass transition temperature (T_g). A small amount of the PEs (~10 mg) was hermetically sealed in an aluminum DSC pan. The samples were first heated to 120°C, cooled to -120°C, and heated again to 120°C at a heating/cooling rate of 10°C min⁻¹. The second heating scan was recorded as the DSC thermogram of the samples. Glass transition temperature (T_g) was determined as the onset of the heat flow step.

Raman spectra of the PEs were measured by a laser Raman spectrophotometer (MRS-3100, JASCO) with a 532 nm laser. The PE was sealed between two glass plates with a rubber spacer (thickness = 5 mm) in an Ar-filled glove box to avoid moisture adsorption. Raman spectra of PCEO_aLiTFSA and PEO_aLiTFSA were measured from 500 to 2400 cm⁻¹ and from 500 to 1600 cm⁻¹, respectively, with a resolution of 4 cm⁻¹. The obtained spectra were normalized based on the methylene vibration of the polyoxetanes (1390–1520 cm⁻¹) and were analyzed with commercially available software for peak fitting (PeakFit™ version 4.12, SeaSolve Co.). A pseudo-Voigt function was used for peak deconvolution.

Ionic conductivity of the PEs was measured by impedance spectroscopy using an LCR meter (3532-80 chemical impedance meter, HIOKI). The PE was placed between two stainless steel electrodes separated by a polytetrafluoroethylene (PTFE) spacer, and the conductivity cell was thermally equilibrated in a thermostatic bath at each temperature for 1 h before the measurements. PEO_aLiTFSA with a low LiTFSA ratio (i.e., high “*a*” value) formed a self-standing membrane; the conductivity was measured without a PTFE spacer.

Self-diffusion coefficients of the ions in PCEO₅LiTFSA or PEO₅LiTFSA were determined by PFG-NMR at 80°C using a modified Hahn spin-echo sequence incorporating a sinusoidal PFG in each τ period. ⁷Li and ¹⁹F spectra were measured for lithium cations and TFSA anions, respectively. In this measurement, the value of the time interval between the two gradient pulses (Δ) was set to 50 ms, and the duration of the field gradient (δ) was adjusted to a constant value. The magnitude of the field gradient (g , 0–13 T m⁻¹) was varied for recording the attenuation of the spin-echo signal intensity (S). Self-diffusion coefficients, D_{Li} and D_{F} , were determined according to the Stejskal-Tanner equation,⁵

$$\ln(S/S_0) = -\gamma^2 g^2 \delta^2 D (4\Delta - \delta)/\pi^2 \quad (1)$$

where γ is the gyromagnetic ratio and S_0 is the initial echo signal intensity.

Linear sweep voltammetry (LSV) and cyclic voltammetry (CV) were performed (scan rate of 1 mV s⁻¹) to study the anodic and cathodic electrochemical stabilities, respectively, with an electrochemical measurement system (HZ-5000, Hokuto Denko) at 70°C. For anodic LSV, lithium metal foil was used as the counter and reference electrodes and a stainless steel disk was used as the working electrode. For CV measurements, lithium metal foil was used as the counter and reference electrodes and a Ni disk was used as the working electrode.

1.3. Results and discussion

1.3.1. Thermal properties

Synthesized PEMO was obtained as a white solid powder whereas PCEO was an only slightly yellowish, sticky solid. Table 1.1 summarizes the molecular weight and thermal properties of the polymers, where M_n is the number average molecular weight, M_w is the weight-average molecular weight, M_n/M_w is the polydispersity index, and ΔH is the enthalpy of fusion derived from the crystalline phase. Successful ROCP yielded high molecular weight polymers. For PCEO, the optimized synthetic procedure allowed us to obtain higher molecular weight than that reported in our previous work ($M_n = 8600$).⁶ Both polymers were semi-crystalline, and the T_m and T_g values of synthesized PEMO and PCEO were higher than $T_m(20^\circ\text{C})$ and $T_g(-71^\circ\text{C})$ of plain PTMO, $-(\text{CH}_2\text{CH}_2\text{CH}_2\text{O})_n-$,⁷ suggesting that introduction of the side substitution group affected the thermal properties of the polyoxetanes. The crystallinity of PEMO and PCEO appears to be not high because their ΔH values were much lower than the reported ΔH of PEO with high crystallinity (160~200 J g⁻¹).⁸ PEMO had higher T_m and ΔH values than PCEO (Table 1.1), indicating that PEMO is more prone to forming a crystalline phase. The lower crystallinity of PCEO is probably due to the longer side chains with nitrile groups that sterically hinder packing of the polymer chains into the regular forms necessary for crystallization. In contrast, the T_g of PCEO was higher than that of PEMO. The dipole-dipole interactions between the polar nitrile groups likely increase the cohesive energy of PCEO, leading to a higher T_g .

Table 1.1 Molecular weights (M_n and M_w), polydispersity index (M_w/M_n), and thermal properties (T_g , T_m , and ΔH) of the synthesized polymers.

	Molecular weight			Thermal characteristics		
	M_n [kg mol ⁻¹]	M_w [kg mol ⁻¹]	M_n/M_w [-]	T_g [°C]	T_m [°C]	ΔH [J g ⁻¹]
PEMO	376	8.81	2.34	-36.3	73.6	34.2
PCEO	45.6	108	2.37	-18.3	55.0	10.8

T_m was observed at 73–75°C in the thermograms of PEMO_aLiTFSA, except for a highly concentrated sample ($a = 3$); however, ΔH decreased with increasing salt concentrations

(Table 1.2). For PCEO_aLiTFSA, T_m was not discernible, even at low salt concentrations ($a < 20$), probably because of the intrinsic low-crystallinity of PCEO.

Table 1.2 Thermal properties (T_g , T_m , and ΔH) of the PEs: PEO_aLiTFSA and PCEO_aLiTFSA.

	a	T_g [°C]	T_m [°C]	ΔH [J g ⁻¹]
PEMO	–	–36.3	73.4	34.2
	40	–34.0	75.4	34.8
	26	–30.1	74.8	35.1
	20	–22.6	74.9	21.0
	10	–24.6	75.3	26.3
	5	–21.4	72.6	16.1
	3	–16.9	–	–
	PCEO	–	–18.3	55.0
40		–16.8	59.5	2.5
30		–16.1	61.6	3.2
20		–16.9	61.2	2.3
10		–15.8	–	–
5		–22.6	–	–
3		–29.5	–	–

Figure 1.2 shows the T_g of the PEs as a function of the molar ratio of possible interaction sites and LiTFSA in the PEs ($[O]+[CN])/[Li]$; the nitrile group was counted in addition to the oxygen atoms in the main and side chains for PCEO. For comparison, literature data for PEO_aLiTFSA and PTMO_aLiTFSA are shown in Figure 1.2.^{9,10} The T_g values of PEO_aLiTFSA and PTMO_aLiTFSA increase with increasing Li salt concentrations because of the formation of an ionically crosslinked structure via coordination of Li⁺ ions with ether moieties in the polymer main chains (complexation). Although the change in T_g of PEO_aLiTFSA was less obvious than that of the reported PEO_aLiTFSA system, T_g gently increased as LiTFSA was added to PEO. The upward tendency of T_g was very similar to that of PTMO_aLiTFSA. The gradual dependence of T_g on the salt concentration was also observed for comb-type polyoxetanes.¹¹ At higher Li salt concentrations, the T_g of PEO_aLiTFSA approached the reported T_g value of PEO_aLiTFSA, suggesting a dense cross-linking between PEO chains by Li⁺ ions.

Interestingly, the T_g of PCEO_aLiTFSA increased only marginally at lower salt concentrations, but was remarkably reduced at higher salt concentrations (Figure 1.2). In our previous work,¹² we also reported that T_g of oligomeric PCEO_aLiClO₄ and PCEO_aLiTFSA decreased with increasing Li salt concentration, implying that the decrease in T_g is independent of molecular weight of PCEO and type of Li salts. This opposite trend for T_g at higher salt concentrations was rarely observed for polyether-based PEs. However, a similar decrease in T_g with the addition of Li salt has been reported for polyacrylonitrile (PAN)-based PEs, especially at high salt concentrations as for polymer-in-salt systems. Forsyth *et al.* reported that the T_g of PAN decreased from 80°C (for pure PAN) to 50°C with the addition of lithium triflate.¹³ The significant decrease in T_g from 43°C (for pristine polymer matrix) to -22°C was also observed for a copolymer of acrylonitrile and butyl acrylate, poly(PAN-co-BuA), in the presence of LiTFSA.¹⁴ This plasticizing effect was interpreted because of highly dissociative Li salts interacting with -C≡N moieties, which weakened the dipole-dipole interactions between the polymer chains. Likewise, the coordination of Li⁺ ions with the nitrile groups of PCEO contribute to the unusual lowering of T_g for PCEO_aLiTFSA, despite ether-based PEs.

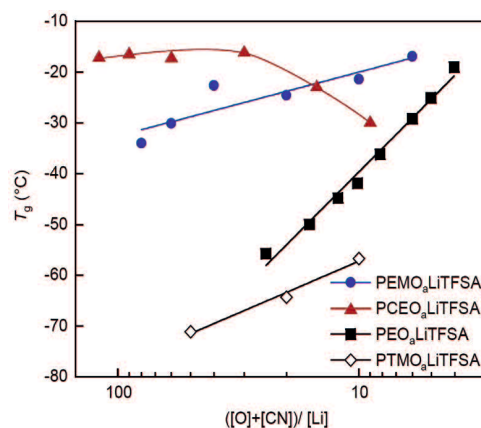


Figure 1.2 T_g as a function of the molar ratio of possible interaction sites and LiTFSA in the PEs $([O] + [CN])/[Li]$ for PEO_aLiTFSA (■), PTMO_aLiTFSA (◇), PEMO_aLiTFSA (●), and PCEO_aLiTFSA (▲). T_g values for PEO_aLiTFSA and PTMO_aLiTFSA were obtained from refs 9 and 10, respectively.

1.3.2. Coordination structure of Li⁺ ions

Raman spectra were measured for the polyoxetane-based PEs with difference salt concentrations to study the Li⁺ coordination. Figure 1.3a shows Raman spectra of PCEO_aLiTFSA from 2200 to 2320 cm⁻¹. Pure PCEO showed a single peak at 2249 cm⁻¹ assigned to C≡N stretching vibrations. With the addition of LiTFSA, the intensity of the band at 2249 cm⁻¹ decreased, whereas a new band emerged at 2277 cm⁻¹ and its intensity increased. Similar peak shift of the C≡N stretching vibration was also observed in IR spectra of oligomeric PCEO-based PEs with different Li salts.¹ Given that the C≡N stretching band of acetonitrile (MeCN) shifted to higher wavenumber by 23 cm⁻¹ upon coordination of Li⁺ ions,¹⁵ this new band can be assigned to the C≡N stretching mode of the nitrile groups that interact with Li⁺ ions in PCEO_aLiTFSA. Even at the highest salt concentration studied here ($a = 3$; that is, the molar ratio of the nitrile groups and Li⁺ ions $c_{\text{CN}}/c_{\text{Li}} = 3$), the original band at 2249 cm⁻¹ was still observed, suggesting that some of the nitrile groups remained uncoordinated in PCEO_aLiTFSA.

Concentration-dependent Raman spectra were analyzed to elucidate the coordination of Li⁺ ions with the nitrile groups. As shown in Figure 1.3b, the experimental spectrum is well explained by deconvolution of the Raman spectra into four bands located at 2248, 2253, 2264, and 2277 cm⁻¹ over the whole concentration range; however, curve fitting the two bands at 2249 and 2277 cm⁻¹ failed to reproduce the experimental data accurately. In this study, I assigned the lower bands at 2248 and 2253 cm⁻¹ to the uncoordinated, free nitrile groups, while the higher bands at 2264 and 2277 cm⁻¹ were due to the nitrile groups bound to Li⁺ ions. In previous studies, the uncoordinated C≡N stretching mode of MeCN was also explained by the combination of two bands.¹⁵ Although there is controversy as to whether the lower second band for MeCN is due to dimerization or a “hot band,”¹⁶ I employed the two-band approach for fitting the peak of the uncoordinated nitrile functionality in PCEO. For the bound nitrile groups, ab initio calculations of Li⁺(MeCN)_x clusters predicted that variation of the C≡N stretch of Li⁺(MeCN)_x from that of isolated MeCN was +10 cm⁻¹ at $x = 1$ and +20 cm⁻¹ at $x = 3, 4$.¹⁵ Therefore, the deconvoluted middle band at 2264 cm⁻¹ and the band at 2277 cm⁻¹ in PCEO_aLiTFSA can be attributed to the bound nitrile groups.

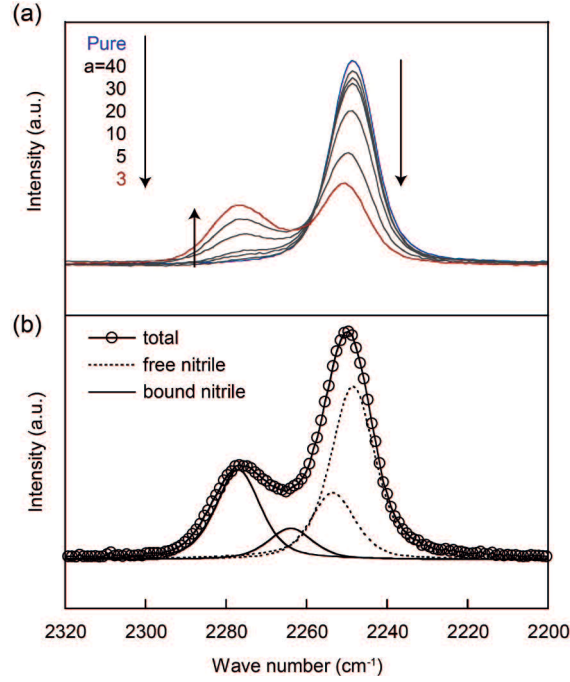


Figure 1.3 Raman spectra of the nitrile group in PCEO_aLiTFSA (2200–2320 cm⁻¹) at room temperature, (a) dependence on Li salt concentration (pure and $a = 3$ –40) and (b) typical result after deconvolution of the spectrum for $a = 5$.

The sum of the integrated intensities of the lower two bands, $I_{\text{r(CN)}} = I_{2248} + I_{2253}$, is related to the concentration of the uncoordinated, free nitrile groups ($c_{\text{r(CN)}}$) in PCEO_aLiTFSA: $I_{\text{r(CN)}} = J_{\text{r(CN)}}c_{\text{r(CN)}}$, where $J_{\text{r(CN)}}$ is the molar Raman scattering coefficient of the free nitrile moieties because $c_{\text{r(CN)}} = c_{\text{CN}} - n_{\text{CN}}c_{\text{Li}}$, where n_{CN} denotes the coordination number of the nitrile group to Li⁺ ions and c_{CN} is the total concentration of the nitrile groups. Thus, the following relationship holds,

$$\frac{I_{\text{r(CN)}}}{c_{\text{Li}}} = J_{\text{r(CN)}} \left(\frac{c_{\text{CN}}}{c_{\text{Li}}} - n \right) = J_{\text{r(CN)}} (a - n_{\text{CN}}) \quad (2)$$

Figure 1.4 shows $I_{\text{r(CN)}}/c_{\text{Li}}$ plotted as a function of a ($= c_{\text{CN}}/c_{\text{Li}}$) for PCEO_aLiTFSA. The linear least-square fitting provides $J_{\text{r(CN)}}$ and n_{CN} from the slope and the intercept, and the n_{CN} value is 0.93 ± 0.67 . This indicates that one nitrile group is coordinated to Li⁺ ions on average, but Li⁺ ions were also coordinated by other sites, such as oxygen atoms in PCEO and TFSA anions because the coordination number of Li⁺ ions is 4–5 in electrolyte solutions and PEs.^{17,18}

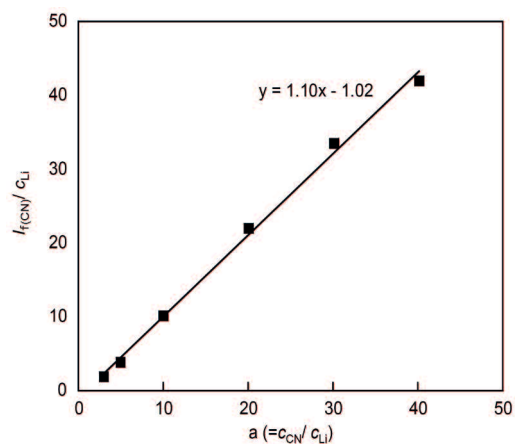


Figure 1.4 $I_{r(CN)}/c_{Li}$ plotted as a function of a ($= c_{CN}/c_{Li}$) for $PCEO_aLiTFSA$. The solid line represents the least-square linear fitting.

Figure 1.5a and b shows Raman spectra from 710 to 780 cm^{-1} for $PEMO_aLiTFSA$ and $PCEO_aLiTFSA$. The observed bands in this range can be assigned to the CF_3 bending vibration coupled with the S-N stretching vibration of TFSA anions. The band at 739–741 cm^{-1} corresponds to a solvent-separated ion pair (SSIP) or a spectroscopically free TFSA anion, whereas the band at 745–746 cm^{-1} results from TFSA anion bound directly to Li^+ ions in the form of a contact ion pair (CIP) or an aggregate (AGG).¹⁹ The spectra are asymmetrically shaped, even at lower salt concentrations for $PEMO_aLiTFSA$ (Figure 1.5a and b), suggesting that different TFSA species (i.e., free or bound) coexisted in the oxetane-based PEs.

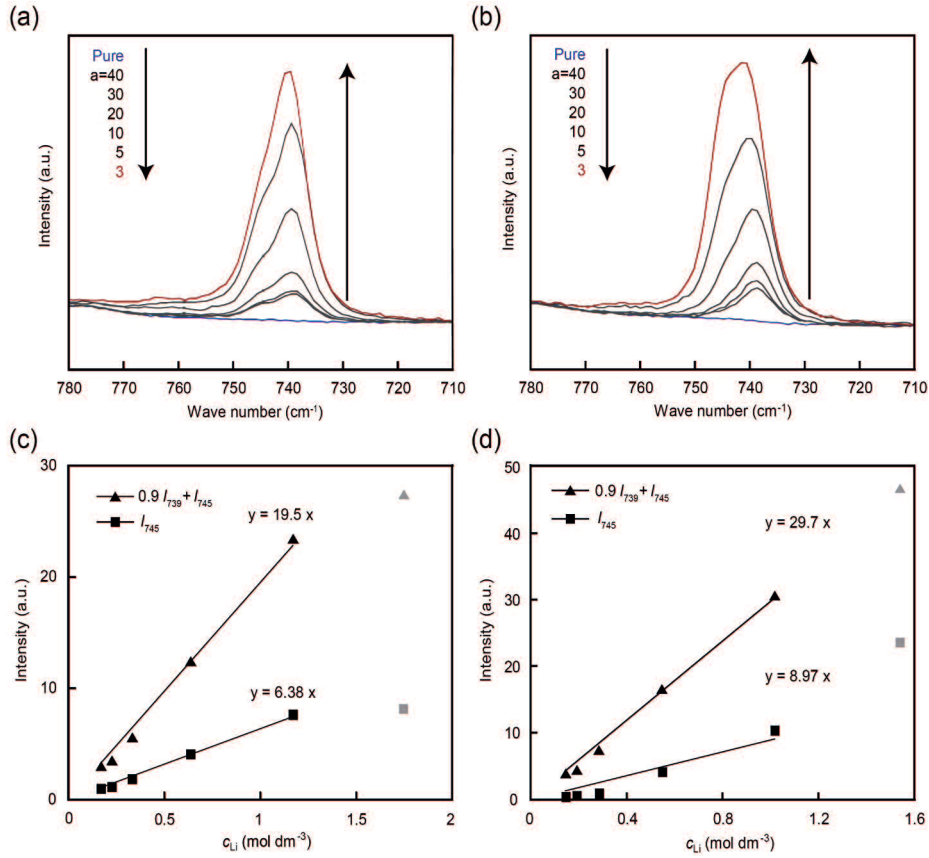


Figure 1.5 Raman spectra (710–780 cm^{-1}) at room temperature for (a) $\text{PEMO}_a\text{LiTFSA}$ and (b) $\text{PCEO}_a\text{LiTFSA}$. The integral intensities plotted as a function of c_{Li} for (c) $\text{PEMO}_a\text{LiTFSA}$ and (d) $\text{PCEO}_a\text{LiTFSA}$. The solid lines represent the least-square linear fitting based on equations (3) and (4).

To estimate the coordination number of TFSA (n_{TFSA}), curve-fitting was performed using two bands at 739 and 745 cm^{-1} , respectively (Figure 1.6). The integrated intensities of the two bands for TFSA, $I_{739(\text{TFSA})}$ and $I_{745(\text{TFSA})}$, can be written as $I_{739(\text{TFSA})} = J_{739(\text{TFSA})}c_{739(\text{TFSA})}$ and $I_{745(\text{TFSA})} = J_{745(\text{TFSA})}c_{745(\text{TFSA})}$, where $J_{739(\text{TFSA})}$ and $J_{745(\text{TFSA})}$ are the molar Raman scattering coefficients of each band. $c_{739(\text{TFSA})} = (1 - n_{\text{TFSA}})c_{\text{Li}}$ and $c_{745(\text{TFSA})} = n_{\text{TFSA}}c_{\text{Li}}$ are the concentrations of TFSA in form of spectroscopically free or SSIP and CIP or AGG, respectively. With the reported ratio of the molar Raman scattering coefficients, $J_{745(\text{TFSA})}/J_{739(\text{TFSA})} = 0.9$,²⁰ I obtained the following two relationships,

$$0.9I_{739(\text{TFSA})} + I_{745(\text{TFSA})} = J_{745(\text{TFSA})}c_{\text{Li}} \quad (3)$$

$$I_{745(\text{TFSA})} = J_{745(\text{TFSA})}n_{\text{TFSA}}c_{\text{Li}} \quad (4)$$

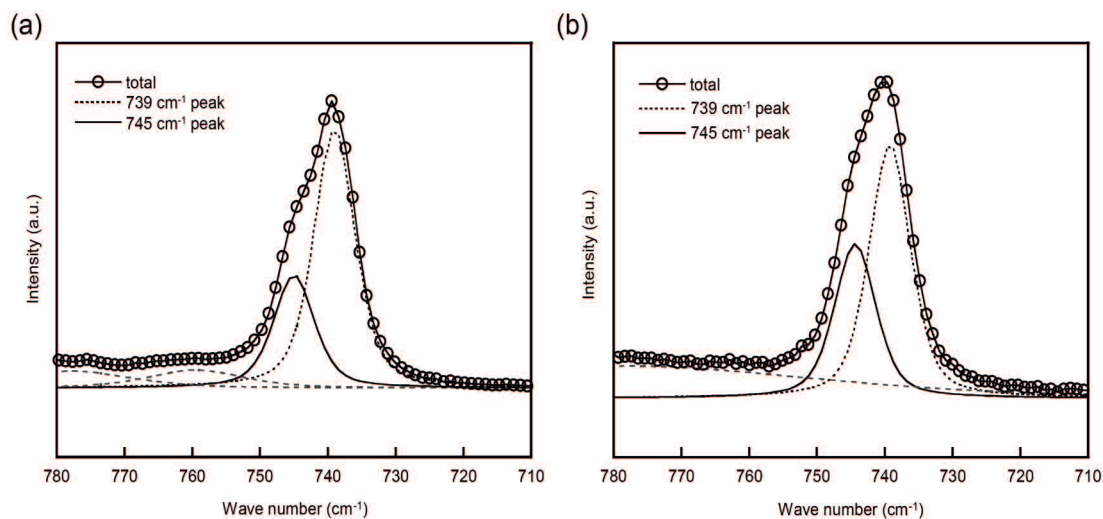


Figure 1.6 Typical Raman spectra and deconvolution results for the TFSA anion from 710 to 780 cm^{-1} at room temperature for (a) $\text{PEMO}_5\text{LiTFSA}$ and (b) $\text{PCEO}_5\text{LiTFSA}$.

As shown in Figure 1.5c and d, the plot of $0.9I_{739(\text{TFSA})} + I_{745(\text{TFSA})}$ vs. c_{Li} gives a straight line, except for the highly concentrated samples of $\text{PEMO}_3\text{LiTFSA}$ and $\text{PCEO}_3\text{LiTFSA}$, and $J_{745(\text{TFSA})}$ was obtained from the slope of the linear fitting. Thus, the averaged n_{TFSA} can be estimated from the plot of $I_{745(\text{TFSA})}$ vs. c_{Li} using the obtained $J_{745(\text{TFSA})}$. This analysis yields $n_{\text{TFSA}} = 0.33 \pm 0.01$ and 0.30 ± 0.04 for $\text{PEMO}_a\text{LiTFSA}$ and $\text{PCEO}_a\text{LiTFSA}$, respectively. Therefore, a similar proportion of TFSA anions coordinated to Li^+ ions in form of CIP or AGG in both PEMO and PCEO in this concentration region on average. Many of TFSA anions remained uncoordinated or in form of SSIP in which Li^+ ions were mainly coordinated by nitrile groups and/or ether oxygens in the PEs. At the highest concentration of PCEO_3TFSA , n_{TFSA} can be estimated to a higher value in Figure 1.5d, suggesting that the fraction of bound TFSA anions increased at higher salt concentration. For $\text{PEMO}_3\text{LiTFSA}$, the plot based on eq. (3) in Figure 1.5c largely deviated from the linear fitting line, so that I did not estimate n_{TFSA} . This may arise from incomplete dissolution of LiTFSA in PEMO at the highest salt concentration. Because it is difficult to discern free TFSA anion from SSIP by Raman band at 739 cm^{-1} , n_{TFSA} was not discussed in correlation with ionic dissociation in the latter section.

Oxygen atoms in both the main chains and the side chains also have the potential to coordinate Li^+ ions. Raman bands between 800 and 900 cm^{-1} have been assigned to a mixture

of modes for CH₂ rocking vibrations and C–O–C stretching vibrations, which are very sensitive to their conformational change upon Li⁺ coordination.^{21,22} Although there were discernible changes in the spectra after addition of LiTFSA (Figure 1.7), the Raman spectra in this range were very complicated because of the crystallinity of the polymers at lower salt concentrations and the significant band overlap in both PEO_aLiTFSA and PCEO_aLiTFSA. Hence, I did not perform further spectroscopic analyses of the Raman spectra in this range. Instead, the coordination number of oxygen atoms (n_O) in both the main chains and the side chains can be roughly estimated from n_{CN} and n_{TFSA} by taking the total coordination number of Li⁺ of 4–5 into account: $n_O = 3–5$ and 2–4 for PEO_aLiTFSA and PCEO_aLiTFSA, respectively.

The above results indicate that mixed coordination occurred in the polyoxetane-based PEs, particularly in PCEO_aLiTFSA. Given the number densities of each coordination site and the Gutmann donor number (DN) of low molecular solvent models, MeCN ($DN = 14.1$ kcal mol⁻¹),²³ ethers ($DN = 15–20$ kcal mol⁻¹),²³ and TFSA anions ($DN = \sim 10$ kcal mol⁻¹),²⁴ it is reasonable that the Li⁺ coordination with the polyoxetane-based oxygen atoms was more dominant than the nitrile groups and TFSA anions in PCEO_aLiTFSA.

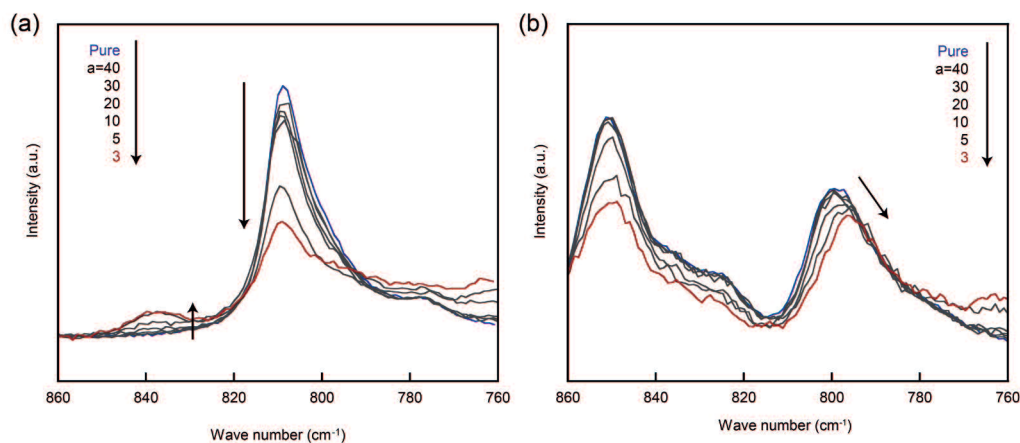


Figure 1.7 Raman spectra of the ether groups from 760 to 860 cm⁻¹ at room temperature for (a) PEO_aLiTFSA and (b) PCEO_aLiTFSA.

1.3.3. Ionic transport

Except for semi-crystalline PEMO_aLiTFSA with T_m below room temperature ($a > 3$), the prepared PEs did not form a rubbery solid membrane but were sticky mixtures. However, a self-standing membrane can be readily prepared by introducing either a physical or chemical cross-linking point on the polymers. Here, I employed both semi-crystalline PEMO_aLiTFSA and the polyoxetane-based sticky PEs to focus on the effects of the polar side chains on the ionic transport properties.

Figure 1.8 shows the concentration dependence of ionic conductivity (σ) at 30°C and above the T_m of the PEs. The estimated molar conductivity (Λ_{est}), which was calculated by dividing conductivity at each temperature by c_{Li} at room temperature, were also shown in Figure 1.9. For PEMO_aLiTFSA, the ionic conductivity and Λ_{est} continued to increase upon addition of LiTFSA at 30°C. Although the increase in Λ_{est} with increasing salt concentrations can be interpreted by Fuoss-Kraus theory for triple ion formation in low polar solvents,²⁵ the decrease in the crystallinity of PEMO would be predominantly responsible for the increased conductivity as evidenced by lower ΔH of melting at higher salt concentration in Table 1.2. The ionic conductivities of semi-crystalline PEMO_aLiTFSA increased by 2–3 orders of magnitude upon melting at 77°C because the ionic conduction was severely restricted in the immobile crystalline phase of PEMO_aLiTFSA. Above T_m (77°C), the ionic conductivity and Λ_{est} reached a maximum at $1/a = 0.2$ ($a = 5$), and then slightly decreased with further increases of the salt concentration. The convex-type behavior of the ionic conductivity is likely typical for liquids and PEs. The increase in the ionic conductivity at lower salt concentrations was due to the increase in the carrier density. The more pronounced dissociation with increasing the salt concentration was first proposed by Cavell and Knight for tributylammonium picrate in 1,2-dichloroethane.²⁶ In previous studies on ether- and PEO oligomer-based liquid electrolytes of LiTFSA, the degree of dissociation was also found to increase with increasing salt concentrations.^{27,28} Likewise, the increase in charge carrier was probably attributed to the increase in the degree of dissociation in PEMO because Λ_{est} also increased with an increase in the salt concentration at lower concentrations (Figure 1.9). The slight decrease in the ionic conductivity at higher salt concentrations was attributed to the decreased mobility of the ions that were associated with the increase in T_g , as shown in Figure 1.2.

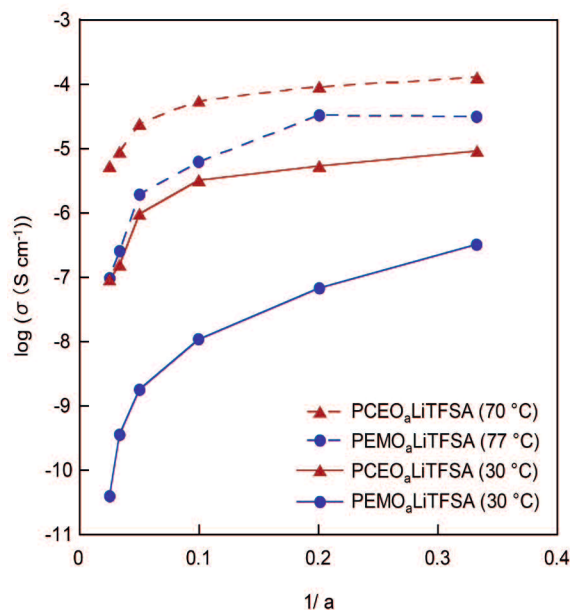


Figure 1.8 Ionic conductivity of the PEs as a function of LiTFSA content ($1/a = [\text{Li salt}]/[\text{monomer unit}]$) at 30°C and above T_m (PEMO_aLiTFSA: 77°C, PCEO_aLiTFSA: 70°C).

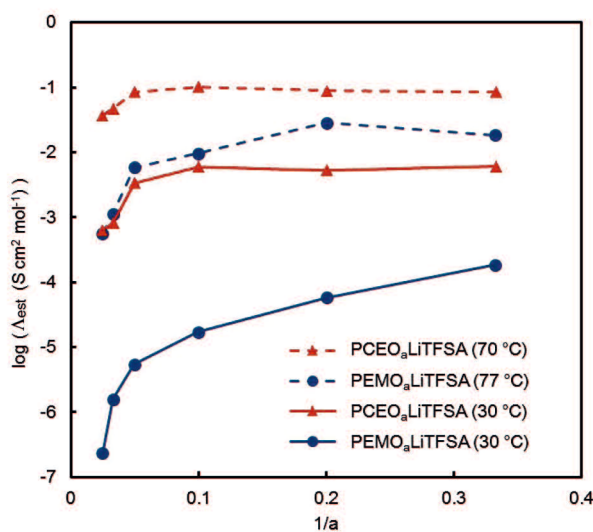


Figure 1.9 Estimated molar conductivity (Λ_{est}) of the PEs as a function of LiTFSA content ($1/a = [\text{Li salt}]/[\text{monomer unit}]$) at 30°C and above T_m (PEMO_aLiTFSA: 77°C, PCEO_aLiTFSA: 70°C). Λ_{est} values were calculated by dividing conductivity at given temperatures by c_{Li} at room temperature.

The ionic conductivity of PCEO_aLiTFSA continued to increase upon addition of LiTFSA up to $1/a = 0.333$ ($a = 3$), irrespective of temperature. The increase in the ionic conductivity at concentrations lower than $1/a = 0.05$ was due probably to the increase in the carrier density (associated by increase in Λ_{est} and thus dissociation degree) in a similar way to PEMO_aTFSA as mentioned above (Figure 1.9). Because the T_g of PCEO_aLiTFSA decreased with increasing the salt concentration (Figure 1.2), the increase in ionic mobility can be a cause for further enhancement of the conductivity at higher salt concentrations. However, almost independent Λ_{est} values on the salt concentration (Figure 1.9) suggest that the increase in the density of the ionic carrier was likely the dominant factor for the increased ionic conductivity. Similar conductivity increases with increasing salt concentrations were recently reported for poly(PAN-*co*-BuA)-LiTFSA¹⁴ and poly(ethylenecarbonate)-lithium bis(fluorosulfonyl amide) (LiFSA)⁴¹ PEs, in which the T_g of the PEs also decreased with increasing salt concentrations.

The conductivity of PCEO_aLiTFSA was lower than that of the previously reported oligomeric PCEO_aLiTFSA (0.73 mS cm^{-1} at 70°C), probably due to larger molecular weight.¹ Among the PEs studied, however, the highest conductivity values for PCEO_aLiTFSA were on the order of $10^{-4} \text{ S cm}^{-1}$ above T_m (70°C), which is comparable to those of the reported PEs, such as poly(PAN-*co*-BuA)-LiTFSA and poly(ethylenecarbonate)-LiFSA, although it was reduced by one order of magnitude at 30°C . Note that PCEO_aLiTFSA had a higher conductivity than PEMO_aLiTFSA despite the higher T_g value of PCEO_aLiTFSA at a lower salt concentration, suggesting that the nitrile functionality in PCEO played an important role in enhancing the ionic conductivity.

To elucidate the ionic transport in the PEs, the self-diffusivity of Li⁺ cations and TFSA anions were measured by PFG-NMR. The ionic transport properties of PEMO₅LiTFSA and PCEO₅LiTFSA were measured at 80°C (Table 1.3). Interestingly, D_{Li} and D_{F} were higher but the ionic conductivity was lower for PEMO₅LiTFSA. Self-diffusion coefficients were simply determined as an average (or equilibrated) value for a time scale of NMR measurements without distinguishing either ionic species or neutral ion-pairs/clusters. The molar conductivity ratio ($\Lambda/\Lambda_{\text{NE}}$) has been employed for liquid electrolytes to estimate how much the diffusion of ionic species effectively contributes to the ionic conduction or apparent

degree of dissociation.^{30,31} Here, Λ is the molar conductivity, and Λ_{NE} can be calculated from the ionic self-diffusion coefficients of cations (D_+) and anions (D_-) using the Nernst–Einstein equation:

$$\Lambda_{\text{NE}} = \frac{F^2}{RT} (D_+ + D_-)$$

where F is the Faraday constant, R is the gas constant, and T is the absolute temperature. For the PEs, D_+ and D_- denote D_{Li} and D_{F} , respectively. In this work, the estimated molar conductivity (Λ_{est}) was used instead of Λ . $\Lambda_{\text{est}}/\Lambda_{\text{NE}}$ for the PEs were lower than reported $\Lambda/\Lambda_{\text{NE}}$ (~ 1) of a PEO oligomer electrolyte with LiTFSA.³² This may be due to less polar trimethylene oxide main chains in PEMO and PCEO compared with ethylene oxide chains in PEO although $\Lambda/\Lambda_{\text{NE}}$ for the present PEs should be underestimated as $\Lambda_{\text{est}}/\Lambda_{\text{NE}}$. $\Lambda_{\text{est}}/\Lambda_{\text{NE}}$ for PCEO₅LiTFSA was higher than PEMO₅TFSA (Table 1.3). This indicates that the diffusion of the Li and TFSA species contributed more effectively to the ionic conduction in PCEO₅LiTFSA.

Table 1.3 The ionic transport properties of polyoxetane-based PEs at 80°C.

	σ [10 ⁻⁵ S cm ⁻¹]	D_{Li} [10 ⁻¹¹ m ² s ⁻¹]	D_{F} [10 ⁻¹¹ m ² s ⁻¹]	$\Lambda_{\text{est}}/\Lambda_{\text{NE}}$ [-]	t_{Li} [-]
PEMO ₅ LiTFSA	4.33	2.88	4.28	0.02	0.40
PCEO ₅ LiTFSA	13.9	1.24	1.50	0.16	0.45

Given the low molecular solvent models, ether solvents generally have high DN values (~ 15 – 25 kcal mol⁻¹) but relatively low dielectric constants ($\epsilon = 7$ – 8) that can cause ionic association between solvated Li⁺ ions and TFSA anions.³³ With such ether solvents, a cation-anion correlative diffusion notably occurs in dilute LiTFSA solutions, as predicted by MD simulations.³⁴ Previous studies of LiTFSA-based liquid electrolytes in ether solvents²⁷ and ammonium salts in 1,2-dichloroethane³⁵ suggested that the degree of dissociation decreased with decreasing salt concentrations. This is the opposite of the behavior of traditional electrolyte solutions in polar solvents, but is likely typical for electrolyte solutions in low polar solvents. A similar scenario would also hold for PEMO₅LiTFSA. In contrast, MeCN, as a model of the nitrile groups, has a high dielectric constant ($\epsilon = 37.5$) and moderate DN

value. Therefore, ionic dissociation can be more pronounced in PCEO because of the nitrile groups.

The t_{Li} value can be approximated by the equation $t_{\text{Li}} = D_{\text{Li}}/(D_{\text{Li}} + D_{\text{TFSA}})$ using the self-diffusion coefficients of Li^+ (D_{Li}) and TFSA (D_{TFSA}), although this value may also be affected by contributions from transient neutral species. In comparison to the reported t_{Li} (~ 0.2) for PEO-based electrolyte having similar M_n , both PEs showed higher t_{Li} .³⁶ This is possibly interpreted as lower $\Lambda/\Lambda_{\text{NE}}$ than that of PEO-LiTFSA: a correlative motion of Li and TFSA in PEO and PCEO can result in higher t_{Li} .³² However, PCEO₅LiTFSA had higher t_{Li} and $\Lambda_{\text{est}}/\Lambda_{\text{NE}}$ values than PEO₅LiTFSA. In PEO₅LiTFSA, Li^+ mobility was more prone to coupling with the segmental motion of the oxetane main chains by Li^+ coordination. As suggested by the coordination structure studied in terms of n_{CN} and n_{O} , entrapment of Li^+ ions by the oxetane main chains can be mitigated by the nitrile groups, and partial Li^+ coordination by the more freely moving nitrile side chains can afford higher Li^+ mobility, leading to a higher t_{Li} value for PCEO₅LiTFSA.

The nitrile groups not only serve as a partial coordination site for Li^+ ions in first coordination shell, but also increase the polarity in the PEs. These two characteristics of the nitrile groups in PCEO would be closely correlated with the enhanced ionic transport properties.

1.3.4. Electrochemical stabilities

The electrochemical oxidation and reduction stabilities are important properties for battery applications. Figure 1.10a shows the LSV curves on a stainless steel electrode for PCEO₅LiTFSA at 70°C. Typical PEO-based PEs are not stable at this potential because the ether moieties are oxidized around 4.0 V vs. Li/Li^+ . Similarly, the apparent oxidative current begins to flow at 4.3 V vs. Li/Li^+ in PCEO₅LiTFSA, which is attributed to the oxidative decomposition of the ether moiety in PCEO. The nitrile functionality did not appear to affect the oxidative stability.

CV was also used to study the cathodic stability on a nickel metal working electrode. Figure 1.10b shows CVs of PCEO₅LiTFSA measured at a scan rate of 1 mV s^{-1} at 70°C. I confirmed the reversible Li deposition/stripping in the polymer solutions: the cathodic

current observed at potentials below 0 V vs. Li/Li^+ is due to lithium deposition, and the anodic current in the reverse scan corresponds to the lithium stripping reaction. At the 1st cycle, additional cathodic peaks were observed at 0.4, 0.7, and 1.2 V vs. Li/Li^+ , suggesting cathodic decomposition of $\text{PCEO}_5\text{LiTFSA}$. α -Hydrogen abstraction of the nitrile functionality in proximity to the electrode surface is perhaps one of the factors responsible for cathodic decomposition. However, the cathodic current became less prominent within several scans (Figure 1.10b). Similar voltammograms were also obtained for oligomeric PCEO-based PEs with different Li salts.¹ Consequently, $\text{PCEO}_5\text{LiTFSA}$ exhibited a relatively wide electrochemical window of ~ 4.3 V after several scans.

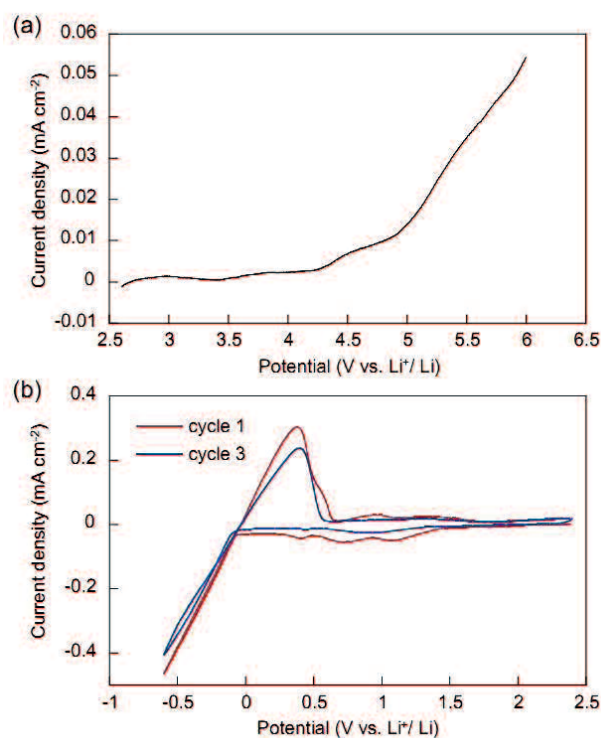


Figure 1.10 Electrochemical stability of $\text{PCEO}_5\text{LiTFSA}$. (a) LSV curves of a $\text{Li}/\text{PCEO}_5\text{LiTFSA}/\text{SUS}$ cell and (b) CV cycles of a $\text{Li}/\text{PCEO}_5\text{LiTFSA}/\text{Ni}$ cell at 70°C .

1.4. Conclusions

I studied the role of polar side chains in Li^+ coordination and transport properties of polyoxetane-based PEs by comparing PCEO containing a nitrile group with PEMO containing an ether group. Raman spectroscopy revealed that mixed coordination occurred in the polyoxetane-based PEs, particularly in $\text{PCEO}_a\text{LiTFSA}$. PCEO with the nitrile groups provided several nontrivial features for enhancing the Li^+ transport properties via partial Li^+ coordination with the nitrile groups: (i) unusual decrease in T_g with an increase in lithium salt concentration, (ii) higher ionic conductivity (on the order of $10^{-4} \text{ S cm}^{-1}$ at 80°C) and transport number of Li, and (iii) higher degree of dissociation of Li salts because of the high dielectric constant of the nitrile moiety. I also confirmed that the nitrile groups did not have more adverse effects on the electrochemical stabilities of the polyoxetane-based PEs than the PEO-based PEs. The electrochemical stability (electrochemical window from 0 to 4.3 V vs. Li/Li^+) of the polyoxetane-based PEs allows for applications in 4 V-class lithium ion batteries; the battery performance is now under investigation and will be published elsewhere. Most PEs reported here did not form solid membranes; therefore, preparation of freestanding PE films is the next challenge toward battery applications. This project is also currently underway.

References

1. Shintani, Y.; Tsutsumi, H. *J. Power Sources* **2010**, *195*, 2863–2869.
2. Ye, L.; Feng, Z.-g.; Su, Y.-f.; Wu, F.; Chen, S.; Wang, G.-q. *Polym. Int.* **2005**, *54*, 1440–1448.
3. Mu, Y.; Jia, M.; Jiang, W.; Wan, X. *Macromol. Chem. Phys.* **2013**, *214*, 2752–2760.
4. Kubota, K.; Tamaki, K.; Nohira, T.; Goto, T.; Hagiwara, R. *Electrochim. Acta* **2010**, *55*, 1113–1119.
5. Price, W. S. *NMR Studies of Translational Motion: Principles and Applications*; Cambridge University Press: Cambridge, 2009.
6. Nakano, Y.; Tsutsumi, H. *Solid State Ionics* **2014**, *262*, 774–777.
7. Pérez, E.; Gómez, M. A.; Bello, A.; Fatou, J. G. *Colloid Polym. Sci.*, **1983**, *261*, 571–576.
8. Pielichowski, K.; Flejtuch, K. *Polym. Adv. Technol.* **2002**, *13*, 690–696.
9. Perrier, M.; Besner, S.; Paquette, C.; Vallée, A.; Lascaud, S.; Prud'homme, J. *Electrochim. Acta* **1995**, *40*, 2123–2129.
10. Kerr, J. B.; Han, Y. B.; Liu, G.; Reeder, C.; Xie, J.; Sun, X. *Electrochim. Acta* **2004**, *50*, 235–242.
11. Kerr, J. B.; Sloop, S. E.; Liu, G.; Han, Y. B.; Hou, J.; Wang, S. *J. Power Sources* **2002**, *110*, 389–400.
12. Shintani, Y.; Tsutsumi, H. *J. Power Sources* **2010**, *195*, 2863–2869.
13. Forsyth, M.; Sun, J. Z.; MacFarlane, D. R. *Solid State Ionics* **1998**, *112*, 161–163.
14. Florjańczyk, Z.; Zygadło-Monikowska, E.; Wieczorek, W.; Ryszawy, A.; Tomaszewska, A.; Fredman, K.; Golodnitsky, D.; Peled, E.; Scrosati, B. *J. Phys. Chem. B* **2004**, *108*, 14907–14914.
15. Xuan, X.; Zhang, H.; Wang, J.; Wang, H. *J. Phys. Chem. A* **2004**, *108*, 7513–7521.
16. Reimers, J. R.; Hall, L. E. *J. Am. Chem. Soc.* **1999**, *121*, 3730–3744.
17. Kameda, Y.; Umabayashi, Y.; Takeuchi, M.; Wahab, M. A.; Fukuda, S.; Ishiguro, S.; Sasaki, M.; Amo, Y.; Usuki, T. *J. Phys. Chem. B* **2007**, *111*, 6104–6109.
18. Henderson, W. A.; Brooks, N. R.; Young, V. G. *J. Am. Chem. Soc.* **2003**, *125*, 12098–12099.
19. Brouillette, D.; Irish, D. E.; Taylor, N. J.; Perron, G.; Odziemkowski, M.; Desnoyers, J. E. *Phys. Chem. Chem. Phys.* **2002**, *4*, 6063–6071.
20. Umabayashi, Y.; Mitsugi, T.; Fukuda, S.; Fujimori, T.; Fujii, K.; Kanzaki, R.; Takeuchi, M.; Ishiguro, S. *J. Phys. Chem. B* **2007**, *111*, 13028–13032.
21. Papke, B. L.; Ratner, M. A.; Shriver, D. F. *J. Electrochem. Soc.* **1982**, *129*, 1434–1438.
22. Matsuura, H.; Fukuhara, K. *J. Polym. Sci. B: Polym. Phys.* **1986**, *24*, 1383–1400.
23. Gutmann, V. *Coord. Chem. Rev.* **1976**, *18*, 225–255.
24. Schmeisser, M.; Illner, P.; Puchta, R.; Zahl, A.; van Eldik, R. *Chem. Eur. J.* **2012**, *18*, 10969–10982.
25. Fuoss, R. M.; Kraus, C. A. *J. Am. Chem. Soc.* **1933**, *55*, 2387–2399.
26. Cavell, E. A. S.; Knight, P. C. *Z. Phys. Chem. Neue Folge*, **1968**, *57*, 331.
27. Zhang, C.; Ueno, K.; Yamazaki, A.; Yoshida, K.; Moon, H.; Mandai, T.; Umabayashi, Y.; Dokko, K.; Watanabe, M. *J. Phys. Chem. B* **2014**, *118*, 5144–5153.

28. Williamson, M. J.; Southall, J. P.; Hubbard, H. V. St. A.; Johnston, S. F.; Davies, G. R.; Ward, I. M. *Electrochim. Acta* **1998**, *43*, 1415–1420.
29. Kimura, K.; Motomatsu, J.; Tominaga, Y. *J. Phys. Chem. C* **2016**, *120*, 12385–12391.
30. Hayamizu, K.; Sugimoto, K.; Akiba, E.; Aihara, Y.; Bando, T.; Price, W. S. *J. Phys. Chem. B* **2002**, *106*, 547–554.
31. Tokuda, H.; Tsuzuki, S.; Susan, M. A. B. H.; Hayamizu, K.; Watanabe, M. *J. Phys. Chem. B* **2006**, *110*, 19593–19600.
32. Chintapalli, M.; Timachova, K.; Olson, K. R.; Mecham, S. J.; Devaux, D.; DeSimone, J. M.; Balsara, N. P. *Macromolecules* **2016**, *49*, 3508–3515.
33. Choquette, Y.; Brisard, G.; Parent, M.; Brouillette, D.; Perron, G.; Desnoyers, J. E.; Armand, M.; Gravel, D.; Slougui, N. *J. Electrochem. Soc.* **1998**, *145*, 3500–3507.
34. Borodin, O.; Smith, G. D. *J. Solution Chem* **2007**, *36*, 803–813.
35. Tokuda, H.; Baek, S.-J.; Watanabe, M. *Electrochemistry* **2005**, *73*, 620–622.
36. Timachova, K.; Watanabe, H.; Balsara, N. P. *Macromolecules* **2015**, *48*, 7882–7888.



**YAMAGUCHI
UNIVERSITY**

Chapter 2

Steric effect on Li⁺ coordination and transport properties in polyoxetane-based polymer electrolytes bearing nitrile groups

2.1. Introduction

Typically, the increase in glass transition temperature (T_g) associated with complexation with Li⁺ ions for PEs, does not occur in poly(3-(2-cyanoethoxymethyl)-3-ethyloxetane) (PCEO); rather, T_g decreases with increasing salt concentration.¹ This could be caused by steric hindrance of the ethyl groups on the main chain and preferential Li⁺ ion coordination with the nitrile side chains. I confirmed that Li⁺ ion coordination with the nitrile groups in PCEO is responsible for improving the ionic transport properties of the PEs.²

In this study, poly(3-(2-cyanoethoxymethyl)-oxetane) (PCHO) was newly synthesized. The only difference between PCEO and PCHO is the absence of an ethyl group on the polyoxetane main chain. To clarify the contribution of the ethyl group to the electrolyte properties such as the ionic conductivity (σ) and lithium transference number (t_{Li^+}), PCHO complexed with lithium bis(trifluoromethanesulfonyl)amide (LiTFSA) were evaluated and were compared with previously reported PCEO electrolytes.² Here, I verified that subtle changes in the chemical structure of the repeating monomer unit of the polyoxetane-based PEs (*i.e.*, the presence or absence of the ethyl group on the main chain) greatly affected the thermal properties and ionic transport, which were well correlated with different Li⁺ ion coordination structures studied by Raman spectroscopy. A Li/LiFePO₄ cell was fabricated and its charge/discharge behavior was examined to demonstrate the applicability of the polyoxetane-based PEs to lithium secondary batteries.

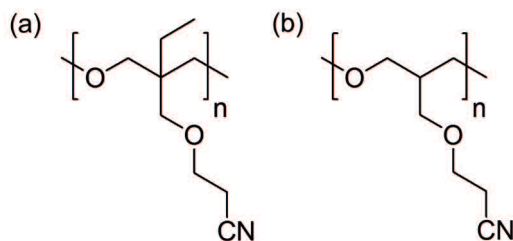


Figure 2.1 Structures of the matrix polymers: (a) PCEO and (b) PCHO.

2.2. Experimental section

2.2.1. Preparation of the monomer

An oxetane derivative, 3-(2-cyanoethoxymethyl)-oxetane (CHO), was synthesized by Michael addition. 3-Oxetanemethanol (5.64 mL, 70.0 mmol) and acrylonitrile (5.24 mL, 80.0 mmol) were mixed with a 20% tetraethylammonium hydroxide solution (0.6 mL) as a catalyst in pure water (3 mL), then stirred at room temperature overnight. The reaction mixture was extracted with chloroform, and the organic phase was washed with a large amount of water. After removal of chloroform by a rotary evaporator, the obtained liquid was applied to a silica column (eluent = ethyl acetate:hexane, 7:3). The product was obtained by removing the eluent and vacuum drying at 60°C (yield: 3.54 g, 35.9%). The synthesized CHO was characterized using time-of-flight mass spectrometry, and ¹H and ¹³C nuclear magnetic resonance (NMR) spectroscopy. The density of the monomer was 1.068 g cm⁻³.

CHO ¹H NMR (δ, ppm from tetramethylsilane (TMS) in CDCl₃): 2.62 (t, 2H, *J* = 6.0 Hz, -CH₂-CN), 3.24 (sept., 1H, *J* = 5.8 Hz, -(CH₂)₃-CH), 3.70 (t, 2H, *J* = 6.0 Hz, -CH₂-CH₂-CN), 3.75 (d, 2H, *J* = 7.0 Hz, -CH-CH₂-O-), 4.46 (t, 2H, *J* = 6.3 Hz, ring, -CH₂-O-CH₂-), 4.81 (dd, 2H, *J* = 1.0 Hz, 6.0 Hz, ring, -CH₂-O-CH₂-).

CHO ¹³C NMR (δ, ppm from CDCl₃ (77.00 ppm)): 18.52 (-CH₂-CN), 34.45 ((CH₂)₂-CH₂-CH₃), 65.39 (-CH₂-CH₂-CN), 72.34 (-CH-CH₂-O-), 74.03 (-CH₂-O-CH₂-), 117.61 (-CN).

2.2.2. Preparation of the polymer

CHO was polymerized by a ring-opening cationic polymerization using BF₃-Et₂O as a cationic initiator. CHO (2.42 mL, 18.3 mmol) and the initiator (50.2 μL, 0.400 mmol) were dissolved in dichloroethane (total volume: 5 mL). The polymerization was performed under an Ar atmosphere at 0°C for 6 h in a salt ice bath. The reaction was quenched with the addition of aqueous 4 M NaCl/1 M NaOH (5 mL). The reaction mixture was added to chloroform, and the solution was washed with water. After removing chloroform using a rotary evaporator, the mixture was poured into a large amount of 2-propanol to precipitate the polymerized CHO (PCHO). The resulting polymer was collected by filtration and dried at 100°C under vacuum (yield: 2.17 g, 84.1%). The chemical structures of PCEO (reported in our previous study) and PCHO are shown in Figure 2.1.

PCHO ^1H NMR (δ , ppm from TMS in CDCl_3): 2.15 (quin., 1H, $J = 5.9$ Hz, $(\text{CH}_2)_3\text{-CH}$), 2.61 (t, 2H, $J = 6.3$ Hz, $-\text{CH}_2\text{-CN}$), 3.43 (m, 4H, $-\text{O-CH}_2\text{-CH-}$), 3.53 (d, 2H, $J = 6.0$ Hz, $-\text{CH-CH}_2\text{-O-}$), 3.64 (t, 2H, $J = 6.0$ Hz, $-\text{CH}_2\text{-CH}_2\text{-CN}$).

PCHO ^{13}C NMR (δ , ppm from CDCl_3 (77.00 ppm)): 18.85 ($-\text{CH}_2\text{-CN}$), 40.20 ($(\text{CH}_2)_3\text{-CH}$), 65.63 ($-\text{CH}_2\text{-CH}_2\text{-CN}$), 69.29 ($-\text{CH-CH}_2\text{-O-}$), 69.38 ($-\text{CH}_2\text{-O-CH-}$), 118.13 ($-\text{CN}$).

2.2.3. Preparation of polymer electrolytes

The PEs were prepared using a solvent casting method. PCHO and 1 M LiTfSA in a tetrahydrofuran (THF) solution were mixed and then heated under vacuum to completely remove THF. In this report, the molar ratio of the repeating monomer unit to LiTfSA is represented as “ a ” ($a = 40, 30, 20, 10, 5,$ and 3) for $\text{PCHO}_a\text{LiTfSA}$. The concentrations of LiTfSA (c_{Li}) in $\text{PCHO}_a\text{LiTfSA}$ were estimated using the corresponding monomer density (1.068 g cm^{-3}) and the reported density of molten LiTfSA (1.970 g cm^{-3}).³ The high temperature data for the density of molten LiTfSA were extrapolated to room temperature. I assumed the additivity of the volumes of the monomers and LiTfSA when calculating the density of the PEs.

2.2.4. Measurements

^1H and ^{13}C NMR spectra of the synthesized substances were recorded using a Fourier transform NMR spectrophotometer (JNM-LA500, JEOL). The molecular weight of the polymer was measured using a gel permeation chromatography (GPC) system (SCL-10AVP, LC-10ADVP, DGU-12A, CTO-10AVP, and RID-10A, Shimadzu). GPC was performed using THF as the elution solvent and polystyrene standards to calibrate the columns.

A differential scanning calorimeter (DSC7020, HITACHI) was used to determine the glass transition temperature (T_g). A small amount of the PEs (~ 10 mg) was hermetically sealed in an aluminum differential scanning calorimetry (DSC) pan. The samples were heated to 120°C , cooled to -120°C , and heated again to 120°C at a heating/cooling rate of $10^\circ\text{C min}^{-1}$. The second heating scan was recorded as the DSC thermogram of the samples. T_g was determined as the onset of the heat flow step.

The ionic conductivity of the PEs was measured by ac impedance spectroscopy using a potentio/galvanostat (SP-150, BioLogic). The PE was placed between two stainless steel electrodes and separated by a polytetrafluoroethylene ring spacer; the conductivity cell

(swagelok cell) was thermally equilibrated in a temperature cabinet (LU-14, ESPEC) at each temperature (temperature range: 20–90°C) for 1 h before the measurements. The conductivity values were calculated using the thickness and inner diameter of the ring spacer filled with the PEs.

Raman spectra of the PEs were measured using a laser Raman spectrophotometer (NRS-3100, JASCO) with a 532-nm laser. The PE was sealed between two glass plates with a rubber spacer (thickness: 5 mm) in an Ar-filled glove box to avoid moisture adsorption. Raman spectra of PCHO_aLiTFSA were measured from 500–2400 cm⁻¹ with a resolution of 4 cm⁻¹. The obtained spectra were normalized with respect to the methylene vibration of polyoxetanes (1390–1520 cm⁻¹) and were analyzed using commercial software for peak fitting (PeakFit™ version 4.12, SYSTAT). A pseudo-Voigt function was used for peak deconvolution.

IR spectra of the PEs were measured using a Fourier Transform Infrared (FT-IR) spectrometer (Nicolet iS50, Thermo Fisher Scientific) with an attenuated total reflection (ATR) accessory (Smart iTX, Thermo Fisher Scientific) equipped with a Ge prism at an incident angle of 45°. Samples were dropped on the ATR prism and hermetically sealed by a glass plate with a rubber spacer (thickness, 5 mm) in an Ar-filled glovebox to avoid moisture adsorption. The measurements were performed at a 4 cm⁻¹ resolution in the 4000–400 cm⁻¹ spectral range; 32 scans were averaged.

The transference numbers of Li ions (t_{Li^+}) in PCHO₅LiTFSA and PCEO₅LiTFSA (the sample reported in the previous report,² $M_n = 4.56 \times 10^4$ g mol⁻¹) were determined using the electrochemical method proposed by Bruce and Vincent.⁴ The required parameters were obtained using potentiostatic polarization and ac impedance spectroscopy with a potentio/galvanostat (SP-150, BioLogic). The PE was placed between two lithium foil electrodes that were separated by a polypropylene spacer, and the cell was stored in a temperature cabinet (LU-114, ESPEC) at 50°C for several days to stabilize the symmetric cell. Then, impedance spectra were measured prior to the potentiostatic polarization. The current was monitored while a potentiostatic polarization was applied to the cell with a potential step of 10 mV. After a steady current was observed, impedance spectra were measured again. The following equation gives the transference number,

$$t_{\text{Li}^+} = [I_{\text{ss}}(\Delta V - I_0 R_0)]/[I_0(\Delta V - I_{\text{ss}} R_{\text{ss}})] \quad (1)$$

where ΔV is the applied potential ($\Delta V = 10$ mV), I_0 is the initial current of the potentiostatic polarization, I_{ss} is the steady state current of the polarization, R_0 is the interfacial resistance before the polarization, and R_{ss} is the steady state interfacial resistance during the polarization.

2.2.5. Charge/discharge test of the Li/PCEO₅LiTFSA/LiFePO₄ cell

The Li|PCEO₅LiTFSA|LiFePO₄ cell was prepared using the previously reported PE based on PCEO.² Lithium metal foil (diameter: 10 mm, Honjo Metal Co., Ltd.) was used as the negative electrode. The positive electrode was composed of LiFePO₄ as the active material (theoretical capacity: 170 mAh g⁻¹), acetylene black (AB) as the conductive supporting agent, polyvinylidene fluoride (PVdF), and PCEO₅LiTFSA as the binder at a weight ratio of LiFePO₄: AB: PVdF: PCEO₅LiTFSA = 75: 15: 10: 1. The materials were suspended in *N*-methylpyrrolidone, and the slurry was coated onto a stainless steel (SUS) foil. After drying at 60°C for 4 h, the electrode was cut into a circular shape (10 mm in diameter) and compressed at 2 kN for 15 min. LiFePO₄ was loaded on the electrode (2 mg cm⁻²). A porous glass filter paper (GA-55, ADVANTEC) was used as a mechanical electrolyte support because the PE used in this study was not self-standing (it was not crystalline and had a low T_g). PCEO₅LiTFSA was heated to 130°C and infiltrated into the glass filter paper under vacuum. A 2032-type coin cell was assembled using the above electrodes and the PE in the Ar-filled glove box.

A charge/discharge test was performed with a charge-discharge unit (HJ1020mSD8, Hokuto Denko). The temperature of the cell was maintained at 70°C in an aluminum bath during the charge/discharge test. The rate capability of the cell was investigated by changing the charge-discharge rate (0.05, 0.1, 0.2, 0.5, 1, and 2 C). The charging cutoff voltage was set to 3.9 V to avoid electrolyte oxidation, while the discharging cutoff voltage was 2.5 V.

2.3. Results and discussion

2.3.1. Thermal properties

Table 2.1 summarizes the molecular weights (M_n and M_w), polydispersity index (M_w/M_n), and T_g of pure PCHO, as determined from the GPC and DSC measurements. The reported data for PCEO are also listed for comparison. PCEO is a semi-crystalline polymer with a small melting peak at 55°C and T_g at -18.3°C.² Although one may expect that the ethyl group on the main chains of PCEO would sterically hinder chain packing to form a crystalline phase, it rather assisted the formation of a small crystalline domain in PCEO. In contrast, the DSC thermogram of PCHO did not contain an endothermic peak corresponding to the melting of the crystalline domain, suggesting that PCHO is amorphous. The T_g of PCHO is lower than that of PCEO (-18.3°C), but higher than the reported T_g of plain poly(trimethyl oxide), $-(CH_2CH_2CH_2O)_n-$, (-71°C).⁵ The presence of side chains could increase T_g , and PCEO having the nitrile and ethyl side chains showed high T_g values because of not only enhanced intermolecular interactions with nitrile groups but also steric exclusion to main chain mobility by side chains. Considering the thermal behavior, PCHO is expected to be more favorable than PCEO for ion transport because of its non-crystallinity and lower T_g .

Table 2.1 Molecular weights (M_n and M_w), polydispersity index (M_w/M_n), and thermal characteristic (T_g and melting point, T_m) of PCHO. Data for PCEO were obtained from ref. 2.

	Molecular weight			Thermal characteristics	
	M_n	M_w	M_w/M_n	T_g	T_m
	[g mol ⁻¹]	[g mol ⁻¹]	[-]	[°C]	[°C]
PCEO	4.56×10 ⁴	1.08×10 ⁵	2.37	-18.3	55.0
PCHO	2.86×10 ⁴	7.94×10 ⁴	2.78	-30.9	Not observed

Figure 2.2 shows the salt concentration dependence of T_g for PCEO_aLiTFSA and PCHO_aLiTFSA: T_g of the PEs values were plotted as a function of the molar ratio of possible interaction sites and LiTFSA, $([O] + [CN])/[Li]$. For comparison, the reported T_g data of PEO_aLiTFSA,⁶ which is the most widely studied PE for lithium secondary batteries, are also shown in Figure 2.2. In PEO-based electrolytes, T_g increases as the salt concentration increases. This is due to ionic cross-linking formed by multi-dentate coordination of the main

chain ether groups to Li^+ ions, in which the polymer segmental motion is highly restricted. In contrast, I report that the T_g value of PCEO decreases as the salt concentration increases.^{1,2} This plasticizing effect is due to relaxation of dipole-dipole interactions between the nitrile groups of PCEO in the presence of the Li salt. This plasticization with the addition of Li salt is not limited to PCEO, but has also been reported for polyacrylonitrile,⁷ and polyethylene carbonate.⁸ In the context of free volume theory for amorphous materials,^{9,10} the reduction in T_g by the addition of Li salt implies that the free volume in the system increases upon Li^+ ion coordination. This is likely the case because sterically hindered Li^+ coordination with the main chains and preferential Li^+ coordination with polar side chains would result in a more loosely-packed segmental arrangement.

For newly synthesized PCHO, T_g increases with increasing salt concentration, although the increase in T_g is gentler than that of $\text{PEO}_a\text{LiTFSA}$. This suggests that PCHO forms an ionically cross-linked structure in the presence of LiTFSA , but the cross-linking density is not as dense as that in $\text{PEO}_a\text{LiTFSA}$. The differences in the thermal behavior between $\text{PCEO}_a\text{LiTFSA}$ and $\text{PCHO}_a\text{LiTFSA}$ suggest that the ethyl group on the polyoxetane main chains plays an important role in the Li^+ ion coordination structure and the resultant thermal behavior in the PEs. The prepared PEs ($\text{PCEO}_a\text{LiTFSA}$ and $\text{PCHO}_a\text{LiTFSA}$) were not a rubbery solid, but were a highly viscous solution due to the low crystallinity and the lower T_g . However, a self-standing membrane can be readily formed by introducing robust cross-linking points into the polymers as reported in the literature.¹¹⁻¹³

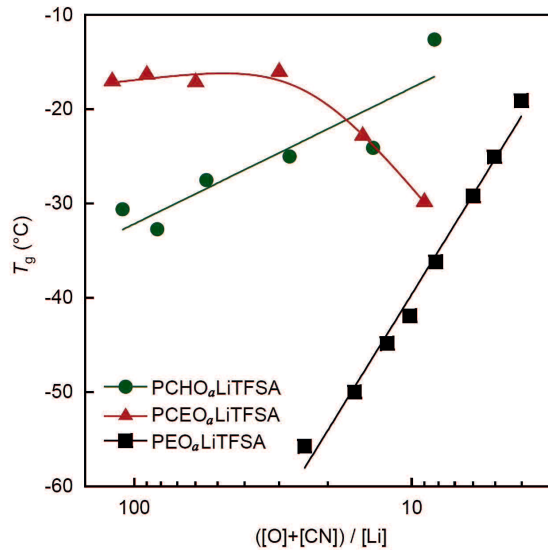


Figure 2.2 T_g as a function of the molar ratio of possible interaction sites and LiTFSA in the PEs $([O] + [CN])/[Li]$ for PCHO_aLiTFSA, PCEO_aLiTFSA, and PEO_aLiTFSA. T_g values for PCEO_aLiTFSA and PEO_aLiTFSA were obtained from refs. 2 and 6, respectively.

2.3.2. Ionic conductivity

In Figure 2.3, the ionic conductivities of PCHO_aLiTFSA at 30°C and 70°C are plotted as a function of the molar ratio of LiTFSA to the repeating monomer unit, $1/a$ (relevant to the salt concentration). For comparison, the conductivity data for PCEO_aLiTFSA are also shown in the same figure. Furthermore, the molar conductivity is also shown in the Figure 2.4. At low values of $1/a$ (i.e., low salt concentration), the ionic conductivity of PCHO_aLiTFSA is higher than that of PCEO_aLiTFSA. This is attributed to the high mobility of ions in PCHO_aLiTFSA. As shown in Figure 2.2, a lower T_g value is evidently responsible for the faster segmental motion and the lower local viscosity of PCHO_aLiTFSA. The ionic conductivity increases for both PEs with increasing $1/a$ (i.e., increasing salt concentration), except for PCHO_aLiTFSA at the highest $1/a$. However, PCHO_aLiTFSA shows only a small change in conductivity and a continuous decrease in molar conductivity with increasing $1/a$ (Figure 2.4). The contribution of the increase in the charge carrier would be negated by the increase in T_g with the addition of Li salt (as shown in Figure 2.2), which would account for the marginal change in the conductivity and the decrease in the molar conductivity at higher $1/a$. The Li salt concentration dependence of the PCHO_aLiTFSA conductivity qualitatively

agrees with that for the PEO-based PEs; the change in conductivity and molar conductivity fall within one order of magnitude, which is comparable to that for PEO-based PEs.^{14,15} Therefore, this typical change is predominantly due to a reduction in mobility by the formation of an ionically cross-linked structure. The ever-increasing conductivity for PCEO_aLiTFSA suggests again that the presence of the ethyl group can inhibit the formation of the cross-linked structures by Li⁺ ion coordination with the ether main chains.

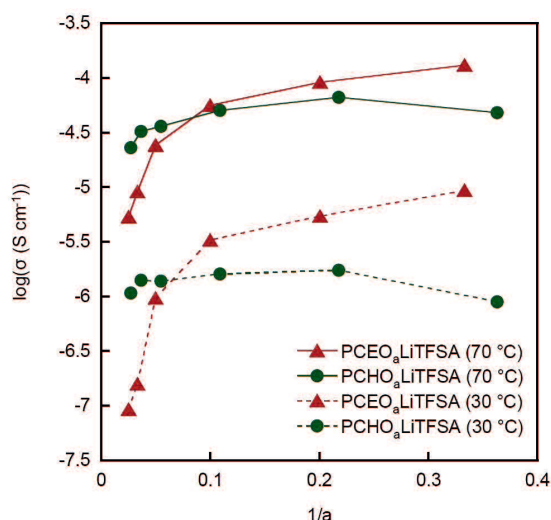


Figure 2.3 Ionic conductivity of the PEs as a function of LiTFSA content ($1/a$) at 30°C and 70°C.

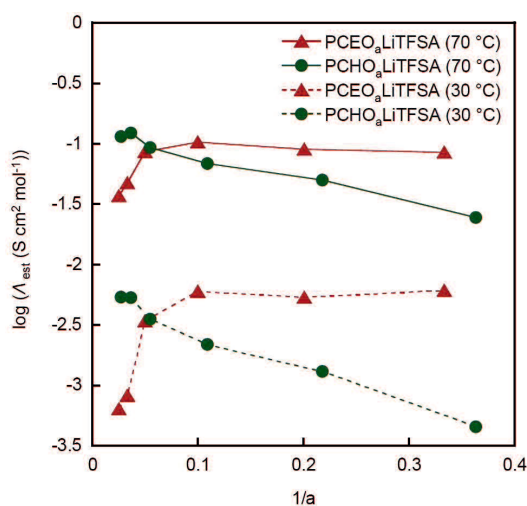


Figure 2.4 Estimated molar conductivity (Λ_{est}) of the PEs as a function of LiTFSA content ($1/a = [\text{Li salt}]/[\text{monomer unit}]$) at 30°C and 70°C. The Λ_{est} values were calculated by dividing the conductivity at each temperature by c_{Li} at room temperature.

The temperature dependent conductivity (σ) was also measured to elucidate the ionic conduction mechanism in $\text{PCEO}_a\text{LiTFSA}$ and $\text{PCHO}_a\text{LiTFSA}$, as shown in Figure 2.5. The Arrhenius plots of the conductivity show non-linear behavior with a curvature that is generally observed for amorphous PEs, and are well described by an empirical expression in relation to the Vogel-Tammann-Fulcher equation,⁵

$$\sigma = AT^{-1/2} \exp\left[\frac{-B}{R(T-T_0)}\right] \quad (2)$$

where A is a fitting parameter relevant to the number of charge carriers, B is the pseudo activation energy of ionic conduction, R is the gas constant, and T_0 is an ideal glass transition temperature. Because T_0 is typically 30–50 K below T_g for many cases, I defined $T_0 = T_g - 50$ K for fitting the conductivity data according to the previous report.¹⁶ Table 2.2 shows the obtained parameters for $\text{PCEO}_a\text{LiTFSA}$ and $\text{PCHO}_a\text{LiTFSA}$. $\text{PCEO}_a\text{LiTFSA}$ with low Li salt concentrations ($a = 20, 30,$ and 40) are crystalline; therefore, these compounds are not included in the fitting analysis.

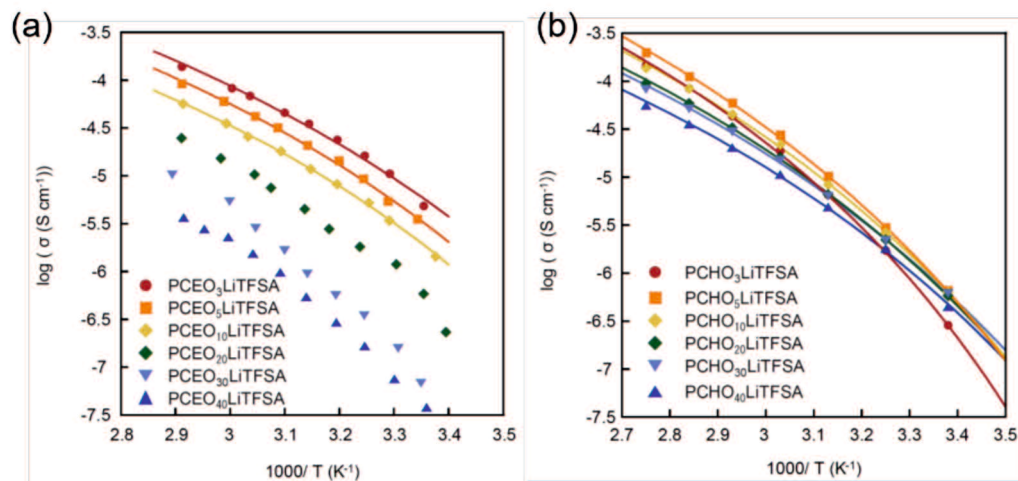


Figure 2.5 Temperature dependencies of the ionic conductivity for (a) $\text{PCHO}_a\text{LiTFSA}$ and (b) $\text{PCEO}_a\text{LiTFSA}$. The solid lines represent the Vogel-Tammann-Fulcher fit results.

Table 2.2 The fitting parameters for PCEO_aLiTFSA and PCHO_aLiTFSA.

Polymer	<i>a</i>	<i>A</i> [S cm ⁻¹ K ^{1/2}]	<i>B</i> [kJ mol ⁻¹]
PCEO	10	1.21	7.96
	5	3.19	8.84
	3	5.75	9.49
PCHO	40	2.21	10.7
	30	4.97	11.5
	20	4.88	10.9
	10	9.34	11.1
	5	11.9	11.6
	3	9.86	10.2

The *A* parameter tends to increase with increasing salt concentration in each PE, indicating that the number of effective charge carriers increases with the addition of the Li salt. The *A* value of PCHO_aLiTFSA was higher than that of PCEO_aLiTFSA at the same *a* value. The absence of ethyl groups in PCHO may result in a higher polarity in the PE, which can promote ionic dissociation of the Li salt, leading to the higher *A* value for PCHO_aLiTFSA. PCHO_aLiTFSA shows slightly larger values of *B* than PCEO_aLiTFSA, indicating that PCHO_aLiTFSA has a little higher activation barrier for ion exchange between the coordination sites in the PEs. This implies that Li⁺ ion coordination is more stabilized in PCHO than in PCEO, and Li⁺ ions are more tightly trapped by the multi-dentate polyether groups in PCHO_aLiTFSA.

In our previous work, we reported that the parameters *A* and *B* for PCEO_aLiBF₄ and PCEO_aLiBF₄ show smaller *A* and larger *B* values than those of PCEO_aLiTFSA at the same *a* value.¹⁷ It seems that the more associative character and smaller size of LiBF₄ are responsible for the smaller *A* value and larger *B* value. The *B* value of the PEO-based PEs dramatically changes with respect to the salt concentration and anion species,¹⁸ and *B* = 24 kJ mol⁻¹ was reported for PEO₁₂LiTFSA.¹⁹ Hence, the smaller *B* values of PCEO_aLiTFSA and PCHO_aLiTFSA than that of the PEO-based PEs suggest that ion migration is promoted more in PCEO and PCHO by preferential Li⁺ ion coordination with the nitrile side chains.

2.3.3. Coordination structure of Li⁺ ions

Raman spectroscopic measurements were carried out to investigate the coordination structure formed in PEs. The Raman spectra of the nitrile group (2200–2320 cm⁻¹) is shown in Figure 2.6. A symmetric peak that can be assigned to the stretching vibration of nitrile groups is observed at 2249 cm⁻¹ for pure PCHO. However, another peak emerges at higher wavenumber in the presence of LiTFSA. This is indicative of Li⁺ ion coordination with the nitrile groups in PCHO_aLiTFSA. The Raman spectra in this region show an isosbestic point at 2255 cm⁻¹ (except that for PCHO₃LiTFSA), indicating that two species (i.e., free and bound nitrile groups) co-exist. Here, each spectrum was further analyzed using the same procedure as that in our previous report,² and each was deconvoluted into four bands at 2249, 2253, 2264, and 2277 cm⁻¹, as shown Figure 2.6b. The peaks at 2249 and 2253 cm⁻¹ are assigned to vibrations of uncoordinated (free) nitrile groups, whereas the peaks at 2264 and 2277 cm⁻¹ are due to nitrile groups bound to Li⁺ ions. The intensity of a peak at x cm⁻¹ is given as $I_{x(\text{CN})}$. To quantitatively determine the coordination number of the nitrile group (n_{CN}), the relationship between the slope and intercept of the linear function plotted as $I_{\text{f}(\text{CN})}/c_{\text{Li}}$ vs. a was analyzed using the following relationship,

$$I_{\text{f}(\text{CN})}/c_{\text{Li}} = J_{\text{f}(\text{CN})}(a - n_{\text{CN}}) \quad (3)$$

where $I_{\text{f}(\text{CN})}$ is the sum of the integrated intensities of the lower two bands ($I_{\text{f}(\text{CN})} = I_{2249(\text{CN})} + I_{2253(\text{CN})}$), and $J_{\text{f}(\text{CN})}$ is the molar Raman scattering coefficient of the free nitrile moieties. For highly concentrated PCHO₃LiTFSA ($a = 3$), the Raman spectrum deviates from the isosbestic point and shifts to a lower wavenumber, suggesting that the Li⁺ ion coordination structure is different from that of the others. Therefore, the data for PCHO₃LiTFSA are excluded from the fitting analysis.

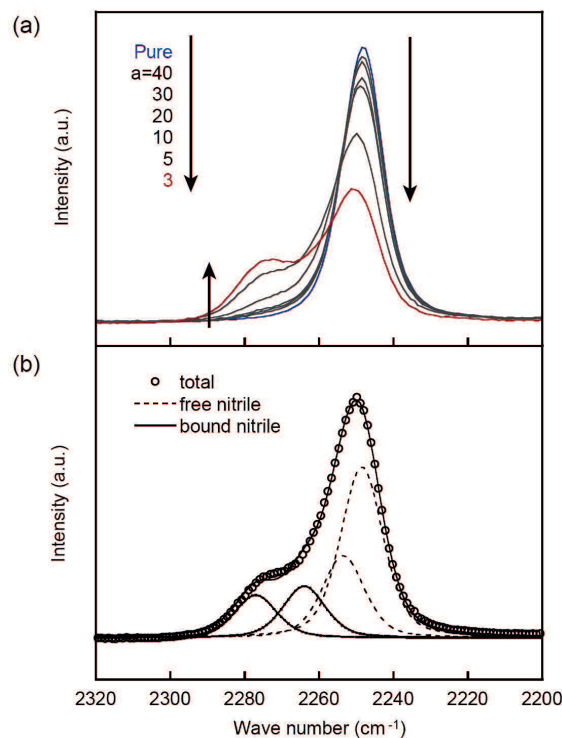


Figure 2.6 Raman spectra of the nitrile group in $\text{PCHO}_a\text{LiTFSA}$ in the frequency range of $2200\text{--}2320\text{ cm}^{-1}$ at room temperature. (a) Dependence on Li salt concentration (pure and $a = 3\text{--}40$) and (b) typical result upon deconvolution of the spectrum for $a = 5$.

Figure 2.7 shows the result of the linear least-square fitting to eq. (3) for the nitrile group in $\text{PCHO}_a\text{LiTFSA}$. From the good linear relationship in Figure 2.7, I could determine the coordination number of the nitrile group in $\text{PCHO}_a\text{LiTFSA}$ ($n_{\text{CN}} = 0.81 \pm 0.40$), which is smaller than the reported n_{CN} of $\text{PCEO}_a\text{LiTFSA}$ (0.93 ± 0.7).² Thus, Li^+ ion coordination with the nitrile groups is less pronounced in $\text{PCHO}_a\text{LiTFSA}$. The Li^+ ion was probably more preferentially coordinated with the ether groups by the absence of the steric hindrance of the ethyl groups on the main chains in $\text{PCHO}_a\text{LiTFSA}$.

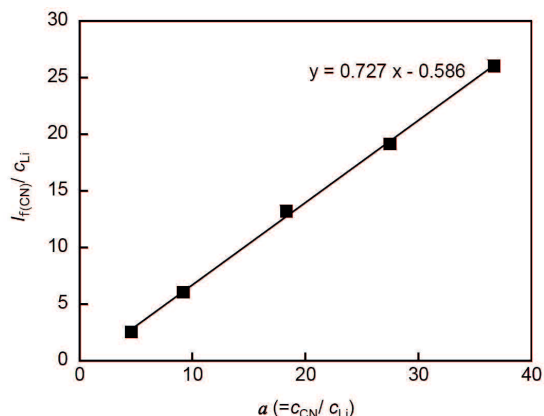


Figure 2.7 $I_{f(CN)}/c_{Li}$ plotted as a function of $a (= c_{CN}/c_{Li})$ for $PCHO_aLiTFSA$. The solid line represents the least-square linear fitting.

The Raman spectra corresponding to the CF_3 bending vibration coupled with the S-N stretching vibration of the TFSA anion are shown in Figure 2.8. To investigate the Li^+ ion coordination with the TFSA anions, these Raman spectra were further deconvoluted into two peaks at 739 and 745 cm^{-1} using the same method as that used in the previous work.² The peak at 739 cm^{-1} can be assigned to TFSA in the form of a free or solvent separated ion pair, whereas the peak at 745 cm^{-1} corresponds to TFSA directly bound to Li^+ ions in the form of a contact ion pair or aggregates. The respective peak intensities ($I_{739(TFSA)}$ and $I_{745(TFSA)}$) were used to determine the coordination number of TFSA anions (n_{TFSA}) according to the following equations,²⁰

$$0.9I_{739(TFSA)} + I_{745(TFSA)} = J_{745(TFSA)}c_{Li} \quad (4)$$

$$I_{745(TFSA)} = J_{745(TFSA)}n_{TFSA}c_{Li} \quad (5)$$

As shown in Figure 2.9, a relatively good linear relationship is obtained for both cases, and the coordination number for $PCHO_aLiTFSA$ is estimated as $n_{TFSA} = 0.16 \pm 0.01$ using the two linear fitting results. This value is nearly half the reported n_{TFSA} value for $PCEO_aLiTFSA$ (0.30 ± 0.04).²

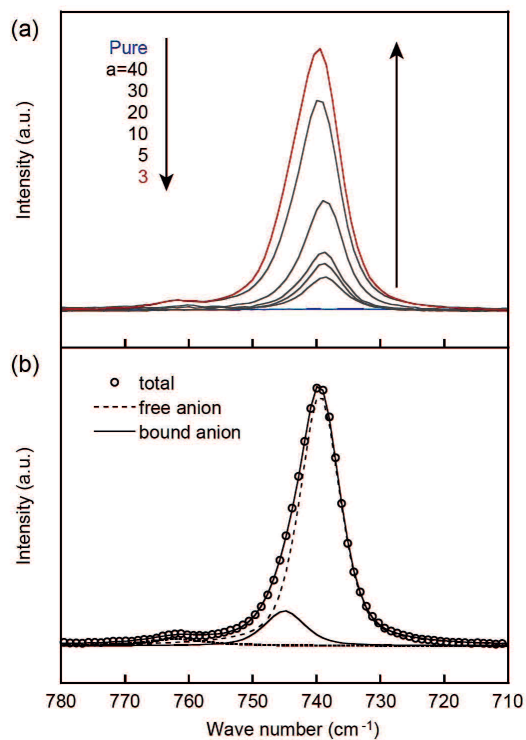


Figure 2.8 Raman spectra in $\text{PCHO}_a\text{LiTFSA}$ in the frequency range of 710–780 cm^{-1} at room temperature. (a) Dependence on Li salt concentration (pure and $a = 3$ –40) and (b) typical result upon deconvolution of the spectrum for $a = 5$.

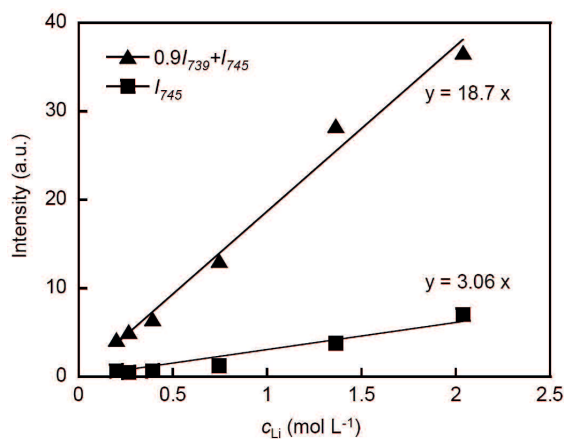


Figure 2.9 $I_{\text{R(CN)}}/c_{\text{Li}}$ plotted as a function of a ($= c_{\text{CN}}/c_{\text{Li}}$) for $\text{PCHO}_a\text{LiTFSA}$. The solid line represents the least-square linear fitting.

Given the total coordination number of Li^+ ions (generally 4–5)^{21,22} and the values of n_{CN} and n_{TFSA} , more ether groups on the main chains can be anticipated to coordinate to Li^+ ions in $\text{PCHO}_a\text{LiTFSA}$ than in $\text{PCEO}_a\text{LiTFSA}$. The difference trend of ether group coordination to Li^+ could be observed from infrared (IR) spectra. Figure 2.10 shows the infrared (IR) spectra corresponding to the asymmetric stretching vibration of ether group's COC (ca. 1095 cm^{-1}). The peaks are very complicated because various vibrational modes are involved in this range; therefore, the coordination number of the ether groups could not be determined from the spectroscopic analysis. But the peak obviously got smaller at high salt concentration ($a > 5$) only for $\text{PCHO}_a\text{LiTFSA}$, which suggest ether groups easily coordinated to Li^+ ions for $\text{PCHO}_a\text{LiTFSA}$ compared than for $\text{PCEO}_a\text{LiTFSA}$. This can form a cross-linked structure based on the main chains in $\text{PCHO}_a\text{LiTFSA}$, which is consistent with the experimental observations: T_g increases with the addition of Li salt (Figure 2.2) and the slightly higher values for the B parameter for ionic conduction (Table 2.2). The ethyl groups in PCEO likely sterically hinder Li^+ ion coordination with the ether groups, which promotes Li^+ ion coordination with the nitrile side chains and TFSA anions, as evidenced by the larger n_{CN} and n_{TFSA} values for $\text{PCEO}_a\text{LiTFSA}$.

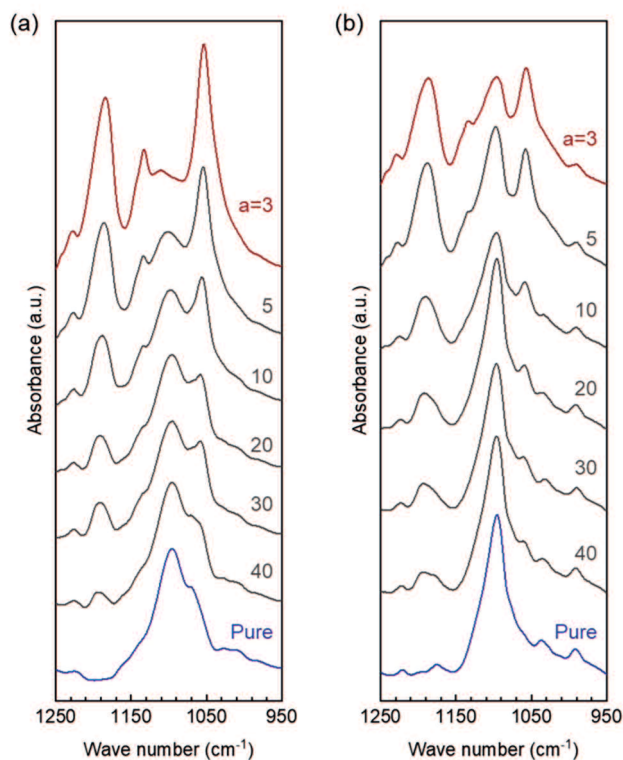


Figure 2.10 IR spectra from 950–1250 cm^{-1} at room temperature for (a) $\text{PCHO}_a\text{LiTFSA}$ and (b) $\text{PCEO}_a\text{LiTFSA}$.

2.3.4. Li^+ ion transference number

To elucidate the transport properties of the Li^+ ions in each PE, the transference number (t_{Li^+}) was measured using an electrochemical method.⁴ As this value increases beyond 0.5, Li^+ migration proceeds at a faster rate relative to TFSA anions in the PEs. The experimental data are shown in the Figures 2.11 and 2.12. t_{Li^+} values of 0.59 and 0.40 are obtained for $\text{PCEO}_5\text{LiTFSA}$ and $\text{PCHO}_5\text{LiTFSA}$, respectively. The lower t_{Li^+} value for $\text{PCHO}_5\text{LiTFSA}$ indicates that the migration of Li^+ ions is more restricted in $\text{PCHO}_5\text{LiTFSA}$, and corroborates the more-pronounced coordination with the ether groups, whereby the mobility of Li^+ ions is coupled with the segmental motion of the ether main chains. The t_{Li^+} values for $\text{PCEO}_5\text{LiTFSA}$ and $\text{PCHO}_5\text{LiTFSA}$ are much larger than those for typically studied PEs, such as $\text{PEO}_a\text{LiTFSA}$ (typically < 0.2).^{23,24} Li^+ ion exchange occurs more frequently between the mono-dentate nitrile side chains and the counter anions than between the multidentate

polyethers on the main chains; therefore, the Li^+ ion can travel more effectively via side chain coordination and site exchange.

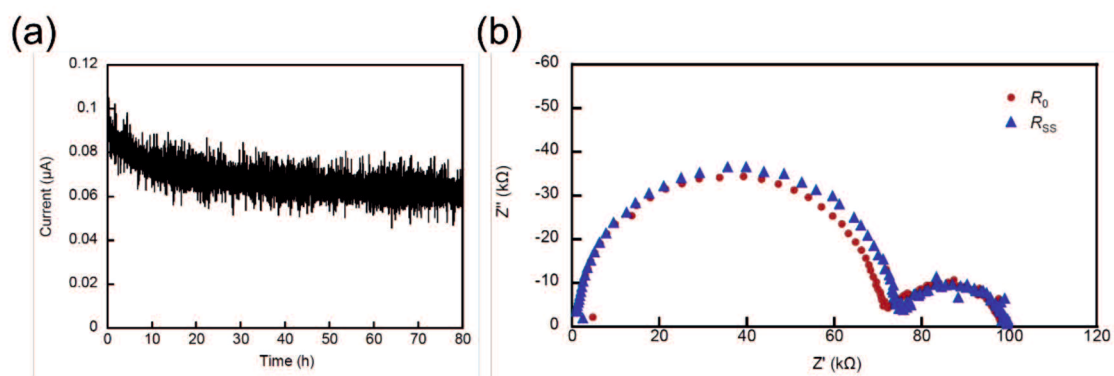


Figure 2.11 Data for various electrochemical measurements used to calculate the transference number of PCEO₅LiTFSA at 50°C. (a) Current with respect to time and (b) Nyquist plots of the initial (R_0) and steady state (R_{ss}).

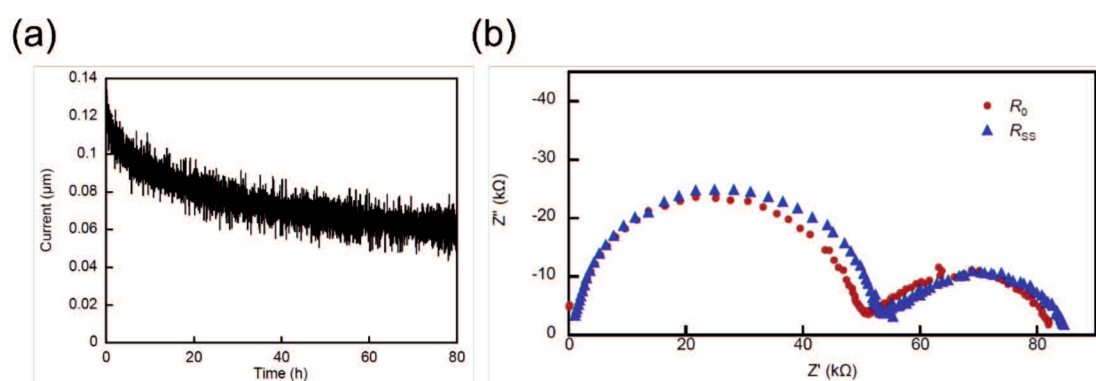


Figure 2.12 Data for various electrochemical measurements used to calculate the transference number of PCHO₅LiTFSA at 50°C. (a) Current with respect to time and (b) Nyquist plots of the initial (R_0) and steady state (R_{ss}).

2.3.5. Charge/discharge tests

Based on the comparative study shown above, I found that PCEO₅LiTFSA exhibits higher Li⁺ ion transport properties. Here, I assembled a lithium-ion half-cell, Li|PCEO₅LiTFSA|LiFePO₄, with PCEO₅LiTFSA as an electrolyte to study whether the polyoxetane-PEs are indeed applicable to Li secondary batteries. No capacity was observed at 30°C even at very low charge-discharge rate (0.05 C), probably due to low ionic conductivity of PCEO₅LiTFSA. The preliminary charge/discharge test from 2.5–4.0 V at 70°C causes an unexpected charging plateau and an apparent overcharge is observed around 3.95 V (Figure 2.13). I previously reported that the electrochemical window of PCEO₅LiTFSA is ~4.0 V vs. Li/Li⁺ on stainless steel electrodes.² This indicates the oxidative decomposition of PCEO₅LiTFSA on the cathode at this potential. Therefore, a further charge/discharge test was performed in the range of 2.5–3.9 V at 70°C.

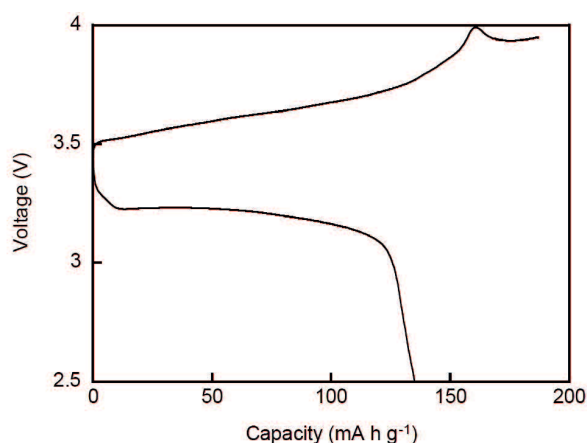


Figure 2.13 Charge/discharge curves of a Li/PCEO₅LiTFSA/LiFePO₄ cell at a 0.05 C rate and 70°C. The measurements were carried out in a range of 2.5–4.0 V (1 C = 117 μ A, 149 μ A cm⁻²).

The charge-discharge curves and cycle performance with different charge-discharge rates are shown in Figure 2.14. The obtained capacities are approximately 100 mAh g⁻¹, even with a low charge-discharge current density at 0.05 C, and are much lower than the theoretical capacity of LiFePO₄ (170 mAh g⁻¹). This is predominantly due to the insufficient electrode/electrolyte interface in the composite cathode, even though PCEO₅LiTFSA is

combined with the composite cathode as the co-binder. To construct better electron/ion pathways, the material composition and the fabrication procedure of the cathode must be further optimized. With an increasing charge-discharge rate, the capacity drastically decreases and the overvoltage increases. In particular, almost no capacity is delivered at rates above 1 C. This is probably caused by the low ionic conductivity of PCEO₅LiTFSA. However, the cell shows a relatively stable cycle performance with only a slight capacity loss at the same rate and high coulombic efficiency of ~99.5%, suggesting that the electrochemical reaction at the positive electrolyte ($\text{LiFePO}_4 \rightleftharpoons \text{FePO}_4 + \text{Li}^+ + \text{e}^-$) is highly reversible in PCEO₅LiTFSA. Thus, these results suggest that the polyoxetane-based PEs with nitrile functionality are applicable to Li secondary batteries.

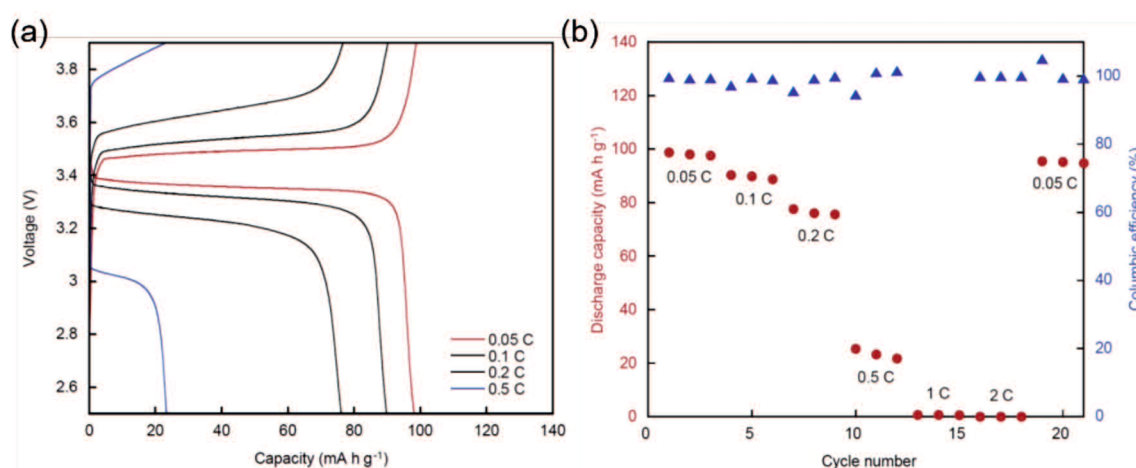


Figure 2.14 (a) Charge/discharge curves and (b) cycle properties of the Li/PCEO₅LiTFSA/LiFePO₄ cell at 70°C. The measurements were carried out in the range of 2.5–3.9 V (1 C = 356 $\mu\text{A cm}^{-2}$). Columbic efficiencies exceeded 110% at 1 C and are not shown in the figure because of the negligible discharge capacities that were higher than the charge capacities recorded in the charge-discharge unit.

2.4. Conclusions

The steric effect of the ethyl group of polyoxetane-based PEs with nitrile side chains was clarified by comparing the thermal properties, Li⁺ ion coordination, and ion transport properties of PCHO_aLiTFSA and PCEO_aLiTFSA. As the Li salt concentration increased, T_g increased for PCHO_aLiTFSA; this behavior is analogous to that of well-studied PEO-based PEs. Conversely, T_g decreased with increasing salt concentrations for PCEO_aLiTFSA. Correspondingly, the ionic conductivity of PCHO_aLiTFSA was lower than that of PCEO_aLiTFSA in the high salt concentration region, mainly because of the higher microviscosity. The Li⁺ ion coordination structure was investigated using Raman spectroscopy, which revealed that the mixed coordination with ether groups, nitrile side chains, and TFSA anions occurred in both PCHO_aLiTFSA and PCEO_aLiTFSA; however, the ether groups were more prone to coordinating with Li⁺ ions in PCHO_aLiTFSA. The more preferential Li⁺ ion coordination with the ether groups resulted in a more pronounced cross-linking of the main chains with Li⁺ ions, leading to an increase in T_g and less effective Li⁺ ion transport (*i.e.*, lower conductivity and t_{Li^+}) in PCHO_aLiTFSA. In other words, the ethyl group played a pivotal role in enhancing the Li⁺ ion transport by sterically inhibiting Li⁺ ion coordination with the ether main chains of the polyoxetanes. In addition, the Li-LiFePO₄ cell using PCEO₅LiTFSA showed a reversible charge-discharge with a relatively stable cycle ability and high coulombic efficiency. Although the conductivity values of PCHO_aLiTFSA and PCEO_aLiTFSA (on the order of 10⁻⁶–10⁻⁵ S cm⁻¹ at 30°C) were not sufficient for practical applications in solid-state Li secondary batteries, this work could provide insight into the molecular design of PEs for pursuing a high ionic conductivity at a level comparable to that of liquid electrolytes, in association with a high Li⁺ ion transference number that rivals that of inorganic solid electrolytes.

References

1. Shintani, Y.; Tsutsumi, H. *J. Power Sources* **2010**, *195*, 2863–2869.
2. Sai, R.; Ueno, K.; Fujii, K.; Nakano, Y.; Shigaki, N.; Tsutsumi, H. *Phys. Chem. Chem. Phys.* **2017**, *19*, 5185–5194.
3. Kubota, K.; Tamaki, K.; Nohira, T.; Goto, T.; Hagiwara, R. *Electrochim. Acta* **2010**, *55*, 1113–1119.
4. Evans, J.; Vincent, C. A.; Bruce, P. G. *Polymer* **1987**, *28*, 2324–2328.
5. Pérez, E.; Gómez, M. A.; Bello, A.; Fatou, J. G. *Colloid Polym. Sci.* **1983**, *261*, 571–576.
6. Perrier, M.; Besner, S.; Paquette, C.; Vallée, A.; Lascaud, S.; Prud'homme, J. *Electrochim. Acta* **1995**, *40*, 2123–2129.
7. Forsyth, M.; Sun, J.; Macfarlane, D. R. *Solid State Ionics* **1998**, *112*, 161–163.
8. Kimura, K.; Motomatsu, J.; Tominaga, Y. *J. Phys. Chem. C* **2016**, *120*, 12385–12391.
9. Larson, R. G. *The Structure and Rheology of Complex Fluids*; Oxford University Press (OUP) USA: Oxford, 1999.
10. White, R. P.; Lipson, J. E. G. *Macromolecules* **2016**, *49*, 3987–4007.
11. Bouchet, R.; Maria, S.; Meziane, R.; Aboulaich, A.; Lienafa, L.; Bonnet, J.-P.; Phan, T. N. T.; Bertin, D.; Gigmès, D.; Devaux, D.; Denoyel, R.; Armand, M. *Nat. Mater.* **2013**, *12*, 452–457.
12. Porcarelli, L.; Gerbaldi, C.; Bella, F.; Nair, J. R. *Sci. Rep.* **2016**, *6*, 19892.
13. Choudhury, S.; Mangal, R.; Agrawal, A.; Archer, L. A. *Nat. Commun.* **2015**, *6*, 10101.
14. Vallée, A.; Besner, S.; Prud'Homme, J. *Electrochim. Acta* **1992**, *37*, 1579–1583.
15. Edman, L.; Doeff, M. M.; Ferry, A.; Kerr, J.; De Jonghe, L. C. J. *J. Phys. Chem. B* **2000**, *104*, 3476–3480.
16. Isa, K. B. M.; Osman, Z.; Arof, A. K.; Othman, L.; Zainol, N. H.; Samin, S. M.; Chong, W. G.; Kamarulzaman, N. *Solid State Ionics* **2014**, *268*, 288–293.
17. Nakano, Y.; Tsutsumi, H. *Solid State Ionics* **2014**, *262*, 774–777.
18. Robitaille, C. D.; Fauteux, D. *J. Electrochem. Soc.* **1986**, *133*, 315–325.
19. Das, S.; Ghosh, A. *J. Appl. Phys.* **2015**, *117*, 174103.
20. Umabayashi, Y.; Mitsugi, T.; Fukuda, S.; Fujimori, T.; Fujii, K.; Kanzaki, R.; Takeuchi, M.; Ishiguro, S.-I. *J. Phys. Chem. B* **2007**, *111*, 13028–13032.
21. Henderson, W. A.; Brooks, N. R.; Young, V. G. *J. Am. Chem. Soc.* **2003**, *125*, 12098–12099.
22. Kameda, Y.; Umabayashi, Y.; Takeuchi, M.; Wahab, M. A.; Fukuda, S.; Ishiguro, S.-I.; Sasaki, M.; Amo, Y.; Usuki, T. *J. Phys. Chem. B* **2007**, *111*, 6104–6109.
23. Timachova, K.; Watanabe, H.; Balsara, N. P. *Macromolecules* **2015**, *48*, 7882–7888.
24. Chintapalli, M.; Timachova, K.; Olson, K. R.; Mecham, S. J.; Devaux, D.; DeSimone, J. M.; Balsara, N. P. *Macromolecules* **2016**, *49*, 3508–3515.



**YAMAGUCHI
UNIVERSITY**

Chapter 3

Importance of lithium coordination structure on lithium-ion transport in polyether electrolyte with cyanoethoxy side-chain: an experimental and theoretical approach

3.1. Introduction

Although acetonitrile, the simplest organic nitrile, spontaneously reacts with the lithium metal due to its poor reductive stability,¹ poly(3-(2-cyanoethoxymethyl)-3-ethyloxetane) (PCEO) achieved a relatively stable cycling performance with only a slight capacity loss for ~20 cycles at 70°C in a Li|PCEO-LiTFSA|LiFePO₄ cell, suggesting the sufficient (electro)-chemical stability of the PCEO electrolyte on both positive and negative electrolytes.² The glass transition temperature (T_g) of PCEO showed unique salt concentration dependency; T_g decreased with increasing salt concentration—the opposite is normally the case.^{3,4} The previous study suggested that (1) the efficient suppression of the coordination of ether oxygen to Li⁺ by steric hindrance of the ethyl groups on the main chain and (2) the weakening of the dipole–dipole interactions between the polar nitrile groups by Li⁺ can be the main reason for the characteristic behavior of T_g .² However, the detailed understanding of the Li⁺ conduction mechanisms, as well as the relevance of the Li⁺ coordination structure on the ionic conductivity is still lacking, mainly because of the difficulty in the experimental clarify the complex interaction between the ions and the polymer matrix in the PCEO electrolyte.

In this work, I use the classical molecular dynamics (MD) simulation combined with the spectro(electro)chemical analysis to overcome the aforementioned obstacles and reveal the complex interaction within the electrolyte. The excellent agreement between MD-simulated results and high-energy X-ray diffraction patterns as well as infrared (IR) spectra allows us to gain detailed insights into the physics of ion transport at play in these electrolytes. From these combined experimental and theoretical techniques, I identify critical elements for the Li⁺ coordination structure, a nitrile group, and ether oxygen; the former moderately stabilizes the Li⁺ and decreases the required energy for the short-range Li⁺ transfer, involving a

decoordination process, and the latter assists the long-range Li^+ transfer. Finally, our work suggests that both short and long-range Li^+ conduction processes can be tuned by designing the Li^+ coordination structure, which can be the alternative strategy for realizing highly Li^+ conducting polymer electrolytes.

3.2. Experimental section

3.2.1. Preparation of the polymer

Polymerized 3-(2-cyanoethoxymethyl)-3-ethyloxetane (PCEO) was synthesized following a reported procedure.^{2,3} 3-(2-cyanoethoxymethyl)-3-ethyloxetane (CEO) was synthesized from 3-ethyl-3-hydroxymethyloxetane (EHO) by Michael addition. EHO (57 mL, 0.500 mol, Tokyo Chemical Industry Co., Ltd.) was mixed with acrylonitrile (60 mL, 0.915 mol, Wako Pure Chemical Co.) in ultrapure water (25 mL, Elix-UV3, Nihon Millipore K.K.) containing a 20% tetraethylammonium hydroxide solution (6.5 mL, Wako Pure Chemical Co.) as a catalyst, and the mixture was stirred at room temperature for 17 h. The reaction mixture was extracted with chloroform and subsequently washed with water. After the solution was dehydrated with magnesium sulfate (Wako Pure Chemical Co.), chloroform was removed using a rotary evaporator. The residue was distilled under reduced pressure (110°C, 2 mmHg). Yield: 47.2 g, 55.8%.

CEO ¹H NMR (δ , ppm from trimethylsilane (TMS) in CDCl₃): 0.90 (t, 3H, $J_{\text{CH}_3\text{-CH}_2} = 7.50$ Hz, $-\text{CH}_3$), 1.75 (q, 2H, $J_{\text{CH}_3\text{-CH}_2} = 7.50$ Hz, $-\text{CH}_2\text{-CH}_3$), 2.63 (t, 3H, $J_{\text{CH}_2\text{-CH}_2} = 6.25$ Hz, $-\text{CH}_2\text{-CH}_2\text{-CN}$), 3.63 (s, 2H, $-\text{C-CH}_2\text{-O-}$), 3.72 (t, 3H, $J_{\text{CH}_2\text{-CH}_2} = 6.25$ Hz, $-\text{CH}_2\text{-CH}_2\text{-CN}$), 4.40 (dd, 4H, $J_{\text{-CH}_2\text{-O-CH}_2\text{-}} = 6.00$ Hz, ring, $-\text{CH}_2\text{-O-CH}_2\text{-}$).

CEO ¹³C NMR (δ , ppm from CDCl₃ (77.00 ppm)): 5.5 ($-\text{CH}_3$), 16.1 ($-\text{CH}_2\text{-CH}_2\text{-CN}$), 23.6 ($-\text{CH}_2\text{-CH}_3$), 40.6 ($-\text{C-}$), 63.0 ($-\text{CH}_2\text{-CH}_2\text{-CN}$), 71.1 ($-\text{C-CH}_2\text{-O-}$), 75.5 ($-\text{CH}_2\text{-O-CH}_2\text{-}$, ring), 115.2 ($-\text{CN}$).

CEO were polymerized using a ring-opening cationic polymerization (ROCP) using boron trifluoride diethyl etherate (BF₃-Et₂O, Wako Pure Chemical. Co.) as an initiator. The molar ratio of the monomer (80 mmol) to the initiator (1.6 mmol) was fixed to 50:1. The monomer was dissolved in 1,2-dichloroethane followed by the addition of BF₃-Et₂O to the solution (total volume: 20 mL). The polymerization was performed under an Ar atmosphere at 0°C in a salt ice bath for 5 h. The ROCP was quenched using 10 mL of a 4 mol dm⁻³ NaCl/ 1 mol dm⁻³ NaOH aqueous solution. Chloroform was then added to the resulting solution, and the mixture was washed with water. The organic phase containing the polyoxetanes was concentrated by rotary evaporation. The residual viscous solution was dropped into a 2-propanol reservoir to reprecipitate the polymerized CEO (PCEO). PCEO were finally collected by filtration using a glass filter and dried at 70°C under vacuum overnight (Yield

32.5%). The successful ROCP was further confirmed by ^1H NMR as the disappearance of double-doublet signals ($\delta = \sim 4.4\text{--}4.5$ ppm for the monomers) of methylene protons in the four-membered ring structure for the oxetane monomers.

PCEO ^1H NMR (δ , ppm from TMS in CDCl_3): 0.85 (t, 3H, $J_{\text{CH}_3\text{--CH}_2} = 7.50$ Hz, $-\text{CH}_3$), 1.39 (q, 2H, $J_{\text{CH}_3\text{--CH}_2} = 7.50$ Hz, $-\text{CH}_2\text{--CH}_3$), 2.58 (t, 3H, $J_{\text{CH}_2\text{--CH}_2} = 6.25$ Hz, $-\text{CH}_2\text{--CH}_2\text{--CN}$), 3.22 (s, 4H, $-\text{C--CH}_2\text{--O-}$), 3.35 (s, 2H, $-\text{C--CH}_2\text{--O-}$), 3.61 (t, 3H, $J_{\text{CH}_2\text{--CH}_2} = 6.00$ Hz, $-\text{CH}_2\text{--CH}_2\text{--CN}$).

PCEO ^{13}C NMR (δ , ppm from CDCl_3 (77.00 ppm)): 7.74 ($-\text{CH}_3$), 18.8 ($-\text{CH}_2\text{--CH}_2\text{--CN}$), 23.2 ($-\text{CH}_2\text{--CH}_3$), 43.6 ($-\text{C-}$), 66.0 ($-\text{CH}_2\text{--CH}_2\text{--CN}$), 71.3 ($-\text{C--CH}_2\text{--O-}$), 77.0 ($-\text{CH}_2\text{--O--CH}_2\text{-}$), 118.2 ($-\text{CN}$).

3.2.2. Electrolyte preparation

The polymer electrolytes (PEs) were prepared using a solvent casting method. PCEO and 1 M lithium bis(trifluoromethanesulfonyl)amide (LiTFSa, Tokyo Chemical Industry Co., Ltd.) in a tetrahydrofuran (THF, Wako Pure Chemical Co.) solution were mixed and subsequently heated under vacuum to completely remove THF. The molar ratios of the repeating monomer unit to LiTFSa were fixed to 1:1, 3:1, and 10:1, and the compound was represented as $\text{PCEO}_a\text{LiTFSa}$ ($a = 1, 3, \text{ and } 10$). The concentrations of LiTFSa (c_{Li}) in $\text{PCEO}_a\text{LiTFSa}$ were estimated using the corresponding CEO monomer density (1.019 g cm^{-3}) and the reported density of molten LiTFSa (1.972 g cm^{-3}).⁵

3.2.3. Characterization methods

Proton and carbon nuclear magnetic resonance (^1H and ^{13}C NMR, respectively) spectra of the synthesized substances were obtained using a Fourier transform NMR spectrophotometer (JNM-LA500, JEOL). The molecular weight of the polymer was measured using a gel permeation chromatography (GPC) system (CBM-20A, LC-20AD, DGU-20A, CTO-20A, and RID-10A, Shimadzu). GPC was performed using THF as the elution solvent and polystyrene standards to calibrate the columns.

A differential scanning calorimeter (DSC7020, Hitachi) was used to determine the glass transition temperature (T_g). A small amount of the PEs (~ 10 mg) was hermetically sealed in an aluminum differential scanning calorimetry (DSC) pan. The samples were first heated to 10 $^\circ\text{C}$ and cooled to -100°C and subsequently reheated from -100 to 100°C at a heating rate

of $10^{\circ}\text{C min}^{-1}$ under a N_2 atmosphere. The T_g was determined from the onset temperatures of the heating thermograms.

Thermogravimetric analysis was performed on a thermogravimetric differential thermal analyzer (Thermo plus EVOII TG8120, Rigaku). A small amount of PEs (~ 5 mg) was put in an aluminum pan. The samples were then heated to 150°C and held for 10 min to completely remove the residual water. Subsequently, the samples were cooled to 50°C and then reheated to 500°C at a heating rate of $20^{\circ}\text{C min}^{-1}$ under He flow. The thermal decomposition temperature (T_d) was defined as the temperature at which 5% weight loss occurred in the thermogravimetry (TG) curves.⁶ The evolved gas during the TG measurement was analyzed by a gas chromatograph-mass spectrometer (GCMS-QP2010 Ultra, Shimadzu). Samples were heated from 100 to 500°C at a heating rate of $20^{\circ}\text{C min}^{-1}$.

Attenuated total reflection infrared (ATR-IR) spectra of the PEs were obtained on a Nicolet iS50 (Thermo Fisher Scientific) spectrometer. Samples were dropped on the ATR prism and hermetically sealed by a glass plate with a rubber spacer (thickness, 5 mm) in an Ar-filled glovebox to avoid moisture adsorption. The measurements were performed at a 4 cm^{-1} resolution in the $4000\text{--}600\text{ cm}^{-1}$ spectral range; 32 scans were averaged. The ATR-IR spectra were recorded using a single-reflection ATR accessory (Smart iTX, Thermo Fisher Scientific) equipped with a Ge prism at an incident angle of 45° . The obtained spectra were deconvoluted by PeakFit software (version 4.12, SYSTAT) using a pseudo-Voigt function.

3.2.4. Electrochemical measurements

The ionic conductivity of the PEs was obtained by AC impedance spectroscopy using a potentiogalvanostat (SP-150, Bio-Logic) in the frequency range of 1 Hz to 500 kHz. The PE was placed between two stainless steel electrodes and separated by a poly(tetrafluoroethylene) ring spacer. The conductivity cell (Swagelok two-electrode cell) was thermally equilibrated in the temperature cabinet at each temperature (temperature range, $30\text{--}110^{\circ}\text{C}$) for at least 1 h before the measurements. The conductivity was calculated by eq 1

$$\sigma = \frac{l}{R_2 \cdot A} \quad (1)$$

where l is the thickness of electrolyte, R_2 is the bulk resistance that was obtained by the Nyquist plot, and A is the surface area of the electrolyte calculated from the inner diameter of the ring spacer.

The transference numbers of Li^+ (t_{Li^+}) were determined using the electrochemical method proposed by Bruce *et al.*,⁷ which was consistent with the electrophoretic NMR method.⁸ The required parameters were obtained using potentiostatic polarization combined with AC impedance spectroscopy measured with a potentiogalvanostat (HZ-Pro S4, Hokuto Denko Co., Ltd.) in a 2032-type symmetric cell. Lithium metal foil (Honjo Metal Co., Ltd.) were used as electrodes. The cell was thermally annealed in a temperature cabinet at 100°C for 1.5 h, followed by stabilization at 70°C for at least 24 h. Impedance spectra were measured prior to the potentiostatic polarization using the aforementioned condition. The impedance spectra were measured immediately after a steady current was observed during a potentiostatic polarization at 10 mV. The t_{Li^+} were determined by the following equation⁹

$$t_{\text{Li}^+} = \frac{[I_{\text{ss}}R_e^{\text{f}}(\Delta V - I_0R_1^{\text{i}})]}{[I_0R_e^{\text{i}}(\Delta V - I_{\text{ss}}R_1^{\text{f}})]} \quad (2)$$

where ΔV is the applied potential ($\Delta V = 10$ mV), I_0 is the initial current of the potentiostatic polarization, I_{ss} is the steady-state current of the polarization, R_e^{i} and R_e^{f} are the initial and final resistances of the electrolyte, respectively, and R_1^{i} and R_1^{f} are the initial and final interfacial resistances, respectively.

3.2.5. Computational methods

All-atom MD simulations were conducted using the GROMACS 2016.5 program under the NTP ensemble condition (298 K and 1 atm) in a cubic cell; the procedural details were similar to those reported in our previous work.¹⁰ The composition (i.e., the number of LiTFSA ion pairs and PCEO molecules) in the simulation box, the resulting box size, and the density at equilibrium are listed in Table 3.1. The polymerization degree of modeled PCEO was set to 8. The total simulation time was set at 15 ns for all of the systems. The X-ray weighted structure factors ($S^{\text{MD}}(q)$) and radial distribution functions ($G^{\text{MD}}(r)$) were determined by analyzing the data collected at 0.1 ps intervals from the last 500 ps. CLaP and OPLS-AA force fields, including intermolecular Lennard–Jones (LJ) and Coulombic

interactions and intramolecular interactions with (1) bond stretching, (2) angle bending, and (3) torsion of dihedral angles, were used for PCEO^{11,12} and TFSA.¹³ The LJ parameter for Li⁺ follows the values proposed by Soetens *et al.*¹⁴ OPLS-AA nonbonded parameters used in this study are listed in Table 3.2.

The $S^{\text{MD}}(q)$ functions were calculated using the trajectory from the MD simulations as follows

$$S^{\text{MD}}(q) = \frac{\sum_i \sum_j w_{ij}(q)}{\left[\sum_k \frac{n_k f_k(q)}{N} \right]^2} \int_0^{r_{\text{max}}} 4\pi\rho_0 (g_{ij}^{\text{MD}}(r) - 1) \frac{\sin(qr)}{qr} dr + 1 \quad (3)$$

$$w_{ij}(q) \equiv \begin{cases} n_i(n_j - 1)f_i(q)f_j(q)/N(N - 1) & (i = j) \\ 2n_i n_j f_i(q)f_j(q)/N^2 & (i \neq j) \end{cases}$$

where n_i and N are the numbers of i atoms and the total number of atoms in the simulation box, and $g_{ij}^{\text{MD}}(r)$ is the atom–atom pair correlation function between atoms i and j . $G^{\text{MD}}(r)$ was obtained from the calculated $S^{\text{MD}}(q)$ by inverse Fourier transformation.

3.2.6. HEXTS measurement

High-energy X-ray total scattering (HEXTS) measurements were performed at room temperature with a high-energy X-ray diffraction apparatus (BL04B2 beamline at SPring-8, JASRI, Japan). The details of the measurements were similar to those described elsewhere.^{10,15} The experimental X-ray structure factor, $S^{\text{exp}}(q)$, per stoichiometric volume, and radial distribution function, $G^{\text{exp}}(r)$, were calculated using equations (4) and (5), respectively.

$$S^{\text{exp}}(q) = \frac{I_{\text{coh}}(q) - \sum n_i f_i(q)^2}{\left[\sum n_i f_i(q) \right]^2} \quad (4)$$

$$G^{\text{exp}}(r) - 1 = \frac{1}{2\pi^2 r \rho_0} \int_0^{q_{\text{max}}} q [S^{\text{exp}}(q) - 1] \sin(qr) \frac{\sin(q\pi/q_{\text{max}})}{q\pi/q_{\text{max}}} dq \quad (5)$$

where $I_{\text{coh}}(q)$ is the corrected coherent scattering obtained from the observed X-ray scattering intensities.^{10,15} n_i is the number of atoms i per stoichiometric volume. The parameters f_i and ρ_0 represent the atomic scattering factor for atom i and the number density of atoms, respectively.

Table 3.1 Li salt concentration (c_{Li}), density (d_{MD}), compositions (number of ion-pairs and PCEO), and box length of the systems used for the MD simulation.

a	c_{Li} [mol dm ⁻³]	d_{MD} [g cm ⁻³]	Li-TFSA	PCEO	Box length
Pure				60	5.170
1	3.121	1.481	480	60	6.292
3	1.533	1.198	160	60	5.654
10	0.554	1.070	48	60	5.335

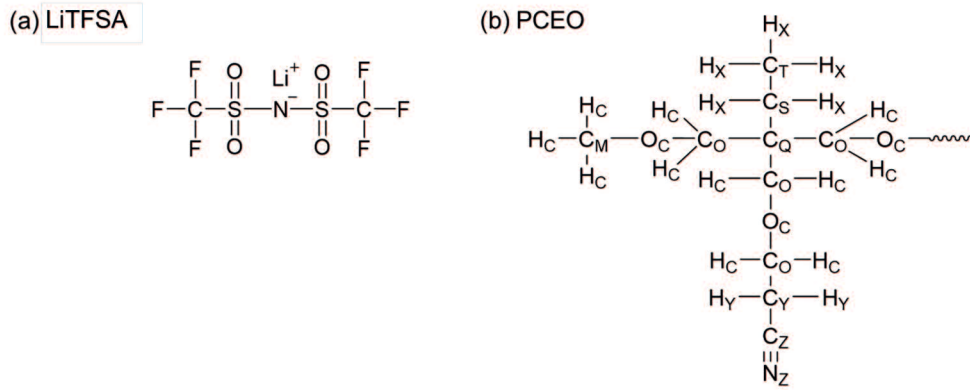


Figure 3.1 The structures of (a) LiTFSA and (b) PCEO with labels used in Table 3.2.

Table 3.2 OPLS-AA nonbonded parameters and atom types for Li⁺, TFSA⁻, and PCEO.

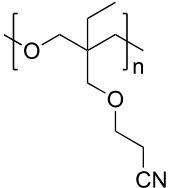
	atom	ϵ [kcal mol ⁻¹]	σ [Å]	q [e]
Li	Li	0.191	1.460	1.000
TFSA	N	0.170	3.250	-0.660
	S	0.250	3.550	1.020
	O	0.210	2.960	-0.530
	F	0.053	2.950	-0.160
	C	0.066	3.500	0.350
PCEO	C _M	0.066	3.500	0.098
	C _O	0.066	3.500	0.140
	C _Q	0.066	3.500	0.000
	C _S	0.066	3.500	-0.120
	C _T	0.066	3.500	-0.180
	C _Y	0.066	3.300	-0.080
	C _Z	0.150	3.650	0.460
	O _C	0.140	2.900	-0.400
	H _C	0.030	2.500	0.034
	H _X	0.030	2.500	0.064
	H _Y	0.015	2.500	0.064
	N _Z	0.170	3.200	-0.560

3.3. Results and discussion

3.3.1. Characterization

PCEO was successfully synthesized via ring-opening cationic polymerization of CEO according to a reported procedure.^{2,3} The obtained polymer was characterized by ¹H and ¹³C NMR spectrometry, which confirms the synthesis of PCEO without any byproducts. The molecular weight and thermal properties of the PCEO are summarized in Table 3.3.

Table 3.3 Molecular weight (M_n , number average and M_w , weight average), polydispersity index (M_w/M_n), and thermal properties (T_g , T_m , and T_d) of the synthesized polymers.

	Molecular weight			Thermal characteristics		
	M_n	M_w	M_n/M_w	T_g	T_m	T_d
	[g mol ⁻¹] ^a	[g mol ⁻¹] ^a	[-]	[°C] ^b	[°C] ^b	[°C] ^c
	9.42×10^3	1.87×10^4	1.98	-20.3	55.3	366

^a Determined by gel permeation chromatography (M_n and M_w)

^b Determined by differential scanning calorimetry (T_g and T_m)

^c Determined by thermogravimetry (T_d)

I then prepared electrolytes via mixing the PCEO with LiTFSA at varied concentrations of $a = 1, 3,$ and 10 , where a is the molar ratio of CEO repeating units to Li^+ , $[\text{CN}]/[\text{Li}^+]$. Differential scanning calorimetry (DSC) confirms a unique salt concentration dependence of T_g for PCEO electrolytes, suggesting pivotal roles of the nitrile groups in the Li^+ coordination structure (Figure 3.2a). Thermogravimetry-mass spectroscopy (TG-MS) analysis confirms the superior thermal stability of the PCEO electrolytes compared to that of the liquid electrolytes currently employed in lithium-ion batteries as well as indicates the salt concentration-dependent change in the Li^+ coordination structure (Figure 3.2b).

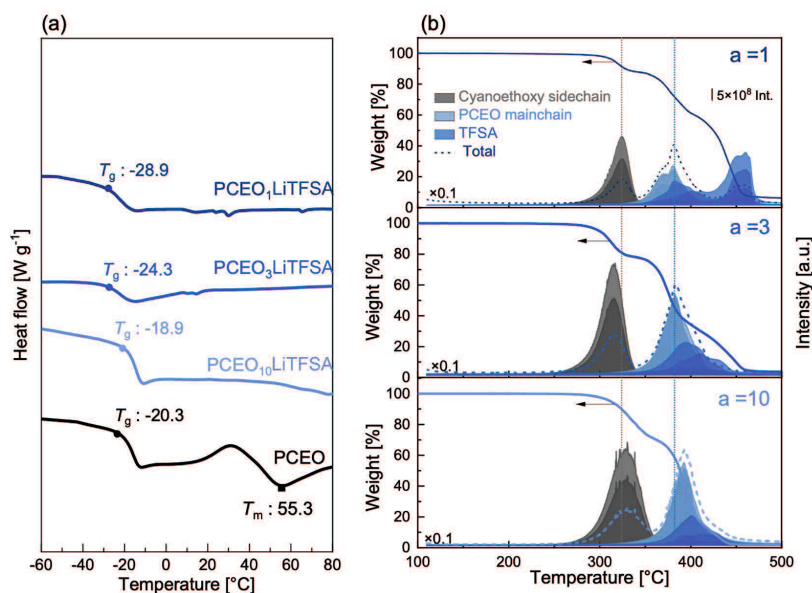


Figure 3.2 (a) Differential scanning calorimetry (DSC) and (b) thermogravimetry (TG) curves and corresponding mass spectrometry (MS) analysis for pristine PCEO and PCEO_aLiTFSA electrolytes ($a = 1, 3, \text{ and } 10$). DSC measurements were performed under a N₂ atmosphere at a heating rate of 10°C min⁻¹. The TG curve was obtained under a He atmosphere at a heating rate of 20°C min⁻¹ after each sample was preheated at 150°C for 10 min. The detected MS fragment was assigned to the cyanoethoxy side chain ($m/z = 26, 53$), the PCEO main chain ($m/z = 29, 41, 55, 84$), and TFSA ($m/z = 48, 64, 69, 85$). The broken line shows the overall MS curve. All of the MS intensities were normalized by the sample mass.

As shown in Figure 3.2a, T_g slightly decreased in proportion to the concentration of the salt (-20.3°C for pure PCEO, -18.9°C for $a = 10$, -24.3°C for $a = 3$, and -28.9°C for $a = 1$), which was consistent with our previous report.^{2,3} It should be pointed out that the T_g for pure PCEO is considerably higher than that of PEO (-64°C),¹⁶ probably due to the dipole-dipole interactions between the polar nitrile groups, which can increase the cohesive energy of pure PCEO. The T_g of the polyether electrolyte is known to increase in line with the concentration of Li⁺ due to the strong ionic interaction between Li⁺ and electron-donating ether oxygen, which restricts the segmental motion.¹⁷ The unusual salt concentration dependence of T_g thus suggests a significant role of Li⁺ coordination structure in the (physico)chemical properties of the PCEO electrolytes.

The thermogravimetric curve for pure PCEO showed a plateau extending up to ca. 380°C, indicating a minimal weight loss and good thermal stability up to 380°C (Figure 3.3). A sharp

decrease observed at $>380^{\circ}\text{C}$ corresponds to the degradation of the PCEO backbone, and PCEO completely dissociated at 450°C . Three weight loss steps, $300\text{--}350$, $350\text{--}400$, and $>400^{\circ}\text{C}$, were observed for the PCEO electrolytes (Figure 3.2b). The first step is up to *ca.* 350°C with a weight loss of around 11.1% ($a = 1$) $<$ 18.3% ($a = 3$) $<$ 23.6% ($a = 10$), which agrees well with the weight fraction of the cyanoethoxy moiety ($\text{CH}_2\text{CH}_2\text{CN}$) for each electrolyte, 12.0% ($a = 1$) $<$ 20.6% ($a = 3$) $<$ 27.6% ($a = 10$). I thus assigned the first weight loss to the decomposition of the cyanoethoxy side chain, further supported by the mass spectrometry (MS) analysis, where the clear peaks corresponding to the cyanoethoxy side chain ($m/z = 26$ and 53) were observed at $300\text{--}350^{\circ}\text{C}$. The slight ($\sim 80^{\circ}\text{C}$) shift of the MS peak of the cyanoethoxy side chain for $a = 3$ suggests the destabilization of the side chain by LiTFSA. The coordination of Li^+ to the nitrile group probably affected the thermal stability of the cyanoethoxy side chain; hence, the shift of the MS fragment for the cyanoethoxy side chain implies the unique contribution of the nitrile group to the Li^+ coordination structure for $a = 3$. The second ($350\text{--}400^{\circ}\text{C}$) and third ($>400^{\circ}\text{C}$) steps can be assigned to the decomposition of a remaining moiety of PCEO (mostly from the PCEO main chain) and LiTFSA, respectively, consistent with the previous studies¹⁸ and TG-MS analyses. The MS peak of the PCEO main chain ($m/z = 29, 41, 55, 84$) shifted to a lower temperature by increasing the salt concentration, which indicated the destabilization of the PCEO main chain under high salt concentrations. A previous study suggests that the interaction between the cation and ether oxygen within the polymer structure lowered its thermal decomposition temperature,¹⁹ and thus, the observation reflects the increasing contribution of ether oxygen on the Li^+ coordination; $a = 1 > a = 3 > a = 10$. The MS fragment for TFSA ($m/z = 48, 64, 69, 85$) observed at *ca.* 450°C for $a = 1$ agreed well with the TFSA fragment observed for the LiTFSA solid (Figure 3.3), which indicates the existence of undissociated salt under high salt concentrations ($a = 1$).

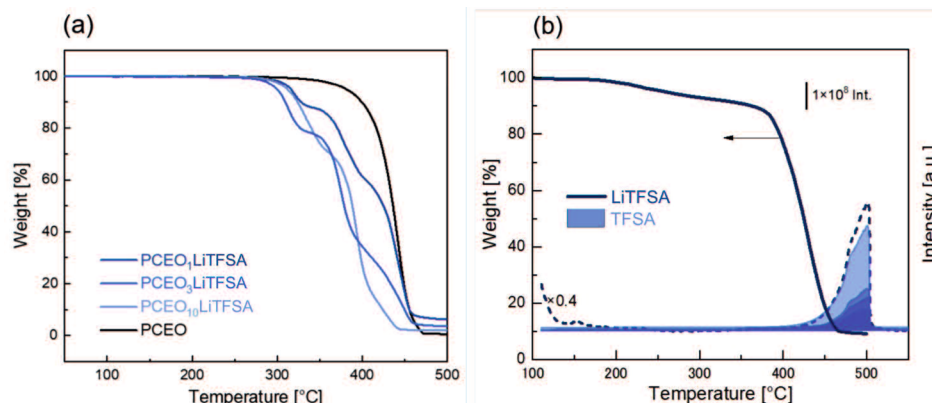


Figure 3.3 (a) Thermogravimetry (TG) curves for pristine PCEO and PCEO_aLiTFSA electrolytes ($a = 1, 3, \text{ and } 10$). (b) thermogravimetry (TG) curves and corresponding mass spectrometry (MS) analysis for pure LiTFSA. TG curve was obtained under He atmosphere at a heating rate of $20^\circ\text{C min}^{-1}$ after each sample was pre-heated at 150°C for 10 min. Detected MS fragment ($m/z = 48, 64, 69, 85$) was assigned to TFSA. Broken line shows overall MS curve.

3.3.2. Lithium-ion coordination structure

A combined spectrochemical and theoretical analysis revealed that the Li^+ coordination structures within PCEO electrolytes varied with salt concentrations. The major components were suggested to be a nitrile group in the PCEO side chain at low salt concentrations ($a > 3$), whereas the TFSA anion became a dominant component at high concentrations ($a = 1$) (Figures 3.7–3.13).

Molecular dynamics (MD) simulations were used to clarify the coordination structures within PCEO electrolytes. To confirm the validity of the force field parameters used in the MD simulations, I performed high-energy X-ray total scattering (HEXTS) experiments and compared them with the MD-derived X-ray radial distribution functions, $G^{\text{MD}}(r)$. The $G^{\text{MD}}(r)$ profiles successfully reproduced the corresponding experimental radial distribution functions, $G^{\text{exp}}(r)$, in the $r^2[G(r)-1]$ form, derived from HEXTS experiments (Figures 3.4 and 3.5). Therefore, the result validates the parameters used in the MD simulations for short-range structures, which enables us to obtain the molecular-level insight into the Li^+ coordination structures within the first coordination shell based on the MD simulations.

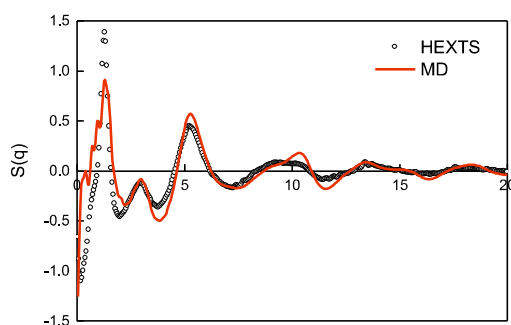


Figure 3.4 Structure factor in the form $S(q)$ for $\text{PCEO}_3\text{LiTFSA}$ obtained from high-energy X-ray total scattering (HEXTS) measurements (open circles) and all-atom molecular dynamics (MD) simulations (continuous red lines).

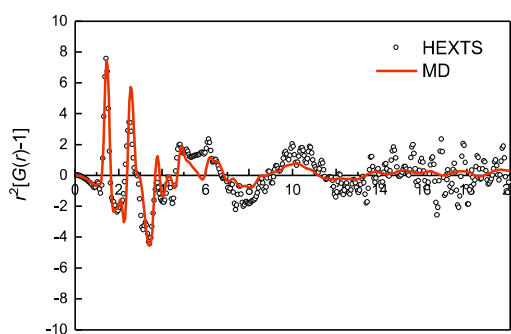


Figure 3.5 Difference radial distribution functions in the $r^2[G(r)-1]$ form for $\text{PCEO}_3\text{LiTFSA}$ obtained from high-energy X-ray total scattering (HEXTS) measurements (open circles) and all-atom molecular dynamics (MD) simulations (continuous red lines).

A detailed analysis of the atom–atom pair correlation functions, $g^{\text{MD}}\text{X}-\text{Y}(r)$, provides a holistic picture of the coordination structure within the PCEO electrolytes (Figures 3.7a and 3.9). To clarify the intermolecular interactions between Li^+ and other components, the total $G^{\text{MD}}(r)$ was divided into $G_{\text{intra}}^{\text{MD}}(r)$ and $G_{\text{inter}}^{\text{MD}}(r)$ (Figure 3.6). The extracted $G_{\text{inter}}^{\text{MD}}(r)$ comprised all of the $g^{\text{MD}}\text{X}-\text{Y}(r)$ values, including the information required to understand the Li^+ coordination structure; $g^{\text{MD}}\text{Li}^+-\text{N}_{\text{PCEO}}(r)$, $g^{\text{MD}}\text{Li}^+-\text{O}_{\text{PCEO}}(r)$, $g^{\text{MD}}\text{Li}^+-\text{O}_{\text{TFSA}}(r)$, and $g^{\text{MD}}\text{Li}^+-\text{N}_{\text{TFSA}}(r)$.

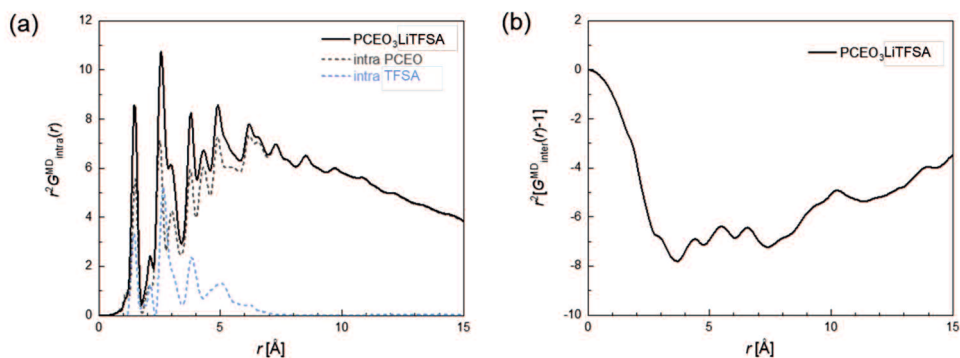


Figure 3.6 Partial $G_{MD}(r)$ s for typical (a) intramolecular and (b) intermolecular contributions in PCEO₃LiTFSA electrolyte.

Salt concentration dependence was clearly observed for the pair correlation functions of $\text{Li}^+-\text{N}_{\text{PCEO}}$ ($g^{\text{MD}}_{\text{Li}^+-\text{N}_{\text{PCEO}}}(r)$) for PCEO electrolytes (Figure 3.7a). A peak appeared at 1.88 Å for all of the systems, which was attributed to the nearest-neighbor $\text{Li}^+-\text{N}_{\text{PCEO}}$ interaction in the first solvation shell.²⁰ The average coordination number $N^{\text{MD}}_{\text{Li}^+-\text{N}_{\text{PCEO}}}(r)$, which was calculated by integrating the $g^{\text{MD}}_{\text{Li}^+-\text{N}_{\text{PCEO}}}(r)$ up to a given r , decreased in proportion to the concentration of the Li salt; 3.58 ($a = 10$) < 2.29 ($a = 3$) < 0.94 ($a = 1$) (see the plateau in $N^{\text{MD}}_{\text{Li}^+-\text{N}_{\text{PCEO}}}(r)$ at $r = 2.0\text{--}3.0$ Å). Given that the coordination number of Li^+ in the organic solution and/or polymer electrolyte is around 4–5,^{21,22} the nitrile group within PCEO can be the major component coordinating to Li^+ at the relatively low salt concentration ($a > 3$).

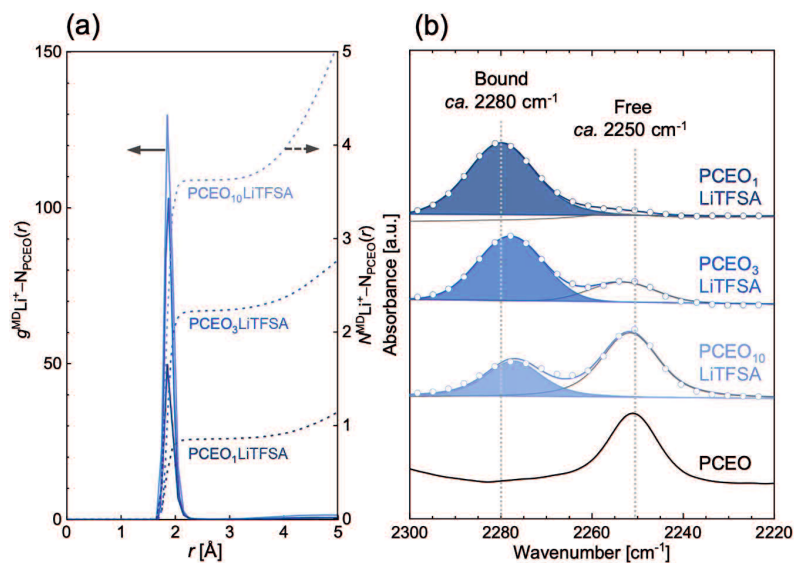


Figure 3.7 Interaction between Li^+ and the nitrile group in PCEO. (a) Li^+ – N_{PCEO} pair correlation functions ($g^{\text{MD}}_{\text{Li}^+-\text{N}_{\text{PCEO}}}(r)$: left axis, solid lines) and corresponding integrated profiles (coordination number $N^{\text{MD}}_{\text{Li}^+-\text{N}_{\text{PCEO}}}(r)$: right axis, broken lines) for $\text{PCEO}_a\text{LiTfSA}$ electrolytes ($a = 1, 3, \text{ and } 10$). N_{PCEO} represents the coordinating N atom in PCEO. (b) ATR–Fourier transform infrared (FTIR) spectra (open circle) and typical curve-fitting results (solid line) of $\nu(\text{C}\equiv\text{N})$ for pristine PCEO and $\text{PCEO}_a\text{LiTfSA}$ electrolytes ($a = 1, 3, \text{ and } 10$) in the frequency range of $2220\text{--}2300\text{ cm}^{-1}$ at room temperature. Peak deconvolution was performed by PeakFit software using pseudo-Voigt functions with a fixed half-width at half-maximum.

Further support comes from infrared spectroscopy, where the estimated coordination number (N^{IR}) obtained from the IR peak area of the deconvoluted CN stretching vibration (*ca.* $2250\text{--}2280\text{ cm}^{-1}$) agreed well with the MD result (Figure 3.7b). A clear peak was observed at *ca.* 2250 cm^{-1} for pure PCEO, which was found to diminish by increasing the salt concentration, in line with the growth of the peak at *ca.* 2280 cm^{-1} . As these two bands (2250 and 2280 cm^{-1}) have similar wavenumbers to those in Raman spectra of the PCEO electrolyte,^{2,3} they were assigned to the characteristic $\text{C}\equiv\text{N}$ stretching mode of the nitrile group in the polymer side chain without (free-CN) and with Li^+ coordination (bound-CN), respectively. The integrated intensities of those two peaks (free-CN and bound-CN) thus can be used to estimate the coordination number for the nitrile group to Li^+ (Table 3.4). The experimentally estimated coordination number (N^{IR}) was calculated by the following equation

$$N^{\text{IR}} = \frac{A_{\text{b(CN)}}}{A_{\text{b(CN)}} + A_{\text{f(CN)}}} \frac{c_{\text{CN}}}{c_{\text{Li}}} \quad (4)$$

where $A_{\text{b(CN)}}$ and $A_{\text{f(CN)}}$ are the IR peak areas for bound-CN (2280 cm^{-1}) and free-CN (2250 cm^{-1}), respectively, and c_{CN} and c_{Li} are the concentrations of CN (repeating PCEO monomer unit) and LiTFSA, respectively.²³ The obtained N^{IR} was 3.58 ($a = 10$) > 2.29 ($a = 3$) > 0.94 ($a = 1$), which showed the similar value and salt concentration dependence expected from MD simulations. The molar absorption coefficient ($\epsilon_{\text{f(CN)}}$) analysis also supports the MD-simulated coordination number (Figure 3.8). The trends in experimentally and theoretically estimated coordination numbers thus suggest the less contribution from the nitrile group to the Li^+ coordination structure as the salt concentration increases.

Table 3.4 IR peak area ratio of bound-CN obtained from the deconvoluted $\nu(\text{C}\equiv\text{N})$ peak. The estimated coordination number for $\text{PCEO}_a\text{LiTFSA}$ ($a = 1, 3, \text{ and } 10$) based on bound-CN peak ratio is also shown.

a	Peak area ratio of bound CN [%]	Estimated coordination number
1	94.23	0.94
3	76.29	2.29
10	35.78	3.58

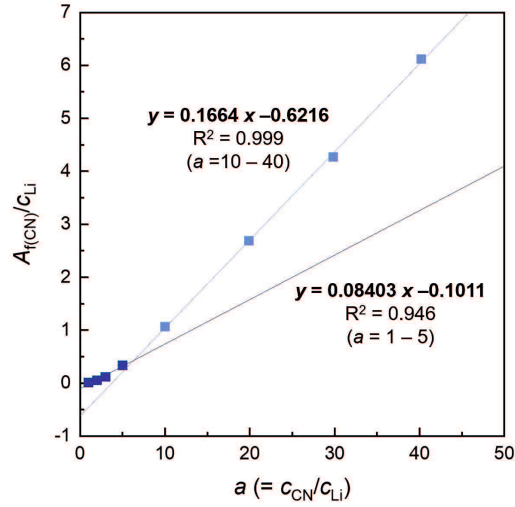


Figure 3.8 $A_{f(CN)}/c_{Li}$ plotted as a function of salt concentration a ($= c_{CN}/c_{Li}$) for PCEO_aLiTFSA. The solid line represents the least-square linear fitting to obtain $J_{f(CN)}$ and N^{IR} from the slope and the intercept, respectively. The linear least-square fitting for low concentration region ($a = 10-40$) and high concentration region ($a = 1-5$) provided average N^{IR} of 3.74 and 1.20, respectively, based on the following relationship,

$$\frac{A_{f(CN)}}{c_{Li}} = \varepsilon_{f(CN)} \left(\frac{c_{CN}}{c_{Li}} - N^{IR} \right) = \varepsilon_{f(CN)} (a - N^{IR}).$$

Ether oxygen within the PCEO structure can coordinate with Li^+ and often play a significant role in ion conduction of polyether electrolytes.²⁴ Based on $g^{MD}Li^+-O_{PCEO}(r)$ from MD simulations (Figure 3.9) and detailed analysis of the IR spectra (Figure 3.11), I propose that the contribution of ether oxygen to the Li^+ coordination structure is notably small for the PCEO system.

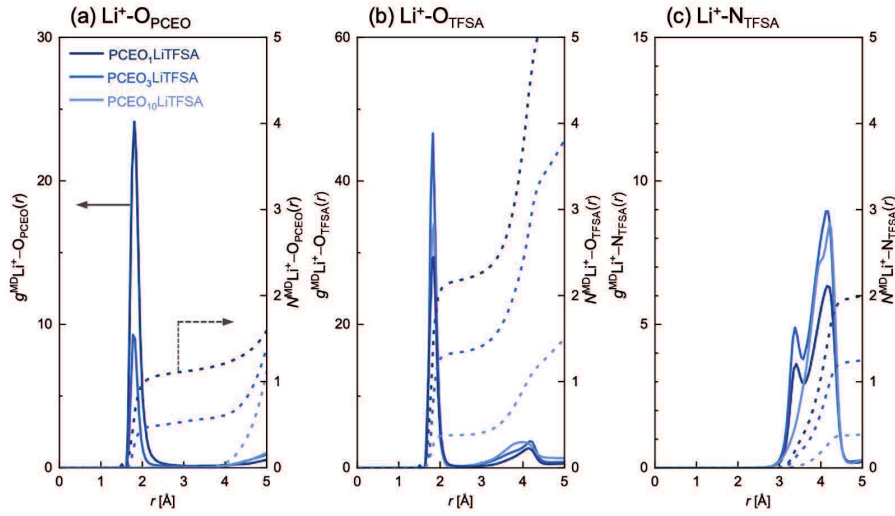


Figure 3.9 Atom–atom pair correlation functions ($g^{\text{MD}}\text{Li}^+-\text{X}(r)$: left axis, solid lines) and the corresponding integrated profiles (coordination number $N^{\text{MD}}\text{Li}^+-\text{X}(r)$: right axis, broken lines) for (a) $\text{Li}^+-\text{O}_{\text{PCEO}}$, (b) $\text{Li}^+-\text{O}_{\text{TFSA}}$, and (c) $\text{Li}^+-\text{N}_{\text{TFSA}}$ for PCEO_aLiTFSA electrolytes ($a = 1, 3, \text{ and } 10$). O_{PCEO} , O_{TFSA} , and N_{TFSA} represent the coordinating O atom in PCEO, including both O atoms in main and side chains, an O atom in TFSA anion, and a N atom in the TFSA anion, respectively.

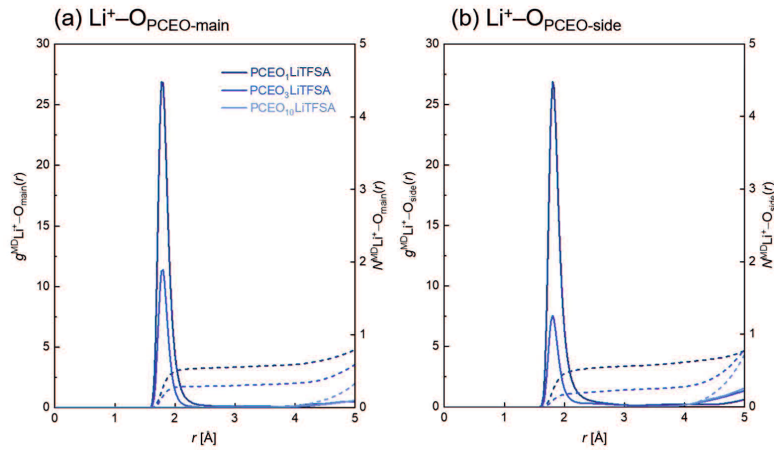


Figure 3.10 Atom–atom pair correlation functions ($g^{\text{MD}}\text{Li}^+-\text{X}(r)$: left axis, solid lines) and corresponding integrated profiles (coordination number $N^{\text{MD}}\text{Li}^+-\text{X}(r)$: right axis, broken lines) for (a) $\text{Li}^+-\text{O}_{\text{PCEO-main}}$ and (b) $\text{Li}^+-\text{O}_{\text{PCEO-side}}$ for PCEO_aLiTFSA ($a = 1, 3, \text{ and } 10$) electrolytes.

Pair correlation functions of $\text{Li}^+-\text{O}_{\text{PCEO}}$ ($g^{\text{MD}}\text{Li}^+-\text{O}_{\text{PCEO}}(r)$, Figure 3.9a) showed a distinct peak at 1.83 Å, attributed to the nearest-neighbor $\text{Li}^+-\text{O}_{\text{PCEO}}$ interaction in the first solvation shell.²⁵ Note that $g^{\text{MD}}\text{Li}^+-\text{O}_{\text{PCEO}}(r)$ contains contributions from oxygen atoms in both the main chain (O_{main}) and side chain (O_{side}), in which almost identical behavior toward Li^+ coordination was confirmed (Figure 3.10). The average coordination number $N^{\text{MD}}\text{Li}^+-\text{O}_{\text{PCEO}}(r)$ increased with increasing concentration of the Li salt; ~ 0 ($a = 10$) < 0.5 ($a = 3$) < 1.1 ($a = 1$). Although $N^{\text{MD}}\text{Li}^+-\text{O}_{\text{PCEO}}(r)$ increases under high salt concentrations ($a = 1$), the Li^+ coordination number is still significantly smaller than that of the previously reported PEO electrolyte (coordination number ~ 3),²⁶ which is in agreement with the preferable coordination of the nitrile group to Li^+ for PCEO electrolytes. The small coordination number for $\text{Li}^+-\text{O}_{\text{PCEO}}$ corresponds to the less strong interaction between Li^+ and ether oxygen, which can be the reason for the unique salt concentration dependency of T_g for PCEO electrolytes (Figure 3.2a). The degree of interaction between ether oxygen and Li^+ , estimated from the C–O–C asymmetric stretching vibration (*ca.* 1105 cm^{-1}) of the PCEO electrolyte with the LiI salt (Figure 3.11), supports the salt concentration dependence of the MD-simulated coordination number for $\text{Li}^+-\text{O}_{\text{PCEO}}$. The observed trend of the Li^+ –ether oxygen interaction from the MD simulation and IR analysis was in agreement with the thermal stability trend of the PCEO main chain observed in TG-MS (Figure 3.2b), which further validates our result.

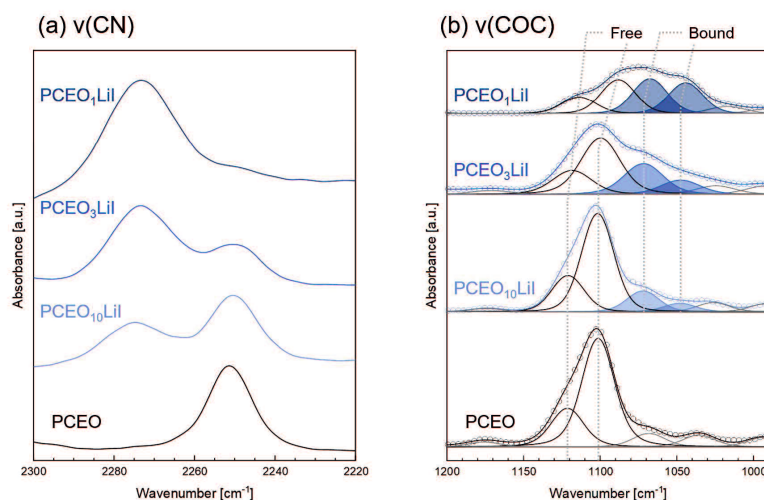


Figure 3.11 ATR-FTIR spectra (open circle) and typical curve-fitting results (solid line) of (a) $\nu(\text{CN})$ and (b) $\nu_{\text{as}}(\text{COC})$ for pristine PCEO and PCEO_aLiI electrolytes ($a = 1, 3,$ and 10) in the frequency range of (a) $2220\text{--}2300\text{ cm}^{-1}$ and (b) $990\text{--}1200\text{ cm}^{-1}$ at room temperature. Peak deconvolution was performed by PeakFit software using pseudo-Voigt functions with fixed half-width at half-maximum.

The intermolecular interaction between Li^+ and the TFSA anion was analyzed by pair correlation functions of $\text{Li}^+\text{--O}_{\text{TFSA}}$ ($g^{\text{MD}}\text{Li}^+\text{--O}_{\text{TFSA}}(r)$, Figure 3.9b) and $\text{Li}^+\text{--N}_{\text{TFSA}}$ ($g^{\text{MD}}\text{Li}^+\text{--N}_{\text{TFSA}}(r)$, Figure 3.9c). The average coordination number for $\text{Li}^+\text{--O}_{\text{TFSA}}$ revealed a low salt dissociation degree under high salt concentrations ($a = 1$), while that of $\text{Li}^+\text{--N}_{\text{TFSA}}$ can be used to determine the ratio of two possible conformers of the TFSA anion, monodentate and bidentate, at varying salt concentrations.

The $g^{\text{MD}}\text{Li}^+\text{--O}_{\text{TFSA}}(r)$ showed a significant peak at 1.83 \AA , which can be assigned to the nearest-neighbor $\text{Li}^+\text{--O}_{\text{TFSA}}$ interaction.^{27–30} The average coordination number ($N^{\text{MD}}\text{Li}^+\text{--O}_{\text{TFSA}}(r)$) tend to increase with an increase in salt concentration; 0.4 ($a = 10$) $<$ 1.3 ($a = 3$) $<$ 2.0 ($a = 1$). The trend thus suggests a decrease in salt dissociation degree within the PCEO electrolytes by increasing the salt concentration, which was in line with the IR analysis of the CF_3 bending vibration (*ca.* $740\text{--}745\text{ cm}^{-1}$) (Figure 3.12) and the TG-MS analysis of the TFSA fragment (Figure 3.2b).

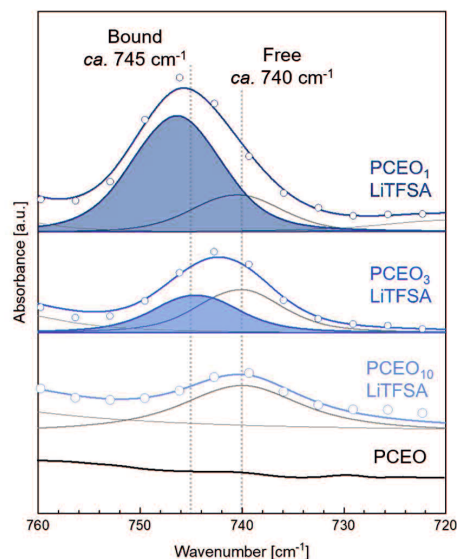


Figure 3.12 ATR-FTIR spectra (open circle) and typical curve-fitting results (solid line) of CF_3 bending vibration for pristine PCEO and $\text{PCEO}_a\text{LiTfSA}$ electrolytes ($a = 1, 3,$ and 10) in the frequency range of $720\text{--}760\text{ cm}^{-1}$ at room temperature. Peak deconvolution was performed by PeakFit software using pseudo-Voigt functions with fixed half-width at half-maximum.

The correlation between Li^+ and the N_{TFSA} atom is known as a probe to distinguish the two possible conformers of TFSA, monodentate and bidentate, in the Li^+ complexes.^{31,32} In the $g^{\text{MD}}\text{Li}^+\text{--N}_{\text{TFSA}}(r)$ for the PCEO system, two intense peaks appeared at 3.38 and 4.13 \AA , which can be ascribed to the TFSA anions coordinating with Li^+ in a bidentate manner (bi-TFSA) and a monodentate manner (mono-TFSA), respectively, based on the previous theoretical and spectroscopic studies^{32,33} (Figure 3.9c). The $g^{\text{MD}}\text{Li}^+\text{--N}_{\text{TFSA}}(r)$ showed salt concentration dependence, where only mono-TFSA exists at a low salt concentration (in this study, $a = 10$) and bi-TFSA started to coexist when increasing the salt concentration ($a < 3$). A similar trend was reported in aqueous and nonaqueous solutions at high salt concentrations, where charged ion aggregates exist in the form of mononuclear complexes, e.g., Li^+ having a four-coordinated structure with the oxygen atom within bi-TFSA.³⁴ The observed trend thus suggests the increased population of the charged ion aggregates (e.g., $\text{Li}(\text{TFSA})_2^-$) at high salt concentrations ($a = 1$).³⁵

Figure 3.13 summarizes the salt concentration dependence of the average coordination number of the $\text{Li}^+\text{--nitrile}$ group, $\text{Li}^+\text{--TFSA}$ anion, and $\text{Li}^+\text{--ether oxygen}$ atom for PCEO

electrolytes obtained from the MD simulation and IR spectroscopic analysis. Both experimental and theoretical values are in excellent agreement, which confirms the validity of the methods used in this study.

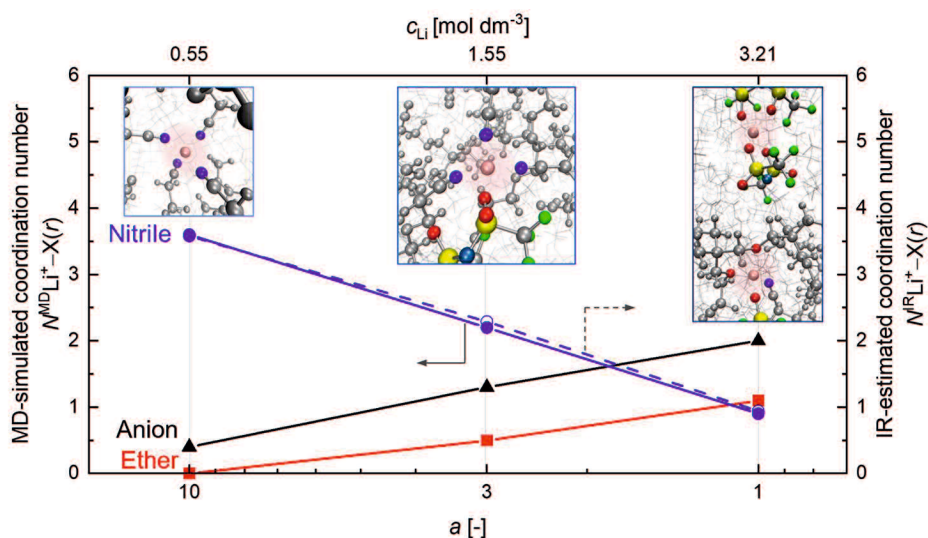


Figure 3.13 Salt concentration dependence of the average coordination number of the Li^+ –nitrile group (Nitrile), Li^+ –TFSA anion (Anion), and Li^+ –ether oxygen atom (Ether) for $\text{PCEO}_a\text{LiTFSA}$ ($a = 1, 3, \text{ and } 10$). The MD-simulated coordination number (solid legend, solid line) was calculated by integrating the $g^{\text{MD}}_{\text{Li}^+-\text{N}_{\text{PCEO}}(r)}$, $g^{\text{MD}}_{\text{Li}^+-\text{O}_{\text{TFSA}}(r)}$, and $g^{\text{MD}}_{\text{Li}^+-\text{O}_{\text{PCEO}}(r)}$, respectively, up to a given r . The IR-estimated coordination number (open legend, broken line) was calculated by integrating the intensities of free-CN and bound-CN peaks (for Li^+ –nitrile group) observed in ATR-IR spectra. The inset shows the typical snapshot of the Li^+ coordination structure found in the PCEO electrolyte at the corresponding salt concentration. Pink, blue, light blue, red, yellow, green spheres represent Li, N_{PCEO} , N_{TFSA} , O, S, and F atoms, respectively. Spectator atoms are depicted as gray spheres for ease of visibility.

Li^+ is mostly surrounded by the nitrile group ($N = 3.58$) within the side chain of PCEO under low salt concentrations ($a = 10$). The trend thus clearly suggests the preferable coordination of the nitrile group to Li^+ compared to ether oxygen. The addition of salt leads to less contribution of the nitrile group to the Li^+ coordination structure and alternatively increases the Li^+ coordination numbers of the TFSA anion and an ether oxygen atom. The nitrile group remains as major species within the Li^+ coordination structure ($N = 2.29$) at $a = 3$, while the TFSA anion becomes dominant species ($N = 2.0$) under a high salt concentration

of $a = 1$, indicating the low salt dissociation at a given concentration. The contribution from ether oxygen on Li^+ coordination remains small ($N < 1.1$) throughout the salt concentration range, which clearly separates the PCEO electrolytes from the PEO-based counterparts.

3.3.3. Ion transport property

To understand the impact of the Li^+ coordination structure on ionic conductivity in detail, I measured ionic conductivity at various temperatures for PCEO electrolytes (Figure 3.14). An almost tenfold increase in the Li^+ conductivity was confirmed for PCEO electrolytes with $a = 3$, which was associated with the enhanced interchain Li^+ transfer, involving the decoordination process, and good segmental mobility of the polymer due to the unique Li^+ coordination structure involving both the nitrile group and ether oxygen.

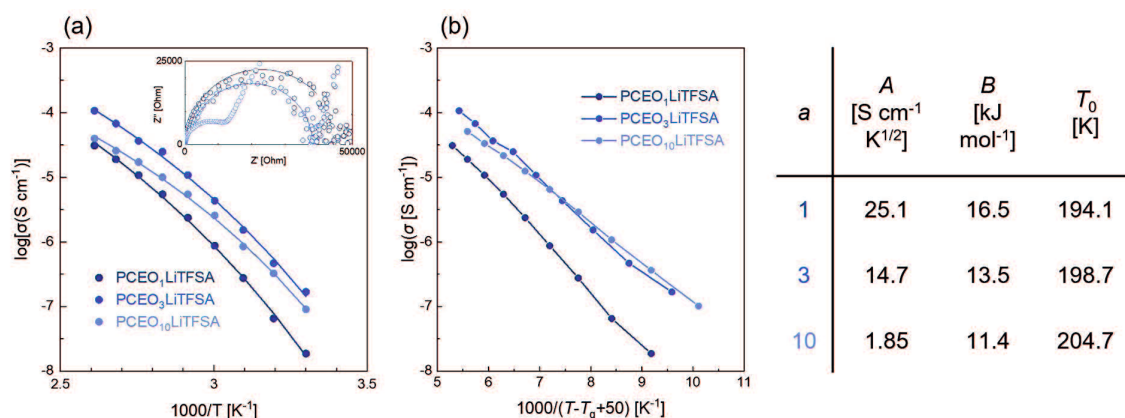


Figure 3.14 Ionic conductivities for $\text{PCEO}_a\text{LiTFSA}$ electrolytes ($a = 1, 3$, and 10) plotted against (a) $1000/T$ and (b) $1000/(T - T_g + 50 \text{ K})$. Fitting curves to the Vogel–Tammann–Fulcher (VTF) equation are shown in solid lines in panel (a). The inset in panel (a) shows representative Nyquist plots at 60°C . The analyzed parameters in the VTF equation are on the right side of the graph.

The ionic conductivity obtained from electrochemical impedance spectroscopy (EIS) displayed the typical curved increase in ionic conductivity upon increasing the operating temperature for all of the PCEO electrolytes, suggesting that ions were transported mainly via a segmental motion of polymer as was the case for PEO-based electrolytes (Figure 3.14a).^{36,37} Note that the overall conductivity for PCEO electrolytes is lower than that of previously reported PEO-based counterparts.³⁸ The primary reason for this low conductivity

is the relatively high T_g of pure PCEO (*ca.* -20°C) compared to that of PEO (-64°C),¹⁶ probably originating from the strong dipole–dipole interaction between the nitrile group. Although T_g is regarded as a comprehensive and global descriptor of ionic conductivity for polymer electrolytes,³⁷ it is not the case for the ionic conductivity trend observed here, considering that the T_g slightly decreased in proportion to the concentration of the salt ($a = 10$ (-18.9°C) $>$ $a = 3$ (-24.3°C) $>$ $a = 1$ (-28.9°C)) (Figure 3.2a).

The effects of the Li^+ coordination structure on the ionic conductivity were evaluated independently from the effects of differences in T_g by plotting the ionic conductivities on a shifted temperature scale of $1000/(T - T_g + 50 \text{ K})$, which highlights the intrinsic conductivity originating from the Li^+ coordination structure, rather than its general flexibility (Figure 3.14b).^{39,40} The trends in conductivity follow the order $\text{PCEO}_{10}\text{LiTFSA} = \text{PCEO}_3\text{LiTFSA} >$ $\text{PCEO}_1\text{LiTFSA}$, which coincides with the trends in Li^+ coordination number of nitrile group (Figure 3.14). A notable improvement in the ionic conductivity observed for $a = 10$ and 3, conditions where Li^+ is coordinated mainly by a nitrile group ($N > 2$), indicates the unique Li^+ -transfer process, which is irrelevant to the segmental motion of the polymer. The nitrile group-dominated coordination structure is preferable for the interchain Li^+ transfer involving the decoordination process (short-range Li^+ conduction), via interconnected coordinating sites in the polymer, probably due to the (1) moderate interaction between Li^+ and the nitrile group and (2) characteristic linear structure of the nitrile group providing large free volume in the direct vicinity of the Li^+ coordination site.

For further understanding of the ion transport properties of PCEO electrolytes, the Vogel–Tammann–Fulcher (VTF) equation (eq 5), i.e., a modified Arrhenius equation proposed for describing the temperature dependence of the viscosity in amorphous glasses, was employed⁵⁶

$$\sigma(T) = AT^{-\frac{1}{2}}\exp\left(-\frac{B}{R(T - T_0)}\right) \quad (5)$$

Here, $\sigma(T)$ is the ionic conductivity at a specific temperature, A is a constant related to the maximum number of charge carriers, B is the pseudoactivation energy of ion conduction, R is the gas constant, T is the temperature, and T_0 is the VTF temperature often chosen to be 50 K below T_g .^{41–43} The experimental data showed a good agreement with the fitting line (solid

lines in Figure 3.14), and the analyzed parameters in the VTF equation are summarized in Figure 3.14.

As expected, A values increased with an increase in salt concentration, which indicates that even at high salt concentrations ($a = 1$), majority of the salt can dissociate into Li^+ and TFSA^- and act as a charge carrier. However, an increase of the A values was not fully proportional to the salt concentration (especially from $a = 3$ to 1), consistent with a decrease in the salt dissociation degree under high salt concentrations suggested by the MD simulation and IR spectroscopy (Figure 3.13). The pseudoactivation energy (B) also increased with increasing salt concentrations ($11.4 (a = 10) < 13.5 (a = 3) < 16.5 (a = 1)$), which indicated a slight mechanistic difference in ion transport under different salt concentrations.⁴³ The slight change can be related to the change in the Li^+ coordination structure and/or the amount of undissociated salt depending on the salt concentration.

Imaginary impedance is known to represent the capacitive response of the impedance measurement, where peak frequency describes the timescale of specific processes (Figure 3.15). Although there is still no consensus for the detailed assignments of imaginary impedance behavior for polymer electrolytes, the slope in the low-frequency region and the peak in the high-frequency region are believed to correspond to ionic (DC) polarization⁴⁴ and ion-pair relaxation or segmental relaxation of polymer chains,⁴⁵ respectively. The peak top frequency for the high-frequency region shows a maximum value at a salt concentration of $a = 3$ followed by $a = 10$ and 1, which follows the observed ionic conductivity trends (Figure 3.14). Thus, the result indicates that local flexibility of ion pairs and/or polymer chains play a significant role in the ion conduction in polymer electrolytes.

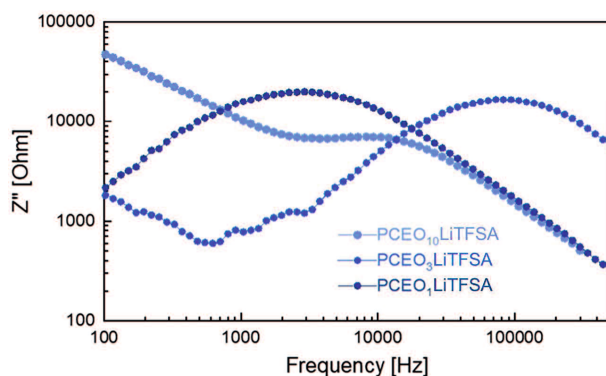


Figure 3.15 Frequency dependence of imaginary impedance (Z'') for $\text{PCEO}_a\text{LiTFSA}$ ($a = 1, 3, \text{ and } 10$) electrolytes during EIS measurement with the conductivity cell [SS | electrolytes | SS] measured at open circuit potential with amplitude of 10 mV at 70°C .

The lithium transference number (t_{Li^+}) calculated by the potentiostatic polarization (Bruce–Vincent) method (Figure 3.16 and Table 3.5) revealed that the t_{Li^+} for PCEO electrolytes increased with increasing salt concentration (Table 3.6).

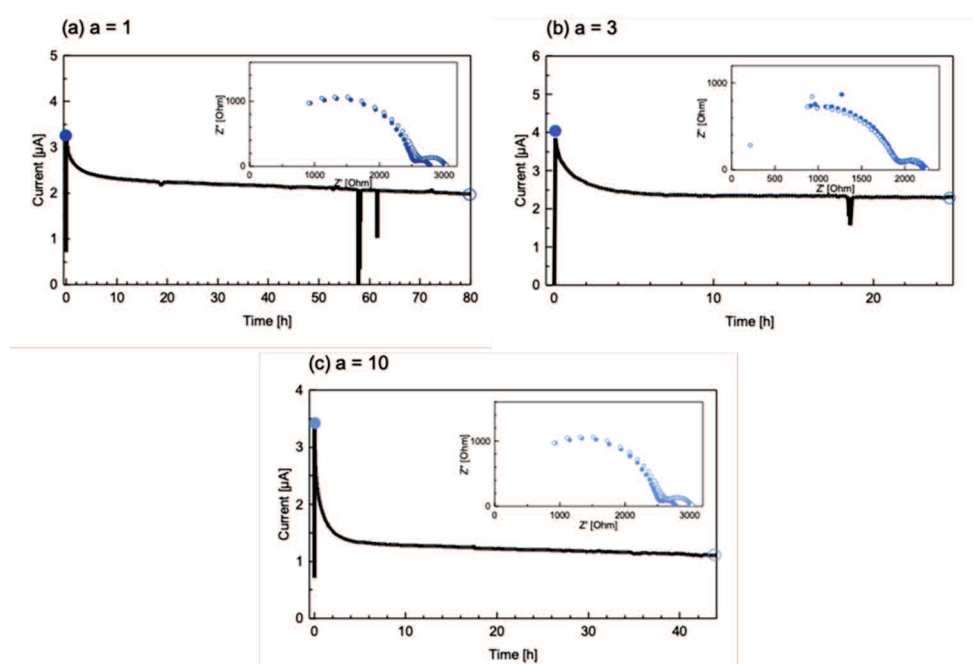


Figure 3.16 Time dependence of DC polarization and corresponding Nyquist plots before and after polarization used to calculate the transference number for $\text{PCEO}_a\text{LiTFSA}$ ($a = 1, 3, \text{ and } 10$). EIS measurement was performed using the symmetric cell of [Li metal | polymer electrolyte | Li metal] at 70°C .

Table 3.5 Measured parameter used to calculate the transference number for PCEO_aLiTFSA (*a* = 1, 3, and 10) and the corresponding calculated values of Li⁺ transference numbers at 70°C.

<i>a</i>	<i>I</i> ₀ [μA]	<i>I</i> _{SS} [μA]	Frequency [Hz]				ΔV [mV]	<i>t</i> _{Li+}
			<i>R</i> _e ⁱ [Ω]	<i>R</i> _e ^f [Ω]	<i>R</i> _i ⁱ [Ω]	<i>R</i> _i ^f [Ω]		
1	3.214	1.982	6309.67		1		10	0.70
			2863.2	3227.0	112.3	197.5		
3	3.861	2.313	166807		1		10	0.58
			1966.6	1974.1	266.8	272.4		
10	3.370	1.110	7943.0		1		10	0.33
			2537.3	2631.9	246.7	399.7		

Table 3.6 List of Li⁺ transference numbers (*t*_{Li+}) for PCEO_aLiTFSA electrolytes (*a* = 1, 3, and 10) at 70°C obtained by a potentiostatic polarization method.^{7,a}

<i>a</i>	<i>t</i> _{Li+}	log σ_{Li+}	σ_{Li+} [S cm ⁻¹]
1	0.70	-5.78	1.66 × 10 ⁻⁶
3	0.58	-5.20	6.26 × 10 ⁻⁶
10	0.33	-5.75	1.80 × 10 ⁻⁶

^a Estimated Li⁺ conductivities (σ_{Li+}) for PCEO_aLiTFSA electrolytes (*a* = 1, 3, and 10) at 70°C calculated by $t_{Li+} \times \sigma$ (70°C) is also shown.

Furthermore, the *t*_{Li+} at *a* > 3 showed a significantly improved value compared to those for PEO-based electrolytes (*t*_{Li+} < 0.3) as well as conventional organic liquid-based electrolytes (*t*_{Li+} ~0.5) under similar salt concentrations.¹⁷ The obtained concentration dependence can be interpreted either in terms of trapping of anions in the Li⁺ complexes^{24,46} or the formation of ionic aggregates.⁴⁷⁻⁵⁰

Estimated Li⁺ conductivities (σ_{Li+}) for PCEO electrolytes showed the highest value at *a* = 3 with moderate *t*_{Li+} = 0.58 and the highest σ_{total} = 1.08 × 10⁻⁵ S cm⁻¹ among the salt concentrations tested. Note that the ionic conductivity poorly correlates with the change in *T*_g for PCEO electrolytes, whereas it coincides with the trends in the Li⁺ coordination number of the nitrile group (Figure 3.14). Therefore, I propose that the Li⁺ coordination structure be one of the key descriptors to understand the unique σ_{Li+} for PCEO electrolytes.

At *a* = 10, Li⁺ interacts preferably with the nitrile group, forming an “isolated” coordination structure with a negligible contribution from the ether oxygen atom (Figure 3.13). Since the ether oxygen atom plays a vital role in the interchain Li⁺ transfer, involving

the decoordination process, proposed as the critical step for Li^+ transport within PEO-based electrolytes,³⁸ the σ_{Li^+} value became significantly low at $a = 10$. The TFSA anion, on the other hand, is preferably transferred owing to the loose interaction with the ether oxygen atom, which can also be the reason for the low t_{Li^+} value at $a = 10$.

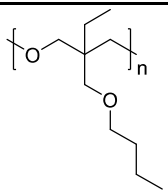
The contribution from the ether oxygen atoms and TFSA anions to Li^+ coordination structure increases at $a = 1$, leading to an increase in t_{Li^+} while decreasing the total conductivity of electrolytes due to the restriction of the anion movement and the presence of ionic aggregates, respectively. The coordination structure at $a = 1$ for dissociated Li^+ contains two oxygen and/or nitrogen atoms from the polymer and one or two oxygen atom(s) from TFSA anions (Figure 3.13). MD simulations indicate that most of the anions become involved in the Li^+ complex structure and no longer transfer freely in volume between the chains. Furthermore, the large concentration of anions is unfavorable for anion transport, in which most of the conduction sites are already occupied. The presence of charged ionic aggregates (e.g., $\text{Li}(\text{TFSA})_2^-$), suggested by MD simulations (Figure 3.9c), may play a significant role in the decrease of ionic conductivity. The relatively large molecular weight and/or volume of charged ion aggregates compared to that of fully dissociated ions hinders the effective ion conduction, resulting in low σ values at $a = 1$.

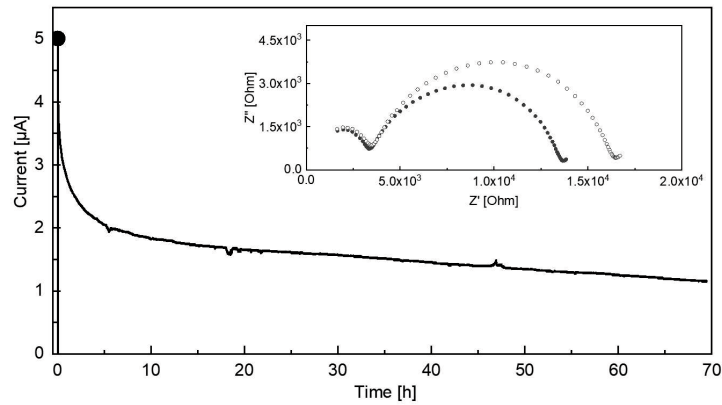
Li^+ interacts with both the nitrile group and ether oxygen atom at $a = 3$ (Figure 3.13), leading to moderately stabilizing Li^+ within the coordination structure. A characteristic coexistent state of the three components (nitrile group, ether oxygen, and TFSA anion) may play a significant role in accelerating the interchain Li^+ transfer involving the decoordination process (short-range Li^+ conduction) as was the case for polyacrylonitrile-based electrolytes.⁵¹ The previous study by Brooks *et al.* suggests that the PEO polymer is too flexible and overly holding onto the Li^+ , leading the Li^+ to stay too long associated with a region of PEO.³⁸ The relaxation of the Li^+ coordination structure by the nitrile group thus has a positive impact on the interchain Li^+ transfer, involving the decoordination process, while maintaining the sufficiently low T_g without inhibiting the segmental motion of the polymer. Furthermore, the characteristic linear structure of the nitrile group may provide large free volume in the direct vicinity of the Li^+ coordination site, which accelerates the intermolecular

coordination of Li^+ , eventually resulting in Li^+ transfer involving the decoordination process, from one coordination site to another in the presence of an electric field.⁵²

An analysis of t_{Li^+} for the PC4EO electrolyte, having C_2H_5 instead of the nitrile group of PCEO (detailed for Chapter 4), further supports our hypothesis. The lithium transference number was indeed affected by the existence of the nitrile group since t_{Li^+} for the PC4EO electrolyte was significantly lower ($t_{\text{Li}^+} = 0.14$) compared to that for the PCEO electrolyte ($t_{\text{Li}^+} = 0.58$, Table 3.6). Therefore, having both the nitrile group and ether oxygen in the Li^+ coordination structure is responsible for reducing the energy barrier of the Li^+ transfer for the PCEO electrolyte at $a = 3$ by accelerating interchain Li^+ transfer involving the decoordination process while maintaining the high segmental mobility of the polymer.

Table 3.7. Molecular weight (M_n , number average and M_w , weight average) of the synthesized PC4EO polymer.

PC4EO	Molecular weight		
	M_n [g mol ⁻¹] ^a	M_w [g mol ⁻¹] ^a	M_n/M_w [-]
	5.66×10^4	1.06×10^5	1.86



	I_0 [μA]	I_{ss} [μA]	Frequency [Hz]				ΔV [mV]	t_{Li^+}
			R_e^i [Ω]	R_e^f [Ω]	R_l^i [Ω]	R_l^f [Ω]		
PC4EO ₃ LiTFSA	5.095	1.300	3129	3198	10693	13429	10	0.14

Figure 3.17 Time dependence of DC polarization and corresponding Nyquist plots before and after polarization used to calculate the transference number for PC4EO_aLiTFSA ($a = 3$). EIS measurement was performed using the symmetric cell of [Li metal | polymer electrolyte | Li metal] at 70°C. The measured parameter and obtained transference number for PC4EO_aLiTFSA ($a = 3$) is summarized below the graph.

3.4. Conclusions

Details of the Li^+ coordination structure and its importance to the ionic conductivity of the PCEO electrolyte, consisting of a polyether having a nitrile group and a LiTFSA salt, were elucidated by combining molecular dynamics (MD) simulations and spectro(electro)chemical analyses. The estimated Li^+ coordination structure from both the MD simulation and infrared spectroscopy was in good agreement, which validates the proposed Li^+ coordination structure at various salt concentrations. The contribution of the nitrile group to Li^+ coordination decreased with an increase in salt concentration, while the contribution of ether oxygen remained relatively small throughout, compared to the typical polyether electrolytes. The distinctive suppression of ether coordination to Li^+ was responsible for (1) a slight decrease of T_g and (2) the characteristic high Li^+ transference number (>0.5) at the high salt concentration ($a > 3$). The importance of the Li^+ coordination structure to Li^+ conductivity was also emphasized; cocontribution of a nitrile group and ether oxygen to the Li^+ coordination structure is a key to accelerate the interchain Li^+ transfer involving a decoordination process (short-range Li^+ conduction) while maintaining good segmental mobility of the polymer (long-range Li^+ conduction). The nitrile group within the Li^+ coordination structure moderately stabilizes the Li^+ without overly holding onto the Li^+ , as well as providing free volume in the direct vicinity of the Li^+ coordination site, which promotes intermolecular coordination of Li^+ . The subsequent Li^+ transfer, involving the decoordination process, from one coordination site to another can be assisted by the existence of ether oxygen within the Li^+ coordination structure. The requirement for highly Li^+ -conductive polymer electrolytes thus fulfilled by designing the coordination structure consisting of the nitrile group and ether oxygen, which achieves the optimized stability of Li^+ within the coordination shell, at the same time, sustains polymer segmental mobility at high salt concentrations. This work provides a strategy to design the Li^+ coordination structure for efficient Li^+ transfer within the polymer electrolyte, which is crucial for the implementation of all-solid lithium-ion batteries.

References

1. Yamada, Y.; Furukawa, K.; Sodeyama, K.; Kikuchi, K.; Yaegashi, M.; Tateyama, Y.; Yamada, A. *J. Am. Chem. Soc.* **2014**, *136*, 5039–5046.
2. Sai, R.; Ueno, K.; Fujii, K.; Nakano, Y.; Shigaki, N.; Tsutsumi, H. *Phys. Chem. Chem. Phys.*, 2017, *19*, 5185–5194.
3. Sai, R.; Ueno, K.; Fujii, K.; Nakano, Y.; Tsutsumi, H. *RSC Adv.* **2017**, *7*, 37975–37982.
4. Shintani, Y.; Tsutsumi, H. *J. Power Sources* **2010**, *195*, 2863–2869.
5. Kubota, K.; Tamaki, K.; Nohira, T.; Goto, T.; Hagiwara, R. *Electrochim. Acta* **2010**, *55*, 1113–1119.
6. Zhang, C.; Ueno, K.; Yamazaki, A.; Yoshida, K.; Moon, H.; Mandai, T.; Umebayashi, Y.; Dokko, K.; Watanabe, M. *J. Phys. Chem. B*, **2014**, *118*, 5144–5153.
7. Evans, J.; Vincent, C. A.; Bruce, P. G. *Polymer* **1987**, *28*, 2324–2328.
8. Rosenwinkel, M. P.; Schönhoff, M. J. *Electrochem. Soc.* **2019**, *166*, A1977–A1983.
9. Abraham, K. M.; Jiang, Z.; Carroll, B. *Chem. Mater.* **1997**, *9*, 1978–1988.
10. Kamiyama, Y.; Shibata, M.; Kanzaki, R.; Fujii, K. *Phys. Chem. Chem. Phys.* **2020**, *22*, 5561–5567.
11. Cornell, W. D.; Cieplak, P.; Bayly, C. I.; Gould, I. R.; Merz, K. M.; Ferguson, D. M.; Spellmeyer, D. C.; Fox, T.; Caldwell, J. W.; Kollman, P. A. *J. Am. Chem. Soc.* **1995**, *117*, 5179–5197.
12. Price, M. L. P.; Ostrovsky, D.; Jorgensen, W. L. *J. Comput. Chem.* **2001**, *22*, 1340–1352.
13. Canongia Lopes, J. N.; Pádua, A. A. H. *J. Phys. Chem. B* **2006**, *110*, 19586–19592.
14. Soetens, J. C.; Millot, C.; Maigret, B. *J. Phys. Chem. A* **1998**, *102*, 1055–1061.
15. Sogawa, M.; Sawayama, S.; Han, J.; Satou, C.; Ohara, K.; Matsugami, M.; Mimura, H.; Morita, M.; Fujii, K., *J. Phys. Chem. C* **2019**, *123*, 8699–8708.
16. Song, J. Y.; Wang, Y. Y.; Wan, C. C. *J. Power Sources* **1999**, *77*, 183–197.
17. Meyer, W. H. *Adv. Mater.* **1998**, *10*, 439–448.
18. Yoshida, K.; Tsuchiya, M.; Tachikawa, N.; Dokko, K.; Watanabe, M. *J. Phys. Chem. C* **2011**, *115*, 18384–18394.
19. Costa, L.; Gad, A. M.; Camino, G.; Gordon Cameron, G.; Younus Qureshi, M. *Macromolecules* **1992**, *25*, 5512–5518.
20. Cabaleiro-Lago, E. M.; Ríos, M. A. *Chem. Phys.* **2000**, *254*, 11–23.
21. Kameda, Y.; Umebayashi, Y.; Takeuchi, M.; Wahab, M. A.; Fukuda, S.; Ishiguro, S. I.; Sasaki, M.; Amo, Y.; Usuki, T. *J. Phys. Chem. B* **2007**, *111*, 6104–6109.
22. Henderson, W. A.; Brooks, N. R.; Young, V. G. *J. Am. Chem. Soc.* **2003**, *125*, 12098–12099.
23. Seo, D. M.; Reininger, S.; Kutcher, M.; Redmond, K.; Euler, W. B.; Lucht, B. L. *J. Phys. Chem. C* **2015**, *119*, 14038–14046.
24. Borodin, O.; Smith, G. D. *Macromolecules* **2006**, *39*, 1620–1629.
25. Ohtomo, N.; Arakawa, K. *Bull. Chem. Soc. Jpn.* **1979**, *52*, 2755–2759.
26. Bruce, P. G. *Electrochim. Acta* **1995**, *40*, 2077–2085.
27. Hayashi, S.; Ozawa, R.; Hamaguchi, H. O. *Chem. Lett.* **2003**, *32*, 498–499.

28. Saha, S.; Hayashi, S.; Kobayashi, A.; Hamaguchi, H. O. *Chem. Lett.* **2003**, *32*, 740–741.
29. Ozawa, R.; Hayashi, S.; Saha, S.; Kobayashi, A.; Hamaguchi, H. O. *Chem. Lett.* **2003**, *32*, 948–949.
30. Holbrey, J. D.; Reichert, W. M.; Nieuwenhuyzen, M.; Johnson, S.; Seddon, K. R.; Rogers, R. D. *Chem. Commun.* **2003**, *3*, 1636–1637.
31. Tong, J.; Wu, S.; von Solms, N.; Liang, X.; Huo, F.; Zhou, Q.; He, H.; Zhang, S. *Front. Chem.* **2020**, *7*, 1–10.
32. Lesch, V.; Li, Z.; Bedrov, D.; Borodin, O.; Heuer, A. *Phys. Chem. Chem. Phys.* **2016**, *18*, 382–392.
33. Monteiro, M. J.; Bazito, F. F. C.; Siqueira, L. J. A.; Ribeiro, M. C. C.; Torresi, R. M. *J. Phys. Chem. B* **2008**, *112*, 2102–2109.
34. Umabayashi, Y.; Mitsugi, T.; Fukuda, S.; Fujimori, T.; Fujii, K.; Kanzaki, R.; Takeuchi, M.; Ishiguro, S. I. *J. Phys. Chem. B* **2007**, *111*, 13028–13032.
35. Molinari, N.; Mailoa, J. P.; Kozinsky, B. *Chem. Mater.* **2018**, *30*, 6298–6306.
36. Boden, N.; Leng, S. A.; Ward, I. M. *Solid State Ionics* **1991**, *45*, 261–270.
37. Angell, C. A. *Solid State Ionics* **1983**, *9–10*, 3–16.
38. Brooks, D. J.; Merinov, B. V.; Goddard, W. A.; Kozinsky, B.; Mailoa, J. *Macromolecules* **2018**, *51*, 8987–8995.
39. Pesko, D. M.; Jung, Y.; Hasan, A. L.; Webb, M. A.; Coates, G. W.; Miller, T. F., III; Balsara, N. P. *Solid State Ionics* **2016**, *289*, 118–124.
40. Ebadi, M.; Eriksson, T.; Mandal, P.; Costa, L. T.; Araujo, C. M.; Mindemark, J.; Brandell, D. *Macromolecules* **2020**, *53*, 764–774.
41. Isa, K. B. M.; Osman, Z.; Arof, A. K.; Othman, L.; Zainol, N. H.; Samin, S. M.; Chong, W. G.; Kamarulzaman, N. *Solid State Ionics* **2014**, *268*, 288–293.
42. Garca-Coln, L. S.; Del Castillo, L. F.; Goldstein, P. *Phys. Rev. B* **1989**, *40*, 7040–7044.
43. Ye, Y.; Elabd, Y. A. *Polymer* **2011**, *52*, 1309–1317.
44. Karan, N. K.; Pradhan, O. K.; Thomas, R.; Natesan, B.; Katiyar, R. S. *Solid State Ionics* **2008**, *179*, 689–696.
45. Gray, F. M.; Vincent, C. A.; Kent, M. J. *Polym. Sci. Part B: Polym. Phys.* **1989**, *27*, 2011–2022.
46. Johansson, P.; Tegenfeldt, J.; Lindgren, J. *Polymer*, 2001, *42*, 6573–6577.
47. Borodin, O.; Smith, G. D.; Henderson, W. *J. Phys. Chem. B* **2006**, *110*, 16879–16886.
48. Łasińska, A. K.; Marzantowicz, M.; Dygaa, J. R.; Krok, F.; Florjańczyk, Z.; Tomaszewska, A.; Zygadło-Monikowska, E.; Zukowska, Z.; Lafont, U. *Electrochim. Acta* **2015**, *169*, 61–72.
49. Pesko, D. M.; Timachova, K.; Bhattacharya, R.; Smith, M. C.; Villaluenga, I.; Newman, J.; Balsara, N. P. *J. Electrochem. Soc.* **2017**, *164*, E3569–E3575.
50. Villaluenga, I.; Pesko, D. M.; Timachova, K.; Feng, Z.; Newman, J.; Srinivasan, V.; Balsara, N. P. *J. Electrochem. Soc.* **2018**, *165*, A2766–A2773.
51. Huang, B.; Wang, Z.; Chen, L.; Xue, R.; Wang, F. *Solid State Ionics* **1996**, *91*, 279–284.
52. Teran, A. A.; Mullin, S. A.; Hallinan, D. T.; Balsara, N. P. *ACS Macro Lett.* **2012**, *1*, 305–309.



**YAMAGUCHI
UNIVERSITY**

Chapter 4

Effect of alkyl side chain length on the lithium-ion conductivity for polyether electrolytes: importance of lithium-ion coordination structure

4.1. Introduction

Designing the steric effect of the alkyl chain is one of the potential strategies to control the coordination structure within the PEs. Redfern *et al.* compared the coordination structures of PEO and poly(tetramethylene oxide) (PTMO) and clarified that steric crowding around lithium-ion for PTMO electrolyte decreased the stability of the coordination structure.¹ However, changing the steric effect of the alkyl chain also affects physicochemical properties, including dielectric constant, internal free volume, and hydrophobicity, which affect the salt dissociability,² polymer segmental mobility,³ and lithium-ion conduction pathway,^{4,5} respectively. Therefore, in order to establish the polymer design strategy based on the fine-tuning of the alkyl chain length, it is essential to clarify the effect of the alkyl chain on the various physicochemical properties, including the coordination structure.

In this study, I investigated the influence of the alkyl side chain on the coordination structure around lithium-ion and ether groups, as well as the lithium-ion transport properties for polyether electrolytes. I systematically compared model polymers with varied alkyl side chain length, poly(3-ethyl-3-(*alkyl*)oxymethyloxetane) (*alkyl*; methyl, ethyl, butyl, hexyl, octyl, and dodecyl, described as PC_mEO, $m = 1, 2, 4, 6, 8,$ and 12) (Figure 4.1), in order to establish a simple and effective polymer design strategy based on the tuning of the alkyl side chain. The length of the alkyl side chain affects the stability of the lithium coordination structure; the electrolyte with a short alkyl side chain ($m = 1$) formed the stable coordination structure due to the multiple interaction between ether groups and lithium-ion. Relatively large steric hindrance of the alkyl side chain ($m = 2-12$) effectively suppressed the interaction between ether oxygen and lithium-ion, which slightly destabilized the lithium coordination structure and improved the segmental mobility as well as the activation energy of lithium-ion transfer at the electrode-electrolyte interface. Polymer segmental mobility was also improved with the extension of the alkyl side chain due to the internal plasticizing effect. The

dielectric constant of the polymers decreased by extending the non-polar alkyl side chain, reducing the salt dissociability. Lithium-ion transference number increased with the extension of the alkyl side chain, indicating the effective suppression of the bulky anion transfer by its steric hindrance. In addition, the space between well-aligned alkyl side chains ($m = 12$) can be act as a rapid lithium-ion pathway, leading to the high lithium-ion conductivity of $2.94 \times 10^{-6} \text{ S cm}^{-1}$ at 70°C . The results highlight that the alkyl side chain length dictates critical factors determining lithium-ion conductivity, such as lithium transfer energetics both in bulk and at the electrode-electrolyte interface, polymer segmental mobility, and salt dissociability. The precise tuning of an alkyl side chain thus can be a simple and effective design strategy to improve the PE properties required for realizing safe and high-performance all-solid rechargeable battery technologies.

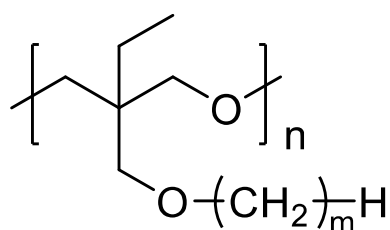


Figure 4.1 The structure of matrix polymer, PC m EO ($m = 1, 2, 4, 6, 8,$ and 12).

4.2. Experimental section

4.2.1. Preparation of polymers

Poly(3-ethyl-3-(*alkyl*)oxymethyloxetane), PCmEO, having an alkyl side chain with various lengths ($m = 1, 2, 4, 6, 8,$ and 12) was used in this study (Figure 4.1). PCmEO was synthesized based on previous studies.^{6,7} The monomers of PCmEO, CmEO, were synthesized from the coupling of 3-ethyl-3-hydroxymethyloxetane (EHO) and alkyl compounds modified with leaving groups, in base solution (Figure 4.2a). Prepared CmEO was polymerized by a ring-opening cationic polymerization (ROCP) using the cationic initiator, $\text{BF}_3\text{-OEt}_2$, in the solvent of 1,2-dichloroethane (Figure 4.2b).

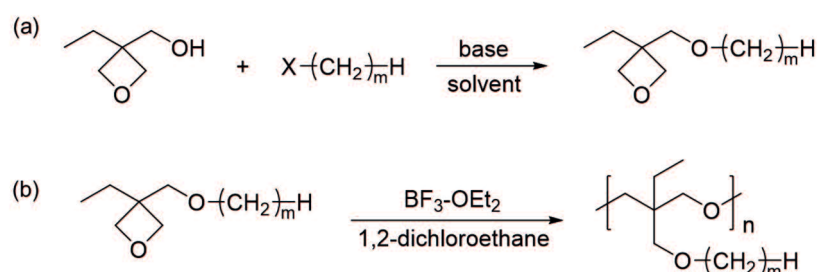


Figure 4.2 (a) Synthesis of 3-ethyl-3-(*alkyl*)oxymethyloxetane (CmEO, $m = 1, 2, 4, 6, 8,$ and 12). X stands for the following leaving groups; iodo, bromo, or methanesulfonyl group. (b) Polymerization of CmEO ($m = 1, 2, 4, 6, 8,$ and 12).

($m = 1$) 3-ethyl-3-methyloxymethyloxetane (C1EO) was synthesized from EHO (8.75 mL, 0.075 mol), iodomethane (6.23 mL, 0.10 mol), and 40–60wt% sodium hydride (4.11 g, 0.10 mol). Sodium hydride dispersed in mineral oil was washed with hexane prior to use. Sodium hydride and EHO were dissolved in 150 mL of tetrahydrofuran (THF) at room temperature under an argon atmosphere, subsequently heated to 50°C to activate EHO. Iodomethane was then added to the activated EHO solution and refluxed overnight for Williamson-ether reaction. THF in the obtained mixture was removed using a rotary evaporator, subsequently diluted with dichloromethane, and washed with water. The obtained organic extract was dehydrated with magnesium sulfate, followed by the removal of dichloromethane by distillation. The residue was distilled under reduced pressure (150°C , 150–200 hPa) by Kugelrohr. Yield: 6.17 g, 63.2%.

C1EO (1.92 mL, 0.015 mol) and the initiator (37.9 μ L, 0.30 mmol) were dissolved in 1,2-dichloroethane (DCE) (total volume: 5 mL). The polymerization was performed at 0°C for 3 h under an argon atmosphere. The reaction was quenched with the addition of aqueous 4 M NaCl/1 M NaOH (5 mL), and the reaction mixture was subsequently added to dichloromethane and washed with water. After removing dichloromethane using a rotary evaporator, the residue was dissolved in a small amount of THF. The solution was poured into a large amount of methanol to precipitate the polymerized C1EO (PC1EO). The resulting polymer was collected by decantation and dried at 130°C under vacuum for overnight. Yield: 1.60 g, 81.9%, colorless crystal.

C1EO ^1H NMR (δ , ppm from tetramethylsilane (TMS) in CDCl_3): 0.89 (t, 3H, $J = 7.3$ Hz, $-\text{CH}_2-\text{CH}_3$), 1.74 (q, 2H, $J = 7.3$ Hz, $-\text{CH}_2-\text{CH}_3$), 3.40 (s, 3H, $-\text{O}-\text{CH}_3$), 3.51 (s, 2H, $-\text{CH}_2-\text{O}-\text{CH}_3$), 4.42 (dd, 4H, $J = 32.0$ Hz, 5.8 Hz, ring, $-\text{CH}_2-\text{O}-\text{CH}_2-$).

C1EO ^{13}C NMR (δ , ppm from CDCl_3 (77.0 ppm)): 7.99 ($-\text{CH}_2-\text{CH}_3$), 26.54 ($-\text{CH}_2-\text{CH}_3$), 43.15 ($>\text{C}<$), 59.14 ($-\text{O}-\text{CH}_3$), 73.30 ($-\text{CH}_2-\text{O}-\text{CH}_3$), 78.27 ($-\text{CH}_2-\text{O}-\text{CH}_2-$).

PC1EO ^1H NMR (δ , ppm from TMS in CDCl_3): 0.84 (t, 3H, $J = 7.5$ Hz, $-\text{CH}_2-\text{CH}_3$), 1.38 (q, 2H, $J = 7.3$ Hz, $-\text{CH}_2-\text{CH}_3$), 3.19 (s, 4H, $-\text{CH}_2-\text{O}-\text{CH}_2-$), 3.23 (s, 2H, $-\text{CH}_2-\text{O}-\text{CH}_3$), 3.29 (s, 3H, $-\text{O}-\text{CH}_3$).

($m = 2$) 3-ethyl-3-ethyloxymethyloxetane (C2EO) was synthesized from EHO (8.75 mL, 0.075 mol), bromoethane (7.46 mL, 0.10 mol) and 40–60wt% sodium hydride (4.00 g, 0.10 mol). Sodium hydride dispersed in mineral oil was washed with hexane prior to use. Sodium hydride and EHO were dissolved in 150 mL of THF at room temperature under argon atmosphere, subsequently heated to 50°C to activate EHO. Bromoethane was then added to the activated EHO solution and refluxed overnight for Williamson-ether reaction. THF in the obtained mixture was removed using a rotary evaporator, subsequently diluted with dichloromethane, and washed with water. The obtained organic extract was dehydrated with magnesium sulfate, followed by the removal of dichloromethane. The distillate residue was applied to a silica column (eluent = ethyl acetate: hexane, 5: 5 (vol)). After removing the eluent by distillation, the residue was distilled under reduced pressure (150°C, 280–240 hPa) by Kugelrohr. Yield: 3.70 g, 34.2%.

C2EO (3.15 mL, 0.020 mol) and the initiator (50.2 μ L, 0.40 mmol) were dissolved in DCE (total volume: 5 mL). The polymerization was performed at 0°C for 4 h under an argon atmosphere. The reaction was quenched with the addition of aqueous 4 M NaCl/1 M NaOH

(5 mL), and the reaction mixture was subsequently added to chloroform and washed with water. After removing chloroform using a rotary evaporator, the residue was dissolved in a small amount of THF. The solution was poured into a large amount of methanol to precipitate the polymerized C2EO (PC2EO). The resulting polymer was collected by decantation and dried at 100°C under vacuum for overnight. Yield: 2.06 g, 71.4%, cloudy white solid.

C2EO ¹H NMR (δ, ppm from TMS in CDCl₃): 0.89 (t, 3H, *J* = 7.3 Hz, ≥C-CH₂-CH₃), 1.21 (t, 3H, *J* = 7.0 Hz, -O-CH₂-CH₃), 1.75 (q, 2H, *J* = 7.3 Hz, ≥C-CH₂-CH₃), 3.53 (q, 2H, *J* = 7.2 Hz, -O-CH₂-CH₃), 3.54 (s, 2H, -CH₂-O-CH₂-CH₃) 4.43 (dd, 4H, *J* = 31.3 Hz, 5.8 Hz, ring, ≥C-CH₂-O-CH₂-C≤).

C2EO ¹³C NMR (δ, ppm from CDCl₃ (77.0 ppm)): 8.08 (≥C-CH₂-CH₃), 14.94 (-O-CH₂-CH₃), 26.60 (≥C-CH₂-CH₃), 43.23 (>C<), 66.72 (-O-CH₂-CH₃), 73.02 (-CH₂-O-CH₂-CH₃), 78.51 (≥C-CH₂-O-CH₂-C≤).

PC2EO ¹H NMR (δ, ppm from TMS in CDCl₃): 0.83 (t, 3H, *J* = 7.5 Hz, ≥C-CH₂-CH₃), 1.15 (t, 3H, *J* = 6.8 Hz, -O-CH₂-CH₃), 1.38 (q, 2H, *J* = 7.5 Hz, ≥C-CH₂-CH₃), 3.20 (s, 4H, ≥C-CH₂-O-CH₂-C≤), 3.25 (s, 2H, -CH₂-O-CH₂-CH₃), 3.42 (q, 2H, *J* = 7.2 Hz, -O-CH₂-CH₃).

(*m* = 4) Butyl methanesulfonate (BuOMs) was synthesized from butanol (22.9 mL, 0.25 mol) and methanesulfonyl chloride (19.3 mL, 0.25 mol). Butanol and methanesulfonyl chloride were dissolved in co-solvent consist of 104 mL of triethylamine and 200 mL of dichloromethane, subsequently stirred for 5 h at 0°C for the butanol mesylation. The reaction mixture was washed with water and aqueous 1M HCl. The obtained organic extract was dehydrated with magnesium sulfate, followed by the removal of dichloromethane by distillation. Yield: 31.86 g, 83.7%.

3-ethyl-3-butyloxymethyloxetane (C4EO) was synthesized from EHO (10.10 mL, 0.087 mol), BuOMs (9.93 mL, 0.072 mol), and 40–60wt% sodium hydride (4.12 g, 0.10 mol). Sodium hydride dispersed in mineral oil was washed with hexane prior to use. Sodium hydride, EHO, and BuOMs were dissolved in 150 mL of THF at room temperature under argon atmosphere, subsequently heated to 50°C, and refluxed overnight for Williamson-ether reaction. THF in the obtained mixture was removed using a rotary evaporator, subsequently diluted with dichloromethane, and washed with water. The obtained organic extract was dehydrated with magnesium sulfate, followed by the removal of dichloromethane by distillation. The residue was distilled under reduced pressure (150°C, 200–150 hPa) by Kugelrohr. Yield: 9.40 g, 75.6%.

C4EO (3.82 mL, 0.020 mol) and the initiator (50.2 μ L, 0.40 mmol) were dissolved in DCE (total volume: 5 mL). The polymerization was performed at 0°C for 3 h under argon atmosphere. The reaction was quenched with the addition of aqueous 4 M NaCl/1 M NaOH (5 mL), and the reaction mixture was subsequently added to chloroform and washed with water. After removing chloroform using a rotary evaporator, the residue was dissolved in a small amount of THF. The solution was poured into a large amount of 2-propanol to precipitate the polymerized C4EO (PC4EO). The resulting polymer was collected by decantation and dried at 130°C under vacuum for overnight. Yield: 2.51 g, 72.9%, colorless, highly viscous liquid.

BuOMs ^1H NMR (δ , ppm from TMS in CDCl_3): 0.95 (t, 3H, $J = 7.3$ Hz, $-\text{CH}_2-\text{CH}_3$), 1.44 (sext., 2H, $J = 7.3$ Hz, $-\text{CH}_2-\text{CH}_3$), 1.73 (quin., 2H, $J = 7.3$ Hz, $-\text{CH}_2-\text{CH}_2-\text{CH}_3$), 3.02 (s, 3H, $-\text{SO}_2-\text{CH}_3$), 4.24 (t, 2H, $J = 6.7$ Hz, $-\text{O}-\text{CH}_2-$).

C4EO ^1H NMR (δ , ppm from TMS in CDCl_3): 0.92 (m, 6H, $\geq\text{C}-\text{CH}_2-\text{CH}_3$, $-\text{CH}_2-\text{CH}_2-\text{CH}_3$), 1.37 (sext., 2H, $J = 6.7$ Hz, $-\text{CH}_2-\text{CH}_2-\text{CH}_3$), 1.56 (quin., 2H, $J = 6.7$ Hz, $-\text{CH}_2-\text{CH}_2-\text{CH}_2-$), 1.74 (q, 2H, $J = 7.3$ Hz, $\geq\text{C}-\text{CH}_2-\text{CH}_3$), 3.46 (t, 2H, $J = 6.7$ Hz, $-\text{O}-\text{CH}_2-\text{CH}_2-$), 3.53 (s, 2H, $-\text{CH}_2-\text{O}-\text{CH}_2-\text{CH}_2-$), 4.39 (dd, 4H, $J = 34.8$ Hz, 6.1 Hz, ring, $\geq\text{C}-\text{CH}_2-\text{O}-\text{CH}_2-\text{C}\leq$).

C4EO ^{13}C NMR (δ , ppm from CDCl_3 (77.0 ppm)): 8.19 ($\geq\text{C}-\text{CH}_2-\text{CH}_3$), 13.90 ($-\text{CH}_2-\text{CH}_2-\text{CH}_3$), 19.32 ($-\text{CH}_2-\text{CH}_2-\text{CH}_3$), 26.71 ($\geq\text{C}-\text{CH}_2-\text{CH}_3$), 31.64 ($-\text{CH}_2-\text{CH}_2-\text{CH}_2-$), 43.40 ($>\text{C}<$), 71.30 ($-\text{O}-\text{CH}_2-\text{CH}_2-$), 73.34 ($-\text{CH}_2-\text{O}-\text{CH}_2-\text{CH}_2-$), 78.63 ($\geq\text{C}-\text{CH}_2-\text{O}-\text{CH}_2-\text{C}\leq$).

PC4EO ^1H NMR (δ , ppm from TMS in CDCl_3): 0.83 (t, 3H, $J = 7.5$ Hz, $\geq\text{C}-\text{CH}_2-\text{CH}_3$), 0.91 (t, 3H, $J = 7.5$ Hz, $-\text{CH}_2-\text{CH}_2-\text{CH}_3$), 1.32–1.40 (m, 4H, $\geq\text{C}-\text{CH}_2-\text{CH}_3$, $-\text{CH}_2-\text{CH}_2-\text{CH}_3$), 1.51 (quin., 2H, $J = 7.0$ Hz, $-\text{O}-\text{CH}_2-\text{CH}_2-$), 3.19 (s, 4H, $\geq\text{C}-\text{CH}_2-\text{O}-\text{CH}_2-\text{C}\leq$), 3.24 (s, 2H, $-\text{CH}_2-\text{O}-\text{CH}_2-\text{CH}_2-$), 3.35 (t, 2H, $J = 6.8$ Hz, $-\text{O}-\text{CH}_2-\text{CH}_2-$).

($m = 6$) 3-ethyl-3-hexyloxymethyloxetane (C6EO) was synthesized from EHO (5.70 mL, 0.050 mol), 1-bromohexane (6.96 mL, 0.050 mol), and tetrabutylammonium bromide (TBAB) (1.62 g, 0.0050 mol). EHO, 1-bromohexane and TBAB were dissolved in co-solvent consist of 250 mL of toluene and 250 mL of aqueous 40wt% NaOH. The solution refluxed overnight at 60°C with a strong stir for Williamson-ether reaction. The obtained reaction mixture washed with water, subsequently dehydrated with magnesium sulfate, and then toluene was removed by distillation. The residue was distilled under reduced pressure (100°C, 1.3 hPa) by Kugelrohr. Yield: 5.90 g, 58.9%.

C6EO (3.21 mL, 0.014 mol) and the initiator (40.0 μ L, 0.32 mmol) were dissolved in DCE (total volume: 4.5 mL). The polymerization was performed at 0°C for 3 h under an argon atmosphere. The reaction was quenched with the addition of aqueous 4 M NaCl/1 M NaOH (5 mL), and the reaction mixture was subsequently added to chloroform and washed with water. After removing chloroform using a rotary evaporator, the residue was dissolved in a small amount of THF. The solution was poured into a large amount of 2-propanol to precipitate the polymerized C6EO (PC6EO). The resulting polymer was collected by decantation and dried at 130°C under vacuum for 1.5 days. Yield: 2.30 g, 80.3%, colorless, highly viscous liquid.

C6EO ^1H NMR (δ , ppm from TMS in CDCl_3): 0.85–0.93 (m, 6H, $\geq\text{C}-\text{CH}_2-\text{CH}_3$, $-\text{CH}_2-\text{CH}_2-\text{CH}_3$), 1.24–1.38 (m, 6H, $-\text{CH}_2-\text{CH}_2-\text{CH}_2-\text{CH}_3$), 1.57 (quin., 2H, $-J = 6.7$ Hz, $-\text{O}-\text{CH}_2-\text{CH}_2-$), 1.74 (q, 2H, $J = 7.3$ Hz, $\geq\text{C}-\text{CH}_2-\text{CH}_3$), 3.45 (t, 2H, $J = 6.7$ Hz, $-\text{O}-\text{CH}_2-\text{CH}_2-$), 3.52 (s, 2H, $-\text{CH}_2-\text{O}-\text{CH}_2-\text{CH}_2-$) 4.39 (dd, 4H, $J = 34.3$ Hz, 6.1 Hz, ring, $\geq\text{C}-\text{CH}_2-\text{O}-\text{CH}_2-\text{C}\leq$).

C6EO ^{13}C NMR (δ , ppm from CDCl_3 (77.0 ppm)): 8.17 ($\geq\text{C}-\text{CH}_2-\text{CH}_3$), 14.09 ($-\text{CH}_2-\text{CH}_2-\text{CH}_3$), 22.59 ($-\text{CH}_2-\text{CH}_2-\text{CH}_3$), 26.70 ($\geq\text{C}-\text{CH}_2-\text{CH}_3$), 29.19 ($-\text{CH}_2-\text{CH}_2-\text{CH}_2-\text{CH}_3$), 29.46 ($-\text{CH}_2-\text{CH}_2-\text{CH}_3$), 31.62 ($-\text{O}-\text{CH}_2-\text{CH}_2-$), 43.37 ($>\text{C}<$), 71.61 ($-\text{O}-\text{CH}_2-\text{CH}_2-$), 73.32 ($-\text{CH}_2-\text{O}-\text{CH}_2-\text{CH}_2-$), 78.62 ($\geq\text{C}-\text{CH}_2-\text{O}-\text{CH}_2-\text{C}\leq$).

PC6EO ^1H NMR (δ , ppm from TMS in CDCl_3): 0.83 (t, 3H, $-J = 7.5$ Hz, $\geq\text{C}-\text{CH}_2-\text{CH}_3$), 0.89 (t, 3H, $-J = 6.5$ Hz, $-\text{CH}_2-\text{CH}_2-\text{CH}_3$), 1.26–1.33 (m, 6H, $-\text{CH}_2-\text{CH}_2-\text{CH}_2-\text{CH}_3$), 1.38 (q, 2H, $J = 7.3$ Hz, $\geq\text{C}-\text{CH}_2-\text{CH}_3$), 1.52 (quin., 2H, $J = 6.9$ Hz, $-\text{O}-\text{CH}_2-\text{CH}_2-$), 3.19 (s, 4H, $\geq\text{C}-\text{CH}_2-\text{O}-\text{CH}_2-\text{C}\leq$), 3.24 (s, 2H, $-\text{CH}_2-\text{O}-\text{CH}_2-\text{CH}_2-$), 3.34 (t, 2H, $J = 6.8$ Hz, $-\text{O}-\text{CH}_2-\text{CH}_2-$).

($m = 8$) 3-ethyl-3-octyloxymethyloxetane (C8EO) was synthesized from EHO (6.84 mL, 0.070 mol), 1-bromooctane (8.64 mL, 0.050 mol), and TBAB (1.62 g, 0.0050 mol). EHO, 1-bromooctane, and TBAB were dissolved in co-solvent consist of 200 mL of toluene and 200 mL of aqueous 40wt% NaOH. The solution refluxed for 3 days at 70°C with a strong stir for Williamson-ether reaction. The obtained reaction mixture washed with water, subsequently dehydrated with magnesium sulfate, and then toluene was removed by distillation. The residue was distilled under reduced pressure (150°C, 5.3 hPa) by Kugelrohr. Yield: 4.02 g, 35.2%.

C8EO (4.09 mL, 0.016 mol) and the initiator (40.0 μ L, 0.32 mmol) were dissolved in DCE (total volume: 5.0 mL). The polymerization was performed at 0°C for 4 h under an argon atmosphere. The reaction was quenched with the addition of aqueous 4 M NaCl/1 M

NaOH (5 mL), and the reaction mixture was subsequently added to dichloromethane and washed with water. After removing dichloromethane using a rotary evaporator, the residue was dissolved in a small amount of THF. The solution was poured into a large amount of 2-propanol to precipitate the polymerized C8EO (PC8EO). The resulting polymer was collected by decantation and dried at 100°C under vacuum for overnight. Yield: 2.33 g, 63.7%, colorless, highly viscous liquid.

C8EO ^1H NMR (δ , ppm from TMS in CDCl_3): 0.85–0.93 (m, 6H, $\geq\text{C}-\text{CH}_2-\text{CH}_3$, $-\text{CH}_2-\text{CH}_2-\text{CH}_3$), 1.22–1.37 (m, 10H, $-\text{CH}_2-\text{CH}_2-\text{CH}_2-\text{CH}_2-\text{CH}_2-\text{CH}_3$), 1.57 (quin., 2H, $J = 6.7$ Hz, $-\text{O}-\text{CH}_2-\text{CH}_2-$), 1.74 (q, 2H, $J = 7.3$ Hz, $\geq\text{C}-\text{CH}_2-\text{CH}_3$), 3.44 (t, 2H, $J = 6.7$ Hz, $-\text{O}-\text{CH}_2-\text{CH}_2-$), 3.52 (s, 2H, $-\text{CH}_2-\text{O}-\text{CH}_2-\text{CH}_2-$) 4.38 (dd, 4H, $J = 34.3$ Hz, 6.1 Hz, ring, $\geq\text{C}-\text{CH}_2-\text{O}-\text{CH}_2-\text{C}\leq$).

C8EO ^{13}C NMR (δ , ppm from CDCl_3 (77.0 ppm)): 8.19 ($\geq\text{C}-\text{CH}_2-\text{CH}_3$), 14.06 ($-\text{CH}_2-\text{CH}_2-\text{CH}_3$), 22.62 ($-\text{CH}_2-\text{CH}_2-\text{CH}_3$), 26.10 ($-\text{O}-\text{CH}_2-\text{CH}_2-\text{CH}_2-$), 26.70 ($\geq\text{C}-\text{CH}_2-\text{CH}_3$), 29.25 ($-\text{O}-\text{CH}_2-\text{CH}_2-\text{CH}_2-\text{CH}_2-$), 29.38 ($-\text{CH}_2-\text{CH}_2-\text{CH}_2-\text{CH}_3$), 29.50 ($-\text{CH}_2-\text{CH}_2-\text{CH}_3$), 31.80 ($-\text{O}-\text{CH}_2-\text{CH}_2-$), 43.37 ($>\text{C}\leq$), 71.61 ($-\text{O}-\text{CH}_2-\text{CH}_2-$), 73.32 ($-\text{CH}_2-\text{O}-\text{CH}_2-\text{CH}_2-$), 78.61 ($\geq\text{C}-\text{CH}_2-\text{O}-\text{CH}_2-\text{C}\leq$).

PC8EO ^1H NMR (δ , ppm from TMS in CDCl_3): 0.83 (t, 3H, $J = 7.5$ Hz, $\geq\text{C}-\text{CH}_2-\text{CH}_3$), 0.88 (t, 3H, $J = 6.5$ Hz, $-\text{CH}_2-\text{CH}_2-\text{CH}_3$), 1.24–1.33 (m, 10H, $-\text{CH}_2-\text{CH}_2-\text{CH}_2-\text{CH}_2-\text{CH}_2-\text{CH}_3$), 1.38 (q, 2H, $J = 7.2$ Hz, $\geq\text{C}-\text{CH}_2-\text{CH}_3$), 1.52 (quin., 2H, $J = 6.8$ Hz, $-\text{O}-\text{CH}_2-\text{CH}_2-$), 3.19 (s, 4H, $\geq\text{C}-\text{CH}_2-\text{O}-\text{CH}_2-\text{C}\leq$), 3.24 (s, 2H, $-\text{CH}_2-\text{O}-\text{CH}_2-\text{CH}_2-$), 3.33 (t, 2H, $J = 6.3$ Hz, $-\text{O}-\text{CH}_2-\text{CH}_2-$).

($m = 12$) 3-ethyl-3-dodecyloxymethyloxetane (C12EO) was synthesized from EHO (6.84 mL, 0.070 mol), 1-Iododecane (10.74 mL, 0.050 mol), and 40–60wt% sodium hydride (3.37 g, 0.070 mol). Sodium hydride dispersed in mineral oil was washed with hexane prior to use. Sodium hydride and EHO were dissolved in 400 mL of THF at room temperature under argon atmosphere, subsequently heated to 60°C to activate EHO. 1-Iododecane was then added to the activated EHO solution and refluxed for 1 day for Williamson-ether reaction. THF in the obtained mixture was removed using a rotary evaporator, subsequently diluted with chloroform, and washed with water. The obtained organic extract was dehydrated with magnesium sulfate, followed by the removal of chloroform by distillation. The distilled residue was applied to a silica column (eluent = ethyl acetate: hexane, 1: 9 (vol)), and then the eluent was removed by distillation. Yield: 5.60 g, 39.4%.

C12EO (5.64 mL, 0.016 mol) and the initiator (40.0 μL , 0.32 mmol) were dissolved in DCE (total volume: 5.0 mL). The polymerization was performed at 0°C for 2 days under an

argon atmosphere. The reaction was quenched with the addition of aqueous 4 M NaCl/1 M NaOH (5 mL), and the reaction mixture was subsequently added to dichloromethane and washed with water. After removing dichloromethane using a rotary evaporator, the residue was dissolved in a small amount of THF. The solution was poured into a large amount of 2-propanol to precipitate the polymerized C12EO (PC12EO). The resulting polymer was collected by decantation and dried at 100°C under vacuum for overnight. Yield: 2.35 g, 51.6%, colorless, highly viscous liquid.

C12EO ^1H NMR (δ , ppm from TMS in CDCl_3): 0.86–0.91 (m, 6H, $\geq\text{C}-\text{CH}_2-\text{CH}_3$, $-\text{CH}_2-\text{CH}_2-\text{CH}_3$), 1.21–1.36 (m, 18H, $-\text{CH}_2-\text{CH}_2-\text{CH}_2-\text{CH}_2-\text{CH}_2-\text{CH}_2-\text{CH}_2-\text{CH}_2-\text{CH}_2-\text{CH}_3$), 1.57 (quin., 2H, $-J = 6.7$ Hz, $-\text{O}-\text{CH}_2-\text{CH}_2-$), 1.74 (q, 2H, $J = 7.3$ Hz, $\geq\text{C}-\text{CH}_2-\text{CH}_3$), 3.45 (t, 2H, $J = 6.7$ Hz, $-\text{O}-\text{CH}_2-\text{CH}_2-$), 3.52 (s, 2H, $-\text{CH}_2-\text{O}-\text{CH}_2-\text{CH}_2-$) 4.39 (dd, 4H, $J = 34.3$ Hz, 6.1 Hz, ring, $\geq\text{C}-\text{CH}_2-\text{O}-\text{CH}_2-\text{C}\leq$).

C12EO ^{13}C NMR (δ , ppm from CDCl_3 (77.0 ppm)): 8.16 ($\geq\text{C}-\text{CH}_2-\text{CH}_3$), 14.09 ($-\text{CH}_2-\text{CH}_2-\text{CH}_3$), 22.66 ($-\text{CH}_2-\text{CH}_2-\text{CH}_3$), 26.10 ($-\text{O}-\text{CH}_2-\text{CH}_2-\text{CH}_2-$), 26.70 ($\geq\text{C}-\text{CH}_2-\text{CH}_3$), 29.51 ($-\text{CH}_2-\text{CH}_2-\text{CH}_2-\text{CH}_2-\text{CH}_2-\text{CH}_2-\text{CH}_2-\text{CH}_2-\text{CH}_3$), 31.89 ($-\text{O}-\text{CH}_2-\text{CH}_2-\text{CH}_2-$), 43.37 ($>\text{C}\leq$), 71.62 ($-\text{O}-\text{CH}_2-\text{CH}_2-$), 73.33 ($-\text{CH}_2-\text{O}-\text{CH}_2-\text{CH}_2-$), 78.61 ($\geq\text{C}-\text{CH}_2-\text{O}-\text{CH}_2-\text{C}\leq$).

PC12EO ^1H NMR (δ , ppm from TMS in CDCl_3): 0.83 (t, 3H, $-J = 7.3$ Hz, $\geq\text{C}-\text{CH}_2-\text{CH}_3$), 0.88 (t, 3H, $-J = 6.8$ Hz, $-\text{CH}_2-\text{CH}_2-\text{CH}_3$), 1.22–1.32 (m, 18H, $-\text{CH}_2-\text{CH}_2-\text{CH}_2-\text{CH}_2-\text{CH}_2-\text{CH}_2-\text{CH}_2-\text{CH}_2-\text{CH}_2-\text{CH}_3$), 1.37 (q, 2H, $J = 7.3$ Hz, $\geq\text{C}-\text{CH}_2-\text{CH}_3$), 1.52 (quin., 2H, $J = 6.6$ Hz, $-\text{O}-\text{CH}_2-\text{CH}_2-$), 3.18 (s, 4H, $\geq\text{C}-\text{CH}_2-\text{O}-\text{CH}_2-\text{C}\leq$), 3.23 (s, 2H, $-\text{CH}_2-\text{O}-\text{CH}_2-\text{CH}_2-$), 3.33 (t, 2H, $J = 6.5$ Hz, $-\text{O}-\text{CH}_2-\text{CH}_2-$).

4.2.2. Preparation of polymer electrolytes

PCmEO electrolytes were prepared by mixing the PCmEO and 1.0 M lithium bis(trifluoromethane sulfonyl)amide (LiTfSA) in tetrahydrofuran (THF) solution, subsequently heated under a vacuum to remove THF, which confirmed using infrared spectroscopy. The mixing ratio of polymer repeating unit and LiTfSA was set to 5. Prepared PEs are denoted as PCmEO-LiTfSA throughout the study.

4.2.3. Characterization methods

The structures of the synthesized compounds were identified using nuclear magnetic resonance (NMR) spectroscopy. The spectra of ^1H NMR and ^{13}C NMR were recorded with an FT-NMR spectrophotometer (JNM-LA-500, JEOL). The molecular weight of the

polymers was measured by a gel permeation chromatography (GPC) system (CBM-20A, LC-20AD, DGU-20A, CTO-20A, and RID-10A, Shimadzu) using THF as the elution solvent and polystyrene standards for the calibration of columns.

The concentration of the LiTFSA in polymer electrolytes was estimated from the reference density value for the LiTFSA melt¹ and the density of the monomer as polymer density. The monomer density was obtained from the mass ratio of each monomer and pure water with the same volume at room temperature (20–25°C). LiTFSA concentration in polymer electrolytes was calculated assuming no density change occurs when mixing the salt and polymers. The concentration was calculated by the following formula;

$$c_{\text{Li}} = \frac{(M_{\text{Li}})}{\left(\frac{w_{\text{Li}}}{\rho_{\text{Li}}}\right) + \left(\frac{w_{\text{p}}}{\rho_{\text{m}}}\right)}$$

c_{Li} is LiTFSA concentration in polymer electrolytes, M_{Li} is the molar number of LiTFSA in polymer electrolytes, w_{Li} is the total weight of LiTFSA in polymer electrolytes, w_{p} is the total weight of the polymer in polymer electrolytes, ρ_{Li} is the density of the LiTFSA melt (here, 1.97 g cm⁻³), and ρ_{m} is estimated polymer density from monomer density.

A differential thermogravimetric analyzer (Thermo Plus Evo II, RIGAKU) was used to determine the thermal decomposition temperature (T_{d}). A small amount of the pure polymers or PEs (~10 mg) was put on an aluminum pan. Pure polymer samples were heated from room temperature to 500°C at a heating rate of 20°C min⁻¹. Polymer electrolytes were first heated to 150°C and kept for 10 min and cooled to 50°C, and then heated again to 500°C at a heating rate of 20°C min⁻¹ to remove absorbed water within the PEs. The final heating scan was recorded as the thermogravimetry (TG) curve of the samples. Thermal decomposition temperature was determined as the intersection of the baseline and the diagonal line of the largest mass loss. Gas chromatography-mass spectrometry (GC-MS) was performed by gas chromatograph/mass spectrometer (GCMS-QP2010 Ultra, SHIMADZU) with double-shot pyrolyzer (PY-2020iD, Frontier Lab) and thermal desorption system (TD-20, SHIMADZU). A small amount of PC1EO-LiTFSA or PC12EO-LiTFSA (~ 0.6 mg) and quartz wool were put on a stainless-steel cup. The sample was first heated to 150°C and kept for 10 min, and then heated again to 600°C at a heating rate of 20°C min⁻¹.

A differential scanning calorimeter (DSC7020, HITACHI) was used to determine the glass transition temperature (T_g), crystallization temperature (T_c), and melting temperature (T_m). A small amount of the polymers or the PEs (~ 10 mg) was hermetically sealed in an aluminum DSC pan. The samples were first heated to 120°C and cooled to -100°C and then heated again to 120°C at a heating/cooling rate of 10°C min⁻¹ (for PC12EO and PC12EO-LiTFSa, the samples were cooled to -150°C). The second heating scan was recorded as the DSC thermogram of the samples. The thermal transition temperatures (T_g , T_c , and T_m) were determined as the intersection of the baseline and the diagonal lines of the second heat flow step.

Infrared (IR) spectra of the PEs were measured by a Fourier transform infrared spectrometer (Nicolet iS50, Thermo-Fisher Scientific) in the wavenumber range of 550–4000 cm⁻¹ with a resolution of 4 cm⁻¹. The measurements were performed by attenuated total reflection (ATR) configuration with ZnSe prism. The polymer electrolyte was sealed between the ATR stage and glass plate with the grease in an Ar-filled glove box to avoid moisture absorption. Raman spectra of the PEs were measured by a laser Raman spectrophotometer (MRS-3100, JASCO) equipped with a 532 nm laser. The polymer electrolyte was sealed between two glass plates having a rubber spacer (5 mm in thickness) in an Ar-filled glove box to avoid moisture absorption. Raman spectra were measured in the wavenumber range of 100–3000 cm⁻¹ with a resolution of 4 cm⁻¹. The spectra of IR and Raman were analyzed with a commercially available peak fitting software (PeakFit™ ver. 4.12, Seasolve Co.). A pseudo-Voigt function was used for the peak deconvolution.

4.2.4. Electrochemical measurements

Linear sweep voltammetry (LSV) and cyclic voltammetry (CV) were performed to study the electrochemical stability of the PEs. Each PCmEO-LiTFSa infiltrated in glass filter paper (GA-55, ADVANTEC) was placed between electrodes in a 2032-type cell. Linear sweep voltammograms were obtained using lithium metal foil as the counter and reference electrode, and a stainless-steel disk as the working electrode. Cyclic voltammograms were obtained using lithium metal foil as the counter and reference electrodes, and a nickel disk as the working electrode. The cell was stabilized by storing in a thermostat chamber (WFO-450ND,

EYELA) at 60°C for several days. Linear sweep voltammetry was performed from the open circuit potential to 7 V vs Li/Li⁺. The potential range was set to 2.5 to -0.5 V vs Li/Li⁺ for CV measurement. Linear sweep voltammetry and CV were carried out at a scan rate of 1 mV s⁻¹ with an electrochemical measurement system (HZ-5000 and HZ-7000, Hokuto Denko) at 70°C in a constant climate cabinet (LU-114, ESPEC).

The ionic conductivity of each PE was measured by electrochemical impedance spectroscopy using an SP-150 potentiogalvanostat (BioLogic). The polymer electrolyte was placed between two stainless-steel electrodes separated by a PTFE spacer, and the cell temperature was controlled from 20°C to 100°C with a constant climate cabinet (SU-242, ESPEC). All the measurements were performed after holding the temperature for at least 1 h. The diameter of the semicircles observed in the Nyquist plot (Figure 4.10) was defined as the electrolyte resistance (R_{Bulk}). The ionic conductivity (σ) was calculated with the following equation,

$$\sigma = \frac{l}{R_{\text{Bulk}} \cdot A} \quad (1)$$

where l and A are the thickness and the surface area of electrolyte, respectively.

The transference numbers of lithium-ion (t_{Li^+}) in the PEs were determined using the electrochemical method proposed by Bruce and Vincent.^{8,9} The required parameters were obtained using potentiostatic polarization and electrochemical impedance spectroscopy with a multi electrochemical measurement system (HZ-Pro S4, Hokuto Denko). The polymer electrolytes infiltrated in glass filter paper (GA-55, ADVANTEC) were placed between two lithium metal foil electrodes in a 2032-type cell. The cell was stored in a thermostat chamber (WFO-450ND, EYELA) at 60°C for several days for stabilization. Electrochemical impedance spectroscopy was performed before and after the potentiostatic polarization at 70°C in a constant climate cabinet (SU-222, ESPEC). The following equation gives the transference number of lithium-ion (t_{Li^+}),

$$t_{\text{Li}^+} = \frac{I_{\text{SS}} R_e^f (\Delta V - I_0 R_I^i)}{I_0 R_e^i (\Delta V - I_{\text{SS}} R_I^f)} \quad (2)$$

where ΔV is the applied potential ($\Delta V = 10$ mV), I_0 is the initial current of the potentiostatic polarization, I_{SS} is the steady-state current of the polarization, R_e^i is the electrolyte resistance before the polarization, and R_e^f is the steady-state electrolyte resistance during the polarization, R_i^i is the interfacial resistance before the polarization, and R_i^f is the steady-state interfacial resistance during the polarization.

Lithium-ion transfer resistance at the lithium metal electrode-polymer electrolyte interface was estimated by electrochemical impedance spectroscopy using a multi-electrochemical measurement system (HZ-Pro S4, Hokuto Denko). A lithium symmetric cell was used as in the t_{Li^+} measuring 2032-type cell. The cell temperature was raised from 60°C to 80°C in a constant climate cabinet (SU-222, ESPEC) and kept for at least 1 h at the target temperature before each measurement.

4.3. Results and discussion

4.3.1. Characterization of polymers and electrolytes

Successful synthesis of PCmEO ($m = 1, 2, 4, 6, 8,$ and 12) was confirmed by ^1H NMR spectrometry. The molecular weight of each PCmEO obtained from the chromatogram of gel permeation chromatography (GPC) (Table 4.1 and Figure 4.3) was more than 10 kg mol^{-1} , which was large enough to exclude the contribution of the molecular weight of the polymer on the physicochemical properties.¹⁰ PCmEO electrolytes were prepared by mixing the PCmEO and 1.0 M lithium bis(trifluoromethane sulfonyl)amide (LiTFSA) in tetrahydrofuran (THF) solution, subsequently heated under a vacuum to remove THF, which confirmed using infrared spectroscopy. The mixing ratio of polymer repeating unit and LiTFSA was set to 5. Prepared PEs are denoted as PCmEO-LiTFSA throughout the study. The amount of LiTFSA in PEs, LiTFSA weight ratio, and LiTFSA concentration are listed in Table 4.2.

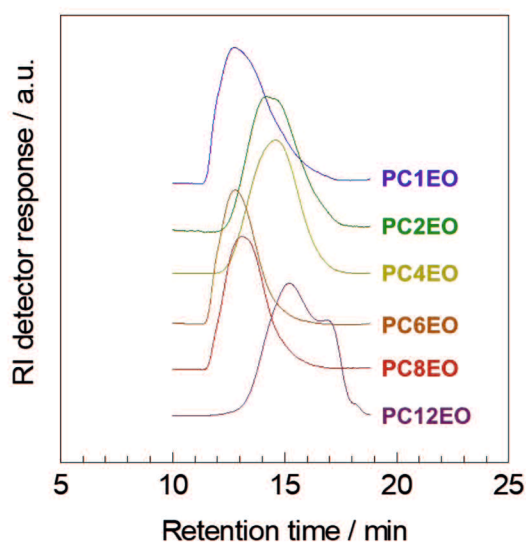


Figure 4.3 The chromatogram of PCmEO (m becomes longer in order from top to bottom; $m = 1, 2, 4, 6, 8,$ and 12) obtained by gel permeation chromatography (GPC) using THF as the elution solvent, deriving polymer molecular weight. The chromatogram was detected by a refractive index (RI) detector.

Table 4.1 The molecular weight of PCmEO obtained from GPC chromatogram calibrated with polystyrene. M_n is the number-average molecular weight, M_w is the weight-average molecular weight, M_w/M_n is the dispersity of molecular weight, M_{monomer} is monomer molecular weight, and DP is the degree of polymerization calculated from division of M_n by monomer molecular weight.

m	M_n [kg mol ⁻¹]	M_w [kg mol ⁻¹]	M_w/M_n	M_{mono} [g mol ⁻¹]	DP
1	59.0	147.0	2.49	130.19	453
2	26.7	48.4	1.81	144.21	185
4	27.1	47.5	1.76	172.27	157
6	101.1	172.7	1.71	200.32	505
8	73.2	135.1	1.85	228.38	321
12	11.0	23.5	2.14	284.48	38.7

Table 4.2 Estimated CmEO monomer density and lithium salt concentration of polymer electrolytes.

m	monomer density [g mL ⁻¹]	LiTFSA ratio [wt%]	LiTFSA concentration [mol L ⁻¹]
1	1.018	30.6	1.28
2	0.915	28.5	1.07
4	0.902	25.0	0.91
6	0.894	22.2	0.79
8	0.894	20.1	0.70
12	0.807	16.8	0.52

4.3.2. Electrochemical and thermal stability

Voltametric and thermogravimetric analysis revealed that the electrochemical and thermal stability of newly synthesized PCmEO-LiTFSA electrolyte partially affected by the length of the alkyl side chain, yet it possessed sufficient electrochemical and thermal stability for ~4 V-class lithium secondary batteries which can operate up to ~250°C (Figure 4.4). The oxidation stability of PCmEO-LiTFSA was assessed with linear sweep voltammetry (LSV) at 70°C (Figure 4.4a, Figure 4.5). Oxidation current was observed from ca. 4.0 V vs. Li/Li⁺ for PCmEO-LiTFSA (m = 1, 4, 6, 8, and 12), which agreed well with the oxidative decomposition potential of polyether electrolytes.^{11,12} Relatively low oxidation stability of ca. 3.5 V for PC2EO-LiTFSA indicates the unique inter/intra molecular interaction within the electrolyte. Cyclic voltammogram for PCmEO-LiTFSA showed stable lithium

deposition/stripping reaction at ca. 0 V vs. Li/Li⁺ (Figure 4.6), suggesting that PCmEO-LiTFSA electrolytes are applicable to the ~4 V-class batteries.¹³

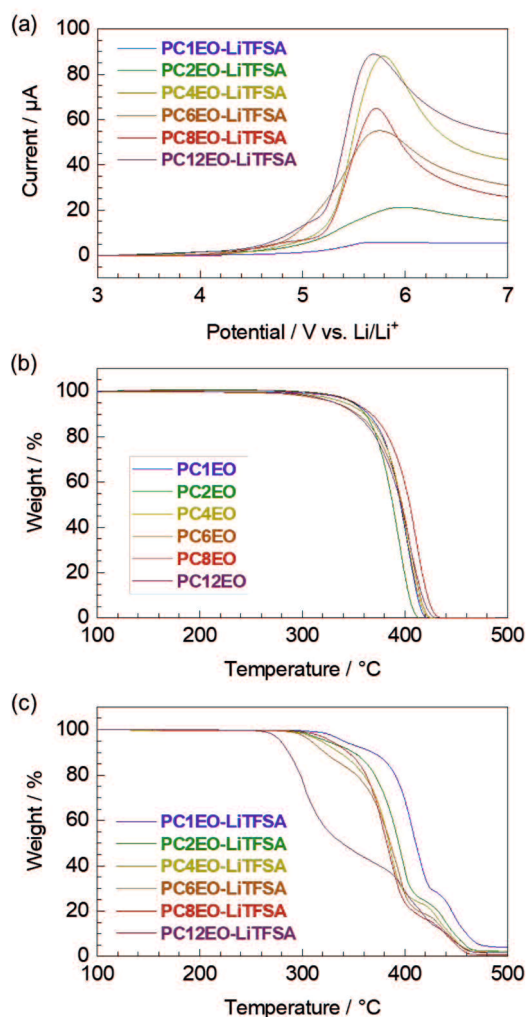


Figure 4.4 Electrochemical and thermal stability of newly synthesized PCmEO and corresponding electrolytes. (a) Linear sweep voltammogram from rest potential (ca. 3.0 V) to 7.0 V for PCmEO-LiTFSA on stainless steel working electrode at a scan rate of 1 mV s⁻¹. Thermogravimetric (TG) curves of (b) PCmEO (pure polymers) and (c) PCmEO-LiTFSA (PEs). TG curve was obtained under He atmosphere at a heating rate of 20°C min⁻¹. Thermogravimetry of the PEs was performed after pre-heating at 150°C for 10 min to remove water. Blue, green, yellow, orange, red, and purple line shows m = 1, 2, 4, 6, 8, and 12, respectively.

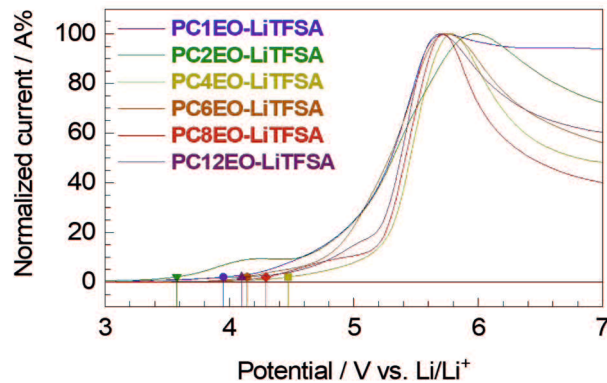


Figure 4.5 Linear sweep voltammogram for PC m EO-LiTFSA on stainless steel working electrode at 70°C normalized by the peak current. Potential was scanned from the rest potential (ca. 3.0 V) to 7.0 V at a scan rate of 1 mV s⁻¹. Symbol marks indicates the starting points of current peak rising; m = 1 (blue circle), m = 2 (green down triangle), m = 4 (yellow square), m = 6 (orange hexagon), m = 8 (red diamond), and m = 12 (purple triangle).

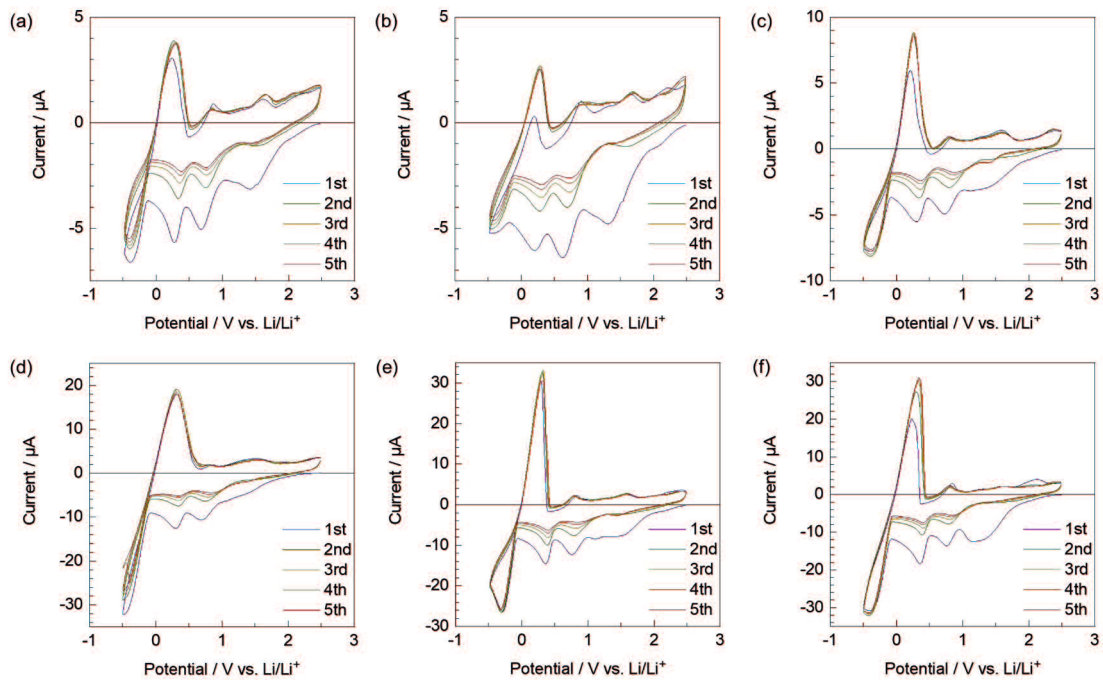


Figure 4.6 Cyclic voltammograms of (a) PC1EO-LiTFSA, (b) PC2EO-LiTFSA, (c) PC4EO-LiTFSA, (d) PC6EO-LiTFSA, (e) PC8EO-LiTFSA, and (f) PC12EO-LiTFSA on Ni electrode at a scan rate of 1 mV s⁻¹ at 70°C.

Thermogravimetric analysis confirms the improvement of the thermal stability of PCmEO-LiTFSA with the shortening of the alkyl side chain (Figure 4.4b, c). The observed trend indicates the effect of the alkyl side chain on the interaction between dissociated ions and PCmEO, which dictates the thermal stability of the electrolytes. Thermogravimetric curves for pure PCmEO showed a plateau extending up to ca. 350°C, indicating minimal weight loss and good thermal stability up to 350°C. A weight-loss observed at >350°C corresponds to the evaporation of short molecules, which can be generated from the thermal decomposition of polymers initiated by the radical cleavage of the C–O or the C–C covalent bond.¹⁴ Thermal decomposition temperature (T_d) of all pure PCmEO was at $370 \pm 15^\circ\text{C}$, which is similar to other polyethers (e.g., T_d of PEO; ca. 400°C)¹⁵ (Table 4.3). Similar T_d for all the pure PCmEO, regardless of the alkyl side chain length, confirms the negligible effect of the alkyl side chains on the thermal decomposition process of pure PCmEO.

The thermal decomposition temperature of PCmEO-LiTFSA ($m \geq 2$) decreased compared to the corresponding pure PCmEO (Figure 4.4b, c), suggesting the acceleration of the thermal decomposition by LiTFSA. PCmEO-LiTFSA ($m \geq 2$) were destabilized due to the interaction between ether groups and lithium-ion, which weakened the C–O covalent bonds.¹⁴ Thermal decomposition temperature (T_d) of PCmEO-LiTFSA ($m \leq 8$) electrolytes showed alkyl side chain length dependence; $m = 1$ (383°C) > $m = 2$ (367°C) > $m = 4, 6,$ and 8 ($359^\circ\text{C}, 352^\circ\text{C},$ and $356^\circ\text{C},$ respectively) (Figure 4.4c, Table 4.3). The observed improvement of the thermal stability for PCmEO-LiTFSA with the shortening of the alkyl side chain ($m \leq 8$) suggested the suppression of the radical cleavage of the covalent bond, which initiated the thermal decomposition of PCmEO-LiTFSA. The previous study on PEO electrolytes (e.g., PEO-LiCl)¹⁴ suggests that the dissociated ion act as a radical trap and effectively inhibit the chained radical decomposition. Therefore, the T_d trend may reflect the amount of the dissociated ion in PCmEO-LiTFSA; the amount of the dissociated ion was increased with the shortening of the alkyl side chain. On the other hand, PC12EO-LiTFSA showed an extremely low T_d of 279°C , which was inconsistent with the explanation based on the ion dissociability. I propose that the alignment of the long alkyl side chain ($m = 12$) via hydrophobic interactions hinders the approach of the dissociated ions at the vicinity of the alkyl side chain,^{4,5} inhibiting the dissociated ions to act as a radical trap effectively. Further

support comes from gas chromatography-mass spectrometry (GC-MS), which confirms the decomposition of the alkyl side chain occurred before that of the polymer main chain for PC12EO-LiTFSA, unlike PC1EO-LiTFSA (Figure 4.7).

Subsequent weight loss was observed at 410–440°C ($m \geq 2$) and $> 440^\circ\text{C}$ ($m = 1$) for PC m EO-LiTFSA (Figure 4.4c), which corresponds to the thermal decomposition of the TFSA anion and the polymer residue. The assignment was supported by (1) the detection of the TFSA anion and trace amount of polymer residue at a given temperature in GC-MS (Figure 4.7), (2) the good agreement with the weight loss and the added weight of TFSA in PC m EO-LiTFSA.

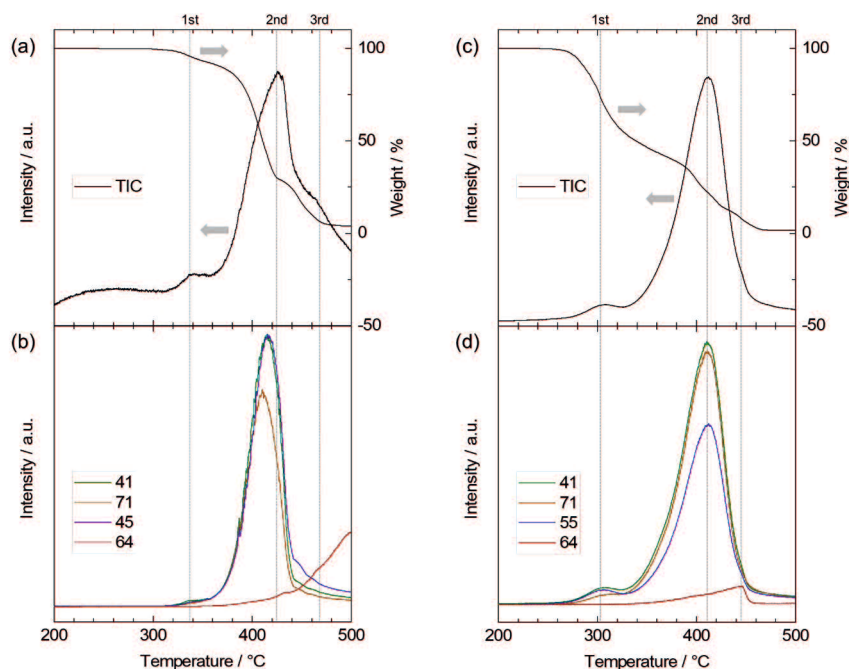


Figure 4.7 Gas chromatography-mass spectrometry (GC-MS) curves for (a), (b) PC1EO-LiTFSA and (c), (d) PC12EO-LiTFSA, recorded from 150°C to 500°C under He flow. TIC in (a) and (c) indicates the total ion chromatogram. Assignment for each m/z is as follows. (b) $m/z = 41$: $\cdot\text{CH}_2\text{-CH=CH}_2$ derived from the decomposition of ethyl group, $m/z = 71$: $\text{O=CH}\cdot\text{-CH-CH=O}$ derived from the decomposition of polymer main chain, $m/z = 45$: $\cdot\text{CH}_2\text{-O-CH}_3$ derived from the decomposition of methoxymethyl group (polymer side chain), and $m/z = 64$: O=S=O derived from the decomposition of TFSA anion. (d) $m/z = 41$: $\cdot\text{CH}_2\text{-CH=CH}_2$ derived from the decomposition of ethyl group or dodecyl group, $m/z = 71$: $\text{O=CH}\cdot\text{-CH-CH=O}$ derived from the decomposition of polymer main chain, $m/z = 55$: $\text{CH}_3\cdot\text{-CH-CH=CH}_2$ derived from the decomposition of dodecyl group, and $m/z = 64$: O=S=O derived from the decomposition of TFSA anion.

4.3.3. Segmental mobility

Differential scanning calorimetry (DSC) revealed that the length of alkyl side chains affects the phase transition behavior of the PCmEO and the corresponding electrolytes. The PCmEO showed crystallinity for $m = 1, 2, 8,$ and 12 except with moderate length alkyls ($m = 4$ and 6), and the crystallinity was confirmed only for PC12EO-LiTFSA among PEs. The extension of the alkyl side chain improved the segmental mobility; the internal plasticizing effect and the steric hindrance of the alkyl side chain are keys to improve the segmental mobility of the polymer and the PE, respectively (Figure 4.8, Table 4.3).

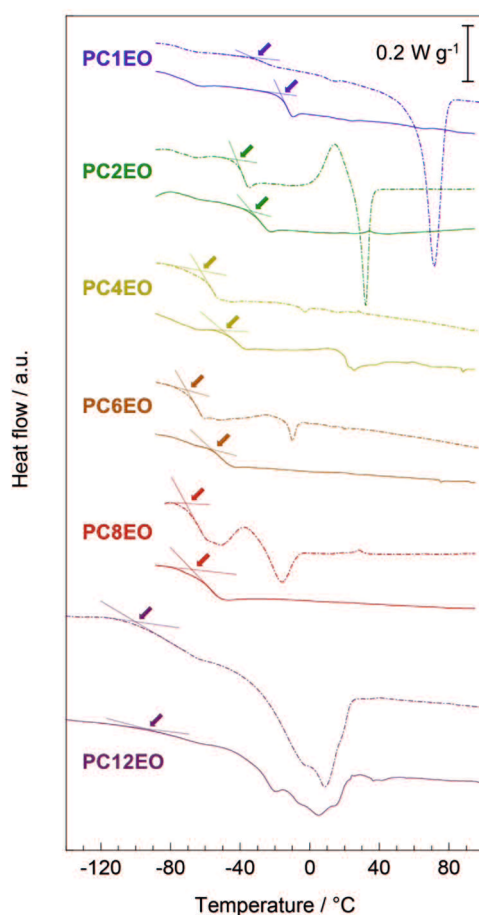


Figure 4.8 Differential scanning calorimetry (DSC) curves for PCmEO (dash line) and PCmEO-LiTFSA (solid line) recorded during the heating step from -100°C to 120°C (PC12EO and PC12EO-LiTFSA were heated from -150°C) after pre-heating up to 120°C under N_2 flow. Guidelines and arrows indicate the glass transition temperature.

Differential scanning calorimetry curves showed distinctive endothermic peaks for pure PCmEO ($m = 1, 2, 8,$ and 12), which corresponds to the transition of the polymer from the crystalline state into the state of viscous flow (Figure 4.8).^{4,16} The crystal melting temperature (T_m) of PC1EO and PC2EO was close to T_m of PEO ($65\text{--}70^\circ\text{C}$),^{17,18} suggesting the formation of a PEO-like crystal phase. The melting temperature of pure PCmEO ($m = 4$ and 6) was not observed, indicating the inhibition of the crystal formation due to the large steric hindrance of the alkyl side chain. Despite the existence of long alkyl side chains, PCmEO ($m = 8$ and 12) showed T_m of -24.7°C and -31.1°C , respectively. The observation suggests the existence of the well-aligned structure of long alkyl side chains via hydrophobic interaction.⁵ The melting temperature was not observed for PCmEO-LiTFSa electrolytes ($m = 1\text{--}8$) due to the sterical suppression of the crystal formation by LiTFSa.¹⁷ The unusual observation of T_m for PC12EO-LiTFSa electrolytes suggests the existence of a unique well-aligned structure even with Li salt, consistent with the exceptionally low T_d of PC12EO-LiTFSa (Figure 4.4c), further suggesting the strong hydrophobic interaction between long alkyl side chains.

The glass transition temperature (T_g) is tied to the polymer segmental mobility, which is one of the important descriptors to determine the ion transport property for PE. The glass transition temperature (T_g) of pure PCmEO decreased with the extension of the alkyl side chain from -34.7°C ($m = 1$) to -100.9°C ($m = 12$) (Figure 4.8). The observed alkyl chain length dependence of T_g can be due to the internal plasticizing effect of alkyl side chains, originating from the large free volume within polymer chains by an alkyl side chain.³ The addition of LiTFSa increased the T_g of PEs for $5\text{--}18^\circ\text{C}$ compared to the corresponding pure PCmEO, mainly due to the multiple interaction (coordination) between ether oxygen and lithium-ion, which inhibited the bond rotation within the polymer required for the smooth segmental motion.¹⁹ The gap of T_g between PCmEO and PCmEO-LiTFSa (ΔT_g) correlates with the length of alkyl side chain; $m = 1$ (18.1°C) $>$ $m = 2, 4,$ and 6 ($8.8^\circ\text{C}, 13.1^\circ\text{C},$ and 13.1°C , respectively) $>$ $m = 8$ and 12 (4.5°C and 5.6°C). The difference of ΔT_g between $m = 1$ and $m \geq 2$ suggests the inhibition of the interaction between ether group and lithium-ion by the steric hindrance of the alkyl side chain ($m \geq 2$), which originates a relatively large gap of T_g between pure polymer and the corresponding electrolyte. The notably small ΔT_g for PC8EO and PC12EO probably derived from the side chain aggregation or alignment in

PC8EO-LiTfSA and PC12EO-LiTfSA. I hypothesize that the hydrophobic phase (mainly consist of side chain aggregation or alignment) determines the segmental mobility, and only minor contribution from hydrophilic phase on the segmental mobility, where the interaction between ether group and lithium-ion mainly affects. Although I could not observe the alkyl side chain aggregation for PC8EO-LiTfSA, our hypothesis is partially supported by the TG and DSC analysis, confirming the side chain alignment for PC12EO-LiTfSA (Figure 4.4c, 4.8).

Table 4.3 List of the thermal transition temperatures obtained by thermogravimetry (TG) and differential scanning calorimetry (DSC). Thermal decomposition temperature (T_d) was determined as the intersection on the baseline and diagonal line of the largest weight loss on the TG curves. Melting temperature (T_m) was defined as the intersection of the baseline and diagonal line of the endothermic peak on the DSC curves. Glass transition temperature (T_g) was determined as the intersection on the baseline and diagonal line of baseline shift on the DSC curves. The gap of T_d and T_g between PCmEO and PCmEO-LiTfSA were described as ΔT_d and ΔT_g , respectively.

m	T_d [°C]		ΔT_d^a	T_m [°C]		T_g [°C]		ΔT_g^b
	Pure	PEs		Pure	PEs	Pure	PEs	
1	373	383	+10	64.4	–	–34.7	–16.6	+18.1
2	368	367	– 1	27.6	–	–41.9	–33.1	+ 8.8
4	375	359	–16	–	–	–63.5	–50.4	+13.1
6	376	352	–24	–	–	–70.3	–57.2	+13.1
8	384	356	–28	–24.7	–	–72.8	–68.3	+ 4.5
12	372	279	–93	–31.1	–34.8	–100.9	–95.3	+ 5.6

$$^a\Delta T_d = T_d(\text{PEs}) - T_d(\text{Pure polymers})$$

$$^b\Delta T_g = T_g(\text{PEs}) - T_g(\text{Pure polymers})$$

4.3.4. Bulk ion transport property

Electrochemical impedance spectroscopy (EIS) revealed that the ionic conductivity (σ) for PCmEO-LiTfSA ($m = 1-6$) at low temperature ($\leq 30^\circ\text{C}$) increased with the extension of the alkyl side chain, while the opposite tendency was the case at high temperature ($\geq 70^\circ\text{C}$) except PCmEO-LiTfSA ($m = 8$ and 12) (Figure 4.9). The observed trend at low and high temperature regions can correlate with polymer segmental mobility and lithium salt dissociability, respectively. The transference number of lithium-ion was increased with a long alkyl side chain, suggesting the dominant effect of alkyl side chain length on the bulky TfSA transport. Furthermore, the aggregated/aligned alkyl side chain within PCmEO-

LiTFSA ($m = 8$ and 12) was suggested to act as a rapid lithium-ion transport pathway (Table 4.4).

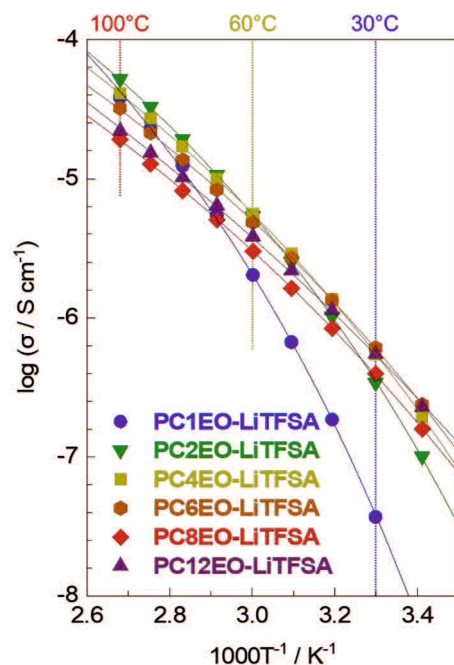


Figure 4.9 Ionic conductivities (σ) for PC m EO-LiTFSA ($m = 1, 2, 4, 6, 8,$ and 12) plotted against $1000T^{-1}$. Vogel–Tammann–Fulcher (VTF) fitting curves are shown in solid line. The measurements were performed at the temperature range of $20\text{--}100^\circ\text{C}$. Each symbol shows $m = 1$ (blue circle), $m = 2$ (green down triangle), $m = 4$ (yellow square), $m = 6$ (orange hexagon), $m = 8$ (red diamond), and $m = 12$ (purple triangle).

The obtained ionic conductivity (σ) increased with the extension of the alkyl side chain ($m = 1\text{--}6$) at low temperature region ($\leq 30^\circ\text{C}$) (Nyquist plots of the electrochemical impedance spectroscopy (EIS) are shown in Figure 4.10); the lowest σ for $m = 1$ ($3.70 \times 10^{-8} \text{ S cm}^{-1}$) and the highest σ for $m = 6$ ($6.09 \times 10^{-7} \text{ S cm}^{-1}$) at 30°C (Figure 4.9 and Figure 4.11). The observation resembles the T_g trend (Table 4.3), suggesting that polymer segmental motion plays a vital role in determining the ionic conductivity especially at low temperatures ($\leq 30^\circ\text{C}$). The Arrhenius plot of σ showed curved shape, further supporting the hypothesis that ionic conductivity heavily depends on the polymer segmental mobility²⁰ similar to polyether electrolytes.^{21,22} The ionic conductivity at high temperature region ($\geq 70^\circ\text{C}$) showed an opposite trend with the alkyl side chain length ($m = 1\text{--}6$); the lowest σ was observed for $m = 6$ ($3.22 \times 10^{-5} \text{ S cm}^{-1}$) and the highest σ for $m = 2$ ($5.19 \times 10^{-5} \text{ S cm}^{-1}$) at

100°C (Figure 4.9 and Figure 4.11). The contribution of the polymer segmental mobility on the ion conduction is known to decrease as the temperature rise.²³ Therefore, I hypothesize that there is a dominant factor determining the σ at high temperature ($\geq 70^\circ\text{C}$) instead of the polymer segmental mobility.

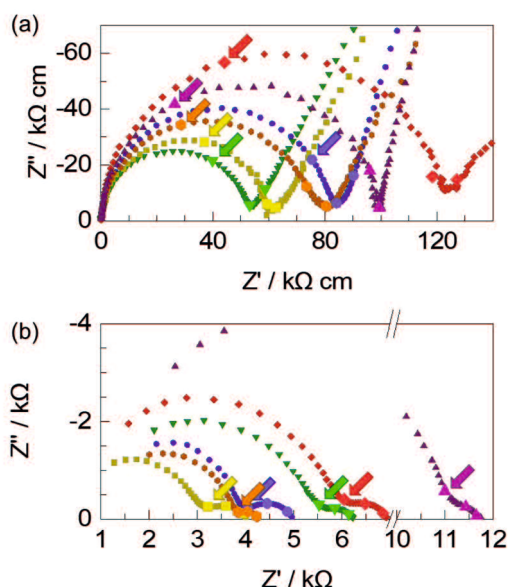


Figure 4.10 Nyquist plot for the electrochemical impedance spectroscopy (EIS) at 80°C using the symmetric cell with (a) stainless-steel blocking electrode for ionic conductivity measurements and (b) lithium non-blocking electrode for analysis of lithium-ion transfer at electrode-electrolyte interface. Three large and bright marks indicate 10000 (indicated with //), 1000, and 100 Hz frequency response.

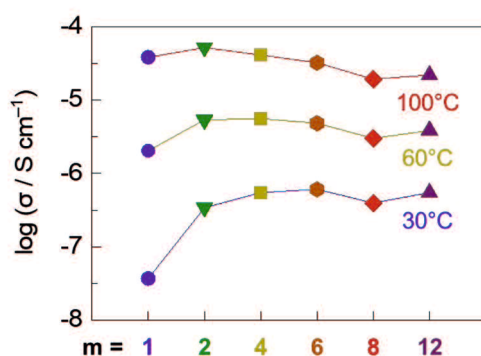


Figure 4.11 Alkyl side chain length dependence of the ionic conductivity (σ) for PC m EO-LiTFSA at 30°C , 60°C , and 100°C . Each symbol shows $m = 1$ (blue circle), $m = 2$ (green down triangle), $m = 4$ (yellow square), $m = 6$ (orange hexagon), $m = 8$ (red diamond), and $m = 12$ (purple triangle).

To clarify the dominant factor determining the σ at high temperature ($\geq 70^\circ\text{C}$), the Vogel–Tammann–Fulcher (VTF) equation (equation 3), i.e., a modified Arrhenius equation proposed for describing the temperature-dependence of viscosity in amorphous glasses, was employed.^{24,25}

$$\sigma = AT^{-1/2} \exp\left[-\frac{B}{R(T-T_0)}\right] \quad (3)$$

Here, A is a parameter that relates to the number of charge carriers, B is the pseudo activation energy for the ion transport, R is the gas constant, and T_0 is an ideal glass transition temperature (here, $T_0 = T_g - 50 \text{ K}$ ²⁴ T_g from DSC measurements (Table 4.3)). The experimental data showed a good agreement with the fitting line for all the electrolytes (Figure 4.9), and the obtained VTF parameters were summarized in Table 4.4.

The A value decreased with the extension of the alkyl side chain except for PCmEO-LiTFSA ($m = 8$ and 12). I propose that the A value trend reflects the decrease in the salt concentration (Table 4.2) and the decrease in salt dissociability. The TG analysis supported the argument, where the thermal stability decreased with the extension of the alkyl side chain due to the lack of dissociated ions (Figure 4.4c). I concluded that the degree of salt dissociability could be a dominant factor determining the ion transport within PCmEO-LiTFSA ($m = 1-6$) at high temperatures ($\geq 70^\circ\text{C}$).

The ionic conductivity of PCmEO-LiTFSA ($m = 8$ and 12) did not follow the above trends; showing the highest segmental mobility and the lowest salt dissociability (Figure 4.4c and Figure 4.8). The pseudo activation energy of the ion transport (B) notably increased for PCmEO-LiTFSA ($m = 8$ and 12) from *ca.* 13 kJ mol^{-1} (PCmEO-LiTFSA ($m = 1-6$)) to $>15 \text{ kJ mol}^{-1}$. The observation suggests the unique ion transport mechanism for PCmEO-LiTFSA ($m = 8$ and 12). The ion transport mechanisms were almost identical for PCmEO-LiTFSA ($m \leq 6$), consistent with the pseudo activation energy value of 0.125 eV ($= 12.1 \text{ kJ mol}^{-1}$) reported for PEO-LiTFSA.²⁶ Therefore, PCmEO-LiTFSA ($m = 1-6$) similarly transfers the ions to the PEO-LiTFSA system, where the ion is transferred via the polymer segmental motion,²² including the reorganization process of a polymer chain.²⁷ I here propose that PCmEO-LiTFSA ($m = 8$ and 12) transfers lithium-ions through a unique ion transport pathway between aligned and/or aggregated long alkyl side chains.⁵ The existence of aligned

and/or aggregated alkyl side chain structure was confirmed by DSC analysis (Figure 4.8) and consistent with the ΔT_g trend discussed in section 4.3.4. The higher ionic conductivity for PC12EO-LiTFSA than PC8EO-LiTFSA suggests the formation of more well-aligned ion transport pathways in PC12EO-LiTFSA, consistent with the stronger hydrophobic interaction between alkyl side chain for $m = 12$ suggested by the T_d and T_m analysis (Figure 4.4c, 4.8). Although the estimated salt dissociability of PC12EO-LiTFSA is low, A value of PC12EO-LiTFSA is relatively high, probably reflecting the higher frequency of the lithium-ion exchange from the coordination site to another through well-aligned ion transport pathways. PC8EO-LiTFSA form incomplete ion transport pathways due to relatively weak hydrophobic interaction of alkyl side chain compared to $m = 12$, resulting in the lower A value than PC12EO-LiTFSA.

Lithium transference number (t_{Li^+}) calculated by the potentiostatic polarization (Bruce-Vincent) method (Details of t_{Li^+} derivations are shown in Figure 4.12 and Table 4.5) revealed that t_{Li^+} increased with the extension of alkyl side chain from $m = 1$ ($t_{Li^+} = 0.15$) to $m = 12$ ($t_{Li^+} = 0.46$) (Table 4.4). The significantly low t_{Li^+} for PC1EO-LiTFSA was comparable to that of PEO-based electrolyte (e.g. PEO-LiTFSA, $t_{Li^+} \leq 0.2$),²⁸⁻³⁰ suggesting PEO-like lithium-ion transport mechanism in PC1EO-LiTFSA. In contrast, the increase of t_{Li^+} for PC m EO-LiTFSA with the extension of the alkyl side chain suggested the contribution of the alkyl side chain to suppress TFSA transport. The steric hindrance of the alkyl side chain selectively suppressed the transport of TFSA anion with a large ionic radius compared to lithium-ion. The highest lithium-ion conductivity (σ_{Li^+}) was achieved for PC4EO electrolyte among the electrolytes tested, indicating the optimized balance between polymer segmental mobility, LiTFSA dissociability, and t_{Li^+} for alkyl side chain length of $m = 4$. Comparable σ_{Li^+} was observed for PC12EO-LiTFSA, probably due to the formation of rapid lithium-ion transport pathways within the hydrophobic phase of the aligned alkyl side chain.

Table 4.4 Parameters of Vogel-Tammann-Fulcher (VTF) equation, lithium-ion transference number (t_{Li^+}), and lithium-ion conductivity (σ_{Li^+}) at 70°C. A is a fitting parameter relevant to the number of charge carriers, B is the pseudo activation energy of ion conduction, and T_0 is an ideal glass transition temperature, defined as $T_0 = T_g - 50$. Lithium-ion transference number (t_{Li^+}) was obtained by electrochemical methods using chronoamperometry and electrochemical impedance spectroscopy. Lithium-ion conductivity (σ_{Li^+}) was calculated by multiplying transference number (t_{Li^+}) and ionic conductivity (σ) at 70°C.

m	A [S cm ⁻¹ K ^{1/2}]	B [kJ mol ⁻¹]	T_0 [K]	t_{Li^+}	σ_{Li^+} at 70°C [$\times 10^{-6}$ S cm ⁻¹]
1	15.03	13.6	206.6	0.15	0.84
2	3.70	12.5	190.1	0.28	2.93
4	2.92	13.7	172.8	0.30	3.02
6	1.72	13.7	166.0	0.34	2.87
8	1.72	15.3	154.9	0.37	1.90
12	7.11	19.7	127.9	0.46	2.94

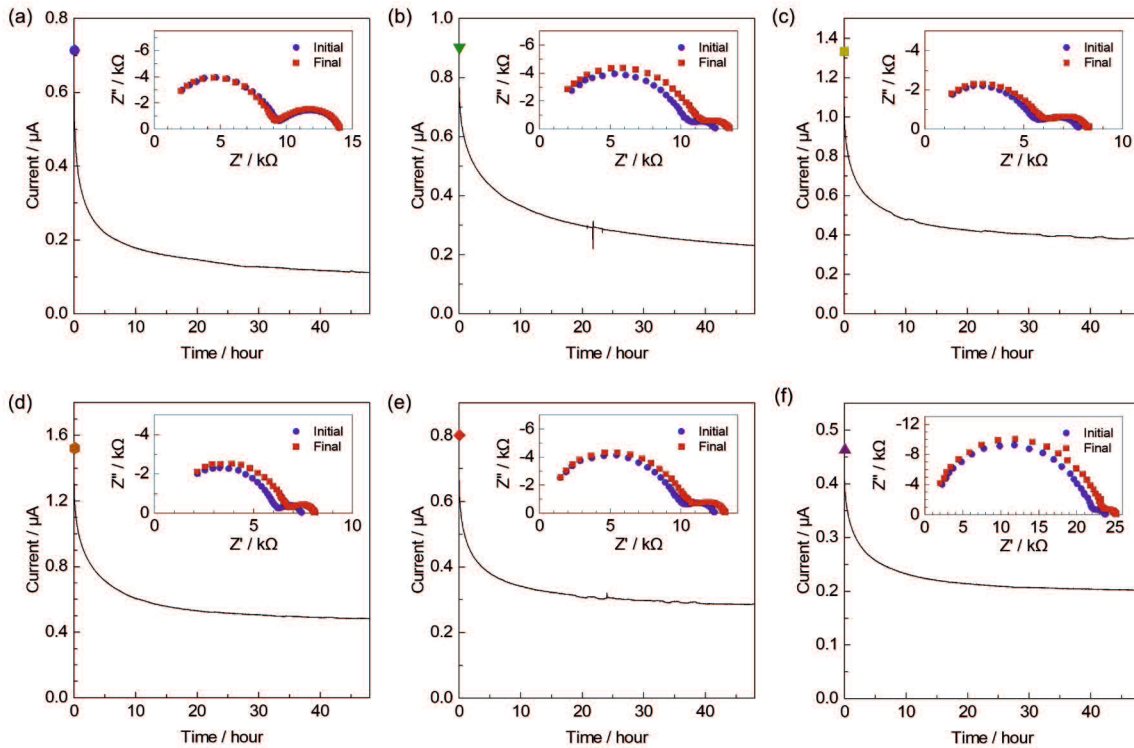


Figure 4.12 Chronoamperogram at 10 mV at 70°C and corresponding Nyquist plot for the electrochemical impedance spectroscopy (EIS) before and after the chronoamperometry; (a) $m = 1$, (b) $m = 2$, (c) $m = 4$, (d) $m = 6$, (e) $m = 8$, and (f) $m = 12$.

Table 4.5 Electrochemical parameters obtained from Figure 4.12, where I_0 is the initial current of the potentiostatic polarization, I_{SS} is the steady-state current of the polarization, R_B^i is the bulk resistance before the polarization, and R_B^f is the steady-state bulk resistance during the polarization, R_I^i is the interfacial resistance before the polarization, R_I^f is the steady-state interfacial resistance during the polarization, and calculated Li^+ transference number (t_{Li^+}).

m	I_0 [μA]	I_{SS} [μA]	R_B^i [$\text{k}\Omega$]	R_B^f [$\text{k}\Omega$]	R_I^i [$\text{k}\Omega$]	R_I^f [$\text{k}\Omega$]	t_{Li^+}
1	0.716	0.111	9.38	9.25	4.17	4.32	0.15
2	0.903	0.231	10.20	11.03	1.75	1.78	0.28
4	1.337	0.380	5.65	6.01	1.92	2.06	0.30
6	1.531	0.483	6.25	6.82	1.06	1.17	0.34
8	0.803	0.285	10.00	10.51	2.15	2.28	0.37
12	0.465	0.201	21.86	23.10	1.91	1.96	0.46

4.3.5. Lithium-ion transfer at the lithium metal electrode-polymer electrolyte interface

The lithium-ion deposition/reduction process at the electrode-electrolyte interface also plays a significant role in the performance of the next-generation lithium secondary batteries. The activation energy of the lithium-ion transfer at the electrode-electrolyte interface (E_{int}) partially depends on the alkyl side chain length; PC1EO-LiTfSA showed the notably high E_{int} of 116.3 kJ mol^{-1} while the rest of PCmEO-LiTfSA ($m \geq 2$) showed E_{int} of 68–82 kJ mol^{-1} (Figure 4.13).

Arrhenius plot of the interface resistance (R_{int}) showed a linear relationship, suggesting that the polymer segmental motion was not involved in the lithium-ion transfer at the electrode-electrolyte interface (Figure 4.13). The activation energy of lithium-ion transfer at the electrode-electrolyte interface (E_{int})^{31–33} became higher in PCmEO-LiTfSA (≥ 68 kJ mol^{-1}) than in liquid electrolytes (53–59 kJ mol^{-1}), where the process is dominated by the (de-)solvation process of the lithium-ion.³¹ The trend in E_{int} suggested that the sluggish (de-)coordination process within polymer matrix compared to that in liquid electrolytes. PC1EO-LiTfSA showed the highest E_{int} of 116.3 kJ mol^{-1} among the PCmEO electrolytes while the PCmEO-LiTfSA ($m \geq 2$) showed E_{int} within the range of 68–82 kJ mol^{-1} . I here propose that the E_{int} reflects the stability of the lithium-ion coordination structure, closely

related to the strength of the interaction between ether oxygen and lithium-ion. The notably high E_{int} value of PC1EO-LiTFSA thus indicates the stable structure around lithium-ion, which was consistent with the largest ΔT_g for PC1EO, suggesting the multiple and stable interaction between lithium-ion and ether group (Table 4.3).

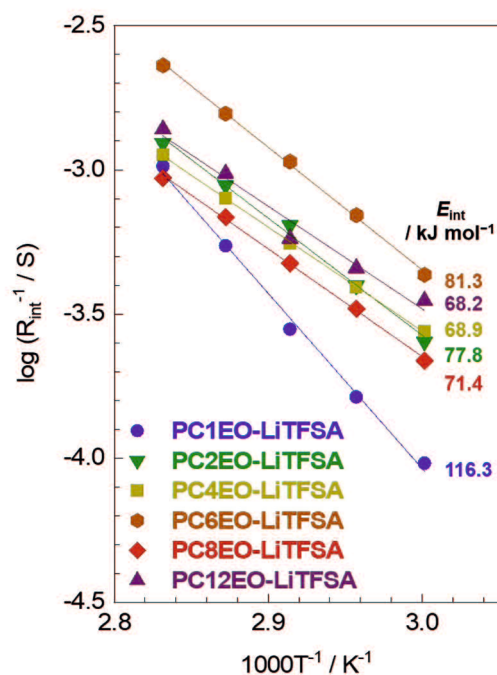


Figure 4.13 Reciprocal of lithium metal electrode-polymer electrolyte interface resistance (R_{int}) for PC m EO-LiTFSA electrolytes ($m = 1, 2, 4, 6, 8,$ and 12) plotted against $1000T^{-1}$. Arrhenius fitting lines are shown in solid lines. The measurements were performed at the temperature range of 60–80°C using lithium symmetric cell.

4.3.6. Interactions around lithium-ion

The infrared (IR) and Raman spectroscopic analysis confirmed that the amount of ether oxygen interacting with lithium-ion was notably larger for PC1EO-LiTFSA compared to PC m EO-LiTFSA ($m \geq 2$), whereas the number of TFSA anion interacting with lithium-ion was increased with the extension of the alkyl side chain (Figure 4.14).

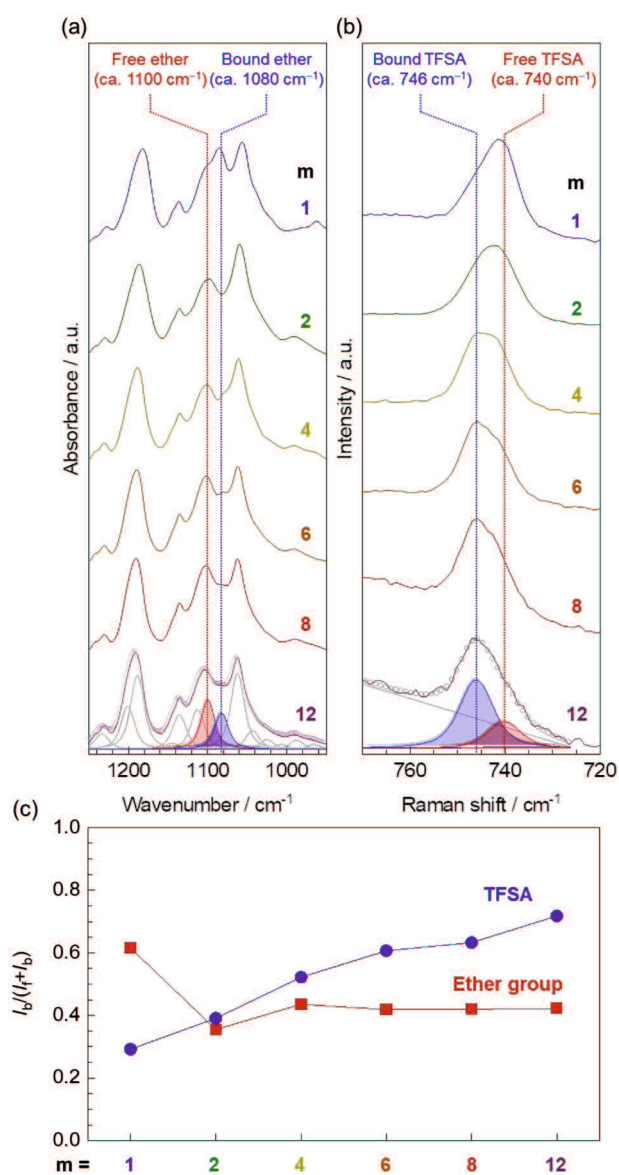


Figure 4.14 The interaction between Li^+ and ether group/TFSA anion in PC $_m$ EO-LiTFSA. (a) Infrared (IR) spectra of $v_{as}(\text{COC})$ region and (b) Raman spectra of $\delta_s(\text{CF}_3)$ region (solid line). The alkyl side chain becomes longer in order from top to bottom; $m = 1, 2, 4, 6, 8,$ and 12 . Peak deconvolution was performed by PeakFit software using pseudo-Voigt functions with a fixed half-width at half-maximum, and representative deconvoluted peaks are shown for PC $_{12}$ EO-LiTFSA. The open circle is shown typical curve-fitting results. (c) The alkyl side chain length dependency of the ratio of the peak area assigned to polar groups (red square for ether groups and blue circle for TFSA anion) interacting with lithium-ion (I_b) to the total peak area ($I_f + I_b$).

Infrared (IR) spectra for pure PCmEO showed the intense peak at 1094–1100 cm^{-1} , which can be assigned to $\nu_{\text{as}}(\text{COC})$ of ether groups on main and/or side chain (Figure 4.15 and 4.17).³⁴ The shouldered peak was observed in the $\nu_{\text{as}}(\text{COC})$ region for the corresponding PCmEO-LiTFSA (Figure 4.14a and Figure 4.17), which could be due to the overlapping of the peaks assigned to ether group without any interactions (denoted as free ether) (ca. 1100 cm^{-1}) and ether group interacting with lithium-ion (denoted as bound ether) (ca. 1080 cm^{-1}). A clear peak shift from 1095 cm^{-1} to 1084 cm^{-1} was confirmed by introducing excessive lithium iodide in PC1EO (Figure 4.18), which validates the newly appeared peak (1084 cm^{-1}) corresponds to the $\nu_{\text{as}}(\text{COC})$ of bound ether. Further support came from the redshift of the peak at 1066 cm^{-1} of $\nu_{\text{as}}(\text{COC})$ of pure tetrahydrofuran to 1043 cm^{-1} for neat LiTFSA solution in tetrahydrofuran (Figure 4.18), indicating the weakening of the C–O bond due to the interaction between ether oxygen and lithium-ion.^{35,36} The ratio of bound ether to all ether groups, i.e., bound and free ether group, was calculated by comparing the deconvoluted $\nu_{\text{as}}(\text{COC})$ peak area. The ratio of bound ether became the largest for $m = 1$ compared to $m = 2$ –12 (Figure 4.14c red square symbol), suggesting the effective inhibition of the interaction between ether oxygen and lithium-ion by the sterically hindered alkyl side chain ($m \geq 2$).²⁴ However, the ratio of the bound ether remained almost the same for PCmEO-LiTFSA with $m \geq 2$, probably due to the hydrophobic exclusion, which inhibits the approach of the alkyl side chain to the vicinity of the hydrophilic Li^+ -coordination site. As a result, the ethyl(-ene) side chain ($m = 2$) connected on ether groups could stay at the vicinity of the ether group, which effectively inhibits the interaction between lithium-ion and ether oxygen.

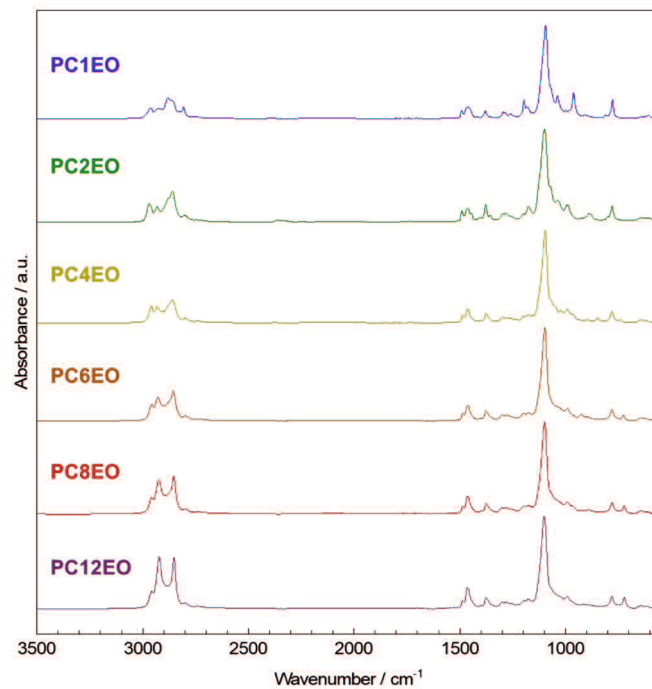


Figure 4.15 Attenuated total reflection (ATR) infrared (IR) spectra of the PCmEO (m becomes larger in order from top to bottom; m = 1, 2, 4, 6, 8, and 12).

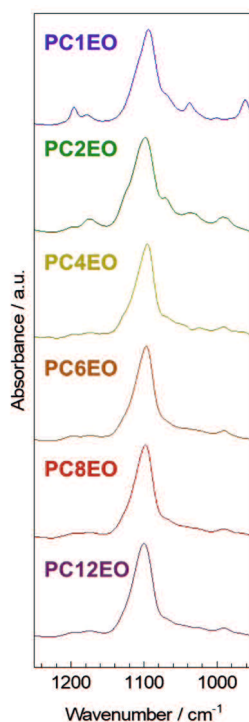


Figure 4.16 Attenuated total reflection (ATR) infrared (IR) spectra of the $\nu_{as}(\text{COC})$ region for PCmEO (m becomes larger in order from top to bottom; m = 1, 2, 4, 6, 8, and 12).

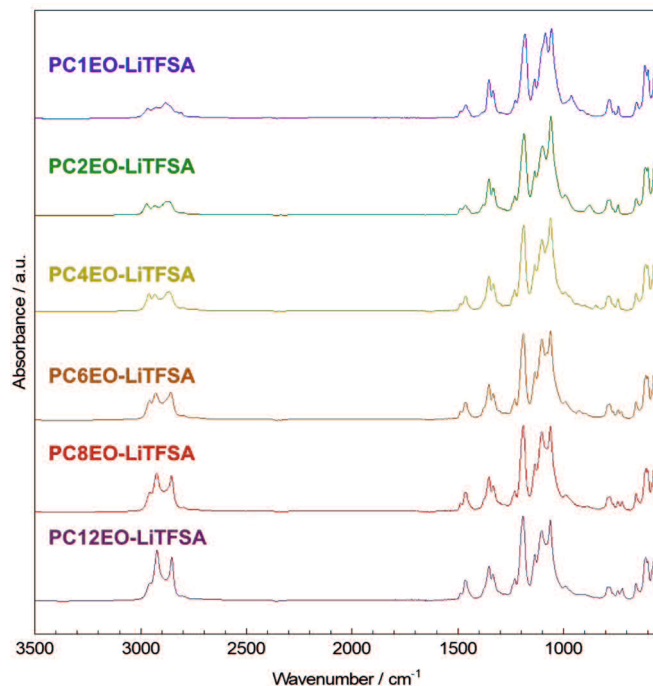


Figure 4.17 Attenuated total reflection (ATR) infrared (IR) spectra of the PC m EO-LiTfSA (m becomes larger in order from top to bottom; $m = 1, 2, 4, 6, 8,$ and 12).

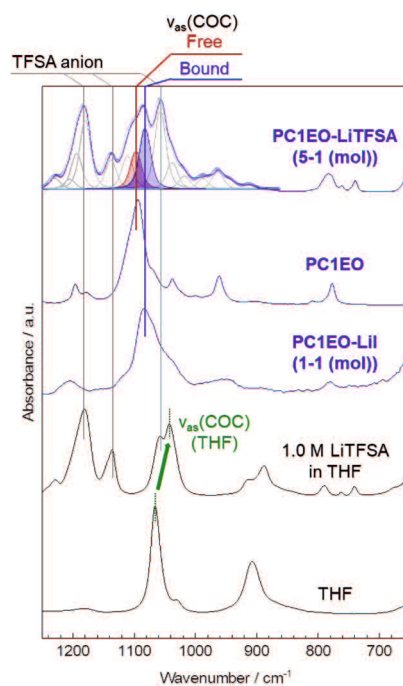


Figure 4.18 Deconvoluted ATR-IR spectra of the $\nu_{as}(\text{COC})$ region for PC1EO-LiTfSA. ATR-IR spectra for pure PC1EO, PC1EO-LiI (1 polymer unit mol / 1 LiI mol), 1.0 M LiTfSA in THF, and pure THF is also shown for comparison.

Raman spectra showed an intense peak at 740–746 cm^{-1} , which corresponds to $\delta_s(\text{CF}_3)$ of TFSA anion (Figure 4.14b).³⁷ The $\delta_s(\text{CF}_3)$ peak can be deconvoluted into two peaks, which were assigned to TFSA anion with (bound TFSA, 746 cm^{-1}) and without (free TFSA, 740 cm^{-1}) interacting to lithium-ion.^{6,38} The increase of the amount of bound TFSA in line with the extension of the alkyl side chain suggest the decreased lithium salt dissociability for PCmEO-LiTFSA with a long alkyl side chain, which confirms the salt dissociability trend suggested from TG and VTF (A value) analysis. The decrease of salt dissociability was probably due to the decrease in the dielectric constant by increasing the non-polarity with the extension of the alkyl side chain.²

The electrolyte properties (including thermal stability, thermal phase transition, segmental mobility, salt dissociability, ionic conductivity, lithium-ion transference number, and lithium-ion transfer at the electrode-electrolyte interface) are heavily affected by the length of the alkyl side chain (Figure 4.19).

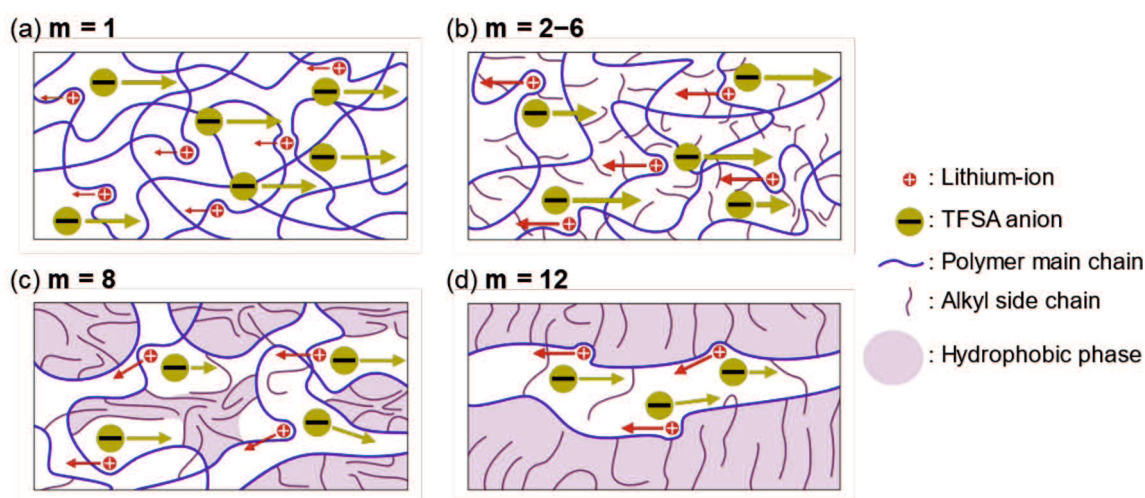


Figure 4.19 The proposed model for the ion transportation within PCmEO-LiTFSA. (a) $m = 1$; ether group interacts well with lithium-ion and isolates the TFSA anion, (b) $m = 2-6$; alkyl side chain dispersed and suppressed the interaction between ether group and lithium-ion as well as TFSA anion and lithium-ion, (c) $m = 8$; alkyl side chain partially aggregates and inhibits the transport of ions, and (d) $m = 12$; alkyl side chain aligned via hydrophobic interaction and provide rapid lithium-ion transport pathways. Red and yellow circles correspond to the lithium-ion and TFSA anion, respectively. Blue and purple curves represent polymer main chain with ether group and alkyl side chain, respectively. The purple area shows a hydrophobic phase with alkyl side chain aggregation.

The short alkyl side chain ($m = 1$) with small steric hindrance showed negligible effect on the interaction between ether groups and lithium-ion, leading to form coordination structure similar to that of PEO electrolytes. The stable coordination structure of PC1EO-LiTFSA significantly increases the glass transition temperature (Figure 4.8 and Table 4.3) and the activation energy of lithium-ion transfer at the electrode-electrolyte interface (E_{int}) (Figure 4.13). On the other hand, relatively large steric hindrance of the alkyl side chain ($m = 2-6$) effectively suppressed the interaction between ether oxygen and lithium-ion, which corresponds to the smaller ΔT_g and E_{int} than PC1EO-LiTFSA (Table 4.3 and Figure 4.13). Although a long alkyl side chain ($m = 8$ and 12) suppressed the interaction between ether oxygen and lithium-ion, it can be partially aligned and/or aggregated due to the large hydrophobic interaction between the side chains, decreasing ΔT_g compared to PC m EO-LiTFSA ($m \leq 6$). In addition, the alkyl side chain with $m = 12$ aligned well in the electrolyte, leading to create rapid lithium-ion transport pathways and give relatively high lithium-ion conductivity (σ_{Li^+}) (Table 4.4).

The unique character of the alkyl side chain associated with the extension of the alkyl groups also plays a significant role in determining the electrolyte properties. Polymer segmental mobility increased with the extension of the alkyl side chain (Table 4.3 and Figure 4.8) due to the increase in the internal plasticizing effect of the alkyl side chain. The extension of the alkyl side chain also decreased the LiTFSA dissociability by reducing the overall dielectric constant of electrolytes derived from the increased contribution from the non-polar alkyl side chain. The decrease in the number of dissociated ions with the extension of the alkyl side chain decreases the thermal stability (Table 4.3) and the ionic conductivity at high temperatures ($> 70^\circ\text{C}$) (Table 4.4). The transference number of lithium-ion (t_{Li^+}) increased with the extension of the alkyl side chain due to the effective inhibition of the transport of bulky TFSA anion by large steric hindrance of the alkyl side chain. The balance between polymer segmental mobility, salt dissociability, and the transference number of lithium-ion decides the σ_{Li^+} ; alkyl side chain with moderate chain length ($m = 4$) showed the highest σ_{Li^+} of $3.02 \times 10^{-6} \text{ S cm}^{-1}$ among the electrolyte tested in this study.

4.4. Conclusions

The influence of alkyl side chain length on the interaction between lithium-ion and ether groups, as well as the lithium-ion transport within polyether-based electrolyte was clarified by thermal, electrochemical, and spectroscopic analysis. The length of the alkyl side chain significantly affects the lithium coordination structure; the electrolyte with a short alkyl side chain ($m = 1$) has the most stable lithium coordination structure surrounded by ether oxygen, while the extension of the alkyl side chain ($m = 2-12$) effectively suppressed the interaction between ether oxygen and lithium-ion, leading to decrease the glass transition temperature and the activation energy of lithium-ion transfer at the electrode-electrolyte interface. Various characteristics of the alkyl side chain associated with the extension of the alkyl groups also play a significant role in determining the electrolyte properties. The increase in the internal plasticizing effect of the alkyl side chain increases the polymer segmental mobility. The decrease in the overall dielectric constant of electrolytes derived from the increased contribution from the non-polar alkyl side chain decreases the LiTfSA dissociability. The decrease in the number of dissociated ions with the extension of the alkyl side chain decreases the thermal stability and the ionic conductivity at high temperatures ($> 70^{\circ}\text{C}$). The transference number of lithium-ion (t_{Li^+}) increased with the extension of the alkyl side chain due to the effective inhibition of the transport of bulky TfSA anion by significant steric hindrance of the alkyl side chain. Furthermore, the hydrophobic phase with aligned and/or aggregated long alkyl side chains ($m = 12$) acts as a rapid lithium-ion transport pathway, leading to high lithium-ion conductivity of $2.94 \times 10^{-6} \text{ S cm}^{-1}$. Alkyl side chain with medium length ($m = 4$) showed the highest lithium-ion conductivity of $3.02 \times 10^{-6} \text{ S cm}^{-1}$, due to the optimized balance between polymer segmental mobility, salt dissociability, and the transference number of lithium-ion. The result thus emphasizes the importance of optimizing the length of the alkyl side chain to improve (electro)chemical properties of PE. Proposed polymer design strategy can be used in combination with existing strategies, including but not limited to the composition tuning of copolymer matrices and the topology design of non-linear polymers, further increasing the lithium conductivity to meet the requirement for implementing the all-solid rechargeable battery technologies.

References

1. Redfern, P. C.; Curtiss, L. A. *J. Power Sources* **2002**, *110*, 401–405.
2. Wheatle, B. K.; Keith, J. R.; Mogurampelly, S.; Lynd, N. A.; Ganesan, V. *ACS Macro Lett.* **2017**, *6*, 1362–1367.
3. Mauritz, K. A.; Storey, R. F.; George, S. E. A. *Macromolecules* **1990**, *23*, 441–450.
4. Liu, G.; Reinhout, M.; Mainguy, B.; Baker, G. L. *Macromolecules* **2006**, *39*, 4726–4734.
5. Liu, J.; Zheng, Y.; Liao, Y.-P.; Apperley, D. C.; Ungar, G.; Wright, P. V. *Electrochim. Acta* **2005**, *50*, 3815–3826.
6. Sai, R.; Ueno, K.; Fujii, K.; Nakano, Y.; Shigaki, N.; Tsutsumi, H. *Phys. Chem. Chem. Phys.* **2017**, *19*, 5185–5194.
7. Mu, Y.; Jia, M.; Jiang, W.; Wan, X. *Macromol. Chem. Phys.* **2013**, *214*, 2752–2760.
8. Evans, J.; Vincent, C. A.; Bruce, P. G. *Polymer (Guildf)*. **1987**, *28*, 2324–2328.
9. Abraham, K. M.; Jiang, Z.; Carroll, B. *Chem. Mater.* **1997**, *9*, 1978–1988.
10. Teran, A. A.; Tang, M. H.; Mullin, S. A.; Balsara, N. P. *Solid State Ionics* **2011**, *203*, 18–21.
11. Kido, R.; Ueno, K.; Iwata, K.; Kitazawa, Y.; Imaizumi, S.; Mandai, T.; Dokko, K.; Watanabe, M. *Electrochim. Acta* **2015**, *175*, 5–12.
12. Wang, G.; Zhu, X.; Rashid, A.; Hu, Z.; Sun, P.; Zhang, Q.; Zhang, L. O. *J. Mater. Chem. A* **2020**, *8*, 13351–13363.
13. Blomgren, G. E. *J. Electrochem. Soc.* **2017**, *164*, A5019–A5025.
14. Costa, L.; Gad, A. M.; Camino, G.; Cameron, G. G.; Qureshi, M. Y. *Macromolecules* **1992**, *25*, 5512–5518.
15. Jones, G. K.; McGhie, A. R.; Farrington, G. C. *Macromolecules* **1991**, *24*, 3285–3290.
16. Pérez, E.; Gómez, M. A.; Bello, A.; Fatou, J. G. *Colloid Polym. Sci.* **1983**, *261*, 571–576.
17. Vallée, A.; Besner, S.; Prud'Homme, J. *Electrochim. Acta* **1992**, *37*, 1579–1583.
18. Chen, J.; Cheng, S. Z. D.; Wu, S. S.; Lotz, B.; Wittmann, J. -C. *J. Polym. Sci. Part B Polym. Phys.* **1995**, *33*, 1851–1855.
19. Siqueira, L. J. A.; Ribeiro, M. C. C. *J. Chem. Phys.* **2005**, *122*, 194911.
20. Fan, J.; Marzke, R.; Sanchez, E.; Angell, C. *J. Non. Cryst. Solids* **1994**, *172–174*, 1178–1189.
21. Kato, Y.; Watanabe, M.; Sanui, K.; Ogata, N. *Solid State Ionics* **1990**, *40–41*, 632–636.
22. Borodin, O.; Smith, G. D. *Macromolecules* **2006**, *39*, 1620–1629.
23. Schmidtke, B.; Hofmann, M.; Lichtinger, A.; Rössler, E. A. *Macromolecules* **2015**, *48*, 3005–3013.
24. Sai, R.; Ueno, K.; Fujii, K.; Nakano, Y.; Tsutsumi, H. *RSC Adv.* **2017**, *7*, 37975–37982.
25. Angell, C. A. *Electrochimica Acta.* **2017**, *250*, 368–375.
26. Das, S.; Ghosh, A. *J. Appl. Phys.* **2015**, *117*, 174103.
27. Matsuoka, S. *J. Res. Natl. Inst. Stand. Technol.* **1997**, *102*, 213–228.
28. Devaux, D.; Bouchet, R.; Glé, D.; Denoyel, R. *Solid State Ionics* **2012**, *227*, 119–127.

29. Pożyczka, K.; Marzantowicz, M.; Dygas, J. R.; Krok, F. *Electrochim. Acta* **2017**, *227*, 127–135.
30. Hayamizu, K.; Akiba, E.; Bando, T.; Aihara, Y. *J. Chem. Phys.* **2002**, *117*, 5929–5939.
31. Abe, T.; Fukuda, H.; Iriyama, Y.; Ogumi, Z. *J. Electrochem. Soc.* **2004**, *151*, 1120–1123.
32. Abe, T.; Sagane, F.; Ohtsuka, M.; Iriyama, Y.; Ogumi, Z. *J. Electrochem. Soc.* **2005**, *152*, A2151–A2154.
33. Minato, T.; Abe, T. *Prog. Surf. Sci.* **2017**, *92*, 240–280.
34. Matsuura, H.; Fukuhara, K. *J. Polym. Sci. Part B Polym. Phys.* **1986**, *24*, 1383–1400.
35. Gámez, F.; Hurtado, P.; Martínez-Haya, B.; Berden, G.; Oomens, J. *Int. J. Mass Spectrom.* **2011**, *308*, 217–224.
36. Wiczorek, W.; Lipka, P.; Żukowska, G.; Wyciślik, H. *J. Phys. Chem. B* **1998**, *102*, 6968–6974.
37. Rey, I.; Johansson, P.; Lindgren, J.; Lassègues, J. C.; Grondin, J.; Servant, L. *J. Phys. Chem. A* **1998**, *102*, 3249–3258.
38. Umebayashi, Y.; Mitsugi, T.; Fukuda, S.; Fujimori, T.; Fujii, K.; Kanzaki, R.; Takeuchi, M.; Ishiguro, S. *J. Phys. Chem. B* **2007**, *111*, 13028–13032.



**YAMAGUCHI
UNIVERSITY**

General conclusions

This work mainly focused on the effect of the coordination structure around Li^+ on the ion transport properties using polyether-based electrolytes. Various polyoxetane derivatives were synthesized with/without nitrile group and alkyl groups on its side chain, and which compared for coordination structure and Li^+ transport properties. I have got insights of the ideal coordination structure and its control method using polymer structural factors, in addition to the simple effect of its characteristics.

- Ether group has high donating ability, which make the coupling of Li^+ transport to polymer segmental motion and contribute to the long-range Li^+ displacement via polymer segmental motion. However, the coordination structure is too stable consisted with the multiple interaction between ether groups and Li^+ .
- Nitrile group has dipole, which induce high dissociability of lithium salt and increase polymer segmental mobility with high Li^+ concentration due to the relaxation of dipole-dipole interaction between nitrile groups. The coordination structure partially contributed by nitrile group was moderately stabilized and provided free volume in the direct vicinity due to its relatively low donating ability and linear structure.
- Alkyl groups on side chain have non-polarity and steric volume, which increase polymer segmental mobility and suppress the anion transport, but which inhibit salt dissociation due to low dielectric constant. The steric restriction also affects the coordination structure. Ethyl group suppress the coordination of adjacent ether groups and contribute to the relaxation of coordination structure. The steric effect on coordination structure is similar even with longer alkyl side chains than ethyl groups.

Previous research had already suggested the negative effect of too stable coordination structure, because which inhibit polymer segmental motion and decrease relative Li^+ conductivity compared than that of anion. This work showed the positive effect of the moderately stabilized coordination structure and the void in the vicinity of coordination structure for efficient Li^+ transport which provides co-contribution of high polymer segmental mobility and frequent and continuous Li^+ exchange. In addition, I can suggest the

simple method to control the coordination structure with the introduction of linear polar group and steric alkyl groups through this work.

There is an urgent demand to improve the safety of electrolytes in order to increase the LIB size and to realize next-generation batteries with even higher performance. Polymer electrolytes can achieve high safety of batteries, but they are required to improve Li^+ conductivity, including polymer segmental mobility, lithium salt dissociability, and efficient Li^+ transport. The control method of the coordination structure suggested from this study is a new design strategy of PEs that can solve fundamental low Li^+ conductivity of polymer electrolytes. I believe that when the design strategy of polymer electrolytes based on moderated coordination structure combines with previous approaches, such as composite material, polymer architecture modification, or monomer design, the next-generation lithium batteries will be realized with ideal polymer electrolytes having sufficient Li^+ conductivity and functionality.

Publication list

Chapter 1

Role of polar side chains in Li⁺ coordination and transport properties of polyoxetane-based polymer electrolytes

Ryansu Sai, Kazuhide Ueno, Kenta Fujii, Yohei Nakano, Naho Shigaki, Hiromori Tsutsumi
Physical Chemistry Chemical Physics **2017**, *19*, 5185–5194.

Chapter 2

Steric effect on Li⁺ coordination and transport properties in polyoxetane-based polymer electrolytes bearing nitrile groups

Ryansu Sai, Kazuhide Ueno, Kenta Fujii, Yohei Nakano, Hiromori Tsutsumi
RSC Advance **2017**, *7*, 37975–37982.

Chapter 3

Importance of Lithium Coordination Structure to Lithium-Ion Transport in Polyether Electrolytes with Cyanoethoxy Side Chains: An Experimental and Theoretical Approach

Riho Matsuoka, Masayuki Shibata, Kousuke Matsuo, Ryansu Sai, Hiromori Tsutsumi, Kenta Fujii, Yu Katayama

Macromolecules **2020**, *53*, 9480–9490.

Acknowledgements

This thesis summarizes the authors studies during 2015–2022 at Tsutsumi laboratory, Division of Life Science, Graduate School of Sciences and Technology for Innovation, Yamaguchi University.

I wish to express my sincere gratitude to *Professor Hiromori Tsutsumi*, Graduate School of Sciences and Technology for Innovation, Yamaguchi University, my main supervisor, for the giving me an affiliation to the laboratory and the research theme for polymer electrolytes.

I greatly appreciate *Associate professor Kazuhide Ueno*, Faculty of Engineering, Division of Materials Science and Chemical Engineering, Yokohama National University, and *Assistant professor Yu Katayama*, Graduate School of Sciences and Technology for Innovation, Yamaguchi University, my supervisors, for the continuous support to my research.

I am particularly grateful to *Professor Kenta Fujii*, Graduate School of Sciences and Technology for Innovation, Yamaguchi University, for the advice to my research, especially to the analysis for spectroscopies and molecular dynamics simulation.

I am also very thankful to *Professor Kenjiro Onimura*, Graduate School of Sciences and Technology for Innovation, Yamaguchi University, *Professor Takashi Nishikata*, Graduate School of Sciences and Technology for Innovation, Yamaguchi University, and *Senior Lecturer Kazuhiro Yamabuki*, Graduate School of Sciences and Technology for Innovation, Yamaguchi University, for the advice to write this dissertation as the examiner.

I want to express my thanks to all the professors, belong to Graduate School of Sciences and Technology for Innovation, Yamaguchi University, for giving me much expertise during the period of my university student and graduate student.

I thank to all the current and graduated members of Tsutsumi laboratory, for having a good time together in the laboratory.

I also thank to my friends for playing around and laughing together.

Finally, I wish to express my gratitude and my love to my family for the supports and the encouragement of my challenging life.

This work was partially supported by Grant-in-Aid for JSPS Research Fellow under Grant Number JP20J14784.

Ryansu Sai

2022